



UNIL | Université de Lausanne

Unicentre

CH-1015 Lausanne

<http://serval.unil.ch>

Year : 2018

INVESTIGATING HUMAN WHITE MATTER ORGANIZATION WITH MULTIMODAL QUANTITATIVE MAGNETIC RESONANCE IMAGING

Slater David

Slater David, 2018, INVESTIGATING HUMAN WHITE MATTER ORGANIZATION WITH
MULTIMODAL QUANTITATIVE MAGNETIC RESONANCE IMAGING

Originally published at : Thesis, University of Lausanne

Posted at the University of Lausanne Open Archive <http://serval.unil.ch>

Document URN : urn:nbn:ch:serval-BIB_B3BCFA1117447

Droits d'auteur

L'Université de Lausanne attire expressément l'attention des utilisateurs sur le fait que tous les documents publiés dans l'Archive SERVAL sont protégés par le droit d'auteur, conformément à la loi fédérale sur le droit d'auteur et les droits voisins (LDA). A ce titre, il est indispensable d'obtenir le consentement préalable de l'auteur et/ou de l'éditeur avant toute utilisation d'une oeuvre ou d'une partie d'une oeuvre ne relevant pas d'une utilisation à des fins personnelles au sens de la LDA (art. 19, al. 1 lettre a). A défaut, tout contrevenant s'expose aux sanctions prévues par cette loi. Nous déclinons toute responsabilité en la matière.

Copyright

The University of Lausanne expressly draws the attention of users to the fact that all documents published in the SERVAL Archive are protected by copyright in accordance with federal law on copyright and similar rights (LDA). Accordingly it is indispensable to obtain prior consent from the author and/or publisher before any use of a work or part of a work for purposes other than personal use within the meaning of LDA (art. 19, para. 1 letter a). Failure to do so will expose offenders to the sanctions laid down by this law. We accept no liability in this respect.



UNIL | Université de Lausanne

Faculté de biologie
et de médecine

Département de Neurosciences Cliniques

**INVESTIGATING HUMAN WHITE MATTER ORGANIZATION WITH
MULTIMODAL QUANTITATIVE MAGNETIC RESONANCE IMAGING**

Thèse de doctorat en Neurosciences

présentée à la

Faculté de Biologie et de Médecine
de l'Université de Lausanne

par

David Slater

Neuroscientifique diplômé de l'Université de King's College London, Royaume-Uni

Jury

Prof. Nicolas Toni, Président
Prof. Bogdan Draganski, Directeur
Dr. Antoine Lutti, Co-Directeur
Prof. Jean-Philippe Thiran, Expert
Prof. Lutz Jäncke, Expert

Thèse n° 225

Lausanne 2018

*Programme doctoral interuniversitaire en Neurosciences
des Universités de Lausanne et Genève*



**UNIVERSITÉ
DE GENÈVE**

Imprimatur

Vu le rapport présenté par le jury d'examen, composé de

Président·e	Monsieur Prof. Nicolas Toni
Directeur·trice de thèse	Monsieur Prof. Bogdan Draganski
Co-directeur·trice de thèse	Monsieur Dr Antoine Lutti
Expert·e·s	Monsieur Prof. Jean-Philippe Thiran Monsieur Prof. Lutz Jäncke

le Conseil de Faculté autorise l'impression de la thèse de

Monsieur David Slater

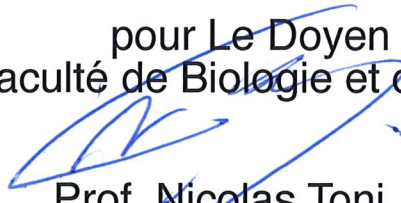
Master of Science in Neuroscience London

intitulée

**Investigating Human White Matter Organization with Multimodal
Quantitative Magnetic Resonance Imaging**

Lausanne, le 20 avril 2018

pour Le Doyen
de la Faculté de Biologie et de Médecine



Prof. Nicolas Toni

Acknowledgements

I would like to thank my supervisors Prof. Bogdan Draganski and Dr. Antoine Lutti for their support and encouragement during my PhD. Working with them has taught me a great deal and provided an environment where I could constantly challenge myself and grow as a researcher. I appreciate the technical support and scientific discussions we have engaged in on a regular basis and the trust that they placed in me and my work.

In addition to my supervisors, I have been fortunate to work with many wonderful and talented individuals within the lab. I would like to thank Lester Melie-Garcia for his guidance and engaging neuroscientific discussions. The PhD students who were already there when I arrived who helped me to get settled and adapt to life in the lab, as well as the later students to arrive who have provided great friendship and support in the final stages of the PhD. I would also like to thank Ferath Kherif and Marzia De Lucia for their input and suggestions during the regular lab meetings.

I thank my lab mates from the LREN, Claudia Modenato, Sandrine Muller, Elisabeth Roggenhofer, Gretel Sanabria-Diaz, Anne Ruef, Sara Lorio, Renaud Marquis, Sandra Martin, Elham Barzegaran, Jing Cui, Borja Rodriguez-Herreros, Lucien Gyger, Maya Jastrzębowska, Elsa Juan, Leyla Loued-Khenissi, Estelle Dupuis and Remi Castella for many happy shared memories in the beautiful city of Lausanne.

During my PhD I have received a great deal of support from my family and friends. I would like to provide a special mention to my parents who have always provided support and encouragement. The wonderful friends I have made in Lausanne have made the experience so enjoyable. I will always remember the lakeside barbeques in summer, days of perfect skiing in the mountains, and various adventure sport activities I was fortunate enough to try during this time.

None of this work would have been possible without the study participants being so generous with their time to come and visit the neuroimaging lab. Additionally, the work in the LREN was supported by grants from the Swiss National Science Foundation, Foundation Synapsis, the Human Brain Project, and the Roger De Spoelberch foundation.

Finally, I would like to thank the thesis jury experts, Prof. Jean-Philippe Thiran and Prof. Lutz Jäncke, and the jury president Prof. Nicolas Toni who kindly agreed to take part in the evaluation of the present work.

Abstract

Quantifying microstructural properties of the human brain's connections is essential for understanding its development, maturation, aging and related diseases. Properties of human brain anatomy change across the lifespan and the white matter is known to play a crucial role in cognitive development, healthy cognition, and cognitive decline in old age. A promising avenue for the investigation of white matter microstructure comes from the development of non-invasive magnetic resonance imaging (MRI) techniques that can quantitatively measure multiple brain tissue properties in a single subject.

Early investigations have begun to map tissue property changes across the lifespan and to link them to topological aspects of network organization. Despite this progress, many studies are limited by their relatively small sample sizes and the use of a small number of tissue measurements that are often non-specific and difficult to interpret directly in neuro-biological terms. In the present thesis, I address these issues by investigating human white matter organization in a large imaging cohort using multi-modal quantitative magnetic resonance imaging (qMRI) across three experimental investigations.

In the first study, I combine qMRI relaxometry measurements of MT, R1 and R2* with diffusion MRI and tractography in a large sample of 801 individuals aged 7-84 years. Robust nonlinear aging effects were observed across tissue measurements and tracts, with tract microstructure measurements expected to peak between the mid-twenties and mid-fifties before losing myelin and changing in microstructural organization with increasing age. I further provide quantitative evidence for the last-in-first-out retrogenesis hypothesis of aging.

In the second study, I apply a data-driven clustering analysis of tissue microstructure changes over the lifespan. I discover five unique white matter modules of synchronized lifespan tissue change that overlap spatially with distinct brain function systems. Pathways within a 'lifespan module' share similar tissue microstructure trajectories over the lifespan. I interpret our findings in the context of ontogenetic modularity along functional and genetic subsystems.

Finally, I investigate the relationships between topological modularity and tissue microstructure in a group of young adult subjects and a large replication dataset taken from the Human Connectome Project (HCP). The results suggest a hierarchically modular organization in human brain anatomical networks with enriched microstructure in the brain's most integrative pathways. My findings support previous data on the structure-function relationships in brain hub regions and concepts of modular organization and specialization in human brain networks.

Results from these studies conducted on an unusually large, single-scanner sample provide one of the most extensive characterizations of human white matter microstructure organization in the present literature.

Résumé

Quantifier les propriétés microstructurelles des connexions cérébrales humaines est essentiel pour comprendre le vieillissement du cerveau et les maladies neuropsychiatriques. La matière blanche du cerveau humain change tout au long de la vie et celle-ci est connue pour jouer un rôle crucial dans le développement, les fonctions exécutives et le déclin cognitif chez les personnes âgées. Le développement de techniques non invasives d'imagerie par résonance magnétique (IRM) - qui permettent de mesurer quantitativement de multiples propriétés des tissus cérébraux chez un même sujet – ouvre de nouvelles perspectives pour l'étude micro-structurelle de la matière blanche.

La plupart des études cartographient les changements de propriétés tissulaires au cours de la vie et les relient aux aspects topologiques de l'organisation du réseau cérébral. Cependant, bon nombre de ces études sont limitées par le nombre réduit d'échantillons ainsi que par l'utilisation d'un petit nombre de mesures tissulaires, souvent non spécifiques et difficiles à interpréter biologiquement.

Dans la présente thèse, j'aborde ces questions en étudiant l'organisation de la matière blanche, autour de trois études expérimentales, basées sur une vaste cohorte de données d'IRM quantitative multimodale (qIRM).

Dans la première étude, j'associe des mesures de relaxométrie qMRI (MT, R1 et R2*), des données de diffusion et de tractographie, sur un large échantillon de 801 individus âgés de 7-84 ans. On peut observer des effets non linéaires marqués du vieillissement des tissus et des connexions cérébrales ; On estime que la microstructure des connexions atteint un pic entre le milieu de la vingtaine et le milieu de la cinquantaine, avant une dégradation progressive de la myéline. Ces observations nous permettent d'apporter des preuves quantitatives de l'hypothèse de retrogénèse « last-in-first-out ».

Dans la deuxième étude, je réalise un clustering multivarié des changements tissulaires au cours de la vie. On observe cinq modules de matière blanche au sein desquels les changements de tissu sont synchronisés au cours du vieillissement. De plus, ces «Lifespan Modules» se chevauchent spatialement avec des systèmes fonctionnels connus. On peut interpréter ces résultats dans le contexte de la modularité ontogénétique dans les sous-systèmes fonctionnels et génétiques.

Enfin, la troisième étude porte sur les relations entre la modularité topologique et la microstructure tissulaire chez un groupe de jeunes adultes, corroborée par un large ensemble de données de vérification issu du Human Connectome Project (HCP). Les résultats suggèrent une organisation modulaire hiérarchique dans les réseaux anatomiques du cerveau humain avec une microstructure enrichie dans les voies les plus intégratives du cerveau. Nos résultats confirment des études préalables sur les relations structure-fonction des « brain hubs » et sur les concepts d'organisation modulaire et de spécialisation dans les réseaux cérébraux humains.

Les résultats de ces études réalisées sur un échantillon aussi large fournissent l'une des caractérisations les plus complètes - dans la littérature actuelle - de l'organisation de la microstructure de la matière blanche chez l'homme.

List of Abbreviations

ACT	Anatomically constrained tractography
AD	Axial diffusivity
AFQ	Automated fiber-tract quantification
AIC	Akaike information criterion
ARC	Arcuate fasciculus
CC. Major	Forceps major of the corpus callosum
CC. Minor	Forceps minor of the corpus callosum
CingC	Cingulum cingulate
CingH	Cingulum hippocampus
CNLLS	Constrained non-linear least-squares
CSD	Constrained spherical deconvolution
CSF	Cerebrospinal fluid
CST	Corticospinal tract
CV	Cross-validation
DTI	Diffusion tensor imaging
DWI	Diffusion-weighted imaging
EM-GMM	Expectation-maximization Gaussian mixture model
EPI	Echo-planar imaging
FA	Fractional anisotropy
FOD	Fiber orientation density
fODF	Fiber orientation distribution function
GLM	General linear model
GM	Grey matter
HARDI	High-angular resolution diffusion imaging
HCP	Human Connectome Project
ICVF	Intracellular volume fraction
IFOF	Inferior fronto-occipital fasciculus
ILF	Inferior longitudinal fasciculus
LME	Linear mixed effects

MD	Mean diffusivity
MPM	Multi-parameter mapping
MRI	Magnetic resonance imaging
MT	Magnetization transfer saturation
NMI	Normalized mutual information
NODDI	Neurite orientation dispersion and density imaging
NOS	Number of streamlines
ODI	Orientation dispersion index
OSLOM	Order statistics local optimization method
P	Participation coefficient
PCA	Principle component analysis
PD*	Effective proton density
qMRI	Quantitative magnetic resonance imaging
$R1=1/T1$	Longitudinal relaxation rate
$R2*=1/T2^*$	Effective transverse relaxation rate
RD	Radial diffusivity
RF	Radio frequency
ROI	Region of interest
SIFT	Spherical-deconvolution informed filtering of tractograms
SLF	Superior longitudinal fasciculus
T1w	Longitudinal relaxation time weighted
TR	Thalamic radiations
UNC	Uncinate fasciculus
WM	White matter
Z	Within-module-degree z-score

Table of Contents

Acknowledgements.....	i
Abstract.....	ii
Résumé.....	iii
List of Abbreviations	iv
Table of Contents.....	vi
List of figures.....	viii
List of tables	ix
1. Introduction.....	1
1.1 Overview and motivation.....	1
1.2 A brief historical perspective on white matter	2
1.3 Contemporary neuroimaging of white matter	5
1.4 White matter changes over the lifespan	11
1.5 Thesis outline	14
2. Evolution of white matter tract microstructure across the lifespan	16
2.1 Introduction	16
2.2 Materials and methods.....	19
2.3 Results.....	25
2.4 Discussion.....	36
3. Lifespan brain tissue changes reveal a modular architecture of human white matter....	43
3.1 Introduction	43
3.2 Materials and methods.....	45
3.3 Results.....	52
3.4 Discussion.....	57
4. Hierarchical modularity and microstructural enrichment of the brain’s integrative architectures	63

4.1	Introduction	63
4.2	Material and methods.....	65
4.3	Results	77
4.4	Discussion.....	85
5.	General Discussion	91
5.1	Main findings.....	91
5.2	Lifespan investigations of the white matter	92
5.3	Tissue microstructure of the human connectome	95
5.4	Methodological considerations	96
5.5	Future perspectives.....	99
	References.....	100
	Supplementary materials	117
	Supplementary methods.....	117
	Supplementary results	122
	Supplementary figures	124
	Supplementary tables	134

List of figures

Figure 1.1. Structural imaging using quantitative MRI	6
Figure 1.2. Dissections of perisylvian language pathways	9
Figure 1.3. Structural brain network reconstructions	10
Figure 1.4. Lifespan trajectories of the white matter	13
Figure 2.1. Major white matter tracts of interest	23
Figure 2.2. The relative timings of tract microstructure peaks	26
Figure 2.3. Association fibre trajectories for MT, R1, R2* and g-ratio	28
Figure 2.4. Association fibre trajectories for FA, MD, ICVF and ODI	29
Figure 2.5. Projection and callosal fibre trajectories for MT, R1, R2* and g-ratio	30
Figure 2.6. Projection and callosal fibre trajectories for FA, MD, ICVF and ODI	31
Figure 2.7. Tissue measurement associations with age, sex, resolution and hemisphere	33
Figure 2.8. Spatial heterogeneity of R1 quadratic aging effects	34
Figure 2.9. Spatial heterogeneity of peak g-ratio values	35
Figure 2.10. Testing the last-in-first-out hypothesis of aging	36
Figure 3.1. MT and ICVF lifespan measures in the white matter network	52
Figure 3.2. Lifespan modules in human white matter	54
Figure 3.3. Variability of lifespan tissue dynamics across lifespan modules	55
Figure 3.4. Interdependencies between lifespan measures	56
Figure 4.1. Hierarchical modularity in human brain anatomical networks	78
Figure 4.2. Consistency of hierarchical modularity between datasets	80
Figure 4.3. Modular node classes of the brain	81
Figure 4.4. Structural characteristics of modular edge class connections	82
Supplementary Figure 2.1. Tissue measurement associations at the higher resolution	124
Supplementary Figure 3.1. Microstructure measurements reliability across resolutions	125
Supplementary Figure 3.2. Aging rate consistency along fascicles	125
Supplementary Figure 3.3. Consistency of clustering results	126
Supplementary Figure 3.4.1. MT lifespan measures and confidence intervals	126
Supplementary Figure 3.4.2. R1 lifespan measures and confidence intervals	127
Supplementary Figure 3.4.3. R2* lifespan measures and confidence intervals	127
Supplementary Figure 3.4.4. MD lifespan measures and confidence intervals	128
Supplementary Figure 3.4.5. ICVF lifespan measures and confidence intervals	128
Supplementary Figure 3.5. Partial correlations of lifespan measures	129
Supplementary Figure 4.1. Edge weight histograms	129
Supplementary Figure 4.2. Modular organization for the CoLauS dataset at level 1	130
Supplementary Figure 4.3. Modular organization for the CoLauS dataset at level 1	131
Supplementary Figure 4.4. Modular edge class microstructure in the HCP dataset	132
Supplementary Figure 4.5. Rich club organization of structural brain networks	132
Supplementary Figure 4.6. Structural characteristics of rich club connections	133

List of tables

Table 4.1. Global network measures	77
Supplementary Table 2.1. Measurement change during maturation and senescence	134
Supplementary Table 2.2. Regression models for MT and R1	135
Supplementary Table 2.3. Regression models for R2* and g-ratio	136
Supplementary Table 2.4. Regression models for FA and MD	137
Supplementary Table 2.5. Regression models for ODI and ICVF	138
Supplementary Table 3.1. Aging model selection using k-fold cross-validation	139
Supplementary Table 4.1. Connector hub nodes	140
Supplementary Table 4.2. Rich club nodes	141

1. Introduction

1.1 Overview and motivation

Understanding how cellular processes in the living brain drive cognitive changes over the lifespan remains a major goal of human neuroscience. While many investigations have focused on the billions of cortical neurons, and trillions of synapses linking them, findings in recent years have made it evident that the white matter is also critically involved in almost every aspect of development, normal behavior, and age related cognitive decline. Though less well studied than the cortex, human white matter comprises approximately half of total brain volume, has been greatly expanded with evolution, and the combined length of connections in the white matter of a typical adult could encircle the Earth more than three times (Schoenemann et al., 2005; Walhovd et al., 2014).

Evidence from clinical neuroanatomy investigations indicates that white matter underpins the communication of distributed neural networks, often conceptualized as the structural basis of evolved human behaviors, and that focal lesions to the white matter can result in disconnection syndromes with particular clinical phenotypes (Catani et al., 2012; Geschwind, 1965). In recent decades the study of white matter organization in health and disease has been greatly aided by the advent of magnetic resonance imaging (MRI), revealing how white matter lesions can lead to disrupted cognition and disease states (Fields, 2008). Advanced MRI methodologies are now capable of non-invasively probing many cellular processes in the white matter including axonal diameters, packing densities, myelin concentrations, and glial organization. These microstructural imaging methods are beginning to be applied to the study of white matter development during childhood (Dean et al., 2014; Deoni et al., 2012; Yeatman et al., 2012a), across the human lifespan (Callaghan et al., 2014; Draganski et al., 2011; Lebel et al., 2012; Yeatman et al., 2014), and in old age (Bender and Raz, 2015; Bennett et al., 2010; Cox et al., 2016). Further efforts are being made to study the microstructural organization of white matter pathways in relation to their role in network communication (Collin et al., 2014; Mancini et al., 2017; van den Heuvel and Yeo, 2017).

The goal of this thesis is to investigate patterns of white matter microstructure organization across the human lifespan using multimodal MRI in a sample of the general

population. The data provides a benchmark for healthy white matter across a large portion of the lifespan using multiple microstructural tissue measurements taken within the same cohort. Due to the quantitative nature of the measurements, an individual scanned at any location in the world could be compared with the normative curves outlined in this work (Yeatman et al., 2014). In a further clustering analysis, we reveal a set of distinct ‘lifespan modules’ which each evolve across the lifespan with a unique microstructural fingerprint. These modules align along broad functional lines and we hypothesize that certain neuropsychiatric disorders may be related to specific dysfunction within a module (Alexander-Bloch et al., 2014). Future work will be needed to test these predictions in clinical populations. Finally, we apply a network based analysis in a subset of young adults to investigate the relationships between white matter microstructure and network topology (Collin et al., 2014; van den Heuvel and Yeo, 2017). The combination of multiple microstructural measurements to assess the organizational principals of human white matter provides an important step toward understanding the biological mechanisms linking white matter to cognition.

1.2 A brief historical perspective on white matter

The first person to clearly distinguish between white and grey matter tissue types in the brain was Andreas Vesalius in 1543 as part of his seminal work *De Humani Corporis Fabrica* (Vesalius, 1543). These results stirred much debate at the time as they challenged the long-held ideas of Galen dating back the second century BC, who had proposed a ‘ventricular theory of the brain’ in which it was the ventricular reservoirs that held specialized functions and communicated with the body via hydraulic mechanisms (Clarke and O’Malley, 1996). The new observations by Vesalius stirred a greater interest in neuroanatomy among Renaissance scholars with Arcangelo Piccolomini describing in finer detail the contrast between the soft ‘ashen-colored’ (grey) and a more solid white body of the brain (Piccolomini, 1586). Continued developments in microscopy and post-mortem tissue preparations revealed the fibrous structure of the brain white matter leading to the first theories of white matter as being composed of tubular filaments (Descartes, 1662; Steno, 1669; van Leeuwenhoek, 1719).

Despite the progress being made in elucidating certain anatomical principals of the brain, the prevailing mechanistic theory of white matter was still based on hydraulic action. At the time this understanding seemed self-evident due to the high levels of water content in the

brain and existing ventricular theories of cognition (Catani et al., 2013). It took the discovery of 'animal electricity' (Galvani, 1791) and extensive investigation in the early nineteenth century to revolutionize our understanding of the electrical properties of the brain. New recording methods were introduced to study the action potential and signal conduction in muscles and peripheral nerves (Bernstein, 1868; Bois-Reymond, 1848; Matteucci, 1830), laying the foundations for modern electrophysiology.

During the second half of the nineteenth century advanced microscopy techniques revolutionized the study of brain anatomy once more. For example, the introduction of the myelin stain by Carl Weigert and Vittorio Marchi, and the development of the serial precision microtome greatly improved the visualization of nerve fibers under the microscope (Bentivoglio and Mazzarello, 2009). Around the same time clinicians began to apply the clinical-anatomical correlation method to better understand the functional correlates of brain topology (Broca, 1861), and disorders of the nervous system began to be described in terms of either cortical damage or as disconnection syndromes (Déjerine and Dejerine-Klumpke, 1895). From the culmination of these findings an idea began to emerge, that the brain should be considered as an interconnected whole and that a true understanding of the brain could only be achieved with a precise description of its connections (Déjerine and Dejerine-Klumpke, 1895; von Bechterew, 1900).

By the early twentieth century two important lines of inquiry had emerged. In the first, detailed descriptions of local micro-circuitry were being made (Cajal, 1893; Golgi, 1873). From these investigations Ramon y Cajal was able to establish certain fundamental laws of neuronal organization such as the arrangement of dendrites and axons as the inputs and outputs of neuronal cells. The astonishing depth of insight gained by Ramon y Cajal has formed much of the basis of modern neuroscience. In the second line, whole brain maps of cyto- and myelo-architecture were being produced leading to the definition of distinct cortical regions and subdivisions (Brodmann, 1909; Campbell, 1905; Flechsig, 1896), as well as early descriptions of maturational trajectories in white matter projection tracts (Flechsig, 1896). These studies led to the idea of regional specialization and the continued division of brain grey and white matter along anatomical lines. These two branches set up separate fields of investigation at greatly differing micro- and macro-anatomical scales. Today, it remains an important goal in

human neuroscience to bridge the gap between neuroanatomical findings at multiple spatial scales (Park and Friston, 2013; van den Heuvel and Yeo, 2017).

Through the mid-twentieth century a great deal of effort was made to describe neuroanatomical and functional correlates in the experimental animal using electrophysiological and histological techniques. Such approaches are exemplified by the work of Mountcastle and Powell (1959) in the somatosensory cortex of the monkey and the work of Hubel and Wiesel (1962) in the visual cortex of the cat. In such investigations single- or multi-cell recordings were made, axonal tracts traced using injected dyes or microlesions, and then the data combined with cytoarchitectural observations made in the same specimen under the microscope post-mortem. Key organizational principles of the brain were discovered including the columnar architecture of the cortex. Concurrent lesion-symptom mapping investigations in the monkey combined with intracortical recordings and tract tracing reinvigorated network based approaches to brain function (Mishkin, 1966). By the end of the 1960s novel tract tracers had been developed which operated on the active transport of proteins and other elements along axonal fibers. After injection into a precisely determined cortical or subcortical region, the tracers were taken up by a neuron and transported to its axonal or dendritic terminations (Morecraft et al., 2009). Investigations utilizing these tract tracing developments led to a wider understanding of the pathways through the deep white matter, leading to concepts such as hierarchical organization, feed-back and feed-forward connectivity, and parallel organization (Felleman and Van Essen, 1991; Mesulam, 1998). Of the connectivity-based findings from the late-twentieth century, the near complete description of neuronal wiring in the nematode worm *Caenorhabditis elegans* using electron microscopy (White et al., 1986) and the detailed description of hierarchical organization in the primate visual system (Felleman and Van Essen, 1991) mark milestone achievements.

One limitation of these animal model approaches is that it remains unclear how much can be extrapolated to humans. Such extrapolations may work as good approximations in sensory and motor networks, but there is far less certainty when looking at highly evolved systems supporting other aspects of cognition such as executive control or language (Rilling et al., 2008; Schoenemann et al., 2005). Furthermore, the sheer invasiveness of the described techniques makes it impossible to perform equivalent investigations in humans, excluding basic histological assessments in post-mortem samples from typically older individuals. Given

the limitations of direct investigations in humans it was the emergence of modern neuroimaging techniques that heralded a new era of human neuroscience research, leading to discoveries and non-invasive methods of investigation that were previously unavailable.

1.3 Contemporary neuroimaging of white matter

Here we provide an overview of some of the major developments in human neuroimaging of the white matter with emphasis on the methods employed in later sections of this thesis. The purpose of this section is to introduce important concepts and to put them in context. More detailed descriptions of key methodologies, including relevant equations, are saved for the material and methods sections of later chapters which have been organized into a manuscript form that can be read and understood in isolation if so desired by the reader.

Structural MRI

A fundamental change to the way in which human neuroscience was conducted came in the 1980s with the advent of MRI technologies. MRI soon became the method of choice for diagnosing a number of disorders including ischemia, for which white matter lesions appeared as 'unidentified bright objects' (Kertesz et al., 1988) before being later classified as regions of water accumulation in the presence of damaged myelin (Anderson et al., 2014). Early investigations made use of the different contrasts between grey and white matter on specially tailored images to assess volumetric differences between subject groups (Gur et al., 1999; Inder et al., 1999; Pfefferbaum et al., 1992). These techniques typically classified the brain images into grey, white and cerebrospinal fluid (CSF) tissue types and / or manually delineated regions of interest (ROIs) by hand before comparing across groups. As neuroimaging methods further developed, more standardized computational neuroscience tools were deployed which could automate much of the image preprocessing, segmentation, normalization and analysis procedures (Ashburner, 2009; Friston and Holmes, 1995). Of these techniques, voxel-based morphometry (VBM) became a staple of the neuroimaging research toolbox, allowing statistical models of tissue volume differences to be tested at the voxel level across the whole brain (Ashburner et al., 1998; Good et al., 2001).

Despite the widespread use of VBM (2000+ studies on PubMed as of Jan 2018), volumetric measures derived from the most widely used T1-weighted images are additionally sensitive to changes in contrast unrelated to volume (Lorio et al., 2014). Such non-specificity has led to a

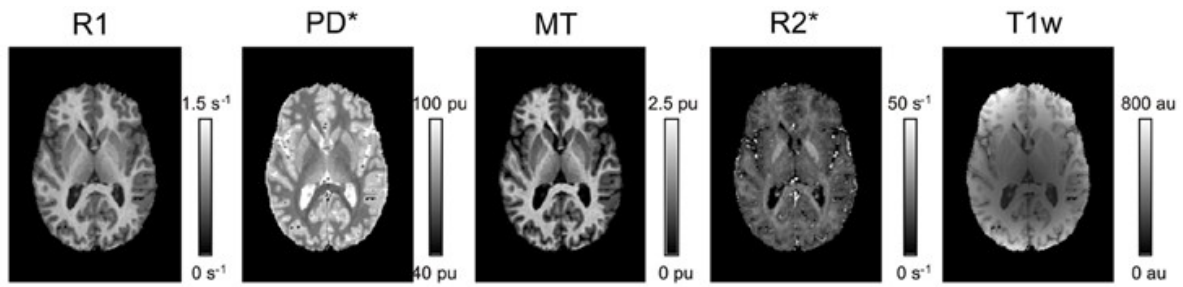


Figure 1.1. Structural imaging using quantitative MRI. Axial slices through MPM derived R1, PD*, MT, R2* and T1w images. The four MPM images provide quantitative measures of tissue microstructure properties and are inherently corrected for issues such as receiver coil bias. In contrast T1w images provide only a relative measure of tissue contrast which makes direct comparisons across sites and timepoints more challenging. Adapted from Weiskopf et al. (2013).

number of contradictory results and made the interpretation of volumetric studies challenging (Walhovd et al., 2016). Given that multiple ongoing tissue processes are in action across the lifespan, voxel-based quantification (VBQ) was suggested as a method to adapt the well-established VBM methodologies to quantitative-MRI (qMRI) images that provide increased measurement specificity to brain microstructure properties (Draganski et al., 2011). In addition to the increased specificity, qMRI also provides absolute measures which can be compared directly across sites and timepoints, allowing for more direct comparisons and pooling of results (Tofts, 2004). A whole host of qMRI techniques have been developed which now make it possible to quantitatively measure and model biological tissue properties such as myelin, iron and water content in the living human brain (Deoni et al., 2012; Mezer et al., 2013; Tofts, 2004; Weiskopf et al., 2013a).

One of these qMRI techniques termed multi-parameter mapping (MPM) makes quantitative measurements of the longitudinal relaxation rate ($R1=1/T1$), effective transverse relaxation rate ($R2^*=1/T2^*$), effective proton density (PD^*), and the magnetization transfer saturation (MT) (Fig. 1.1). Detailed investigations of the biophysical basis of these measurements have shown that the contrasts of MT and R1 are principally driven by differences in local myelin content (Draganski et al., 2011; Lutti et al., 2014; Stanisz et al., 1999), $R2^*$ to iron deposition (Fukunaga et al., 2010; Stüber et al., 2014), and PD to voxel water volume (Lin et al., 1997). The short acquisition times, inter-site reproducibility and specificity of the measurements to microstructural processes makes MPM imaging an efficient and reliable tool for the study of white matter organizational principles (Draganski et al., 2011; Weiskopf et al., 2013a).

Diffusion-weighted MRI

A major development in the study of human white matter came from the application of MRI based diffusion-weighted imaging (DWI) (Thomsen et al., 1987; Wesbey et al., 1984) and later diffusion tensor imaging (DTI) (P. Basser et al., 1994; Pierpaoli and Basser, 1996). The DTI model appreciates that highly organized cellular structures, such as tightly packed coherent axonal fibers, create an environment in which water diffusion can deviate substantially from isotropy. The simplest way to model the ‘anisotropic’ water diffusion measured in the brain was to describe the measurements using a symmetric diffusion tensor (P. Basser et al., 1994). In this fashion an ellipsoid tensor is used to model the orientation and extent of Gaussian diffusion along three principle axes (for a detailed review see Jones, 2008). By measuring local water diffusion properties around the highly organized cytoarchitecture of the brain, DTI established novel insights into the structure and orientation of white matter fiber bundles (Jones and Williams, 2002; Kraus et al., 2007; Pajevic and Pierpaoli, 2000).

One of the most useful properties of DTI is that it is easy to derive summary statistics about the local diffusion environment. Two of the most widely used DTI measures are mean diffusivity (MD) which averages diffusivity along the three axes, and fractional anisotropy (FA) which measures the fraction of the tensor that can be associated with anisotropic diffusion, scaling from 0 (isotropic) to 1 (fully anisotropic). Biophysical investigations have shown that the diffusion signal driving MD and FA is principally governed by local interactions with cellular membranes (Beaulieu, 2002). The difference between the two measures is that MD is most sensitive to how free (unhindered) the water molecules are by their cellular environment, while FA principally describes the level of cellular membrane coherence in the local environment. These measures have been used successfully to observe white matter abnormalities in clinical populations (Forkel et al., 2014; Jones et al., 2006; Kraus et al., 2007; Stricker et al., 2009), and to describe normal developmental and aging trajectories across the lifespan (Barnea-Goraly et al., 2005; Lebel et al., 2012; Sexton et al., 2014; Westlye et al., 2010b).

Though DTI has proven very successful at measuring white matter microstructure differences among individuals, the last decade has seen a growing appreciation of its limitations. Firstly, the DTI model assumes Gaussian diffusion along all measurement directions. This assumption may be a good approximation in coherent white matter regions but breaks down when

multiple fiber populations are present, as intra-voxel crossing, fanning or bending cannot be adequately described by a single tensor (Jones, 2008). Indeed recent evidence suggests that up to 90% of white matter voxels may contain crossing fiber populations (Jeurissen et al., 2012). Secondly, when trying to interpret the biological properties driving observed difference in FA it becomes extremely challenging as FA is potentially sensitive to axonal packing densities, fiber crossing, fiber dispersion, myelination, and cellular membrane permeability. This has led a number of researchers to incorrectly label FA differences as reduced 'white matter integrity' regardless of their precise biological origins (Jones et al., 2013).

In an attempt to overcome some of the limitations of DTI a number of biophysical models have been proposed to more precisely model the diffusion signal (Alexander et al., 2010; Assaf and Basser, 2005; Panagiotaki et al., 2012; Zhang et al., 2012). In recent years the neurite orientation dispersion and density imaging (NODDI) model of diffusion (Zhang et al., 2012) has attracted particular interest within the imaging community due to its increased specificity over DTI measures and the clinically feasible scan times required for the acquisition (Chang et al., 2015; Colgan et al., 2016; Cox et al., 2016; Kodiweera et al., 2016; Kunz et al., 2014). The NODDI model characterizes white matter by modelling three distinct tissue compartments: a restricted component within a set of dispersed axons; an extracellular component of hindered diffusion; and an isotropic component to compensate for CSF partial volume effects. The model estimates maps for the intracellular volume fraction (ICVF), orientation dispersion index (ODI) and CSF volume fraction, and these measures have been shown to be highly sensitive to the effects of age related tissue change (Cox et al., 2016).

Diffusion tractography

In addition to the application of diffusion imaging for microstructural assessments of the brain, early efforts utilizing DTI realized that the principle direction of diffusion could be used to model the trajectories of major white matter fiber bundles by piecing together discrete (voxel-based) estimates of local fiber orientations (Conturo et al., 1999; Jones et al., 1999). The connection estimates made in this manner are often referred to as 'streamlines'. Diffusion tractography based techniques could now, for the first time, non-invasively map the major fiber bundles of the brain, revealing tracts that had previously only been described in animal



Figure 1.2. Dissections of perisylvian language pathways. a) Dejerine's (1895) and b) Klinger's (1956) post-mortem dissections of the arcuate fasciculus. c) A virtual in-vivo dissection of the arcuate fasciculus using DTI tractography. Images adapted from a) Déjerine and Dejerine-Klumpke (1895), b) Ludwig and Klingler (1956), and c) Catani et al. (2002).

models or from the use of time consuming preparations in post-mortem tissue (Fig. 1.2 ; Catani et al., 2002; Déjerine and Dejerine-Klumpke, 1895; Ludwig and Klingler, 1956). We will use the terms fiber bundle, fascicle and tract interchangeably to describe the major white matter pathways of the brain.

The use of diffusion tractography has become a crucial tool for both the discovery of previously undescribed white matter organization within the human brain (Behrens et al., 2003; Thiebaut de Schotten et al., 2011) and, by sampling tissue microstructure measurements along a pathway, the assessment of disease states and lifespan changes within the white matter (Forkel et al., 2014; Jones et al., 2006; Kanaan et al., 2006; Lebel et al., 2012; Yeatman et al., 2014). Over time more advanced techniques, known as high-angular resolution diffusion imaging (HARDI), have been developed to overcome some of the limitations of DTI's Gaussian assumptions by modeling multiple fiber populations within a voxel, facilitating the delineation of crossing fiber bundles in the brain (Dell'acqua et al., 2010; Descoteaux et al., 2007; Tournier, 2010; Tournier et al., 2007; Wedeen et al., 2005).

Connectomics

One of the most recent developments in the study of human white matter stems from a desire to map, across multiple scales, a full description of human brain wiring - the human connectome (Sporns et al., 2005). Connectomic approaches to the brain make use of well-developed theories from the field of graph theory to describe network properties at global (whole-brain) and regional (local) levels of organization (Rubinov and Sporns, 2010). At the macroscopic level, diffusion tractography represents the only available tool to non-invasively map the trajectories of white matter pathways within the living human brain.

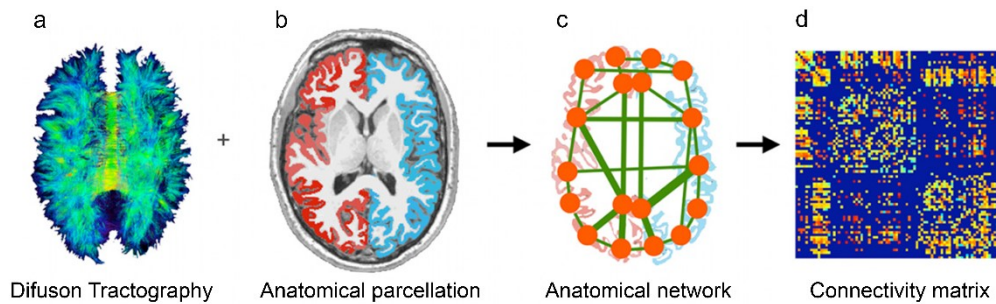


Figure 1.3. An illustration of the different steps of a typical structural brain network reconstruction. a) Diffusion tractography is performed across the white matter (whole-brain) and b) matched with an anatomical parcellation of the grey matter estimated on a high resolution anatomical image. c) The terminal end-points of the tractography streamlines are mapped to their nearest brain region (node, orange circles) to define the set of network connections (edges, green lines). d) Structural brain network can be described by a connectivity matrix, whereby each region-by-region connection is represented as an element of the matrix, and the values define either the total number of connecting streamlines (weighted graph) or a binary indication of a connection's presence (binarized graph). Adapted from van den Heuvel and Sporns (2011).

Hagmann et al. (2008) were the first to develop an analysis framework for modeling the human brain as a network composed of cortical regions (nodes) interconnected by tractography derived streamlines (edges) (Fig. 1.3a-c). The inter-regional connections of the brain are then summarized and described as a graph (connectivity matrix) which is amenable to the tools of graph theory (Fig. 1.3d), allowing the estimation of network properties such as network efficiency, modularity and centrality (Rubinov and Sporns, 2010). The findings of these authors and others have shown that a number of highly connected regions, densely situated along the midline of the brain, occupy a central place in the brain's overall architecture and network topology (Bassett et al., 2008; Bullmore and Sporns, 2009; Hagmann et al., 2008). These 'hubs' have been of particular interest from a network perspective, as central regions in a network are known to be particularly important for integration across segregated systems and for the efficient communication of information. In addition to being densely connected to the network, a number of key brain regions have been shown to be 'richly' inter-connected with each other, the so called 'rich club' of the brain (van den Heuvel et al., 2012; van den Heuvel and Sporns, 2011). These findings are suggestive of a densely and widely connected anatomical subnetwork in mammalian brains which is responsible for attracting and integrating information.

Further to the study of network topology, it is becoming increasingly clear that additional factors of brain organization will be required to understand how network organization

supports and facilitates complex behavior in humans (Fields et al., 2015; Scholtens et al., 2014). Preliminary investigations have begun to investigate the microstructural investment of brain regions (both grey and white matter) as related to their location in the network (Collin et al., 2014; Mancini et al., 2017; Scholtens et al., 2014), however the degree to which the brain's developmental processes invest additional resources in the most crucial communicative pathways remains unclear (Bullmore and Sporns, 2012).

1.4 White matter changes over the lifespan

Evidence from animal models

Invasive studies in animal models and those using post-mortem histology provide an important backdrop from which to interpret neuroimaging results of tissue changes across the human lifespan. Beginning just before birth and continuing throughout childhood and young adulthood axons increase in caliber and oligodendrocytes wrap these axons in myelin (Emery, 2010). Despite a large number of underused axons being pruned during development to free space for more established axons (LaMantia and Rakic, 1994, 1990), interstitial space is reduced as the outer diameters of the axons increase with each additional layer of myelin leading to a higher tissue density in the white matter (Dobbing and Sands, 1973).

Myelination processes are determined by a combination of intrinsic genetic and extrinsic environmental factors (Barres and Raff, 1993; Douglas Fields, 2015; Emery, 2010). The precise levels of myelination are influenced by the electrical activity of axons, meaning that myelination levels are changed by experience (Barres and Raff, 1993; Douglas Fields, 2015; Ishibashi et al., 2006). There is further evidence to suggest that axonal calibers may be influenced by experience, increasing in size in response to electrical activity (Fancy et al., 2011; Voyvodic, 1989). Levels of myelination and axonal calibers play a pivotal role in network communication, controlling conduction velocities and the signaling properties emitted by a pathway (Caminiti et al., 2009; Perge et al., 2009, 2012).

During young adulthood through middle age the white matter experiences a period of relative stability where degraded myelin is continually replaced with remyelinated sheaths (Fancy et al., 2011) before rapid changes to the white matter begin to occur in later life. Although it has been shown that the number of cortical neurons remains fairly constant with age, there is

extensive axonal loss and degeneration within the white matter (Peters, 2002). Axonal packing densities in the optic nerve have been observed to reduce by 40% in old as compared to mature monkeys (Sandell and Peters, 2001). The degeneration of axonal fibers is accompanied by a loss of their myelin sheaths, with large increases in the number of astrocyte and microglia cell populations in aging fascicles each containing substantial amounts of phagocytosed myelin (Peters and Sethares, 2003). In addition to the loss of myelin, new oligodendrocytes develop from progenitor cells and fanning astrocyte processes expand to fill the spaces left by the degenerating tissue (Sandell and Peters, 2002).

Postmortem lifespan studies in the human brain are more challenging due to the difficulty in obtaining samples from healthy individuals across the entire lifespan; rather, most available samples are taken from elderly individuals or patients who were unwell before death. Despite the challenges of conducting postmortem lifespan studies, a variety of structural brain changes have been reported including for overall brain weight (Dekaban and Sadowsky, 1978), myelination (Benes et al., 1994; Yakovlev and Lecours, 1967), and synaptic density (Huttenlocher, 1979; Huttenlocher and de Courten, 1987).

Neuroimaging results

Early investigations of lifespan brain changes in humans using MRI typically tested differences in white matter volume with age. White matter volumes are seen to undergo ‘inverted U-shaped’ trajectories, increasing in volume during childhood and adolescence, attaining a peak value at around the fourth decade, before declining in volume in later life (Good et al., 2001; Lebel et al., 2012; Walhovd et al., 2011; Westlye et al., 2010b) (Fig. 1.4a). DTI based studies report robust increased in FA and decreases in MD during development across the majority of the brains major tracts (Barnea-Goraly et al., 2005; Eluvathingal et al., 2007; Lebel et al., 2008; Schmithorst et al., 2002). In later life DTI results demonstrate opposing trends, with decreases in FA and increases in MD during old age (Abe et al., 2002; Ota et al., 2006; Pfefferbaum et al., 2000). Fewer studies have explicitly assessed DTI changes

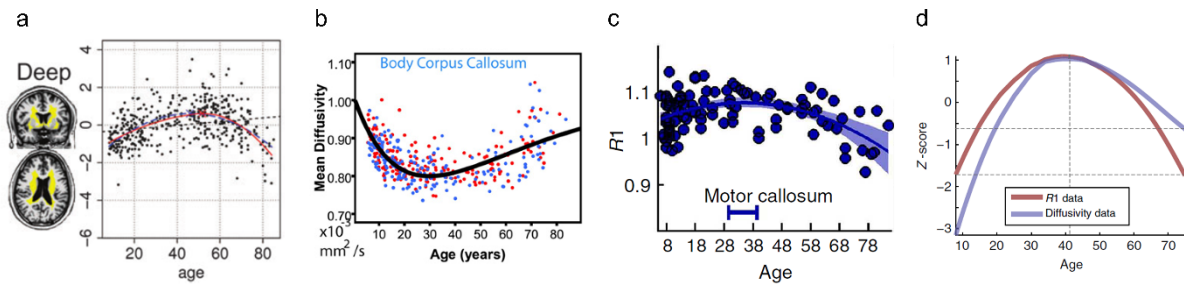


Figure 1.4. Lifespan trajectories for a) deep white matter volume, b) MD measures in the fibers of the corpus callosum midbody, and c) R1 measured in the fibers of the motor callosum. d) MD and R1 follow significantly different lifespan trends suggestive of their sensitivity to separate tissue processes. Adapted from a) Westlye et al. (2010), b) Lebel et al. (2012), c) & d) Yeatman et al. (2014).

across the full lifespan, though these studies demonstrate clear nonlinear aging trends in the white matter (Lebel et al., 2012; Westlye et al., 2010b; Yeatman et al., 2014) (Fig. 1.4b).

White matter is made up of many different tissue types including axons, myelin, astrocytes, oligodendrocytes and microglia, and each of these cell types might change over the typical lifetime according to its own unique time course (Wandell and Yeatman, 2013; Yeatman et al., 2014). Such observations have motivated recent studies to apply multiple tissue measurements within the same aging cohort to provide complimentary evidence of the multiple ongoing and concurrent tissue processes (Cox et al., 2016; Yeatman et al., 2014). In a large aging cohort of 3,513 subjects aged 44-77 years, Cox et al. (2016) combined DTI and NODDI measures of tissue microstructure to investigate (nonlinear) aging effects of the major fascicles of the brain. The authors found that MD was the most sensitive measure to aging effects with the largest changes observed in thalamic radiation and association fiber bundles. In contrast, the pathways supporting motor and visual functions were relatively stable in old age.

In a separate study Yeatman et al. (2014) also combined multiple tissue measurements, this time combining DTI and quantitative R1 in a lifespan cohort of 102 individuals aged 7-85 years. In their analysis they focused on a comparison of MD and R1, using the later as an index for myelination. They found substantial differences in the amount of observed tissue change across white matter fascicles. Interestingly MD and R1 were also seen to follow different aging trends with R1 being well described by a symmetric (quadratic) aging curve and MD being better represented by an asymmetric Poisson curve (Fig. 1.4c-d). The authors interpret these

findings as evidence for multiple biological processes driving changes in white matter tissue properties over the lifespan.

1.5 Thesis outline

In the following chapters three research projects are outlined in full manuscript form. Here I will provide a summary of the projects and their principle contributions.

Evolution of white matter tract microstructure across the lifespan

Age associations are assessed in 20 major white matter tracts of the brain in a large lifespan cohort of 801 individuals aged 7 to 84 years. The combination of multiple qMRI measures provides an extensive characterization of lifespan tissue change, contributing to a greater understanding of myelination and white matter organization principles from adolescence through old-age. Peak ages of maturation are reported across tracts and microstructure measurements, with peaks typically observed between the mid-twenties and mid-fifties, though we report substantial spatial heterogeneity and heterochronicity. A correlational analysis of maturational timings versus quadratic aging effects provides supportive evidence for the last-in-first-out retrogenesis hypothesis of aging, suggesting a relationship between maturational timing and rates of decline in old-age.

Lifespan brain tissue changes reveal a modular architecture of human white matter

We describe human brain connections as a graph using the connectome framework outlined in Fig. 1.3. Tissue microstructure measurements were sampled along the edges of the network and these edges modeled for aging effects across individuals. After summarizing key maturational and senescence parameters for each edge and measurement, a clustering algorithm was used to group edges into modules (clusters) of coherent multivariate tissue change. A five-module solution occupied a local maximum in the mean model responsibility and divided the brain's white matter into distinct functional-anatomical subsystems. We relate the findings to previous work investigating genetic gradients in the brain, neurodevelopmental modules in the cortex, and the possible link to brain disorders.

Hierarchical modularity and microstructural enrichment of the brain's integrative architectures

Based on their interconnectivity profiles, cortical regions subdivided into 12 modules which further grouped into 4 and then 2 larger modules at progressively higher levels of

network hierarchy. The use of an information-based measure found the modular architecture to be highly similar in a replication dataset, both in terms of module-by-module and full modular organization comparisons. Depending upon the characteristic topological role that a pathway plays in the network, distinct microstructural fingerprints exist, suggesting that the most integrative pathways of the brain exhibit higher wiring costs, elevated levels of myelination and increased white matter organization. We compare our results to previous studies that have linked topological measures to tissue microstructure as well as exploring how our findings align with current understanding of the brain's network hub architectures.

2. Evolution of white matter tract microstructure across the lifespan

2.1 Introduction

In-depth understanding of brain changes across the lifespan is required to link maturational processes during childhood to degenerative processes of old age and to provide an informed basis from which to study patterns of divergence in brain disorders. Lifespan studies of the postmortem human brain have demonstrated structural changes to total brain volume (Dekaban and Sadowsky, 1978), myelination (Benes et al., 1994; Yakovlev and Lecours, 1967) and synaptic density (Huttenlocher, 1979; Huttenlocher and de Courten, 1987). Neuroimaging studies report changes to regional brain volumes (Bartzokis et al., 2001; Good et al., 2001; Walhovd et al., 2011), cortical thickness (Sowell ER et al., 2003; Storsve et al., 2014; Westlye et al., 2010a), microstructural organization (Cox et al., 2016; Kochunov et al., 2012; Lebel et al., 2012; Westlye et al., 2010b; Yeatman et al., 2014) and myelination (Callaghan et al., 2014; Grydeland et al., 2013; Li et al., 2014; Yeatman et al., 2014) across much of the lifespan. These studies typically describe rapid changes to brain organization during childhood and adolescence, followed by a slowing of developmental processes in young adulthood, before achieving a maturational peak, reversing in trend, and declining in later adulthood and old age.

Findings in recent years have made it apparent that the white matter (WM) plays a critical role in cognitive development, normal cognition and cognitive decline in old age (Ameis and Catani, 2015; Bells et al., 2017; Filley and Fields, 2016). Most of the studies investigating age related changes in human white matter have used diffusion tensor imaging (DTI; Basser et al., 1994). These investigations report robust increases in fractional anisotropy (FA) and decreases in mean diffusivity (MD) during childhood and adolescence (Barnea-Goraly et al., 2005; Eluvathingal et al., 2007; Schmithorst et al., 2002), and reverse trends in old age (Abe et al., 2002; Cox et al., 2016; Ota et al., 2006; Pfefferbaum et al., 2000). A number of recent studies have extended investigations to cover most of the lifespan, revealing the full extent of nonlinear ‘U-shaped’ and ‘inverted U-shaped’ lifespan trajectories within the major WM tracts, typically reaching peak maturation between the early twenties and mid-forties (Kochunov et al., 2012; Lebel et al., 2012; Westlye et al., 2010b; Yeatman et al., 2014).

One potential confound of the DTI analyses relates to the inherent non-specificity of the measurement. Observed changes in FA may be due to changes in any combination of axonal dispersion, fiber crossing, myelination or axonal densities (Beaulieu, 2002; Jones et al., 2013). In an attempt to provide more easily interpreted and specific microstructural measures, the neurite orientation dispersion and density imaging (NODDI) biophysical model of diffusion has been proposed (Zhang et al., 2012). The NODDI model aims to disentangle the effects of fiber dispersion and axonal packing into two independent and clinically relevant measures, the intracellular volume fraction (ICVF) and the orientation dispersion index (ODI). The few studies that have investigated aging effects using NODDI point towards increased sensitivity to aging differences as compared to DTI, increased fiber dispersion with age and increased axonal packing during adolescence and young adulthood (Billiet et al., 2015; Chang et al., 2015; Kodiweera et al., 2016). The investigation of nonlinear lifespan trajectories was precluded in these studies due to the relatively small sample sizes (47-66 participants) and the inclusion of few subjects over the age of 55 years. One recent study investigated aging effects in later life (45-77 years) using the NODDI model in a large cohort of over 3000 individuals (Cox et al., 2016). The findings from this work suggest that axonal packing decreases in old age and that, for most tracts, a nonlinear model better approximates data.

Beyond the microstructural measures provided by diffusion weighted imaging (DWI), the development of non-invasive MR biomarkers for myelin has facilitated early investigations into myelin development and decline across the lifespan. One such methodology, multi-parameter mapping (MPM; Weiskopf et al., 2013), provides estimates for the magnetization transfer (MT) and relaxation rates R_1 and R_2^* , each providing a level of sensitivity to local myelination and/or iron deposition (Draganski et al., 2011; Fukunaga et al., 2010; Lutti et al., 2014; Stüber et al., 2014). Preliminary findings suggest significant demyelination in human WM with age (Callaghan et al., 2014; Draganski et al., 2011), particularly in later life after myelination has matured to a peak density before reversing in trend and declining with age (Li et al., 2014; Yeatman et al., 2014). Progressive myelin loss may be caused by defective cholesterol clearance mechanisms which lead to an imbalance between de-myelination and re-myelination processes in the brain (Cantuti-Castelvetri et al., 2018). Early evidence suggests that the age at which myelination peaks across different WM tracts varies from the late-twenties to mid-forties (Yeatman et al., 2014), though the precise timing of the peaks may

depend upon a measurement's specificity to myelin (Li et al., 2014). As an extension to myelin imaging, recent work has proposed a method for non-invasively estimating the g-ratio (Stikov et al., 2015), a fundamental property of axonal organization and conduction that describes the proportion of myelin investment in relation to an axon's caliber. Preliminary investigations of g-ratio change across the lifespan in small imaging cohorts (n = 38-92) have reported linear increases with age in the deep WM (Cercignani et al., 2016), with little age related change observed across the mid-sagittal portion of the corpus callosum (Berman et al., 2017).

Of the previous studies investigating microstructural changes over the lifespan, investigations typically fall into either region-of-interest or diffusion tractography based studies. Although a tractography based approach offers robust estimates of microstructural tissue properties across an entire tract, does not require spatial registration to standardized space, and has been shown to be more reliable than a region-of-interest analysis (Kanaan et al., 2006), the time investment required to accurately dissect the major pathways using manual methods (Catani et al., 2002) has made tractography analyses challenging, particularly in large cohorts. To overcome this obstacle, automated fiber-tract quantification (AFQ) methodologies have been developed (Yeatman et al., 2012b) and successfully applied to the study of tissue microstructure across the lifespan (Yeatman et al., 2014). The aging models used in previous studies have generally taken the form of linear, quadratic or Poisson curve models, each model offering a different level of flexibility and parameterization. Quadratic models tend to fit certain measures of myelination well but enforce a symmetry between developmental and degenerative processes (Yeatman et al., 2014). A Poisson curve can similarly model nonlinear aging effects but is capable of modelling asymmetric trajectories, albeit with certain constraints on the curve's form, and has been shown to approximate well to lifespan trajectories of MD (Lebel et al., 2012).

In this study, we combine DTI tractography with DWI and MPM tissue microstructure characterization to provide a detailed assessment of multi-parametric tissue changes over the lifespan (7-84 years) in a large cohort of healthy individuals (n=801). Cross-validation was used to select appropriate aging models for each of the quantitative microstructure measurements and robust curve fitting approaches applied to estimate ages of peak maturation within a tract. Finally, age, sex and hemisphere associations were investigated using multiple linear regression.

2.2 Materials and methods

Subjects

801 healthy volunteers (410 females) were recruited from the Lausanne regional area of Switzerland based on fliers, university newsletters and, for the majority of subjects (N=624), their ongoing participation in the CoLaus | PsyCoLaus cohort (Preisig et al., 2009). Study approval was granted by the local ethics committee and informed consent was collected for all subjects and/or a parent/guardian. Subjects were aged between 7 and 84 years (mean age 50 ± 17 years) and distributed as follows: 106 subjects aged 7-24 years; 108 subjects aged 25-39 years; 245 subjects aged 40-54 years; 242 subjects aged 55-69 years; and 100 subjects aged 70-84 years. Subjects had no self-reported history of neurological or psychiatric disease and were screened carefully for brain abnormalities and movement artefacts. Handedness is sometimes reported in WM microstructure studies under the assumption that this plays a role in tract development. A recent study on a large cohort of over 3000 individuals found no substantive differences in tract characteristics between right- and left-handed subjects (Cox et al., 2016) and we therefore chose not to assess handedness as part of our investigation.

MR data acquisition

All imaging was performed on a 3T whole-body MRI system (Magnetom Prisma, Siemens Medical Systems, Germany) using a 64-channel RF receive head coil and body coil for transmission.

Multi-parametric mapping (MPM)

The qMRI protocol consisted of three whole-brain multi-echo 3D fast low angle shot (FLASH) acquisitions with predominantly magnetization transfer-weighted (MTw: $TR/\alpha = 24.5\text{ms}/6^\circ$), proton density-weighted (PDw: $TR/\alpha = 24.5\text{ms}/6^\circ$) and T1-weighted (T1w: $24.5\text{ms}/21^\circ$) contrast (Helms et al., 2009, 2008; Weiskopf et al., 2013b). The MT-weighted contrast was obtained using a Gaussian-shaped radio frequency (RF) pulse prior to the RF excitation (4ms duration, 220° nominal flip angle, 2 kHz frequency offset from water resonance). Multiple gradient echoes were acquired for each contrast with alternating readout polarity. The minimal echo time was 2.34ms and the echo spacing was 2.34ms. The number of echoes was 6/8/8 for the MTw/PDw/T1w acquisitions to keep the TR value identical

for all contrasts. The image resolution was 1 mm³ isotropic, the field of view and the matrix size were 256 × 240 × 176 mm. Parallel imaging was used along the phase-encoding direction (acceleration factor 2 with GRAPPA reconstruction) (Griswold et al., 2002), partial Fourier (factor 6/8) was used along the partition direction. Data were acquired to calculate maps of the RF transmit field B1+ using the 3D echo-planar imaging (EPI) spin-echo (SE) and stimulated echo (STE) method described in (Lutti et al., 2012, 2010). The image resolution of the B1-mapping data was 4mm³, and the echo and repetition times were set to 39.06ms and 500ms respectively. The nominal flip angle of the SE pulse was decreased from 230° to 130° in steps of 10° (Lutti et al., 2012, 2010). B0-field mapping data was acquired using a 2D double-echo FLASH sequence to correct for geometric distortions in the 3D EPI data (Lutti et al., 2012, 2010). The total acquisition time was 27 min.

A subset of participants (N=84, 7-75 yrs) underwent an equivalent 1.5 mm³ MPM protocol. The acquisition parameters for this protocol differed for the following parameters: field of view = 240 × 225 × 180 mm, matrix size = 160 × 150 × 120. The total acquisition time was 13 min. Image resolution was included as a regressor in all curve fitting and statistical models.

Diffusion weighted imaging (DWI)

The diffusion weighted MRI data were acquired using a 2D echo-planar imaging sequence with the following parameters: TR/TE = 7420/69ms, parallel GRAPPA acceleration factor = 2, FOV = 192 x 212 mm², matrix size = 96 x 106, 70 axial slices, 2 mm isotropic voxel dimension, 118 isotropically distributed diffusion sensitization directions (15 at b = 650 s/mm², 30 at b = 1000 s/mm² and 60 at b = 2000 s/mm²) and 13 b=0 images interleaved throughout the acquisition. The lower resolution acquisition used for a subset of participants (N=84, 7-75 yrs) was acquired using the same 118 direction sampling scheme and the following imaging parameters: TR/TE = 3906/88 ms, parallel GRAPPA acceleration factor = 0, FOV = 192 x 209 mm², matrix size = 96 x 106, 60 axial slices, 2.2 mm isotropic voxel dimension, multi-band factor = 2.

MR data preprocessing

Structural data

The R2*, MT and R1 quantitative maps were calculated as previously described (Draganski et al., 2011) using in-house software running under SPM12 (Wellcome Trust Centre for Neuroimaging, UCL -London, UK; www.fil.ion.ucl.ac.uk/spm) and Matlab (Mathworks, Sherborn, MA, USA). The R2* maps were calculated from the regression of the log-signal of the eight PD-weighted echoes. The MT and R1 maps were computed as described in (Helms et al., 2008), using the MTw, PDw and T1w images averaged across all echoes. The R1 maps were corrected for local RF transmit field inhomogeneities using the B1+ maps computed from the 3D EPI data (Helms et al., 2008) and for imperfect RF spoiling using the approach described by (Preibisch and Deichmann, 2009).

Diffusion preprocessing

DWIs were preprocessed to correct for eddy currents and subject motion using the FSL EDDY tool (Andersson and Sotiropoulos, 2016) and the gradient directions were appropriately rotated to correct for subject movement (Leemans and Jones, 2009). The B0 maps acquired as part of the structural imaging session were used to correct for EPI susceptibility distortions with the SPM field mapping toolbox (Hutton et al., 2002). The DWI images were then rigid body aligned to the MT image with the aid of the mean b=0 image using SPM12.

Diffusion tensor imaging (DTI) maps were estimated on the b=0 s/mm², b=650 s/mm², and b=1000 s/mm² data using a constrained non-linear least-squares (CNLLS) algorithm (Koay et al., 2006). The neurite orientation dispersion and density imaging (NODDI; Zhang et al., 2012) maps were processed with the AMICO toolbox (Daducci et al., 2014) using multi-shell diffusion data across all of the acquired b-values. For each subject, we thus generated DTI tissue microstructure maps for fractional anisotropy (FA) and mean diffusivity (MD), in addition to NODDI maps for intracellular volume fraction (ICVF) and orientation dispersion index (ODI).

G-ratio estimation

The g-ratio is defined as the ratio between the inner axonal radius and the myelinated fiber radius and represents a fundamental property of axonal morphology and conduction (Waxman, 1975). Here we apply a recently developed technique (Campbell et al., 2012;

Mohammadi et al., 2015; Stikov et al., 2015) which estimates the g-ratio using a combination of non-invasive diffusion microstructure and myelin imaging measures. The g-ratio, g , was estimated voxel-wise via the following equation:

$$g = \sqrt{\frac{1}{1 + \frac{MVF}{AVF}}} = \sqrt{\frac{1}{1 + \frac{\alpha MT}{(1 - \alpha MT)(1 - v_{iso})v_{ic}}}}$$

where MVF is the myelin volume fraction, AVF is the axonal volume fraction, MT is the quantitative magnetization transfer measurement, and v_{iso}/v_{ic} are respectively the isotropic (ISO) and intracellular (ICVF) volume fraction estimates from the NODDI diffusion model. We estimated the normalization factor, α , by following the previous literature (Cercignani et al., 2016; Mancini et al., 2017; Mohammadi et al., 2015). An ROI was selected in the splenium of 11 subjects (mean age 26.5 ± 1.41 years) and a value of $\alpha = 0.23$ chosen as the median normalization factor required to constrain the splenium g-ratio to a value of 0.7 across subjects, mirroring reported g-ratio values made in the splenium using electron microscopy (Graf von Keyserlingk and Schramm, 1984).

Tractography and microstructure sampling

The AFQ software package (Yeatman et al., 2012b) was used to estimate average tissue microstructural properties across 20 bilateral and callosal tracts (Fig. 2.1). The subset of DWI data used to calculate the DTI maps was provided to the software and used to generate a whole brain tractogram using default settings (step size = 1mm; FA threshold = 0.2; angle threshold = 30°). More advanced HARDI tractography procedures were tested but determined to provide little benefit to tract identification while introducing additional instabilities in certain subjects. A detailed optimization of the AFQ software package to work with HARDI tractography data was deemed to be beyond the scope of the present study.

Given the whole-brain tractogram, AFQ first segments each tract using an ROI inclusion approach before cleaning spurious streamlines which are considered outliers in terms of their length and/or distance from the tract core. After the segmentation and cleaning procedures, the accepted streamlines were used to sample each of the previously computed tissue microstructure maps (MT, R1, R2*, g-ratio, FA, MD, ICVF & ODI) and averaged along the tract

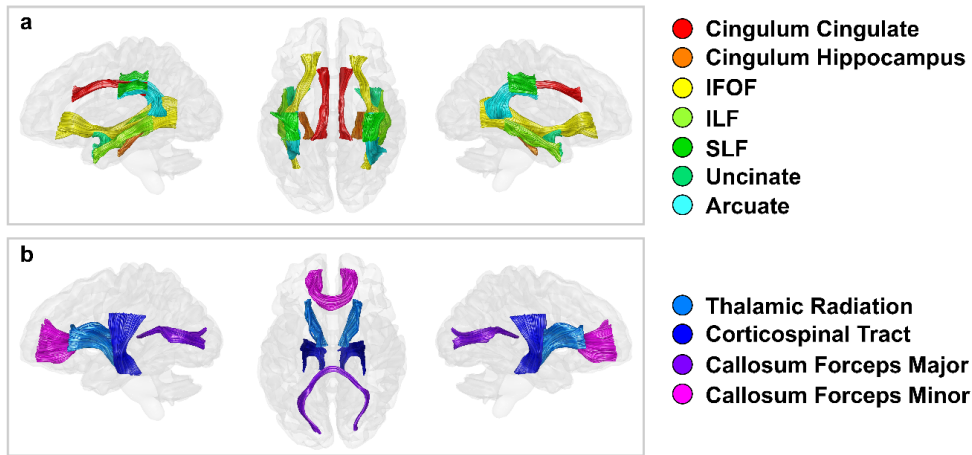


Figure 2.1. Major white matter tracts of interest. Tracts dissected using an automated fiber identification procedure on whole brain tractograms. Tracts are rendered in left-lateral, superior and right-lateral views.

length to provide mean tissue microstructure estimates for each of the tracts and metrics. Full details of the AFQ segmentation, cleaning and sampling procedures can be found in the original research article (Yeatman et al., 2012b).

Curve fitting

We considered three possible aging trajectory models (linear, quadratic & Poisson curve), each of which has been identified as a suitable description of tract evolution across the lifespan for a particular microstructure measurement (Bartzokis et al., 2012; Cox et al., 2016; Kochunov et al., 2012; Lebel et al., 2012; Yeatman et al., 2014). The linear model describes the relationship between age and tract microstructure according to the following equation:

$$Y = \beta_1 + \beta_2 * Age$$

where Y is a tract microstructure measurement (e.g. for MT) while β_1 and β_2 parameterize the intercept and slope respectively. The quadratic curve extends the linear model via the following equation:

$$Y = \beta_1 + \beta_2 * Age + \beta_3 * Age^2$$

where β_3 parameterizes a nonlinear quadratic aging term. The Poisson curve model is capable of modelling asymmetric nonlinear aging trajectories as described by the following equation:

$$Y = \beta_1 + \beta_2 * Age * \exp^{-\beta_3 * Age}$$

Linear and quadratic models were evaluated using a GLM which included additional regressors for sex, resolution, hemisphere and sex-age interactions. The Poisson curve was estimated using a nonlinear optimization in Matlab after the regression of covariates. Model selection was performed for each microstructure metric using repeated 5-fold cross-validation. For each tract, a total of 10^4 repetitions were performed, each time using a randomized division of subjects into folds. The winning model was selected as the model which minimized mean cross-validated error across fold, repetitions and tracts. Bootstrapping with replacement was repeated 1000 times using the winning model to estimate the age at which tract microstructure measurements peaked. Peak age was estimated for the quadratic and Poisson curve models as the age at which the measurement first derivative with respect to age equaled zero (the global minima/maxima). The mean of the bootstrapped sampling distribution was taken as the peak age estimate and standard errors were calculated as the standard deviation of the bootstrapped sampling distribution.

Age, sex and hemisphere associations

GLMs were run to test for the association of age, sex, hemisphere, image resolution and their interactions for each tract and metric. Two GLMs were considered, one which included only first-order aging terms:

$$Age + Sex + Resolution + Hemisphere + Age \times Sex + Age \times Resolution + Age \times Hemisphere$$

and a second GLM which included a second-order aging term:

$$Age + Age^2 + Sex + Resolution + Hemisphere + Age \times Sex + Age \times Resolution + Age \times Hemisphere$$

The Akaike information criterion (AIC) was used to assess which of the two GLMs was best supported by a tract's lifespan microstructure trajectory.

Retrogenesis of white matter tracts

Theories within the aging literature have suggested that lifespan tissue processes may obey a retrogenic sequence ordering, which can be broadly broken down into "gain-predicts-loss" and "last-in-first-out" hypotheses of aging (Raz, 2000; Reisberg et al., 2002; Yeatman et

al., 2014). The gain-predicts-loss hypothesis predicts that the rate of tissue change during development equals the rate of decline during old age. Equivalently knowledge of a tissue state in late-childhood should predict the tissue state at a symmetric age post-peak. We investigated this hypothesis by assessing whether a simple quadratic aging model (symmetric) was a more appropriate description of microstructure evolution over the human lifespan than either linear or Poisson curve models (asymmetric).

The last-in-first-out hypothesis predicts that structures which develop slower ontogenetically will also be the most vulnerable to age related decline. Previous assessments of this theory have formulated the problem in different fashions (Davis et al., 2009; Douaud et al., 2014; Yeatman et al., 2014), often using qualitative assessments (Brickman et al., 2012; Gao et al., 2011; Madden et al., 2012; Stricker et al., 2009). Here we formulate the problem in terms of age of maturity predicting the extent of quadratic tissue change over the lifespan. First, each tissue measurement of a tract was normalized by the mean across subjects to determine the percentage deviations from the sample mean. Second, a GLM containing regressors for age, sex, hemisphere, resolution and their interactions (see the second-order aging model in *Age, sex and hemisphere associations*) was evaluated for each tract and metric to estimate quadratic aging terms. Finally, Pearson's correlations were made between the bootstrapped peak age estimates and quadratic aging effects to quantitatively test the prediction that age of maturity predicts percentage tissue variation across the major white matter fiber bundles. This approach to formulating the last-in-first-out hypothesis assesses the relationship between two fundamental lifespan curve parameters and, by the nature of the quadratic term, tests the prediction that late maturation is associated with an accelerated rate of decline post-peak and a greater absolute level of microstructural change from adolescence to old age.

2.3 Results

Lifespan changes within WM tracts

Each of the white matter tracts followed similar general lifespan trajectories. MT, R1, g-ratio, FA, ICVF and ODI measurements most accurately followed a quadratic aging model, while R2* and MD trajectories were better fit using a Poisson curve. MT, R1 and ICVF increased from adolescence into adulthood before reaching a peak and declining into old age at a rate

symmetric to that observed before the peak; $R2^*$ increased into adulthood before reaching a peak value and then declining at a slower rate; MD trends were opposite to $R2^*$, characteristically decreasing initially, achieving a minimum, and then increasing at a slower rate; FA and ODI typically increased during development before declining with senescence, though certain tracts exhibited very little quadratic change or inverted trajectories across the lifespan; the g-ratio showed a period of relative stability from adolescence into the third decade before increasing with further age. The estimates for age of peak MT, R1, $R2^*$, g-ratio, MD and ICVF were robust and had standard errors of 0-6 years (mean error ± 3.2 years; Fig. 2.2). For FA and ODI the estimates for peak age were less reliable with average standard errors of 13.2 and 10.6 years respectively. The reliability of peak age estimates relates to the extent of nonlinear (quadratic) aging effects within a tract and this, as well as the precise timing of peak maturation, can vary substantially from tract to tract. The percentage change of a tissue

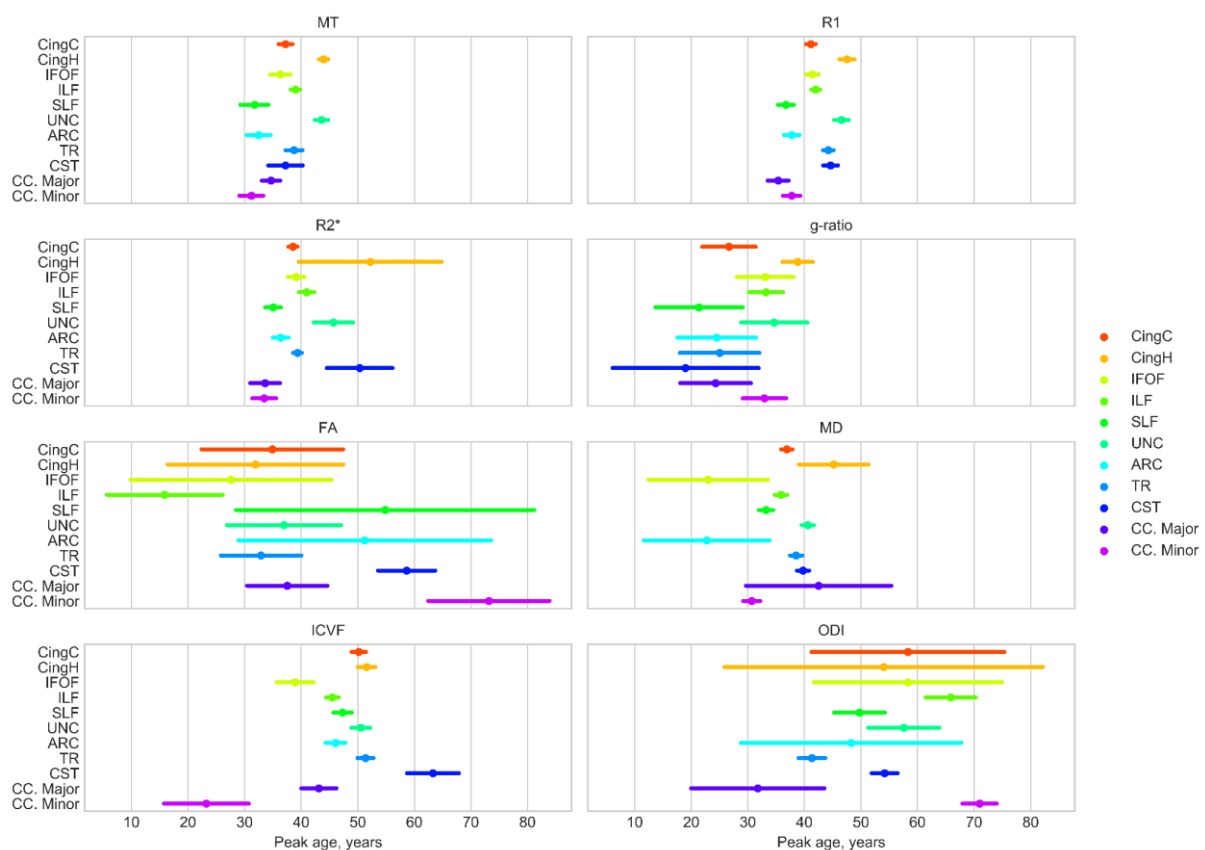


Figure 2.2. The relative timings of tract microstructure peaks for MT, R1, $R2^*$, g-ratio, FA, MD, ICVF and ODI. The mean bootstrapped age of peak microstructural development is shown for each tract (circle) along with the bootstrapped standard error (bars). The age scale is consistent across all measurement types. CingC: cingulum-cingulate; CingH: cingulum-hippocampus; IFOF: inferior fronto-occipital fasciculus; ILF: inferior longitudinal fasciculus; SLF: superior longitudinal fasciculus; UNC: uncinate fasciculus; ARC: arcuate fasciculus; TR: thalamic radiations; CST: corticospinal tract; CC. Major: corpus callosum forceps-major; CC. Minor: corpus callosum forceps-minor.

measurement from age 15 years to the peak age as well as the percentage change from peak age to age 75 years are provided in Supplementary Table 2.1. These values provide an overview of the absolute tissue measurement change observed during maturation and decline.

Limbic tracts

Lifespan trajectory scatter plots for the cingulum-cingulate and cingulum-hippocampus tracts are shown in the first two rows of Fig. 2.3 and Fig. 2.4. The peak ages of the cingulum-cingulate were intermediate relative to the other tracts (Fig. 2.2). In contrast, the cingulum-hippocampus displayed exceptionally late maturation for MT, R1, R2*, g-ratio and MD. Increases in MT, R1 and R2* during maturation were moderate for the cingulum-cingulate (MT / R1 / R2*, 3.1% / 3.5% / 7.2%) but large for the cingulum-hippocampus (7.2% / 6.5% / 12.2%). Decreases during senescence were generally moderate for both tracts although the cingulum-hippocampus showed a particularly small decline in R2* (1.9%). The ODI developmental estimates in the cingulum-hippocampus tract approximated a linearly increasing slope. The peak age and maturation estimates for ODI in the cingulum-hippocampus tract should therefore be interpreted with caution and this uncertainty is reflected in the bootstrapped confidence interval of Fig. 2.2. Across the other tissue measurements, the two tracts possessed relatively intermediate values of maturation and decline.

Association tracts

The lifespan trajectories for the association fibers are shown in rows 3-7 of Fig. 2.3 and Fig. 2.4. The inferior fronto-occipital fasciculus (IFOF) attains its peak value early for FA, MD and ICVF while peaking at intermediate ages for all other tissue measures (Fig. 2.2); the inferior longitudinal fasciculus (ILF) peaks early for FA, late for ODI and at intermediate ages for all other measurements; the superior longitudinal fasciculus (SLF) peaks relatively early for MT, R1, R2* and g-ratio with intermediate peak ages for the other measures; the uncinate fasciculus observes a late peak for MT and R1 with all other measurements taking intermediary ages; the arcuate fasciculus is the earliest to peak for MD and also peaks relatively early for MT, R1 and R2*. Of note, we see that the IFOF has a relatively small amount of change during senescence for the g-ratio (1.5%), a small amount of MD change during

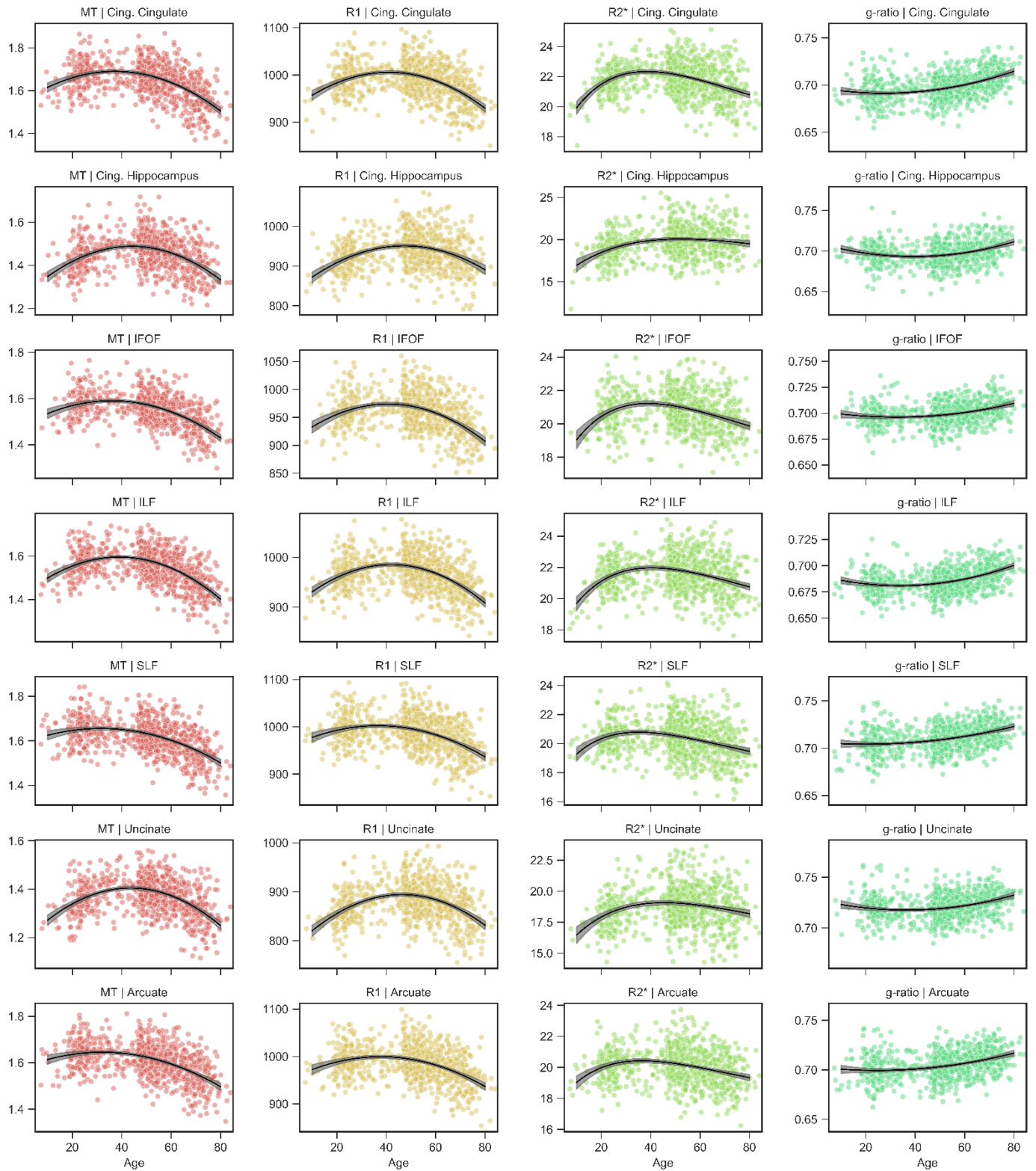


Figure 2.3. Association fibre trajectories for MT, R1, R2* and g-ratio. Scatter plots indicate the tract microstructure measurement distribution across the sample with age; black lines denote the aging regression line for quadratic (MT, R1, g-ratio) or Poisson curve (R2*) models (grey shading 95% CI). Red: MT; orange: R1; green: R2*; turquoise: g-ratio. Cing. Cingulate: cingulum-cingulate; Cing. Hippocampus: cingulum-hippocampus; IFOF: inferior fronto-occipital fasciculus; ILF: inferior longitudinal fasciculus; SLF: superior longitudinal fasciculus; UNC: uncinate fasciculus; ARC: arcuate fasciculus.

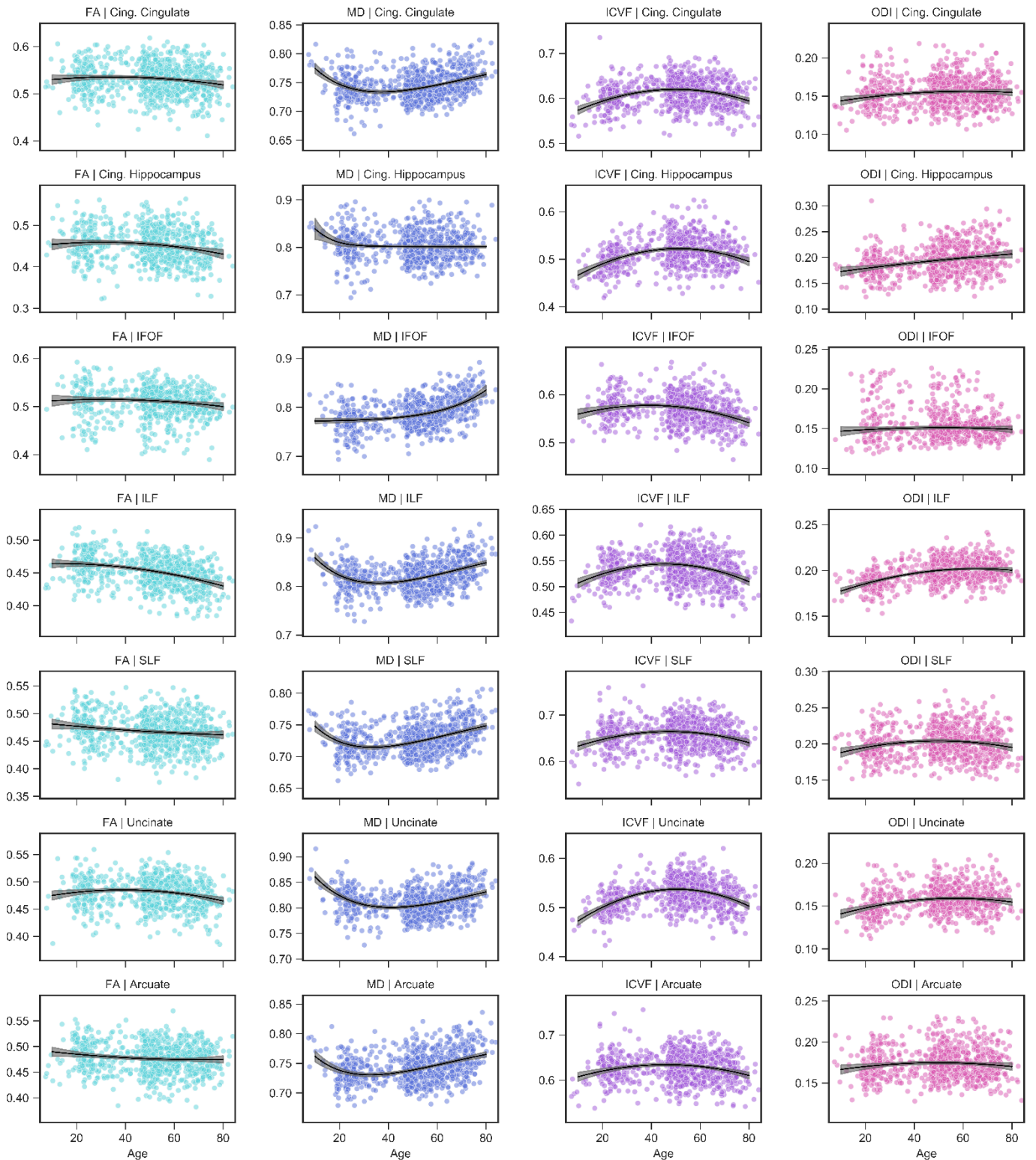


Figure 2.4. Association fibre trajectories for FA, MD, ICVF and ODI. Scatter plots indicate the tract microstructure measurement distribution across the sample with age; black lines denote the aging regression line for quadratic (FA, ICVF, ODI) or Poisson curve (MD) models (grey shading 95% CI). Light blue: FA; dark blue: MD; purple: ICVF; pink: ODI. Cing. Cingulate: cingulum-cingulate; Cing. Hippocampus: cingulum-hippocampus; IFOF: inferior fronto-occipital fasciculus; ILF: inferior longitudinal fasciculus; SLF: superior longitudinal fasciculus; UNC: uncinate fasciculus; ARC: arcuate fasciculus.

maturation (1.3%) and a large amount of MD change during decline (5.7%); the uncinate displays large increases during development for ICVF (10.0%), MD (4.5%), MT (7.2%), R1 (6.5%) and R2* (10.4%); and the arcuate exhibits only a small change during maturation for MD (1.1%).

Projection tracts

The ageing trajectories of the thalamic radiation and corticospinal tract projection fibers are shown in the first two rows of Fig. 2.5 and Fig. 2.6. The thalamic radiations typically peak at intermediate-to-late ages for all tissue measures excluding ODI, which peaks earlier than all pathways excluding the forceps minor of the corpus callosum. The corticospinal tract peaks late for the R1, R2*, FA and, most notably, the ICVF measurements while peaking earliest for the g-ratio. Across the remaining measures the corticospinal tract peaks at intermediate values. Supplementary Table 2.1 contains the percentage change in tissue measurements

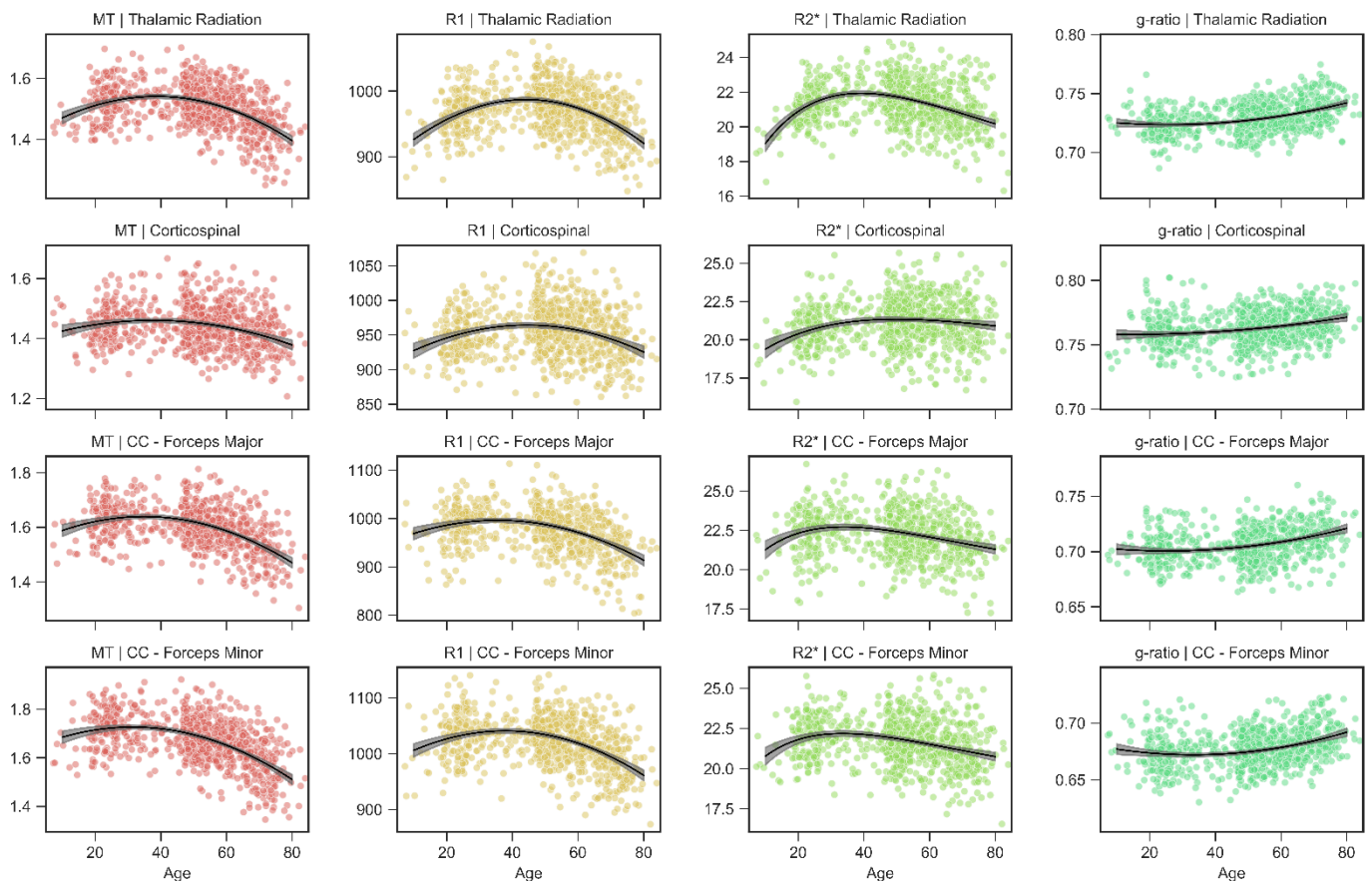


Figure 2.5. Projection and callosal fibre trajectories for MT, R1, R2* and g-ratio. Scatter plots indicate the tract microstructure measurement distribution across the sample with age; black lines denote the aging regression line for quadratic (MT, R1, g-ratio) or Poisson curve (R2*) models (grey shading 95% CI). Red: MT; orange: R1; green: R2*; turquoise: g-ratio. CC: corpus callosum.

during maturation and decline for the projection tracts. We highlight the large changes in FA (4.6%), ODI (11.3%) and $R2^*$ (6.5%) during senescence for the thalamic radiations; the corticospinal tract was particularly stable after peak maturation, exhibiting little change during senescence for the ICVF (0.4%), MT (4.5%), R1 (3.0%) and $R2^*$ (1.6%) measures.

Commissural tracts

The lifespan trajectory curves for the commissural tracts of the corpus callosum – the forceps major (occipital) and the forceps minor (frontal) – are presented in the bottom two rows of Fig. 2.5 and Fig. 2.6. We observe that the commissural fibers are often some of the earliest to mature across the multiple tissue measurements (Fig. 2.2). The forceps major peaks early across R1, $R2^*$, g-ratio, ICVF and ODI measurements while peaking at relatively intermediate ages across the remaining tissue measures. Similarly, the forceps minor peaks particularly early across MT, R1, $R2^*$, MD and ICVF measurements while also peaking

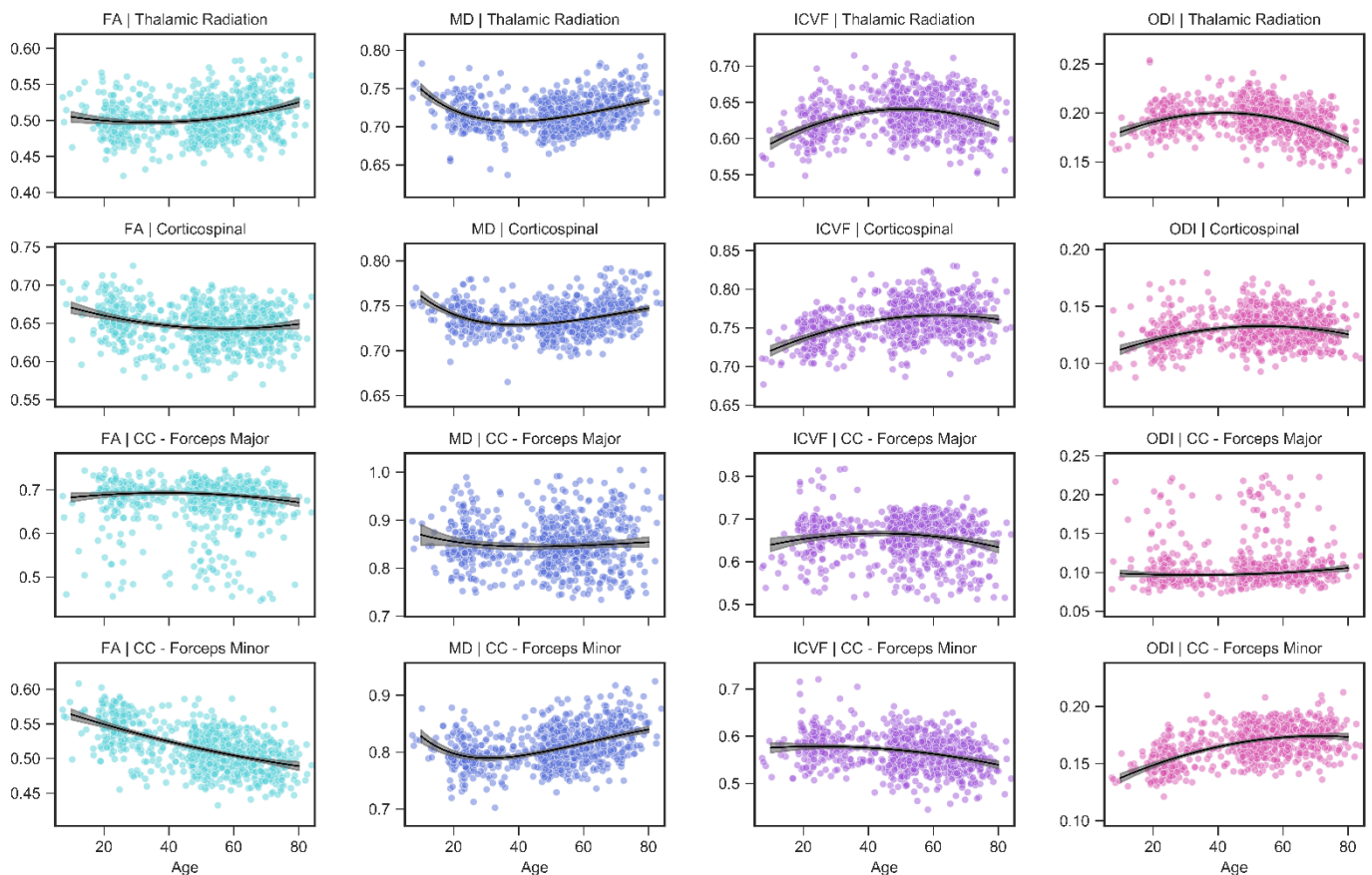


Figure 2.6. Projection and callosal fibre trajectories for FA, MD, ICVF and ODI. Scatter plots indicate the tract microstructure measurement distribution across the sample with age; black lines denote the aging regression line for quadratic (FA, ICVF, ODI) or Poisson curve (MD) models (grey shading 95% CI). Light blue: FA; dark blue: MD; purple: ICVF; pink: ODI. CC: corpus callosum.

exceptionally late in FA and ODI measures, both of which are sensitive to alterations of fiber crossing and dispersion. The amount of tissue measurement change during maturation and decline for the commissural fibers can differ quite substantially as compared to the other major tracts of the brain (Supplementary Table 2.1). The forceps major displays little change during maturation for R1 (1.8%) and R2* (3.8%), and senescence for MD (0.88%), while also following an inverted ODI trend, decreasing during maturation (1.3%) and increasing during senescence (7.5%); the forceps minor shows particularly large change during maturation for FA (11.5%) and ODI (21.6%), small changes during maturation for ICVF (0.2%) and R2* (3.7%), with large changes during senescence for ICVF (5.6%), MD (5.7%) and MT (10.1%).

Tract associations with age, sex, image resolution and hemisphere

Associations with age were predominantly non-linear excluding FA, ODI and g-ratio measurements across a few isolated tracts (Fig. 2.7 and Supplementary Tables 2.2-2.5), indicating reducing tissue change slopes with age up to a peak value before a reversal and steeping of slopes with further increases in age. These general aging curve trends lead to the *inverted* U-shaped (e.g. MT, R1, R2*, ICVF) and U-shaped (e.g. MD, g-ratio) lifespan trajectories detailed in Fig. 2.3-2.6. Significant quadratic aging terms were consistently observed for MT ($\bar{\beta} = -1.65$), R1 ($\bar{\beta} = -1.67$), R2* ($\bar{\beta} = -1.11$), g-ratio ($\bar{\beta} = 0.62$), MD ($\bar{\beta} = 1.45$) and ICVF ($\bar{\beta} = -1.08$) with a degree of spatial heterogeneity observed across tracts (Fig. 2.8 & Supplementary Tables 2.2-2.5). Quadratic associations with age were particularly robust in association (IFOF, ILF, SLF, arcuate and uncinate fasciculi), thalamic radiation and cingulum bundles (Fig. 2.7). In contrast, the corticospinal tract and callosal pathways generally exhibited more modest nonlinear associations with age. Significant though less consistent quadratic aging terms were observed for the water diffusion coherence measures of FA ($-0.55 \leq \beta \leq 0.81$) and ODI ($-1.58 \leq \beta \leq 0.54$; Supplementary Tables 2.2-2.5). The quadratic aging model was found to provide a significantly better fit than a linear model for all metrics and tracts except for FA in the ILF for which older age was significantly associated with lower coherence of water diffusion ($\beta = -0.43$).

Sex differences and their interactions with age were modelled for all tracts and tissue measurements (Fig. 2.7 and Supplementary Tables 2.2-2.5). Sex differences were generally weak and inconsistent, with the only significant results showing trends for higher R1 in males

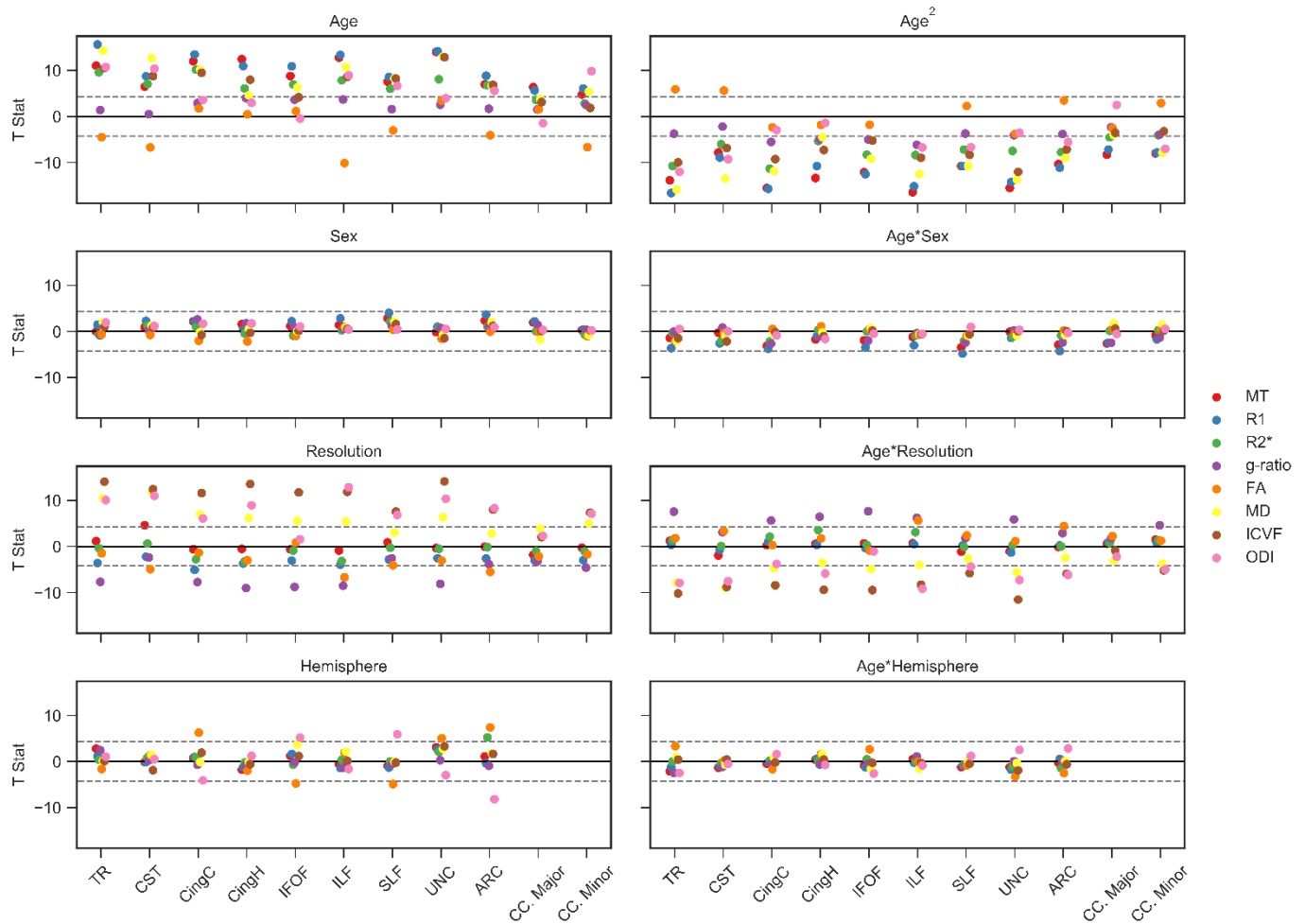


Figure 2.7. Tissue measurement associations with age, sex, resolution and hemisphere. GLMs were used to estimate T-statistics for MT, R1, R2*, g-ratio, FA, MD, ICVF and ODI with age, sex, resolution, hemisphere and their interactions with age. Male, high resolution and left hemisphere coded as 0. The valance of the g-ratio and MD associations have been reflected for visualization purposes across each of the panels. Horizontal dashed grey lines display the FEW-corrected significance level at $p \leq 0.001$. Full details of the regression coefficients are provided in Supplementary Tables 2.2-2.5.

in the SLF ($\beta = 0.28$) and arcuate fasciculus ($\beta = 0.26$). Interactions between age and sex were significant for R1 across the thalamic radiation, cingulum cingulate, IFOF, SLF and arcuate fasciculus ($\beta \geq -0.36$), and for MT in the SLF ($\beta = -0.25$), suggestive of a marginally higher association with age in females as compared to males.

Associations with MR imaging resolution were generally small and insignificant for MT, R1 and R2* with larger effects apparent for the diffusion derived MD, ODI, ICVF and g-ratio measurements. The lower resolution scans were typically associated with higher MD ($\bar{\beta} = -0.41$) and lower ODI, ICVF and g-ratio values ($\bar{\beta} \leq 0.69$). A secondary analysis in the subset of

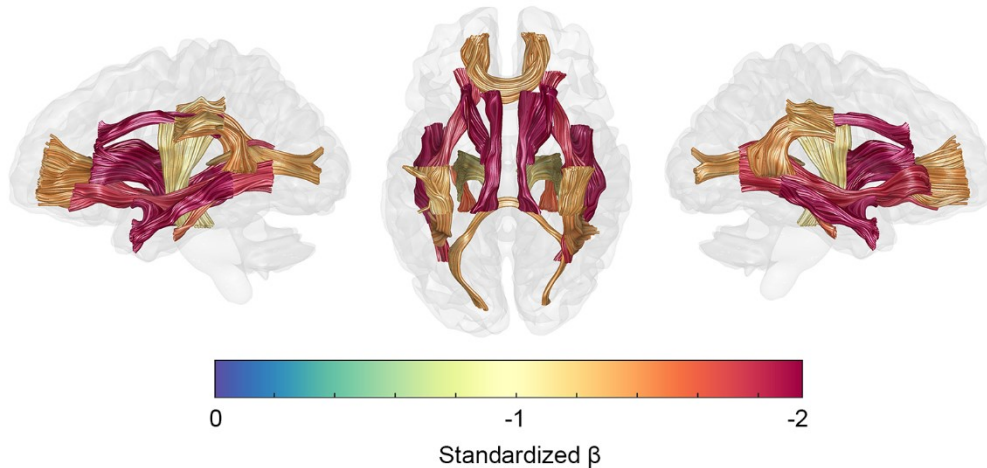


Figure 2.8. Spatial heterogeneity of R1 quadratic aging effects. A glass brain visualization with 20 major fascicles displayed on left-lateral, superior and right-lateral views. R1 was the most sensitive measure to aging effects. Age² coefficient values (standardized β s) are from the GLM model results detailed in Supplementary Figure 1.

subjects with high-resolution scans ($n = 718$) produced highly consistent age, sex and hemisphere associations to those observed in the full dataset (Supplementary Fig. 2.1).

Asymmetries in tract microstructure were examined for all bilateral tracts (Fig. 2.7 and Supplementary Tables 2.2-2.5). Associations by hemisphere revealed left-right asymmetries in FA and ODI for several bilateral tracts. FA was higher and ODI lower in the left hemisphere for the cingulum-cingulate (FA | ODI; $\beta = 0.45$ | $\beta = -0.31$) and the arcuate fasciculus ($\beta = 0.52$ | $\beta = -0.57$) and in the right hemisphere for the IFOF ($\beta = -0.45$ | $\beta = 0.48$) and SLF ($\beta = -0.34$ | $\beta = 0.39$). Further left-sided asymmetries were observed with higher FA in the left uncinate fasciculus ($\beta = 0.41$), higher R2* in the left arcuate ($\beta = 0.38$) and lower MD in the left IFOF ($\beta = -0.31$). There were no significant associations between hemispheres for any of the MT, R1, g-ratio or ICVF measurements. Interactions between age and hemisphere were weak to non-existent across all tracts and measurements excluding FA in the thalamic radiations, for which we observed a trend towards larger associations with age in the left versus right hemisphere ($\beta = 0.26$).

Spatial heterogeneity of the myelin g-ratio

Peak g-ratio values for the major white matter fasciculi are presented in Fig. 2.9. Tract specific g-ratio values center around $g=0.7$ with a range of 0.67-0.76. The forceps-minor of the corpus callosum achieves the lowest value of all the fasciculi ($g=0.67$). The association fibers of the brain and the forceps-major reach intermediate g-ratios centered around $g=0.7$

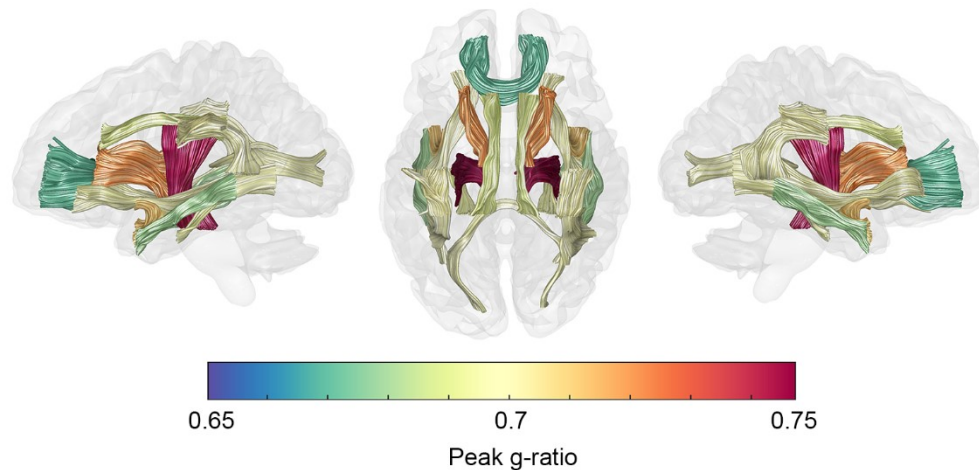


Figure 2.9. Spatial heterogeneity of peak g-ratio values. A glass brain visualization with 20 major fascicles displayed on left-lateral, superior and right-lateral views. Peak values were estimated from the peak age estimates of Fig. 2 and the aging curves of Fig. 3 & 5.

(cingulum-cingulate, $g=0.69$; cingulum-hippocampus, $g=0.69$; IFOF, $g=0.7$; ILF, $g=0.68$; SLF, $g=0.70$; uncinate, $g=0.71$; arcuate, $g=0.70$; forceps-major, 0.70). The thalamic radiations ($g=0.72$) and the corticospinal tract ($g=0.76$) attain relatively higher peak g-ratio values. Across all tracts, the g-ratio remains reasonably stable around these peak values into the third decade (Fig. 2.3 & 2.5). After this period of stability g-ratios are observed to begin increasing at ever accelerating rates with age (Supplementary Table 2.3). The cingulum-cingulate, forceps-major and forceps-minor show the greatest percentage change from their peak up until age 75 (2.36-2.76%) while the corticospinal tract and IFOF exhibit the smallest percentage g-ratio increases (1.53% & 1.54% respectively).

Retrogenesis of white matter tracts

In support of the ‘last-in-first-out’ hypothesis, robust correlations ($r \geq 0.65$) between age of peak maturation and quadratic aging effects were observed for MT ($r = 0.81$), R1 ($r = 0.66$), R2* ($r = 0.65$) and g-ratio ($r = 0.82$) measurements (Fig. 2.10). Conversely, peak age was negatively correlated with quadratic aging effect for ODI ($r = -0.66$). Weak and inconsistent correlations were seen for the FA ($r = -0.23$), MD ($r = 0.12$) and ICVF ($r = 0.32$) measurements. Across the MT, R1, R2* and ICVF microstructure measurements the corticospinal tract is a noticeable outlier, typically exhibiting weaker quadratic aging effects than the age of maturity would suggest. The ‘gain-predicts-loss’ hypothesis necessitates symmetric developmental and aging trajectories relative to a peak. We find robust evidence for this hypothesis across MT, R1 and ICVF measures which are best described by a symmetric quadratic aging model (Fig.

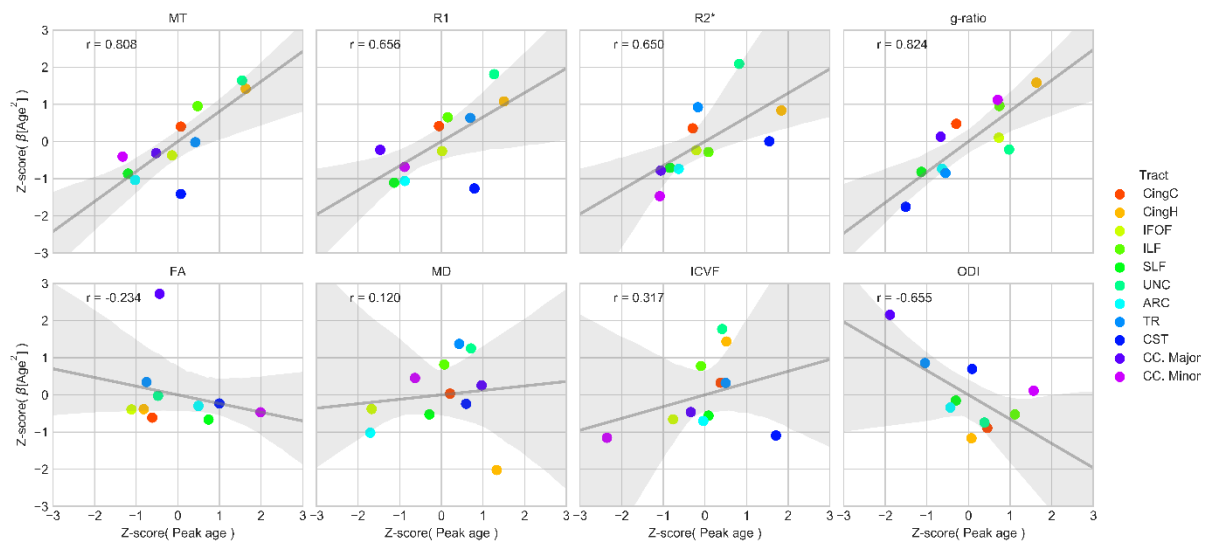


Figure 2.10. Testing the last-in-first-out hypothesis of aging. The last-in-first-out hypothesis predicts that a later developmental timing for a tract is associated with increased vulnerability on old age. The age of peak maturation was correlated with the quadratic aging effects of a tract across MT, R1, R2*, g-ratio, FA, MD, ICVF and ODI measurements. Grey line indicates linear regression line (shaded area 95% bootstrapped CI). Pearson's r correlation annotated in upper left of each box. CingC: cingulum-cingulate; CingH: cingulum-hippocampus; IFOF: inferior fronto-occipital fasciculus; ILF: inferior longitudinal fasciculus; SLF: superior longitudinal fasciculus; UNC: uncinate fasciculus; ARC: arcuate fasciculus; TR: thalamic radiations; CST: corticospinal tract; CC. Major: corpus callosum forceps-major; CC. Minor: corpus callosum forceps-minor.

2.3-2.6). A quadratic aging model also best describes g-ratio, FA, and ODI measurements though the quadratic aging effects, and therefore the evidence for symmetric maturation and decline, is less robust (Fig. 2.8 & Supplementary Tables 2.2-2.5). R2* and MD measurements have highly asymmetric periods of maturation and decline which do not align well with the predictions of the 'gain-predicts-loss' hypothesis.

2.4 Discussion

This study contributes to our understanding of changes in white matter microstructure across the human lifespan. Robust nonlinear aging effects were consistently observed across tissue measurements and tracts. Using a combination of quantitative MRI measures, we were able to observe that R1, MT and MD were the most sensitive parameters to aging effects across the major white matter fascicles of the brain. Tract microstructure measurements are expected to peak between the mid-twenties and mid-fifties, with g-ratio measurements peaking earliest and ODI measurements peaking latest on average. Levels of tract myelination (as most specifically measured by MT and R1) typically peak between the ages of 35 and 45 years. After reaching a peak level of microstructural organization the major white matter

tracts became less healthy with increasing age, losing myelin, decreasing in maintenance of microstructural organization and deviating from the optimal g-ratios needed for efficient signal conduction.

A more detailed look at tract microstructure trajectories highlights that increasing age between adolescence and mid-adulthood is most strongly associated with increased myelination (MT, R1, R2*) and microstructural organization (FA, MD, ICVF, ODI) in association fasciculi (cingulum-cingulate, cingulum-hippocampus, IFOF, ILF, SLF, uncinate and arcuate) and thalamic radiations. The corticospinal tract and corpus callosum segments (forceps-major and forceps-minor) follow similar trajectories during this period but with a smaller amount of microstructural change, indicative of their early development and stability (Bartzokis et al., 2012; Kinney et al., 1988; Yakovlev and Lecours, 1967; Yeatman et al., 2014). During senescence, a reversal in microstructural change is typically observed, with association fasciculi and the forceps-minor of the corpus callosum displaying notable vulnerability to white matter degeneration. These aging associations are generally in line with predicted lifespan trends, adding considerable support to the findings of past investigations reporting increasing MT, R1, R2*, FA, ICVF and decreasing MD during development and young adulthood, and reversing trends during senescence (Callaghan et al., 2014; Chang et al., 2015; Cox et al., 2016; Kochunov et al., 2012; Lebel et al., 2012; Li et al., 2014; Saito et al., 2009; Sexton et al., 2014; Westlye et al., 2010b; Yeatman et al., 2014).

The estimates at which each tract reaches peak maturity are in good agreement with the previous studies investigating lifespan changes in R1 (Yeatman et al., 2014) and MD (Hasan et al., 2010; Lebel et al., 2012; Westlye et al., 2010b). Frontal and temporal fasciculi (cingulum bundles, SLF and uncinate fasciculus) consistently showed intermediate-to-late peak maturation timings across the multiple microstructure measurements, suggestive of prolonged developmental periods. Our findings are consistent with previous DTI (Hasan et al., 2010; Lebel et al., 2012; Westlye et al., 2010b) and R1 (Yeatman et al., 2014) reports of prolonged maturation within these tracts. These tracts have also been shown to mature particularly slowly during childhood as compared to core sensory and motor pathways (Lebel et al., 2008; O'Muircheartaigh et al., 2014; Tamnes et al., 2010). The ages of peak maturation for the corticospinal tract and callosal connections vary more widely across microstructure measures and this may be reflective of their relative stability over the lifespan (weaker

quadratic aging effects) and advanced levels of maturation before the end of adolescence (Lebel et al., 2008; O'Muircheartaigh et al., 2014; Tamnes et al., 2010).

Sex differences were observed across five tracts for R1 but were generally weak and inconsistent. Of these tracts, sex differences in the SLF were the most robust, indicating higher R1 in males than females. These findings were not confirmed in the MT and R2* measurements which share myelination and/or iron sensitivities with R1 (Kucharczyk et al., 1994; Lutti et al., 2014; Stüber et al., 2014), perhaps suggesting that the observed sex differences in the SLF are driven by the additional sensitivity of R1 to water volume within a voxel (Fatouros and Marmarou, 1999; Gelman et al., 2001). Reported sex differences in tract microstructure measurements have generally been weak and inconsistent with differences reported varyingly across corticospinal, cingulum, ILF and forceps major tracts (Abe et al., 2002; Cox et al., 2016; Lebel et al., 2012; Ota et al., 2006). Hemispheric associations were most robustly observed for FA in the cingulum-cingulate, IFOF, SLF, uncinate and arcuate fasciculi. Across these tracts leftward asymmetries were found for the cingulum-cingulate, arcuate and uncinate fasciculi, and rightward asymmetries observed in the IFOF and SLF. These findings contribute to previous DTI studies reporting hemispheric differences in tract microstructure across various age ranges (Cox et al., 2016; Hasan et al., 2010).

One unique aspect of our investigation is the inclusion of novel g-ratio measurements (Stikov et al., 2015) in a large lifespan cohort of 801 subjects. Appropriate levels of WM myelination are crucial for optimal signal conduction and timing in the human brain and the g-ratio represents a fundamental organizational principle for controlling these properties (Pajevic et al., 2014; Waxman, 1975), with lower g-ratios representing a greater investment in myelination for a given axonal caliber. Theoretical arguments have suggested an optimal g-ratio of around 0.6 (Rushton, 1951), though histological investigations have found g-ratios closer to 0.7 in the splenium of the corpus callosum (Graf von Keyserlingk and Schramm, 1984). It is possible that the differences between theoretical optimal values and empirical findings may relate to a trade-off between metabolic and spatial constraints in brain organization (Bullmore and Sporns, 2012; Chomiak and Hu, 2009). Here we demonstrate that peak g-ratio levels have tract specific values in the range 0.67-0.76, consistent with a previous findings in younger adults (20-40 years; Cercignani et al., 2016). Spatial heterogeneity exists across the white matter fasciculi with projection fibers (corticospinal and thalamic radiation)

attaining the highest peak g-ratio values and the forceps-minor of the corpus callosum and association fasciculi reaching low to intermediate values. These findings suggest that the largest investments in myelination for a given axonal caliber occur in the anterior callosal fibers (forceps-minor) while conversely the lowest myelination investments occur in corticospinal fibers. Interestingly, the genu of the corpus callosum is known to possess axons of exceptionally small caliber - just 2.6 μ m on average (Aboitiz et al., 1992) - while the human spinal cord has been reported to contain axons exceeding 10 μ m in diameter (Häggqvist, 1936; Liewald et al., 2014). Future work will be needed to better understand the relationships between functional specialization, axonal caliber and myelin investment in the adult human brain.

Of the two previous lifespan g-ratio studies, both had fewer than 100 participants which precluded the investigation of nonlinear associations with age (Berman et al., 2017; Cercignani et al., 2016). Here, with a large sample size of 801 individuals, we observed significant quadratic aging effects for the g-ratio across all tracts excluding the corticospinal tract and forceps-major, both of which are well developed by young adulthood and increase steadily in their g-ratio values thereafter. These results are in good agreement with the findings of Cercignani et al. (2016). A contrasting report by Berman et al. (2017) found little evidence of g-ratio associations with age in callosal sub-regions. This discrepancy may result from the linear models applied in their investigation and their lower density of subjects at higher ages, as our results suggest that the accelerating increases in g-ratio values become most apparent from the third decade onwards. Our observed increases in the g-ratio across all tracts during senescence provides evidence of widespread demyelination processes in the aging human brain which cannot be explained as the sole consequence of axonal degeneration. Investigations in the experimental animal have shown extended periods of myelin degradation in aging primates in the absence of overt axonal loss (Peters, 2009; Peters and Sethares, 2003). However, it has been challenging to determine how translatable these findings are to human aging due to the shorter lifespan of rhesus monkeys (Tigges et al., 1988) and the extensive phylogenetic changes observed in human white matter (Rilling et al., 2008; Schoenemann et al., 2005). Our results provide novel evidence of myelin specific degradation processes occurring in the human brain during normal aging.

The noticeable differences in microstructural aging trends across the brain, in terms of both heterochronicity and spatial heterogeneity, provide support for the last-in-first-out retrogenesis hypothesis of aging (Raz, 2000). We demonstrate a strong correlational relationship between peak maturational timing and the extent of quadratic measurement change across the lifespan for the most myelin sensitive measures (MT, R1, R2* & g-ratio, each with Pearson's $r \geq 0.65$), suggesting a relationship between extended ontological development during adulthood and senescent vulnerability to myelin loss. This supports the findings in post-mortem and DWI studies which have reported distinct ontological differences between early myelinating projection and posterior callosal fibers, and the later developing frontal and association pathways (Huttenlocher and Dabholkar, 1997; Kinney et al., 1988; Lebel et al., 2012; Stricker et al., 2009; Westlye et al., 2010b). Support for the last-in-first-out hypothesis was less consistent for the DWI related measures (FA, MD, ICVF & ODI). Both MD and ICVF displayed only weak correlational evidence for the last-in-first-out hypothesis ($r \leq 0.32$), though it is possible that certain outlier tracts (cingulum-hippocampus / corticospinal tract respectively) could be masking genuine relationships. Interestingly, both fiber dispersion measures (FA & ODI) displayed negative correlational trends. For example, in contrast to the myelin specific measures, ODI in the posterior portion of the corpus callosum - the forceps major - peaks exceptionally early as well as having the greatest quadratic aging effect. These negative correlations indicate that earlier peaks in water diffusion coherence are associated with greater lifespan reorganization.

Previous studies have typically provided qualitative descriptions of increased age-related vulnerability in the late myelinating pathways of the white matter (Brickman et al., 2012; Gao et al., 2011; Madden et al., 2012; Stricker et al., 2009). One recent study by Yeatman et al. (2014) went further by formulating quantitative definitions for the retrogenesis hypotheses. In contrast to our results they found no direct evidence for the last-in-first-out hypothesis using R1 and MD measurements. One potential explanation for this discrepancy comes from the differences in hypothesis formation. While we focused on peak timing predicting the rate of quadratic (accelerating) microstructure change either side of the peak, Yeatman et al. (2014) used a piecewise linear model to test the relationship between peak age and the duration of maturational stability (plateau). Our combined findings suggest that the late myelination of a region is predictive of relative levels of myelin reorganization (during decline

and post-adolescent maturation) but not the duration of peak maturational stability (Yeatman et al., 2014).

The gain-predicts-loss hypothesis (Reisberg et al., 2002) necessitates that symmetric aging trends should occur either side of a maturational peak. A cross-validated model selection procedure designated a symmetric (quadratic) aging model for MT, R1, g-ratio, FA, ICVF and ODI measurements. R2* and MD displayed highly asymmetric aging trends which were better described using an asymmetric Poisson curve model. These findings are in good agreement with the Yeatman et al. (2014) assessment of the gain-predicts-loss hypothesis that found supportive evidence for R1 but not MD tissue measurements.

The participants included in this study and taken from the general population were in relatively good health as we excluded any individuals with known neurodegenerative or psychiatric disease and screened all imaging data for overt pathology or signs of neurovascular abnormalities. One potential concern for cross-sectional study designs is that modeled trajectories may inaccurately describe within subject aging trends (Lindenberger et al., 2011). These designs also suffer from subject bias as there is no clear way to guarantee that the young individuals in the cohort will develop into the relatively healthy older individuals included in the study. Nonetheless, longitudinal studies of large cohorts represent a huge logistical and financial challenge, and the study duration required to test all subjects prospectively over the lifespan (≈ 75 years) is prohibitive. These considerations have led the few previous longitudinal studies to typically adopt semi-longitudinal designs whereby a relatively small number of subjects are recruited, over a reduced age range and/or then followed for a small number of years ($\approx 2-4$ years) (Barrick et al., 2010; Bender and Raz, 2015; de Groot et al., 2016; Lebel and Beaulieu, 2011; Sexton et al., 2014; Teipel et al., 2010). Such challenges have led to the majority of studies adopting cross-sectional designs (Callaghan et al., 2014; Cox et al., 2016; Hasan et al., 2010; Kochunov et al., 2012; Lebel et al., 2012; Li et al., 2014; Westlye et al., 2010b; Yeatman et al., 2014). Nevertheless, though the present study provides a well-powered investigation into cross-sectional aging trajectories, a full examination of intra-individual trends will require future prospective imaging studies which, in a fully longitudinal design, would require many decades of work to cover a comparable age range.

A further consideration for this study relates to the quality of the diffusion measurements and sampling schemes. The diffusion acquisition was made using a highly-optimized sequence of 118 imaging volumes and preprocessed images underwent a detailed quality checking process. The tractography was performed using an automated procedure (Yeatman et al., 2012b) which eliminated any investigator bias in tract definitions. Furthermore, the tract sampling scheme used here applies a Gaussian weighting function to weight points at the tract core more highly than peripheral streamlines, reducing the influence of partial volume effects at the tract periphery. Despite these controls we cannot rule out the possibility of partial volume effects - either from grey matter or cerebrospinal fluid contamination - biasing certain tract microstructure measurements (Vos et al., 2011) and as with previous investigations we advise caution when interpreting the data.

In conclusion, this single-scanner study provides an important contribution to our understanding of microstructural organization of the white matter across the human lifespan. The well-powered study sample of 801 individuals affords the description of detailed nonlinear aging trends across 20 major white matter pathways of the brain. Heterochronicity and spatial heterogeneity across tracts and microstructure measurements highlights the importance of using multiple tissue measurements to investigate each region of the white matter. Our data on g-ratio evolution over the human lifespan provides novel aging associations and an important baseline from which to assess dysfunctional g-ratio development and maintenance in a variety of psychiatric disorders (Du and Ongür, 2013). Furthermore, a quantitative assessment of the retrogenesis hypotheses of aging provides additional support for prolonged myelin maturation being associated with greater myelin reorganization and vulnerability with age. These findings present an important baseline from which to assess divergence from normative aging trends in developmental and degenerative disorders, and to further investigate the mechanisms connecting white matter microstructure to cognition.

3. Lifespan brain tissue changes reveal a modular architecture of human white matter

3.1 Introduction

Findings in recent years have made it clear that in-depth knowledge about the processes governing human white matter are of unique importance for understanding the behavioral consequences of brain maturation, healthy aging and an array of developmental and neurodegenerative disorders (Fornito et al., 2015). Human cognitive flexibility may emerge from the integration of hierarchical modular brain networks (see Park and Friston, 2013) and network analyses support both structural and functional brain modularity (Melie-Garcia et al., 2017; Sporns and Betzel, 2015). Neurodevelopmental investigations have also begun to reveal patterns of modular tissue change within the cerebral cortex (Krongold et al., 2015) with the suggestion that certain developmental disorders may target specific grey matter modules (Alexander-Bloch et al., 2014). Such investigations have yet to be extended to the study of white matter development and aging.

Evidence from animal models suggests that widespread alterations to tissue morphology and chemical composition occur across neuronal and glial cell types throughout the lifespan. Many axonal fibers in white matter swell and degenerate (Peters, 2009), axons may remain intact but undergo repeated periods of myelin loss and remyelination (Fancy et al., 2011), glial cells differentiate and proliferate in response to external signals (Fancy et al., 2011; Sandell and Peters, 2002), cellular debris accumulates (Neumann et al., 2009), and glial scars may begin to form (Silver and Miller, 2004). It is likely that developmental and age-related dysfunction partially results from disruption to a specific subset of these processes which, taken together, might provide a highly informative fingerprint for brain disease states.

Within the human brain, non-invasive neuroimaging results suggest widespread age-related changes to volume (Bartzokis et al., 2001; Walhovd et al., 2011) and myelin (Bartzokis et al., 2012; Callaghan et al., 2014; Draganski et al., 2011; Lebel et al., 2012; Westlye et al., 2010b; Yeatman et al., 2014). Lifespan trajectories vary across the major white matter pathways under the influence of genetic and environmental factors (Emery, 2010; Gibson et al., 2014), whilst the timing and degree of tissue change across brain systems may be linked

to evolutionary novelty (Hill et al., 2010; Rilling, 2014). The majority of magnetic resonance imaging (MRI) investigations of white matter changes associated with ageing have focused solely on diffusion tensor imaging (DTI) (Imperati et al., 2011; Kochunov et al., 2012; Lebel et al., 2012; Peters et al., 2014; Westlye et al., 2010b). DTI derived measures such as fractional anisotropy (FA) are inherently non-specific (Jones et al., 2013) and using these measures alone risks lifespan descriptions that are insensitive to important tissue changes while also lacking the ability to disentangle the relative trajectories of concurrent tissue processes. More recent biophysical models such as neurite orientation dispersion and density imaging (NODDI) (Zhang et al., 2012) aim to overcome such issues by estimating specific tissue organizational properties from the diffusion signal. In addition to the use of DTI derived indices a few studies have begun to investigate lifespan changes to myelin (Bartzokis et al., 2012; Yeatman et al., 2014) and iron (Callaghan et al., 2014) with the application of quantitative MRI techniques.

By combining multiple quantitative and specific measurements of tissue microstructure within the same cohort the complex, multiple and independent tissue processes acting upon white matter cell types (Fancy et al., 2011; Peters, 2009; Sandell and Peters, 2002) might be better characterized and separated than by univariate analyses of individual measurement types alone (Tardif et al., 2016; Yeatman et al., 2014). Such an approach necessitates a multivariate data-driven analysis to reveal the lifespan trajectory interactions across measurement types.

In this work we applied quantitative magnetic resonance imaging (qMRI) biomarkers indicative of tissue myelination and iron levels (multi-parameter mapping, MPM) (Draganski et al., 2011) in combination with state-of-the-art diffusion-weighted (DWI) microstructural imaging and tractography. We map whole-brain connections using a “connectome” approach, which offers a robust framework for the study of tissue microstructure changes across the lifespan using data-driven methods. Furthermore, by defining connections based on their cortical terminations microstructural observations in white matter can be directly compared with structural and functional measurements made within the cortex (Collin et al., 2014; Scholtens et al., 2014). The data collected from a large cohort of the general population forms a multi-parametric description of tissue property trajectories from adolescence through old age, achieving contrasting sensitivity to the multiple concurrent biological processes supporting and characteristic of normal aging.

3.2 Materials and methods

Subjects

The participants were healthy volunteers recruited from the Lausanne regional area of Canton Vaud, Switzerland based on fliers, university newsletters and, for the majority of subjects (N=504), their ongoing participation in the CoLaus | PsyCoLaus cohort (Preisig et al., 2009). All participants were screened for brain disorders. A total of 659 (335 female) participants (cross-sectional) were included in the study aged 7-84 years (mean age 51.8 ± 15.7 yrs). The age distribution can be broken down as follows: 61 participants aged 7-24; 69 participants aged 25-39; 241 participants aged 40-54; 212 participants aged 55-69; and 76 participants aged 70-84. The Centre Hospitalier Universitaire Vaudois (CHUV) Institutional Review Board approved all data collection procedures and written informed consent was given by participants or a parent/guardian. The authors state that they have obtained approval from CHUV and the CoLaus | PsyCoLaus Data Sharing and Publications Committee for use of the data and confirm that the data was analyzed anonymously.

MRI data acquisition

All imaging was performed on a 3T whole-body MRI system (Magnetom Prisma, Siemens Medical Systems, Germany) using a 64-channel RF receive head coil and body coil for transmission. Visual inspection of study participant data confirmed an absence of neither macroscopic brain abnormalities nor obvious vascular pathology.

Multi-parameter maps (MPMs)

The qMRI protocol consisted of three whole-brain multi-echo 3D fast low angle shot (FLASH) acquisitions with predominantly magnetization transfer-weighted (MTw: $TR/\alpha = 24.5\text{ms}/6^\circ$), proton density-weighted (PDw: $TR/\alpha = 24.5\text{ms}/6^\circ$) and T1-weighted (T1w: $24.5\text{ms}/21^\circ$) contrast (Helms et al., 2009, 2008; Weiskopf et al., 2013b). The MT-weighted contrast was obtained using a Gaussian-shaped radio frequency (RF) pulse prior to the RF excitation (4ms duration, 220° nominal flip angle, 2 kHz frequency offset from water resonance). Multiple gradient echoes were acquired for each contrast with alternating readout polarity. The minimal echo time was 2.34ms and the echo spacing was 2.34ms. The number of echoes was 6/8/8 for the MTw/PDw/T1w acquisitions to keep the TR value identical

for all contrasts. The image resolution was 1 mm³ isotropic, the field of view and the matrix size were 256 × 240 × 176 mm. Parallel imaging was used along the phase-encoding direction (acceleration factor 2 with GRAPPA reconstruction) (Griswold et al., 2002), partial Fourier (factor 6/8) was used along the partition direction. Data were acquired to calculate maps of the RF transmit field B1+ using the 3D echo-planar imaging (EPI) spin-echo (SE) and stimulated echo (STE) method described in (Lutti et al., 2012, 2010). The image resolution of the B1-mapping data was 4mm³, and the echo and repetition times were set to 39.06ms and 500ms respectively. The nominal flip angle of the SE pulse was decreased from 230° to 130° in steps of 10° (Lutti et al., 2012, 2010). B0-field mapping data was acquired using a 2D double-echo FLASH sequence to correct for geometric distortions in the 3D EPI data (Lutti et al., 2012, 2010). The total acquisition time was 27 min.

A subset of participants (N=84, 7-75 yrs) underwent an equivalent 1.5 mm³ MPM protocol. The acquisition parameters for this protocol differed for the following parameters: field of view = 240 × 225 × 180 mm, matrix size = 160 × 150 × 120. The total acquisition time was 13 min. In total, 38 study participants were scanned using both image resolution protocols. The data from these subjects was used to assess the consistency of edge microstructure measures across image resolutions and this was shown to be comparable to test-retest reproducibility at 1 mm³ (Supplementary Fig. 3.1).

Diffusion weighted imaging (DWI)

The diffusion weighted MRI data were acquired using a 2D echo-planar imaging sequence with the following parameters: TR/TE = 7420/69ms, parallel GRAPPA acceleration factor = 2, FOV = 192 x 212 mm², matrix size = 96 x 106, 70 axial slices, 2 mm isotropic voxel dimension, 118 isotropically distributed diffusion sensitization directions (15 at b = 650 s/mm², 30 at b = 1000 s/mm² and 60 at b = 2000 s/mm²) and 13 b=0 images interleaved throughout the acquisition.

MRI data preprocessing

Multi-parameter maps (MPMs)

The R2*, MT and R1 quantitative maps were calculated as previously described (Draganski et al., 2011) using in-house software running under SPM12 (Wellcome Trust Centre for

Neuroimaging, London, UK; www.fil.ion.ucl.ac.uk/spm) and Matlab (Mathworks, Sherborn, MA, USA). The $R2^*$ maps were calculated from the regression of the log-signal of the eight PD-weighted echoes (Weiskopf et al., 2014). The MT and R1 maps were computed as described in (Helms et al., 2008), using the MTw, PDw and T1w images averaged across all echoes. The R1 maps were corrected for local RF transmit field inhomogeneities using the B1+ maps computed from the 3D EPI data (Helms et al., 2008) and for imperfect RF spoiling using the approach described by (Preibisch and Deichmann, 2009).

Each participant's MT image was processed using the FreeSurfer version 5.3.0 software package pipeline (www.surfer.nmr.mgh.harvard.edu). The standard pipeline reconstructs an individual's cortical and white matter surfaces from the participant's structural image data. The following steps comprise the surface preprocessing pipeline: correction of image intensity variations due to MR inhomogeneities (Dale et al., 1999); skull stripping (Ségonne et al., 2004); cortical grey matter (GM) and white matter (WM) segmentation (Dale et al., 1999); separation of the brain hemispheres and subcortical structures (Dale et al., 1999; Fischl et al., 2004, 2002); and finally a set of grey/white matter interface and pial surfaces for both brain hemispheres (Dale et al., 1999). After surface reconstruction, the individual participant's surfaces were used to estimate the transformation that achieved maximal correspondence between the sulcal and gyral patterns of the individual and those of an average brain (Fischl et al., 1999a, 1999b). This information was later used to bring a high-resolution cortical parcellation (Gordon et al., 2016) into each individual's native image space.

The FSL FAST tool (Smith, 2002; Zhang et al., 2001) was used to segment MT images into tissue probability maps for WM, GM and CSF. Subcortical structures were segmented using the FSL FIRST tools (Patenaude et al., 2011). These structural segmentation preparations are described in detail in Smith et al. (2015a) and are necessary for the anatomically constrained tractography (ACT; Smith et al., 2012) procedures used later to build the structural connectome.

Diffusion weighted imaging (DWI)

DWIs were preprocessed to correct for eddy currents and subject motion using the FSL EDDY tool (Andersson and Sotiropoulos, 2016) and the gradient directions were appropriately rotated to correct for subject movement (Leemans and Jones, 2009). The B0 maps acquired

as part of the structural imaging session were used to correct for EPI susceptibility distortions with the SPM field mapping toolbox (Hutton et al., 2002). The DWI images were then rigid body aligned to the MT image with the aid of the mean $b=0$ image using SPM12.

Diffusion tensor imaging (DTI) maps were estimated on the $b=0$ s/mm², $b=650$ s/mm², and $b=1000$ s/mm² data using a constrained non-linear least-squares (CNLLS) algorithm (Koay et al., 2006). Fractional anisotropy (FA) measures were estimated but later excluded from further analysis as FA is a non-specific measure of tissue microstructure, particularly in regions of crossing fibers (Bartzokis et al., 2012; Jones et al., 2013), and was shown to have inconsistent developmental rates along the length of a fascicle (Supplementary Fig. 3.2). The remaining qMRI measurements included in this study were shown to have strong and consistent aging effects along the length of a fascicle. The neurite orientation dispersion and density imaging (NODDI; Zhang et al., 2012) maps were processed with the AMICO toolbox (Daducci et al., 2014) using multi-shell diffusion data across all of the acquired b -values.

Quality assurance procedures

The data for all subjects included in the study underwent a stringent quality control assessment. An experienced investigator visually assessed the preprocessed neuroimaging data based on the following criteria: 1) Quantitative MPM maps (MT, R1, R2*) rated for movement artifacts and abnormal white matter signal intensities; 2) Diffusion and structural MRI image alignment; 3) Quality of the diffusion FA maps and tensor residuals; 4) Reliability of the pial and white matter surface reconstructions; 5) Accuracy of the tissue type segmentation and parcellations. If data failed any of these quality assessment criteria the relevant subject was excluded from the study. In total, data from 939 subjects were assessed in this manner with a total of 659 participants passing each of the quality checks and consequently being included in the study.

Diffusion tractography

All processing procedures described within this section were performed using the MRTrix3 software package (www.mrtrix.org; Tournier et al., 2012). The constrained spherical deconvolution (CSD; Tournier et al., 2007, 2004) fiber orientation densities (FODs) were calculated using a multi-shell, multi-tissue CSD (MSMT-CSD) algorithm ($l_{\max} = [0, 2, 6, 10]$ for WM) which has been shown to reduce the presence of spurious fiber orientation distribution

function (fODF) peaks in voxels containing GM and/or CSF partial volumes (Jeurissen et al., 2014). All tractography streamline reconstructions were made using the probabilistic 2nd-order Integration over fiber orientation distributions (iFOD2) algorithm (Tournier et al., 2010) in conjunction with the ACT framework (Smith et al., 2012). The following parameters were used for the streamline tracking of each study participant's data: number of accepted streamlines 20 million, step size 1 mm, maximum curvature per step 45°, length 5-250 mm, FOD amplitude threshold 0.1. We used a dynamic seeding algorithm (R. E. Smith et al., 2015b) to promote optimal streamline densities supported by the FODs during tracking. The SIFT algorithm (Smith et al., 2013) was applied to filter down to the 10 million streamlines best supported by the FOD data before applying the SIFT2 algorithm (R. E. Smith et al., 2015b) to provide relative weights of the remaining 10 million streamlines. This state-of-the-art diffusion tractography pipeline has been shown to produce robust and reproducible connectomes, reducing streamline density and connectivity biases associated with earlier approaches (R. E. Smith et al., 2015a).

Connectome construction and quantification of tissue properties

As part of the structural preprocessing procedures a high-resolution cortical parcellation (Gordon et al., 2016) was projected on the cortical surfaces of each subject. The surface parcellations were converted into volume images by projecting the surface labels onto voxels between the GM/WM interface and pial surfaces. Subcortical structures segmented by the FSL FIRST (Patenaude et al., 2011) procedure were added to the parcellation volumes for each subject. For each study participant, there now existed a parcellation image in native space containing a total of 349 structures (333 cortical and 16 subcortical).

Tractography streamline endpoints were mapped to their nearest parcellation nodes. If a node was not located within a 4 mm radius of a streamline termination then this streamline was excluded from the connectome construction (R. E. Smith et al., 2015a). Streamlines connecting to the same node at both ends were excluded, and thus the diagonal entries were zero for all adjacency matrices. In addition to counting the absolute number of streamlines connecting any two parcellation nodes, we generated adjacency matrices weighted by quantitative tissue measures along the connecting streamlines: for each streamline a quantitative MRI measure was sampled along its length; these samples were then averaged

along the length of each streamline; finally, these values were averaged across all streamlines corresponding to each edge in the connectome (i.e. connecting the same nodes). This provided mean microstructure measures for each edge of the connectivity matrix. For each subject, we generated 5 quantitative MRI adjacency matrices (weighted by MT, R1, R2*, MD, and ICVF) in addition to the adjacency matrix weighted by total streamline count. All adjacency matrices had their streamline contributions weighted by the corresponding SIFT2 weights to improve robustness and biological accuracy of the structural connectomes (R. E. Smith et al., 2015a).

A connectome mask was generated to select the set of edges to be assessed in later steps. The connectome matrices weighted by streamline count were averaged across all subjects to produce a mean connectivity matrix. We binarized the mean connectivity matrix to a density of $\rho \approx 5\%$, resulting in a streamline threshold of 329 streamlines/edge. This binarized connectome mask thus contained the 5% (3,015) most densely connected edges, each of which comprised on average 1,650 (95% CI: 350-6,850) connecting streamlines. A sparse connectome density of 5% lies within the range typically used to describe structural brain networks (Achard and Bullmore, 2007; Hagmann et al., 2008) and focuses the analysis on a subset of the most strongly connected edges. For network visualization purposes all images were generated using the BrainNet Viewer software package (Xia et al., 2013; www.nitrc.org/projects/bnv).

Model fitting

We investigated the use of four aging models to explain patterns of WM tissue microstructure change with age (see Supplementary Methods for detailed descriptions). Repeated 5-fold cross-validation was applied to quantify model accuracy: the data were split into 5-folds, each containing 20% of the data. The model was then fit to 80% of the data and used to predict the remaining 20% of data points. This process was cycled through for each of the 5-folds, and then the process repeated with randomization to provide a total of 10^5 model prediction instances. The winning model for a tissue microstructure measure was chosen as the model which minimized cross-validated error across the network. The cross-validation results indicate that MT and R1 are most accurately modeled with a second order polynomial,

R2* with a Poisson curve, while the smoothing spline is most appropriate for MD and ICVF. Cross-validation results are supplied in Supplementary Table 3.1.

Bootstrapping was used to test for the reliability of all parameter estimates. Unless otherwise stated the results throughout this paper use the median and bootstrapped 95% CI to represent the central tendency and uncertainty for each parameter estimate (e.g. peak age estimates). All modeling procedures included nuisance regressors for sex and structural image resolution. We summarized the lifespan tissue microstructure trajectories using three parameters which characterize the aging curves regardless of model type. These three lifespan measures were: a) peak age; b) peak value; and c) lifespan change. These parameters define the age at which a tissue measure is expected to peak, the expected peak value and the cumulative amount of measurement change across the lifespan. Full definitions for the four aging models and three lifespan features are provided in the Supplementary Methods section.

Clustering lifespan trajectories

Network edges with similar multivariate aging trajectories were clustered together into lifespan modules. Lifespan features for each quantitative MRI metric were z-score normalized and entered into a principle component analysis (PCA) to reduce dimensionality and the statistical dependence between the (partially) correlated tissue measurements. The first 10 principle component scores (explaining 95% of variance) were then used as features for an expectation-maximization Gaussian mixture model (EM-GMM) algorithm. The EM-GMM algorithm finds the Gaussian mixture model with maximum likelihood for the multi-dimensional lifespan data. Mean model responsibilities were tested for models with k=2-50 clusters. A clear local maximum in model responsibility was observed for k=5 clusters and was therefore chosen as the clustering number of interest. Cluster mean centers and partial correlations between all lifespan measures were used to assess discriminating features between the modules.

To provide additional assurance of the lifespan module robustness we clustered lifespan trajectories using non-parametric linear mixed effects (LME) modeling in a manner similar to Krongold et al. (2015). Overlapping age bins were defined every 5 years from 20 to 65 years with a window width of 20 years. A linear model was fit to data falling within the age bins for all network edges and tissue parameters. The mid-window tissue values and maturational

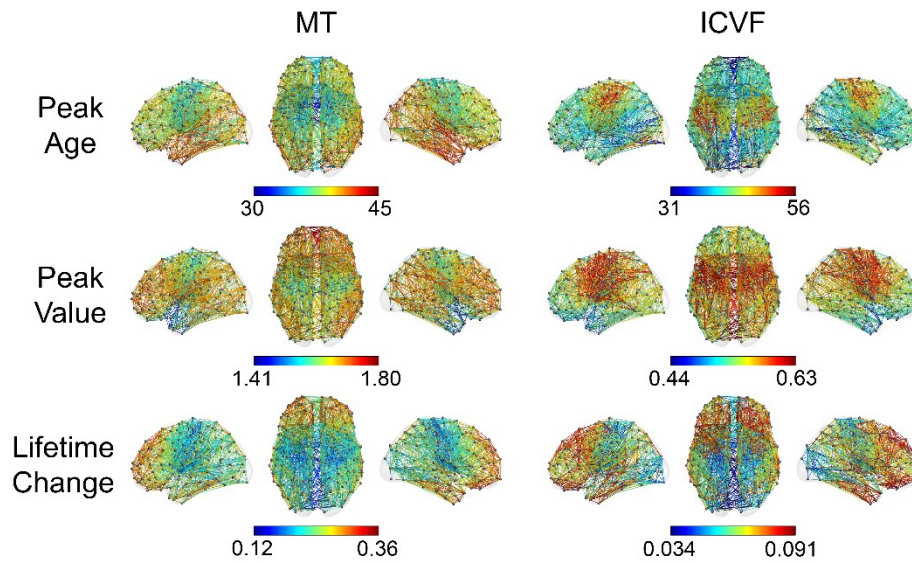


Figure 3.1. MT and ICVF lifespan measures for each network edge reveal the complex patterns of tissue change evident across human white matter. Lifespan measures for the age of peak maturity (Peak Age), the tissue value at peak maturity (Peak Value) and the cumulative tissue change from age 10 to age 75 (Lifetime Change) are shown for each of the 3,015 network edges connecting 349 cortical and sub-cortical nodes. Great variability in maturational timings, tissue composition and lifespan tissue change exist across human white matter. All visualized network edges have highly significant quadratic aging effects ($p < 0.001$ Bonferroni corrected). Peak Age values are in years; Peak Value and Lifetime Change measures are expressed in percentage points for MT, and fractional units for ICVF.

gradients formed the lifespan features which were first entered into a PCA, before clustering the scores explaining 95% of variance using the EM-GMM algorithm. A comparison of module classifications for the model based and non-parametric LME lifespan modules is provided in Supplementary Fig. 3.3.

3.3 Results

Lifespan tissue changes in human white matter

Over the lifespan, MT undergoes substantial change with peak ages between 30 and 45 years across different WM edges (Fig. 3.1). Motor and callosal pathways peak first followed by frontal and parietal association pathways and finally, temporal white matter. Prefrontal white matter has the highest MT values at peak maturity and displays the greatest change over the lifespan. In contrast, the early myelinating motor connections achieve a moderate peak value for MT and demonstrate little change over the lifespan, exhibiting only one third of the total change observed in prefrontal connections.

Significant age-related change to ICVF is observed across white matter networks (Fig. 3.1). Callosal fibers reach mature ICVF values earliest, to a high peak value of $ICVF \approx 0.6$ and are the most stable connections over the lifespan, particularly in mid- to posterior-segments connecting motor and visual areas. In contrast to the observed patterns for MT lifespan trajectories, motor pathways have the latest ICVF peak age (>50 years) with some of the highest peak ICVF values. Frontal and temporal lobe pathways mature at an earlier age with intermediate mature ICVF values but exhibit a large amount of change across the lifespan (for R1, R2* and MD lifespan measures see Supplementary Fig. 3.2-3.4).

The largest tissue changes year-on-year occur in frontal and temporal pathways (for relative rates of change over the lifespan see Supplementary Video 1). At age 40 years most measurement change has slowed, while the increases in ICVF continue at a reduced rate within cortico-striatal connections and along the inferior longitudinal fasciculi. As the brain moves into late middle- and old-age the frontal lobes are the first to see significant decline, being the most vulnerable to MT and ICVF losses. Temporal lobe white matter is also particularly vulnerable to age-related decline; while motor and callosal fibers, though still declining, will typically do so at a slower rate. For all measures and edges we observe significant nonlinear aging effects (quadratic effects, $p < 0.001$ Bonferroni corrected), with MD following U-shaped and all other measures following inverted U-shaped aging trajectories. During the transition from middle- to old-age an anterior to posterior gradient of accelerating decline is observed throughout the white matter network.

Modular lifespan tissue changes in white matter networks

Clustering network edges based on their representative aging features reveals developmentally related lifespan modules (Fig. 3.2). This organization is driven by the shape of the multivariate aging trajectories without any imposition of spatial priors. The five-cluster solution divides human white matter into broadly defined fronto-striatal (blue), callosal (red), fronto-parieto-occipital (green), prefronto-temporal (pink) and limbic (yellow) modules. This should not be taken to mean that the estimated network modules comprise solely of connections associated with their assigned name, but rather as a guide to the set of dominant pathways within each module.

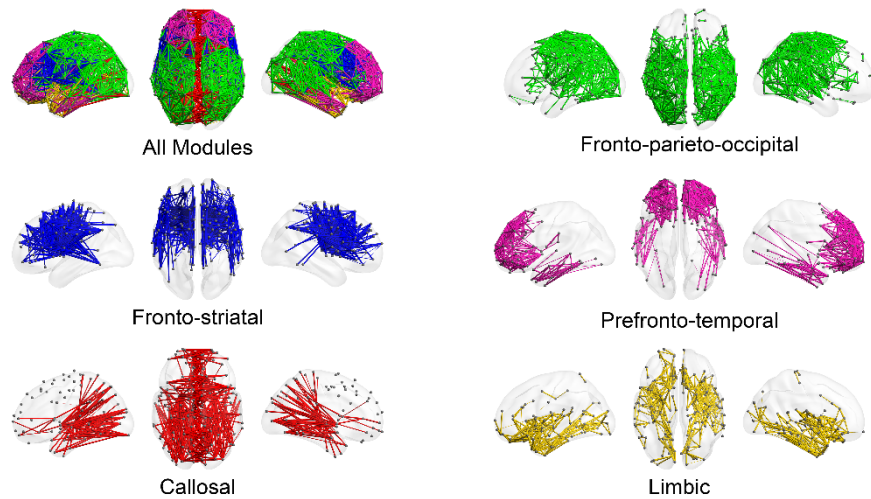


Figure 3.2. Lifespan modules in human white matter. Lifespan measures (Peak Age, Peak Value & Lifetime Change) for 5 quantitative MRI biomarkers (MT, R1, R2*, MD & ICVF) were entered as features for Gaussian mixture model clustering of network edges. The number of clusters, $K=5$, was determined by examining mean model responsibility (or posterior-probability) across a range of K . The resulting lifespan modules represent groups of edges with similar lifespan trajectories across the 5 tissue biomarkers. Regions of coherent multivariate tissue change localize along functionally described brain systems.

By performing a spatial correlation between the cortical terminations of a module and fMRI intrinsic connectivity networks described by Yeo et al. (2011) we observe how each of the lifespan modules connects to specific functional networks. We find that the fronto-parieto-occipital (green), comprising of many short range superficial fibers connecting neighboring structures, is densely connected to regions within the visual, dorsal attention and motor cortices; the prefronto-temporal (pink) module connects fronto-parietal, default mode and limbic networks; while the limbic (yellow) module densely connects cortical regions of the limbic network. The callosal module (red) contains all inter-hemispheric connections, thus we term this module based on the uniqueness of these connections. However, this module does also contain edges connecting subcortical and visual cortices (e.g. optic radiation projections) and this is reflected in a relatively strong spatial correlation with cortical regions subserving the visual network.

To investigate which lifespan features most clearly discriminate between modules, the cluster centers for each module and qMRI metric are analyzed (Fig. 3.3). The callosal module (red) is the first to reach peak maturity with the earliest peak values across all qMRI measures excluding MD and R2* for which it peaks slightly later than the fronto-striatal module (blue). Similarly, the fronto-striatal module achieves peak MT, R1, R2* and MD early while also being

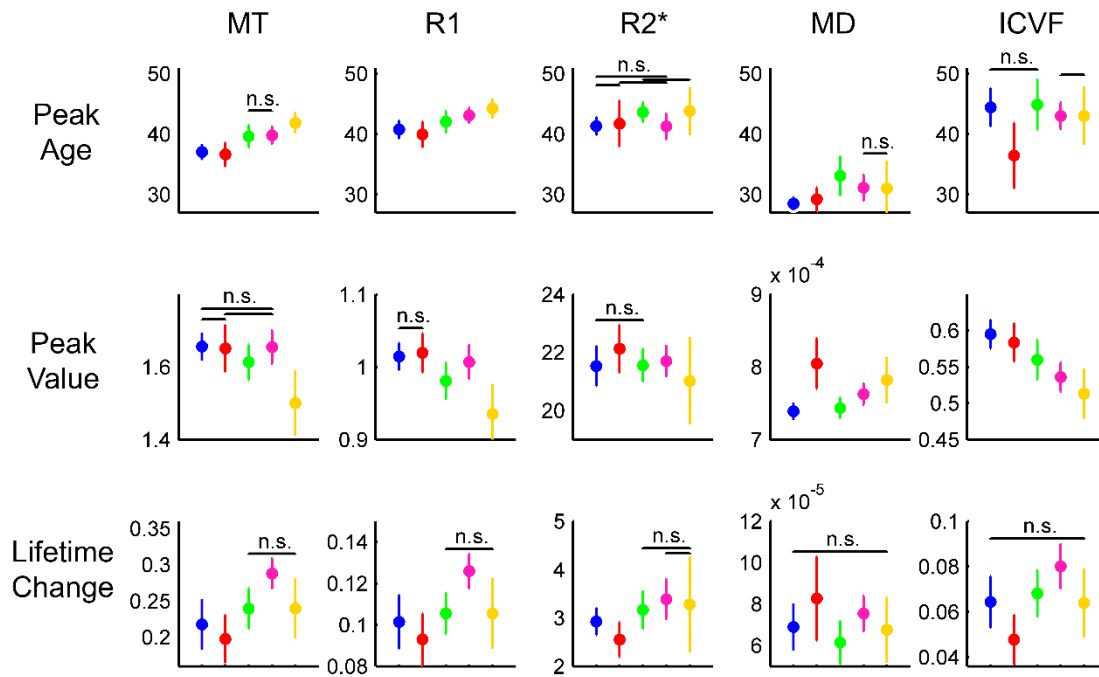


Figure 3.3. Variability of lifespan tissue dynamics across lifespan modules. Cluster centers (solid colored circles) and standard deviations (vertical lines) are shown across lifespan measures and MRI biomarkers. The edges comprising fronto-striatal (blue), callosal (red), motor-parieto-occipital (green), prefronto-temporal (pink) and limbic (yellow) lifespan modules were used to compare module centers using a Welch's t-test. Non-significant differences are highlighted, all other comparisons reached significance ($p < 0.05$ Bonferroni corrected). Fronto-striatal and callosal modules reach peak maturity first followed by prefronto-temporal, motor-parieto-occipital and limbic modules. Fronto-striatal and callosal modules are also typically very stable in contrast to the prefronto-temporal module which exhibits large dynamic change across the lifespan (developmental increases and aging decline). Peak value and lifetime change measures are expressed in units of percentage points for MT, s^{-1} for R1 and R2*, mm^2s^{-1} for MD, and fractional units for ICVF.

relatively stable over the lifespan. The callosal and fronto-striatal modules reach high peak values in MT, R1 and ICVF with intermediate to high values in R2*.

The limbic module (yellow) peaks late for the MT, R1 and R2* measurements, with low peak values at maturity and displaying an intermediate amount of change over the lifespan. The prefronto-temporal module (pink) displays considerable microstructural alteration, possessing the largest lifetime changes in MT, R1, R2* and ICVF. This module also matures relatively late and reaches high peak values, particularly for the most myelin specific measures (MT and R1). Finally, fascicles within the fronto-parieto-occipital module (green) are slow to mature in R2* and diffusion measures while characteristically displaying intermediate peak value and lifetime change estimates.

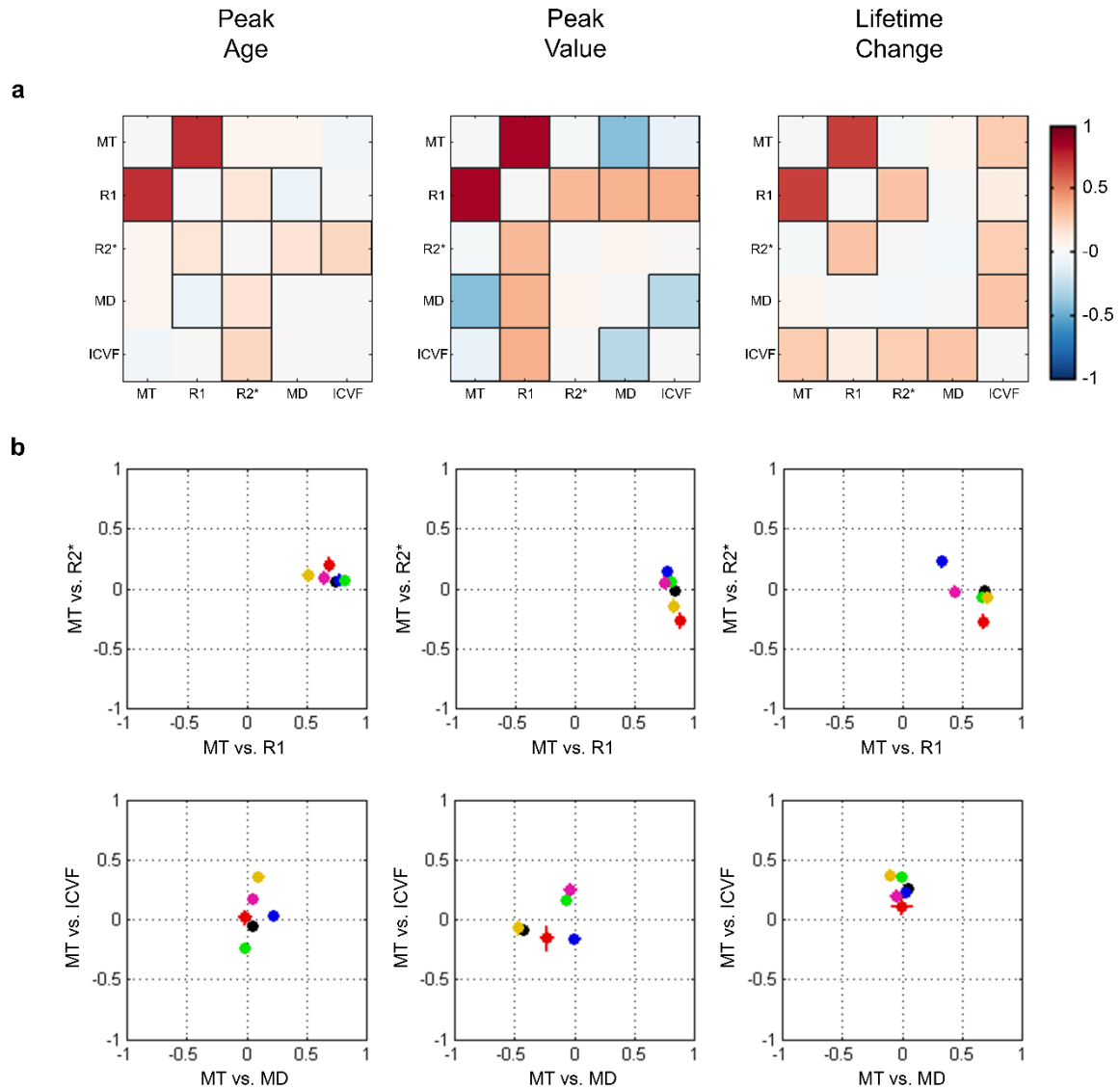


Figure 3.4. Interdependencies between lifespan measures across the entire white matter and within lifespan modules. (a) Partial correlations between MRI biomarkers for each of the lifespan measures using all network edges. Significant correlations ($p < 0.05$, Bonferroni corrected) are highlighted using an outlined box. (b) Partial correlations for MT and other MRI biomarkers (first rows/columns of a) are expanded to show the differing microstructural relationships within fronto-striatal (blue), callosal (red), motor-parieto-occipital (green), prefronto-temporal (pink) and limbic (yellow) lifespan modules.

Interdependence of brain tissue measures to developmental processes

We observe a strong interdependence of certain tissue property measurements based on the partial correlations of all lifespan measures (Fig. 3.4a). First, we will highlight the relationships that emerge globally across the entire white matter before looking at localized relationships within each of the lifespan modules. Strong global correlations are observed for MT and R1 (peak age, $r = 0.74$, $p < 0.001$; peak value, $r = 0.84$, $p < 0.001$; lifetime change, $r = 0.69$, $p < 0.001$), and to a lesser extent for R1 and R2* (peak age, $r = 0.14$, $p < 0.001$; peak value, $r =$

0.33, $p < 0.001$; lifetime change, $r = 0.29$, $p < 0.001$). MT and R2* remain globally uncorrelated (peak age, $r = 0.05$, $p = n.s.$; peak value, $r = -0.02$, $p = n.s.$; lifetime change, $r = -0.02$, $p = n.s.$). The global correlations between MT and the DWI measures were not significant except in the cases of MT vs. MD peak value ($r = -0.43$, $p < 0.001$) and MT vs. ICVF lifetime change ($r = 0.26$, $p < 0.001$). Between the two DWI indices, MD and ICVF, moderate correlations exist for peak age ($r = -0.28$, $p < 0.001$) and lifetime change ($r = 0.29$, $p < 0.001$).

Local relationships within a lifespan module often differ substantially from globally observed relationships (Fig. 3.4b). The relationship between MT and R1 remains strong and consistent within each of the developmental modules ($0.33 \leq r \leq 0.89$, $p < 0.001$). We observe moderate partial correlations between MT and R2* within the callosal module for peak age ($r = 0.20$, $p < 0.05$) and peak value ($r = -0.27$, $p < 0.001$), and for lifetime change in the callosal ($r = -0.27$, $p < 0.001$) and fronto-striatal ($r = 0.22$, $p < 0.001$) modules. For peak age MT vs. ICVF strong inter-module differences exist between the fronto-parieto-occipital ($r = -0.24$, $p < 0.001$) and limbic ($r = 0.36$, $p < 0.001$) modules. For MT vs. MD the only significant peak age correlation was observed within the fronto-striatal module ($r = 0.22$, $p < 0.001$). For MT vs. MD peak values we observe strong negative correlations in line with the global results for callosal ($r = -0.23$, $p < 0.01$) and limbic ($r = -0.47$, $p < 0.001$) modules while this relationship breaks down within fronto-striatal ($p = n.s.$), fronto-parieto-occipital ($p = n.s.$) and prefronto-temporal ($p = n.s.$) modules (for the complete set of all possible global and intra-modular partial correlation see Supplementary Fig. 3.5).

3.4 Discussion

In this study, we investigate age-related trajectories of multiple tissue property measures of the brain's white matter to demonstrate a unique modular spatial pattern of lifespan change. The modules comprise cortico-cortical and cortico-subcortical pathways of synchronized lifespan tissue change, revealing prominent distinctions between fronto-striatal, callosal, fronto-parieto-occipital, prefronto-temporal and limbic networks.

The lifespan modules emerge from a data-driven assessment of the multivariate age-related trajectories measured across human white matter. The five-module solution is supported by maximizing the mean model responsibility (or posterior-probability) and a highly coherent modular organization emerges independent of the methods used to model the

tissue property trajectories (Supplementary Fig. 3.3). The callosal module is the earliest to mature and is typically the most stable over the lifespan. This is in agreement with previous results, which have described early maturation and relative stability for the corpus callosum and optic radiations (Kochunov et al., 2012; Lebel et al., 2012; Westlye et al., 2010; Yeatman et al., 2014). The fronto-striatal module also follows this pattern of early maturation and low lifetime change. In contrast, the prefronto-temporal and limbic modules peak late and exhibit the largest lifetime changes, corroborating previous reports of particularly large lifespan change in frontal and temporal white matter (Bartzokis et al., 2012; Kochunov et al., 2012; Lebel et al., 2012; Yeatman et al., 2014).

One previous study (Imperati et al., 2011) attempted to cluster lifespan trajectories at the voxel level to reveal white matter regions of coherent lifespan change. The authors reported that major fiber bundles possessed coherent lifespan trajectories along their length, however the work was restricted to an analysis of FA measures and the study population of 144 participants did not extend beyond 48 years of age. In the present study, the choice of clustering edge rather than voxel-based features was made in order to classify pathways with coherent microstructural change across the lifespan. These pathways are defined in relation to their cortical terminations allowing future work to investigate the relationship between white matter and grey matter lifespan trajectories (Storsve et al., 2016) and the influence of topological organization on microstructural tissue change (Collin et al., 2014; Scholtens et al., 2014).

The qMRI measurements used within this study are principally sensitive to local changes in myelin tissue volume (MT, R1) (Draganski et al., 2011; Lutti et al., 2014), iron deposition (R2*) (Fukunaga et al., 2010), intracellular volume fractions (ICVF) (Zhang et al., 2012) and cellular membrane organization (MD) (Beaulieu, 2002). Relating the qMRI measures to the aging brain, we note that myelin is particularly high in macromolecular and iron content, which would predict increasing MT, R1 and R2* during maturation. During this process, as increased numbers of axons become myelinated and axon diameters increase (Emery, 2010; Peters et al., 2001), an overall decrease in interstitial space takes place, leading to increased ICVF and decreased MD. During the repair process, degraded myelin is replaced with remyelinated sheaths of reduced length and thickness (Fancy et al., 2011), resulting in early increases to MD and decreases to MT and R1. With ongoing aging, degenerative processes begin to take

precedence and myelin sheaths become damaged or lost with a portion of axons degenerating (Peters, 2009). These processes would lead to significant decreases in MT, R1, R2* and ICVF. The degradation of cellular tissue increases interstitial space resulting in higher MD values in old age. These predictions are well supported by our data and occur globally across the white matter network.

Beyond the general trend of maturation, maintenance and degradation periods across the brain it is the precise timings and extent of localized tissue change that provide the features that shape the lifespan module classifications. Multiple biological tissue processes are in action over the lifespan and the differing time-courses of these processes are beginning to be isolated and measured using multi-modal microstructure imaging (Yeatman et al., 2014). By combining multiple qMRI measurements with sensitivities to differing tissue processes, subtle alterations to neuronal and glial cell types might be characterized more formally (Sandell and Peters, 2002, 2001; Yeatman et al., 2014). However, the partially overlapping sensitivities of the qMRI measures should be carefully considered for accurate interpretation of results when inferring the biological processes driving an observed qMRI change. Additional sensitivities to iron deposition (R1) (Stüber et al., 2014), myelination (R2*, MD, ICVF) (Beaulieu, 2002; Stüber et al., 2014), voxel water volume (R1) (Gelman et al., 2001) and intracellular volume fractions (MD) (Beaulieu, 2002) provide important secondary signal contributions. If two qMRI measurements were to share a primary or secondary tissue sensitivity one might expect to observe robust correlations for all lifespan measures and modules. We do not observe robust partial correlations between MT, R2*, MD or ICVF, suggesting that these measures are largely independent or, perhaps, that an asynchronicity exists between their underlying microscopic processes (Fig. 3.4). In contrast the lifespan measures are very strongly correlated between MT and R1 both globally and within lifespan modules. This is reflective of these two measures being principally sensitive to the same myelination processes. Any differences between the measures are likely driven by the secondary dependence of R1 to the water volume within a voxel and localized iron content (Gelman et al., 2001; Stüber et al., 2014). R2* is primarily sensitive to such localized iron content (Fukunaga et al., 2010) and this shared sensitivity results in weaker but significant relationships between the R1 and R2* lifespan measures.

Examining the rates of change across the lifespan reveals a posterior-anterior gradient during maturation followed by a reverse anterior-posterior gradient of decline in old age

(Supplementary Video 1). This observation is consistent with genetically mediated gradients of cortical surface expansion (Chen et al., 2013) and MRI descriptions of aging white matter (Gao et al., 2011). Furthermore, differences in peak maturation timings are apparent across the reported lifespan modules and act as a discriminating factor between modules (Fig. 3.3). One possible explanation for the timing differences between the lifespan modules is that functional neuroanatomy plays a role in organizing tissue change along a hierarchical sequence of development (Greenfield, 1991). Connections that mediate more basic interhemispheric, motor or visual functions would reach maturity earlier than those involved in higher-order executive, social and emotional processing. Indeed, work in the macaque has shown protracted development and synaptic refinement in executive relative to sensory regions (Elston et al., 2009). Developmental studies in humans also provide evidence of earlier maturation in sensory-motor regions relative to higher-order association cortex (Krongold et al., 2015; Sotiras et al., 2017). Many of the cortical regions that develop latest are also the most evolutionarily novel (Hill et al., 2010), and increased evolutionary novelty has recently been associated with greater age related change (Sotiras et al., 2017). Within human white matter some of the most striking evolutionary expansion is reported to take place within prefrontal and ventral temporal regions (Rilling, 2014; Rilling et al., 2008). The topological correspondence of these observations with the prefronto-temporal module, for which we note delayed maturation and pronounced age-related vulnerability, provides a plausible link between evolutionary novelty, prolonged maturation, and age-related vulnerability in human white matter.

The processes governing lifespan tissue changes are controlled via a combination of intrinsic genetic programs and extrinsic environmental influences. Evidence suggests that within mammalian white matter, levels of myelination (Emery, 2010; Gibson et al., 2014) and axonal caliber (Fancy et al., 2011) vary in response to electrical activity leading to ongoing experience dependent plasticity. Furthermore, appropriate levels of myelination are likely controlled by a number of intracellular signaling pathways which promote and/or inhibit myelination processes (Fancy et al., 2011). Within the human cortex, regional variations in maturational patterns have been shown to relate to shared genetic influences which may localize along functional lines (Chen et al., 2013) and extend to a regulation of tissue dynamics across the lifespan (Fjell et al., 2015). White matter microstructure is also heavily determined

by genetics (Chiang et al., 2009; Pfefferbaum et al., 2001), particularly during adolescence and in subjects with an above average intelligence quotient (IQ) (Chiang et al., 2011). These findings suggest that the degree of genetic control acting upon human white matter may vary across the lifespan and interact with environmental factors.

How might dysfunction to a specific lifespan module manifest itself in a disease state? A number of studies have begun to link functional and developmental modules to disease vulnerability within human grey matter (Alexander-Bloch et al., 2014; Douaud et al., 2014; Seeley et al., 2009). We hypothesize that disruptions to a specific subset of the mechanisms coordinating a white matter lifespan module may underlie certain network dysfunction across a range of developmental and neurodegenerative disorders (Alexander-Bloch et al., 2014; Zhang et al., 2013). Such questions demand future investigations linking genetic and environmental influences to maintenance and degradation processes in human white matter.

The study population of 659 individuals used to conduct this analysis represents one of the largest investigations of white matter tissue changes from adolescent development to old age senescence. Previous reports have typically studied populations comprising 100-430 individuals (Bartzokis et al., 2012; Lebel et al., 2012; Westlye et al., 2010; Yeatman et al., 2014). Furthermore, these data provide the first benchmark of non-linear MT, $R2^*$ and ICVF changes across the lifespan and a multivariate assessment of 5 uniquely specific tissue measurement trajectories. One point of consideration is that by using cross-sectional data only one measurement per subject was made and as such the observed trajectories do not necessarily represent the expected lifespan changes within individuals. Longitudinal studies offer a more powerful assessment of intra-subject tissue change however, only a few studies of longitudinal lifespan tissue change have been conducted to date (Sexton et al., 2014; Storsve et al., 2016) while the vast majority of investigations have studied cross-sectional datasets (Bartzokis et al., 2012; Callaghan et al., 2014; Kochunov et al., 2012; Lebel et al., 2012; Westlye et al., 2010; Yeatman et al., 2014). Future longitudinal studies conducted on large subject populations from childhood through old age may be able to apply more complex models to the investigation of tissue microstructure trajectories across the lifespan.

Conclusion

This data-driven assessment of MT, R1, R2*, MD, and ICVF age-related trajectories demonstrates modular patterns of coordinated tissue change across the human lifespan and contributes toward greater understanding of white matter development and aging. By characterizing normal maturation and aging trajectories as well as their spatial variation, optimal windows of intervention in certain disease phenotypes might be deduced, enabling a mitigation of neurocognitive decline. Future work linking coordinated white matter development to genetic, environmental and behavioral data may begin to shed light on the complex relationships between biological tissue processes, cognition and disease vulnerability.

4. Hierarchical modularity and microstructural enrichment of the brain's integrative architectures

4.1 Introduction

Healthy cognitive function is dependent upon the global integration of information between segregated brain systems communicating across a complex axonal architecture, the human connectome (Sporns et al., 2005). Recent work suggests that modular and hierarchical connectivity architectures are best suited for the dual requirements of local (segregated) functional specialization and global integration of segregated brain functions (Moretti and Muñoz, 2013 ; for a review see Park and Friston, 2013 and/or Sporns, 2013). Across the brain, certain regions (nodes) play a more prominent role in the integration of brain functions than others (Bertolero et al., 2015; Heuvel et al., 2010; Zuo et al., 2012). Lesions to these putative 'hub' regions have been implicated in an array of brain disorders (Crossley et al., 2014; van den Heuvel et al., 2013), often resulting in pervasive cognitive impairment (Aerts et al., 2016; Warren et al., 2014). It is an intuitive and appealing idea to consider brain networks as organized into modular systems across many scales, progressively grouping together to form local circuits and cortical columns, all the way up to specialized regions and brain systems (Park and Friston, 2013). At each level, nodes form denser intra- to inter-modular connectivity and group together with increasing scale to form a network hierarchy. The importance of hierarchical modularity in cognition and behavior is underscored by evidence that these architectures are responsible for an expanded range of neural dynamics, facilitating cognitive flexibility and complex behaviors (Moretti and Muñoz, 2013; Rubinov et al., 2011). The concept of hierarchically modular brain architectures has been around for more than 50 years (Simon, 1962) but investigations of such organization in human structural brain networks has only begun to be addressed recently (Bassett et al., 2008; Betzel et al., 2013; Lohse et al., 2014).

The most common method for identifying brain network hubs has been to report regions with above average connectivity (degree) and a central role within the network (Buckner et al., 2009; Gong et al., 2009; Hagmann et al., 2008). A subset of the most densely connected hub regions have 'rich' interconnectivity between themselves and form what has been termed the brain's anatomical 'rich club' (van den Heuvel and Sporns, 2011). The rich club architecture

of the human brain has been shown to exhibit a high wiring cost (van den Heuvel et al., 2012) and preliminary evidence suggests that rich club regions and connections exhibit elevated levels of metabolic energy usage and microstructural organization (Collin et al., 2014; Mancini et al., 2017). The high cost feature of rich club brain architectures might be compensated by the crucial role these structures play in facilitating whole-brain communication (Bullmore and Sporns, 2012).

Although descriptions of rich-club organization highlight the importance of a densely interconnected and central subnetwork, these descriptions do not directly consider the integration of information between segregated and (hierarchically) modular network structures. An alternative route to identifying integrative brain regions is to investigate brain network modularity (see Sporns and Betzel, 2015 for a review) and to classify nodes based on their connectivity to other modules (participation) and level of connectivity within their own module (within-module degree) (Guimerà and Nunes Amaral, 2005; Meunier et al., 2009). Topological analyses of tract tracing data from the macaque cerebral cortex have revealed modular connectivity architectures in which network communities are cross-linked by a small number of densely interconnected hub regions (Harriger et al., 2012). Further work has begun to link macroscopic measures of brain modularity, such as a region's participation coefficient, with cortical microstructure measures of neuronal complexity (Scholtens et al., 2014). Despite growing evidence for a relationship between modular network architectures and tissue microstructural organization in the macaque such questions remain poorly understood in humans (Harriger et al., 2012; van den Heuvel and Yeo, 2017). Bridging the gap between microscale and macroscale descriptions of brain network hierarchy may elucidate how features of nervous system organization across multiple scales interact to support cognitive function and how disruption to these processes results in mental disorders (Fields et al., 2015; Fornito et al., 2015; Petersen and Sporns, 2015; van den Heuvel and Yeo, 2017).

Here we focus on the relationship between the modular organization of structural networks and non-invasive measures of tissue microstructure in the living human brain. We acquired structural connectivity data using state-of-the-art diffusion weighted imaging (DWI) tractography procedures (Jeurissen et al., 2014; Smith et al., 2015a, 2012). We hypothesized that by applying a novel modularity detection algorithm (OSLOM; Lancichinetti et al., 2011) hierarchically modular architectures would be revealed in human structural connectivity

networks (Betzel and Bassett, 2016; Park and Friston, 2013). To provide additional support to our findings each stage of the analysis was reproduced on an independent replication dataset from the Human Connectome Project (<http://www.humanconnectome.org>; Van Essen et al., 2013). It was hoped that the discovery of consistent properties across the two complimentary datasets would underscore both the replicability and robustness of the findings. The integration of diffusion tractography data with microstructural imaging has been proposed as an important direction for future connectivity analyses (Daducci et al., 2016; van den Heuvel and Yeo, 2017). We therefore combined the structural connectivity data with quantitative magnetic resonance imaging (qMRI) tissue microstructure measurements. The multi-modal tissue microstructure measurements used in this study provide sensitivities to myelin - MT, R1 & T1w/T2w (Draganski et al., 2011; Glasser and Van Essen, 2011; Lutti et al., 2014); axonal packing densities and fiber dispersion - ICFV, FA & ODI (Jones et al., 2013; Zhang et al., 2012); cellular membrane organization - MD (Beaulieu, 2002); and local iron concentrations - R2* (Fukunaga et al., 2010). Given a modular network architecture, we further hypothesized that regions and pathways supporting the integration of information across communities would exhibit elevated levels of microstructural enrichment in line with the critical nature of these structures for ensuring coherent communication across the network (Bullmore and Sporns, 2012; Collin et al., 2014; Scholtens et al., 2014). We compare our results to previous studies that have linked topological measures to tissue microstructure as well as exploring how our findings align with current understanding of the network hub architectures of the human brain.

4.2 Material and methods

Subjects

The principle CoLaus dataset comprised imaging data from 38 healthy volunteers (16 female) recruited from the Lausanne regional area of Canton Vaud, Switzerland as part of their ongoing participation in the CoLaus | PsyCoLaus Study (Firmann et al., 2008; Preisig et al., 2009). All volunteers (mean age 21.7 ± 1.9 yrs) were screened for brain disorders prior to study acceptance. The local ethics committee approved all data collection procedures and written informed consent was given by each participant. The authors state that they have obtained

approval from the ColaUS Data Sharing and Publications Committee for use of the data and confirm that the data were analyzed anonymously.

MRI data acquisition

All imaging for the principle dataset was performed on a 3T whole-body MRI system (Magnetom Prisma, Siemens Medical Systems, Germany) using a 64-channel RF receive head coil and body coil for transmission. Visual inspection of study participant data confirmed an absence of neither macroscopic brain abnormalities nor obvious vascular pathology. The imaging data for all subjects included in the study underwent a stringent quality control assessment (see Quality assurance procedures).

Multi-parameter maps (MPMs)

The qMRI protocol consisted of three whole-brain multi-echo 3D fast low angle shot (FLASH) acquisitions with predominantly magnetization transfer-weighted (MTw: $TR/\alpha = 24.5\text{ms}/6^\circ$), proton density-weighted (PDw: $TR/\alpha = 24.5\text{ms}/6^\circ$) and T1-weighted (T1w: $24.5\text{ms}/21^\circ$) contrast (Helms et al., 2009, 2008; Weiskopf et al., 2013b). The MT-weighted contrast was obtained using a Gaussian-shaped radio frequency (RF) pulse prior to the RF excitation (4ms duration, 220° nominal flip angle, 2 kHz frequency offset from water resonance). Multiple gradient echoes were acquired for each contrast with alternating readout polarity. The minimal echo time was 2.34ms and the echo spacing was 2.34ms. The number of echoes was 6/8/8 for the MTw/PDw/T1w acquisitions to keep the TR value identical for all contrasts. The image resolution was 1 mm^3 isotropic, the field of view and the matrix size were $256 \times 240 \times 176\text{ mm}$. Parallel imaging was used along the phase-encoding direction (acceleration factor 2 with GRAPPA reconstruction) (Griswold et al., 2002), partial Fourier (factor 6/8) was used along the partition direction. Data were acquired to calculate maps of the RF transmit field $B1+$ using the 3D echo-planar imaging (EPI) spin-echo (SE) and stimulated echo (STE) method described in (Lutti et al., 2012, 2010). The image resolution of the $B1+$ -mapping data was 4mm^3 , and the echo and repetition times were set to 39.06ms and 500ms respectively. The nominal flip angle of the SE pulse was decreased from 230° to 130° in steps of 10° (Lutti et al., 2012, 2010). $B0$ -field mapping data was acquired using a 2D double-echo FLASH sequence to correct for geometric distortions in the 3D EPI data (Lutti et al., 2012, 2010). The total acquisition time was 27 min.

Diffusion weighted imaging (DWI)

The diffusion weighted MRI data were acquired using a 2D echo-planar imaging sequence with the following parameters: TR/TE = 7420/69ms, parallel GRAPPA acceleration factor = 2, FOV = 192 x 212 mm², matrix size = 96 x 106, 70 axial slices, 2 mm isotropic voxel dimension, 118 isotropically distributed diffusion sensitization directions (15 at b = 650 s/mm², 30 at b = 1000 s/mm² and 60 at b = 2000 s/mm²) and 13 b=0 images interleaved throughout the acquisition.

Human Connectome Project (HCP) Data

Data for the secondary HCP dataset comprising 244 subjects (mean age = 24.2 ± 2.4 yrs; 92 female) were downloaded from the Human Connectome Project (HCP) database (<https://db.humanconnectome.org/>; Marcus et al., 2011) to form the secondary replication dataset. The ‘Structural Extended Preprocessed’ and ‘Diffusion Preprocessed’ data packages were downloaded for each subject. Full details regarding the HCP data acquisition and preprocessing strategies have been reported previously (Feinberg et al., 2010; Glasser et al., 2013; Jenkinson et al., 2012, 2002; Milchenko and Marcus, 2013; Moeller et al., 2010; Setsompop et al., 2013, 2012, Sotiropoulos et al., 2013a, 2013b). The diffusion spin-echo EPI data were acquired with the following parameters: TR/TE = 5520/89.5ms; flip angle = 78°, refocusing flip angle = 160°; FOV = 210x180mm, matrix = 168x144; slice thickness = 1.25mm, 111 slices, 1.25mm isotropic voxels; multiband factor = 3; phase partial Fourier factor = 6/8; b-values 1000, 2000, 3000 s/mm². The T1w (3D MPRAGE) and T2w (3D T2-SPACE) images both had an isotropic voxel resolution of 0.7mm. We took the ratio of these images to form T1w/T2w ratio images which have previously been proposed to reflect indirect levels of tissue myelination (Glasser and Van Essen, 2011; Shafee et al., 2015).

MRI data preprocessing

Multi-parameter maps (MPMs)

The R2*, MT and R1 quantitative maps were calculated as previously described (Draganski et al., 2011) using in-house software running under SPM12 (Wellcome Trust Centre for Neuroimaging, London, UK; www.fil.ion.ucl.ac.uk/spm) and Matlab 7.11 (Mathworks, Sherborn, MA, USA). The R2* maps were calculated from the regression of the log-signal of the eight PD-weighted echoes. The MT and R1 maps were computed as described in (Helms

et al., 2008), using the MTw, PDw and T1w images averaged across all echoes. The R1 maps were corrected for local RF transmit field inhomogeneities using the B1+ maps computed from the 3D EPI data (Helms et al., 2008) and for imperfect RF spoiling using the approach described by Preibisch and Deichmann (2009).

Surface reconstruction and subcortical segmentation

For the principle dataset each participant's MT image was processed using the FreeSurfer version 5.3.0 software package pipeline (www.surfer.nmr.mgh.harvard.edu). FreeSurfer is optimized to work with T1w images, however MT images have comparable GM/WM contrast to T1w images and we found the surface reconstructions to be of comparably high quality. Any subjects with surface defects were either fixed or excluded from the analysis (see *Quality assurance procedures*). The standard FreeSurfer pipeline reconstructs an individual's cortical and white matter surfaces from the participant's structural image data. The following steps comprise the surface preprocessing pipeline: correction of image intensity variations due to MR inhomogeneities (Dale et al., 1999); skull stripping (Ségonne et al., 2004); cortical grey matter (GM) and white matter (WM) segmentation (Dale et al., 1999); separation of the brain hemispheres and subcortical structures (Dale et al., 1999; Fischl et al., 2004, 2002); and finally a set of grey/white matter interface and pial surfaces for both brain hemispheres (Dale et al., 1999). For the secondary HCP dataset a similar FreeSurfer pipeline is run by default and included in the 'Structural Extended Preprocessed' packages. After surface reconstruction, the surfaces for each individual participant were used to estimate transformations that achieved maximal correspondence between the sulcal and gyral patterns of the individual and those of an average brain (Fischl et al., 1999a, 1999b). This information was later used to bring a high-resolution cortical parcellation (Gordon et al., 2016) into each individual's native image space.

The FSL FAST tool (Smith, 2002; Zhang et al., 2001) was used to segment MT or T1w (for HCP data) into tissue probability maps for WM, GM and CSF. Subcortical structures were segmented using the FSL FIRST tools (Patenaude et al., 2011). These structural segmentation preparations are described in detail in Smith et al. (2015a) and are necessary for the anatomically constrained tractography (ACT; Smith et al., 2012) procedures used later to build the structural connectome.

Diffusion weighted imaging (DWI)

DWIs were preprocessed to correct for eddy currents and subject motion using the FSL EDDY tool (Andersson and Sotiropoulos, 2016) and the gradient directions were appropriately rotated to correct for subject movement (Leemans and Jones, 2009). The B0 maps acquired as part of the structural imaging session were used to correct for EPI susceptibility distortions with the SPM field mapping toolbox (Hutton et al., 2002). The DWI images were then rigid body aligned to the MT image with the aid of the mean b=0 image using SPM12.

Diffusion tensor imaging (DTI; Basser et al., 1994) maps were estimated on the b=0 s/mm² and b=1000 s/mm² data using a constrained non-linear least-squares (CNLLS) algorithm (Koay et al., 2006). Tensor summary statistic maps were saved for fractional anisotropy (FA), mean diffusivity (MD), radial diffusivity (RD) and axonal diffusivity (AD). The neurite orientation dispersion and density imaging (NODDI; Zhang et al., 2012) maps were processed with the AMICO toolbox (Daducci et al., 2014) using multi-shell diffusion data across all of the acquired b-values. NODDI output maps were saved for the intracellular volume fraction (ICVF) and orientation dispersion index (ODI).

Estimation of g-ratio maps

The g-ratio is defined as the ratio between the inner axon radius and the outer, myelinated, axon radius and is a fundamental property of axonal organization and conduction (Waxman, 1975). We applied a recently developed technique (Campbell et al., 2012; Mohammadi et al., 2015; Stikov et al., 2015) for estimating the g-ratio non-invasively using a combination of diffusion microstructure and quantitative myelin imaging. The MRI derived g-ratio, g , was calculated voxel-wise as

$$g = \sqrt{\frac{1}{1 + \frac{MVF}{AVF}}} = \sqrt{\frac{1}{1 + \frac{\alpha MT}{(1 - \alpha MT)(1 - v_{iso})v_{ic}}}}$$

where MVF is the myelin volume fraction, AVF is the axonal volume fraction, MT is the quantitative magnetization transfer measurement and v_{iso} / v_{ic} are respectively the isotropic (ISO) and intracellular (ICVF) volume fractions estimated from the NODDI diffusion model. The normalization factor, α , was estimated following previous approaches (Cercignani et al., 2016; Dean et al., 2016; Mancini et al., 2017; Mohammadi et al., 2015). The α value was selected by

normalizing the MR g -ratio to a value of $g=0.7$ in the splenium across 11 subjects (mean age = 26.5 ± 1.41 yrs) taken from an independent dataset with an identical acquisition protocol. The value of $g=0.7$ has been described for the type of large axons typically found within the splenium using *ex-vivo* electron microscopy (Graf von Keyserlingk and Schramm, 1984). The median value derived across the 11 subjects was found to be $\alpha=0.23$ and this was used as the normalization factor in all further processing of the main CoLaus dataset.

Quality assurance procedures

The data for all subjects included in the study underwent a stringent quality control assessment. An experienced investigator visually assessed the preprocessed neuroimaging data based on the following criteria: 1) Quantitative MPM maps (MT, R1, R2*) rated for movement artifacts and abnormal white matter signal intensities; 2) Diffusion and structural MRI image alignment; 3) Quality of the diffusion FA maps and tensor residuals; 4) Reliability of the pial and white matter surface reconstructions; 5) Accuracy of the tissue type segmentation and parcellations. If data failed any of these quality assessment criteria the error was either corrected or the relevant subject was excluded from the study.

Diffusion tractography

All processing procedures described within this section were performed using the MRTrix3 software package (www.mrtrix.org; Tournier et al., 2012) and were run for the principle and secondary datasets. The constrained spherical deconvolution (CSD; Tournier et al., 2007, 2004) fiber orientation densities (FODs) were calculated using a multi-shell, multi-tissue CSD (MSMT-CSD) algorithm ($l_{\max} = [0, 2, 6, 10]$ for WM) which has been shown to reduce the presence of spurious fiber orientation distribution function (fODF) peaks in voxels containing GM and/or CSF partial volumes (Jeurissen et al., 2014). All tractography streamline reconstructions were made using the probabilistic 2nd-order Integration over fiber orientation distributions (iFOD2) algorithm (Tournier et al., 2010) in conjunction with the ACT framework (Smith et al., 2012). The following parameters were used for streamline tracking of each study participant: number of accepted streamlines 20 million, step size 1 mm, maximum curvature per step 45° , length 5-250 mm, FOD amplitude threshold 0.1. We used a dynamic seeding algorithm (R. E. Smith et al., 2015b) to promote optimal streamline densities supported by the FODs during tracking. The SIFT algorithm (Smith et al., 2013) was applied to filter down to the

10 million streamlines best supported by the FOD data before applying the SIFT2 algorithm (R. E. Smith et al., 2015b) to provide relative weights of the remaining 10 million streamlines. This state-of-the-art diffusion tractography pipeline has been shown to generate robust and reproducible connectomes, avoiding streamline density and connectivity biases associated with earlier approaches (R. E. Smith et al., 2015a).

Connectome construction

As part of the structural preprocessing procedures a high-resolution cortical parcellation (Gordon et al., 2016) was projected on the cortical surfaces of each subject. The surface parcellations were converted into volume images by projecting the surface labels onto voxels between the GM/WM interface and pial surfaces. For each study participant, there now existed a parcellation image in native space containing a total of 332 cortical structures.

Tractography streamline endpoints were mapped to their nearest parcellation nodes. If a node was not located within a 4 mm radius of a streamline termination then this streamline was excluded from the connectome construction (R. E. Smith et al., 2015a). Streamlines connecting to the same node at both ends were excluded, and thus the diagonal entries were zero for all adjacency matrices.

The effects of false positives and false negatives in structural connectivity datasets can have detrimental effects on the estimation of topological network measures (Zalesky et al., 2016). We applied a group-thresholding approach (de Reus and van den Heuvel, 2013) designed to balance between the elimination of false positive and false negative connections present in the individual subject connectomes. First of all, for each subject, if any connection was found to possess less than 10 streamlines it was considered spurious and therefore deleted (van den Heuvel et al., 2012). The remaining connections were compared across subjects and only those edges found to be present in at least 60% of individuals were preserved, the remaining edges were deleted. The group threshold of 60% has been suggested as a suitable value for balancing trade-offs between false positives and false negatives (de Reus and van den Heuvel, 2013). Group-averaged weighted connectivity matrices were then estimated by taking the average connection strength across individuals.

Quantification of white matter tissue properties

In addition to counting the absolute number of streamlines connecting any two parcellation nodes, we generated adjacency matrices weighted by quantitative tissue measures along the connecting streamlines: for each streamline a quantitative MRI measure was sampled along its length; these samples were then averaged along the length of each streamline; finally, these values were averaged across all streamlines corresponding to each edge in the connectome (i.e. connecting the same nodes). This provided mean microstructure measures for each edge of the connectivity matrix. For each subject of the principle dataset, we generated 10 quantitative MRI adjacency matrices (weighted by MT, R1, R2*, FA, MD, RD, AD, ICVF, ODI and g-ratio) in addition to the adjacency matrices weighted by total streamline count and mean streamline length. In the secondary dataset we generated 7 tissue microstructure weighted adjacency matrices (weighted by FA, MD, RD, AD, ICVF, ODI and T1w/T2w). All adjacency matrices had their streamline contributions weighted by the corresponding SIFT2 weights to improve robustness and biological accuracy of the structural connectomes (R. E. Smith et al., 2015a). The variability of mean streamline edge lengths across subjects was considered as a potential confound and was therefore regressed out of all microstructure weighted adjacency matrices.

Structural covariance

Intracortical measures for MT, R1, R2* and MD were sampled from each subject's mid-cortical surface. These individuals' intracortical measures, as well as FreeSurfer generated cortical thickness estimates, were averaged across each of the 332 parcellated node regions. Prior to the correlation analysis linear regression was performed on every region to remove the effects of age, gender and age-gender interaction. The residuals of this regression were then used to determine the statistical similarity or synchronized co-variations in nodal (micro-)structure by computing the Pearson's correlation coefficient across subjects (He et al., 2007). Hence Pearson's correlation matrices were constructed for each measure which described the region by region co-variation across subjects.

Modularity estimation

Several methods have been proposed to detect modular organization (also termed community structure) in network data. One of the most widely applied methods is known as

modularity maximization (Newman and Girvan, 2004) and this has been used to detect modules in experimental animal and human brain networks (Bassett et al., 2010; Crossley et al., 2013; Harriger et al., 2012; Lohse et al., 2014; Towlson et al., 2013). Despite the widespread use of modularity maximization techniques there is a growing appreciation for the method's shortcomings and practical considerations (Betzel and Bassett, 2016; Sporns and Betzel, 2015). As network size and the number of modules increases, the number of partitions which achieve near optimal separation grows exponentially resulting in a degeneracy of partitions with high evidence (Good et al., 2010). The degeneracy of plausible modularity assignments becomes particularly problematic if the partitions are dissimilar and due to the fact that modularity maximization procedures require network nodes to be assigned to a single module. Furthermore, a resolution limit exists whereby modules of a sufficiently small size may become impossible to detect under certain conditions (Fortunato and Barthélemy, 2007).

A recently proposed method for community detection termed Order Statistics Local Optimization Method (OSLOM) (Lancichinetti et al., 2011) overcomes a number of these issues by applying statistical tests of how likely a putative partition is relative to an appropriate null model (Lancichinetti et al., 2010). OSLOM applies a growing-pruning model to test for the significance of adding and removing putative nodes to a module and resolves the set of nodes with maximal statistical evidence. This also allows OSLOM to check for the statistical significance of partitions generated from alternative schemes such as the modularity maximization algorithm. Because the optimization scheme operates on local network information OSLOM does not suffer from the resolution limit problem, is robust to small changes to global rather than local network structure and allows for nodes to be assigned to multiple modules if their inclusion as such leads to maximal model evidence. Finally, OSLOM inherently checks if the smallest detected modules can be grouped into larger communities and if these can then be grouped into even larger communities, making OSLOM unique in its ability to innately detect hierarchically modular organization in network data.

Here, we estimated structural network partitions/covers by entering the group-averaged weighted-connectivity matrices into the OSLOM community detection algorithm (Lancichinetti et al., 2011). We define a *cover* of the network as the set of modules such that each node is assigned to *at least* one module, extending the concept of network partitions to

include cases of overlapping communities. The community detection algorithm proceeded as follows: First, 100 network partitions were estimated for each of the InfoMap (Rosvall and Bergstrom, 2008), Louvain (Blondel et al., 2008) and Copra (Gregory, 2010) modularity detection algorithms. In addition, 200 instances of the OSLOM community detection search algorithm were run making a total of 500 putative network covers to be assessed for significance. The algorithm then applies the growing-pruning model to determine the most probable node groupings before combining the results of all cover estimates by comparing the scores of each module (see Lancichinetti et al., 2011 for full details). The use of multiple algorithms and a large number of cover instances is motivated by the idea that this will lead to a better exploration of possible network covers (Sporns and Betzel, 2015) and to account for evidence that the use of multiple community detection algorithms can reveal subtle differences in the set of putative community assignments (Power et al., 2011).

Connector, satellite, provincial and peripheral node classes

Given the existence of a viable network cover, each node's topological role was assigned by measuring the node's participation coefficient (P) and within-module-degree z-score (Z) (Guimerà and Nunes Amaral, 2005). Edge weights were used to calculate P in order to model the relative bandwidth that a node is dedicating to inter-modular communication as well as to minimize the influence of low weight false-positive connections (Zalesky et al., 2016). Because the OSLOM community detection algorithm allows for nodes to be assigned as members of multiple communities a large number of community structure vectors are possible, accounting for each combination of node-module assignments. The total number of possible community structure vectors scales exponentially with the number of nodes assigned to multiple modules and the number of modules these nodes are simultaneously assigned to. Thus, we calculated P and Z for each node as the average value estimated across 10,000 possible community structure permutations. The 70th percentiles for P and Z were set as the threshold to allocate each node into one of 4 classes: connector hubs (high P , high Z); satellite nodes (high P , low Z); provincial hubs (low P , high Z); and peripheral nodes (low P , low Z). Similar approaches have been used within the literature to assign modular node classes via P and Z thresholds (Bertolero et al., 2015; Guimerà and Nunes Amaral, 2005; Meunier et al., 2009; Nicolini et al., 2017). This process of modular node classification was applied at each

level of the detected hierarchically modular network structure to provide node classes across multiple levels of network organization.

For each subject, connecting white matter edge classes were defined based on the modular node classes of their cortical terminations. Four distinct connection types were examined in order to study differences in microstructural organization from the most highly integrative to the most highly segregated connections: connector-connector, connector-satellite, peripheral-provincial and peripheral-peripheral network edges.

Rich club organization of the human connectome was investigated in order to compare modular class organization to the spatial distribution of nodes comprising the anatomical rich club. Full details of the anatomical rich club analysis are included as part of the supplementary methods material.

Structural properties across modular node classes and connections

White matter connectivity and microstructural organization

Following previous approaches within the literature (Collin et al., 2014; Mancini et al., 2017), structural connectivity data derived from the tractography, DTI, NODDI, MPM and g-ratio pre-processing were used to examine differences in white matter connectivity properties across the four modular edge classes. The number of streamlines (NOS) was used as a semi-quantitative measure of connection strength between nodes. Due to the state-of-the-art tractography scheme used in this study the NOS measure can be thought of as analogous to a pathway's cross-sectional area (Raffelt et al., 2012; R. E. Smith et al., 2015a, 2015b). The length measure between two nodes was taken as the mean length of connecting streamlines. The edge cost measure (or connection volume) is defined as the total number of connecting streamlines forming an edge multiplied by their mean length (van den Heuvel et al., 2012). Measures of microstructural organization and myelination (FA, MD, RD, AD, MT, R1, R2* ICVF, ODI, g-ratio and T1w/T2w) were taken from the microstructure weighted adjacency matrices (see *Quantification of white matter tissue properties*). For each individual subject, mean values of the white matter edge measures were computed for connector-connector, connector-satellite, peripheral-provincial and peripheral-peripheral modular edge classes by averaging the measure across all edges assigned to a particular class at the lowest hierarchical level.

Structural covariance of grey matter tissue properties

We estimate structural covariance measures between cortical structures to investigate how intracortical microstructure (MT, R1, R2* and MD) and cortical thickness measures covary in the study population (Chen et al., 2008; Melie-Garcia et al., 2017). These measures provide node-to-node estimates but provide one population averaged covariance matrix rather than one microstructural matrix per subject (as per the *White matter connectivity and microstructural organization* assessment). As with the white matter measures, mean values for the structural covariance metrics were computed for connector-connector, connector-satellite, peripheral-provincial and peripheral-peripheral modular edge classes by averaging the measure across all edges assigned to a particular class.

Statistical testing

Statistical differences between classes were assessed with permutation testing (Collin et al., 2014; van den Heuvel et al., 2012). Node classes were randomly reassigned across 10,000 permutations, each of which preserved the original number of nodes assigned to each class. For each permutation, edge classes were determined based on the permuted cortical node classes and the metric of interest was averaged over each of these edge classes. The differences between the mean values of each edge class, across all permutations, formed the null-distribution of differences which could be observed under the null hypothesis stating that modular edge classifications show no significant differences. *P*-values were determined by calculating the proportion of random null-distribution values which were greater than the differences observed in the true modular classification.

The consistency of modular structures for the CoLaus and HCP datasets were assessed via the *normalized mutual information* (NMI), a reliable measure of community structure similarity derived from information theory (Danon et al., 2005). For each dataset a node by module (N×M) matrix was constructed such that the *ij*th element indicated if the *i*th node was a member of the *j*th module. Pair-wise NMI measures, estimating the similarity of each module across the two datasets, were then estimated (Meilă, 2007). Furthermore the global cover similarities were assessed by applying a NMI measure that takes into account the presence of overlapping communities (Lancichinetti et al., 2009). To test for significance a set of randomized control networks were constructed for each dataset which redistributed the

Dataset	Global efficiency, E		Characteristic path length, PL		Average clustering coefficient, C		Modularity index, Q	
	Binary	Weighted	Binary	Weighted	Binary	Weighted	Binary	Weighted
CoLaus	0.551±0.006	0.0169±0.0043	2.030±0.025	92.943±34.566	0.619±0.005	0.0043±0.0011	0.411±0.013	0.638±0.020
HCP	0.529±0.011	0.0165±0.0042	2.108±0.024	98.613±27.565	0.623±0.006	0.0048±0.0013	0.422±0.015	0.650±0.012

Table 4.1. Global network measures for the principle CoLaus dataset and human connectome project (HCP) replication dataset.

weighted network edges, shuffling topology and decorrelating weights whilst maintaining the original network strength sequence (Alstott et al., 2014; Rubinov and Sporns, 2011).

Community structure was then estimated for each randomized control network using the same OSLOM algorithm, before estimating the module-by-module and global NMI measures (100,000 pair-wise random network comparisons). This provided a null-distribution of possible network similarity measures that could be observed under the null hypothesis stating that the community structures of the two datasets show no significant similarities (Traag et al., 2013).

4.3 Results

General network properties and topological observations

The group averaged connectivity matrix had a network density of 17%. The mean number of streamlines across connecting edges was 411 with standard deviation 1302 forming a heavy tailed distribution (Supplementary Fig. 4.1). 47.0% of the total streamline density was observed within associative pathways of the left hemisphere, 46.3% within right hemisphere association pathways and 6.7% of streamlines formed inter-hemispheric connections (homotopic and heterotopic). Global network measures for the principal and secondary datasets are detailed in Table 4.1.

Hierarchical modularity

Modularity estimation was performed on the CoLaus group averaged connectivity matrix using the OSLOM community detection algorithm (Lancichinetti et al., 2011). The resulting cover (Fig. 4.1a) divided the 332 cortical nodes into 12 modules at the first and lowest hierarchical level (colored lines), 4 modules at the second hierarchical level (dashed lines) and 2 modules at the third and highest hierarchical level (dotted lines).

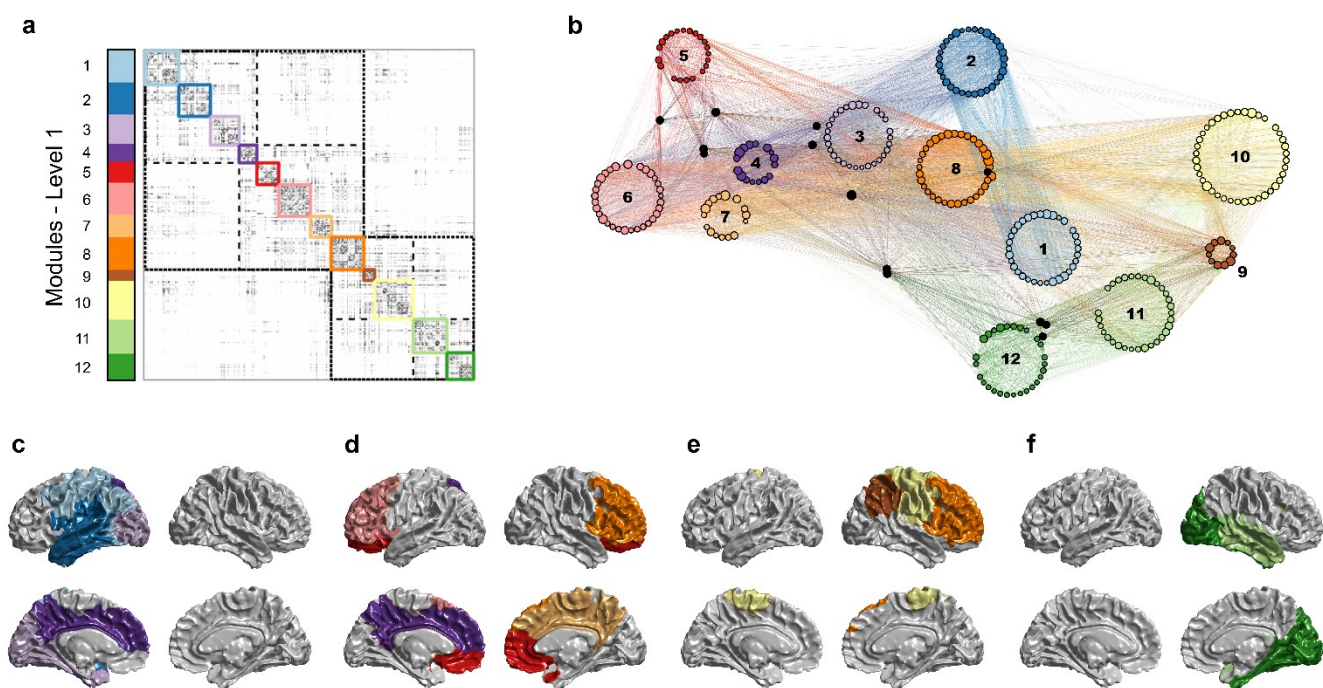


Figure 4.1. Hierarchical modularity in human brain anatomical networks. a) Adjacency matrix displaying the three-level modular cover structure. Modules at level 1 (lowest level) are highlighted with colored boxes; modules at level 2 are indicated using dashed lines; at level 3 (highest level) the brain divides into two modules indicated by dotted lines. b) Level 1 hierarchical circular graph layout. Nodes (circles) are organized into colored rings defined by their level 1 module participation and scaled by their degree. Modules are placed near to each other if many intermodular connections exist. If a node was found to be statistically associated with multiple modules it was placed equidistant between its member modules (black circles). Edges are scaled by their total number of connecting streamlines and colored as a combination of the two connecting modules. c-f) Cortical surface maps displaying the spatial organization of level 1 modules into the four modules of level 2.

The 12 modules at level 1 are represented on a hierarchical circular graph layout (Fig. 4.1b), where the nodes are placed in circles if they belong to the same module, and modules are placed near to each other if they possess many inter-modular connections and/or group together to form modules at higher levels. A total of 13 nodes were determined to lie across multiple modules (2 modules in each instance) and these are represented as black nodes placed equidistantly between their multiple community assignments. The modules at level 1 cover the cortex into spatially contiguous communities which broadly align with well described brain systems specialized for different domains of behavior and cognition. The 12 modules can be summarized as follows: 1) left central-parietal (light-blue); 2) left temporo-insular (dark-blue); 3) left ventral visual stream (light-purple); 4) left medial (dark purple); 5) bilateral orbitofrontal (red); 6) left prefrontal (pink); 7) right medial (light orange); 8) right prefrontal (orange); 9) right posterior parietal (brown); 10) right motor (yellow); 11) right

lateral temporal (light green); 12) right ventral visual stream (dark green). Modular organization at hierarchical level 1 is expanded upon in Supplementary Fig. 4.2. In general, the modular patterns for the left and right hemispheres are highly symmetric, with each module in the left hemisphere possessing an equivalent module in the right hemisphere. One exception of note relates to the modules containing nodes connected by the major language pathways (modules 1, 2, 9 & 11; Catani et al., 2005) where superior parietal and central modules are separated in the right (but not left) hemisphere and the left temporo-insular module extends rostrally to include portions of the pars opercularis.

At the second hierarchical level four sub-modules of the left hemisphere group together to form a large posterior module connecting occipital, temporal, sensorimotor and medial cortices (Fig. 4.1c; modules 1-4). A second bilateral module connects prefrontal, orbitofrontal and medial cortices (Fig. 4.1d; modules 4-8). The third and fourth modules at the second hierarchical level connect right-hemispheric fronto-parietal (Fig. 4.1e; modules 8-10) and occipito-temporal (Fig. 4.1f; modules 11 & 12) cortices respectively. It is worth noting that modules 4 and 8 are both assigned to two modules at the second hierarchical level (one lateralized, one bilateral) suggesting high levels of intra- and inter-hemispheric connectivity for the medial and prefrontal modules. At the third and highest level of hierarchical modularity sub-modules combine to form predominantly left (modules 1-8) and right (modules 8-12) hemispheric communities.

Community detection in the HCP replication dataset revealed a highly consistent pattern of modular organization to that observed in the main CoLaus dataset (Supplementary Fig. 4.3). As in the principle dataset the OSLOM community detection algorithm found 12 modules at the lowest hierarchical level, 4 communities at the second level and 2 communities at the third and highest level. Each of the level 1 modules in the CoLaus dataset has a high degree of similarity (normalized mutual information, NMI; Meilă, 2007) with a single corresponding module in the HCP dataset (Fig. 4.2a). Furthermore, an analysis of similarities between the complete modular structure of the principle and replication datasets (while taking into

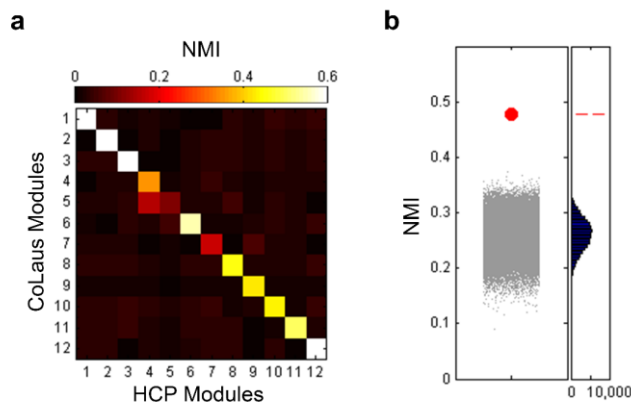


Figure 4.2. Consistency of hierarchical modularity definitions between the principal and replication datasets. a) Module-by-module comparisons at level 1 reveal highly consistent spatial organization. b) Similarity between the full hierarchical modularity definitions is significantly greater than that observed in randomized control graphs. NMI: normalized mutual information.

account the overlapping structure of network communities; Lancichinetti et al., 2009) revealed a high degree of cover similarity (NMI=0.48, $p<0.001$; Fig. 4.2b).

Nodal roles in network integration and communication

The nodes of a network possessing modular organization can be classified based on their inter- and intra-module connectivity (Fig. 4.3a). The participation coefficient, P , describes the relative proportion of a node's connections that communicate directly with other modules. The within-module-degree z-score, Z , indicates the relative level of intra-modular connectivity for a node as compared to other nodes within the same module. By combining node measures of P and Z each node was classified as either a connector hub, satellite connector, provincial hub or peripheral node (Fig. 4.3b; Bertolero et al., 2015; Guimerà and Nunes Amaral, 2005). When the modular node classes are projected onto a hierarchical circular graph layout (Fig. 4.3c) we observe that connector hub nodes are widely distributed across all modules except for modules 3 (left ventral visual stream) and 9 (right posterior parietal). Though module 9 did not contain any connector hub nodes this was because the module was fully connected (each node in the module connected to every other node) resulting in the same value of Z for each node. Therefore, one or more of the module 9 satellite connector nodes might perform integrative functions similarly to a connector hub node but this organization could not be discriminated along Z . The wide distribution of connector hub nodes suggests that modules typically have at least one, or more often multiple, nodes that are specialized for integrative network communication, dedicating a large proportion of their connections to inter-modular connectivity whilst also possessing above average intra-modular connectivity. In particular, the left and right medial modules (4 & 7) have an abnormally high proportion of connector

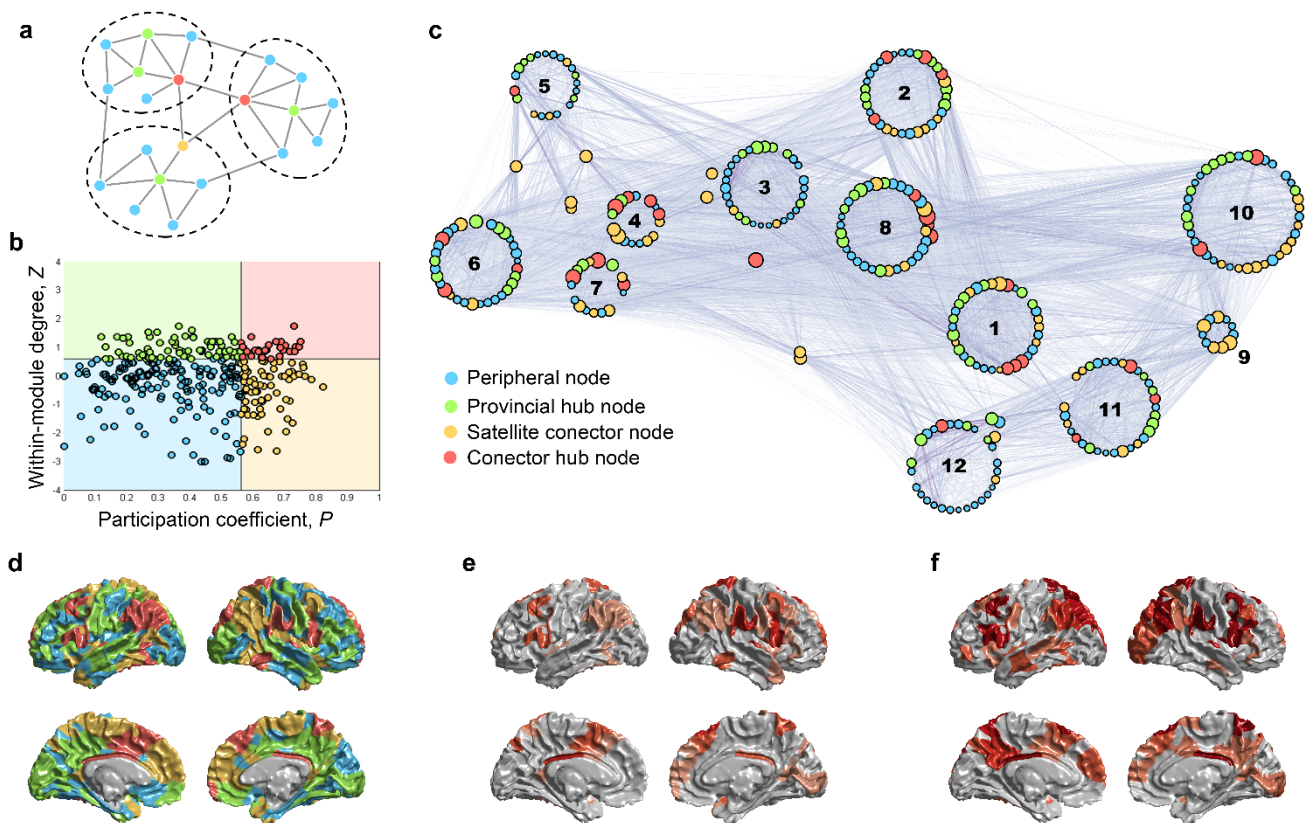


Figure 4.3. Modular node classes of the brain. a) A toy network showing how nodes can be grouped into modules (dashed lines) based on their inter-nodal connectivity. b) Nodes can then be assigned as peripheral (blue), provincial hub (green), satellite connector (orange) or connector hub (red) nodes based on their within-module degree, Z , and participation coefficient, P , values. Here we set the cut-off for P and Z as the 70th percentile node. c) A hierarchical circular graph layout displaying the modular node classes in relation to their level 1 module definitions. Nodes are displayed on the cortex and color coded according to d) their modular node class, e) the number of times a region is assigned as a connector hub across the three hierarchical levels, and f) a regions rich club participation level for comparison.

hub nodes for their size at 22.2% and 19.1% respectively as compared to the average proportion of connector hub nodes across all modules (9.6%).

The distribution of modular node classes on the cortical surface reveals a mosaic-like pattern of nodal network roles (Fig. 4.3d). By counting the number of times that a node was classified as a connector hub across the multiple levels of hierarchical modularity, we observe the regions that provide the highest levels of integrative network function (Fig. 4.3e). The regions forming this highly integrative set include posterior parietal, posterior cingulate, superior frontal, precuneus and anterior medial cortices (see Supplementary Table 4.1). Many (though not all) of these regions are also obtained when assessing the network's topological rich club (Fig. 4.3f; Supplementary Table 4.2; van den Heuvel and Sporns, 2011).

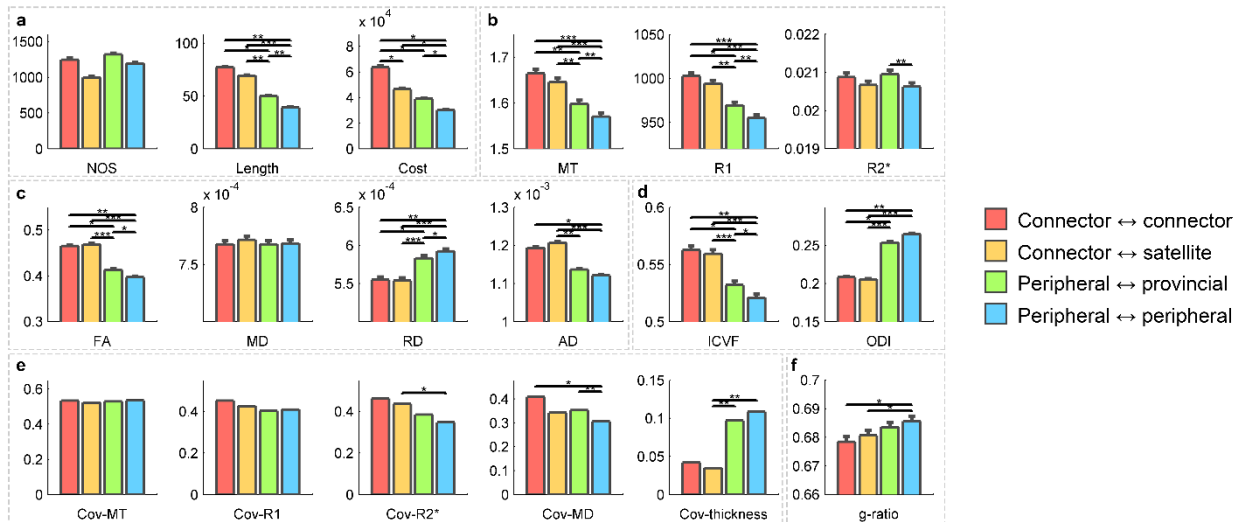


Figure 4.4. Structural characteristics of modular edge class connections. Edge class types ordered from most- to least-integrative are connector-connector (red), connector-satellite (orange), peripheral-provincial (green) and peripheral-peripheral (blue) connections. Bar graphs show the mean microstructural tissue property values across the edge classes for multiple structural measurements. Data on edge class values are provided for: a) the number of streamlines (NOS) and length of edges for the 4 edge classes; b) quantitative measures of MT, R1 and R2*; c) DTI measures of FA, MD, RD and AD; d) NODDI measures of ICVF and ODI; e) structural covariance of MT, R1, R2*, MD and cortical thickness; and f) the g-ratio tissue measurements. The general trends show increased microstructural organization and investment in the brain's most integrative connections. Error bars express the standard deviation of a measurement over the group of subjects. Significance assessed using permutation testing (10,000 permutations): * $P < 0.05$, ** $P < 0.01$, *** $P < 0.001$.

Topological roles predict tissue microstructural organization

Measures of microstructural organization across network edges were assessed across 4 classes of connections and will be defined in the subsequent sections as follows: connector hub to connector hub – Con-Con; connector hub to satellite node – Con-Sat; peripheral node to provincial hub – Per-Pro; peripheral node to peripheral node – Per-Per.

Wiring cost economy: streamline density and length

No significant effects were observed for the average number of streamlines (NOS) between edge classes (Fig. 4.4a). Con-Con and Con-Sat connections were significantly longer than Per-Pro ($p < 0.05$ | $p < 0.01$) and Per-Per ($p < 0.01$ | $p < 0.001$) connections. Per-Pro connections were also longer than Per-Per connections ($p < 0.01$). The wiring costs of Con-Con connections were on average significantly greater than Con-Sat ($p < 0.05$), Per-Pro ($p < 0.05$) and Per-Per ($p < 0.5$) connections. Con-Sat and Per-Pro connections also had higher average wiring costs than Per-Per connections ($p < 0.05$ | $p < 0.05$). These results are in agreement with

previous findings suggesting that integrative connections represent a particularly high-cost feature of brain organization (Collin et al., 2014; van den Heuvel et al., 2012).

Myelination and iron content: MT, R1 & R2*

MT and R1 (measures of tissue myelination) were compared across the 4 modular edge classes (Fig. 4.4b). Consistent statistical results were found for both measures. Con-Con connections had higher MT and R1 values than Per-Pro ($p < 0.01$ | $p < 0.05$) and Per-Per ($p < 0.001$ | $p < 0.001$) connections. Con-Sat connection measures for MT and R1 were greater than Per-Pro ($p < 0.01$ | $p < 0.01$) and Per-Per connections ($p < 0.001$ | $p < 0.001$). MT and R1 values in Per-Pro connections were also greater than those observed in Per-Per connections ($p < 0.01$ | $p < 0.01$). Measures of R2* (sensitive to both iron and myelin content) were elevated for Per-Pro connections as compared to Per-Per connections ($p < 0.01$). No effect was observed between the other edge classes.

Diffusion tensor imaging (DTI)

Four DTI derived metrics (FA, MD, RD & AD) were assessed across the different edge classes (Fig. 4.4c). Con-Con and Con-Sat connections had higher FA on average than Per-Pro ($p < 0.05$ | $p < 0.001$) and Per-Per ($p < 0.01$ | $p < 0.001$) connections. The average FA across Per-Pro connections was also greater than that of Per-Per connections ($p < 0.05$). There was no effect between any of the classes for MD. RD showed the opposite relationship to FA, with higher RD on average for Per-Pro and Per-Per connections as compared to Con-Con ($p < 0.05$ | $p < 0.01$) and Con-Sat ($p < 0.001$ | $p < 0.001$) connections. The mean RD of Per-Per connections was also greater than those of Per-Pro connections ($p < 0.05$). For AD, Con-Con connections had a higher AD on average than Per-Per connections ($p < 0.05$) and AD across Con-Sat connections was greater than Per-Pro ($p < 0.01$) and Per-Per ($p < 0.001$) connections. These results suggest a high level of microstructural organization for the most integrative Con-Con and Con-Sat connections as compared to Per-Pro and, in particular, Per-Per connections. The elevated FA in integrative pathways is the result of both reduced RD (tighter axonal packing, reduced extracellular space) as well as increased AD (reduced dispersion, larger axonal calibers) and the relative changes to both RD and AD leads to no effects being observed for MD which combines these measures.

NODDI and q-ratio imaging

Microstructural tissue organization was investigated across edge classes using ICVF (indicative of axonal packing and caliber) and ODI (a measure of fiber dispersion) estimated using the NODDI biophysical diffusion model (Fig. 4.4d). ICVF was higher on average for Con-Con and Con-Sat as compared to Per-Pro ($p < 0.05$ | $p < 0.001$) and Per-Per ($P < 0.01$ | $p < 0.001$) connections. ICVF was also greater for Per-Pro than Per-Per connections ($p < 0.05$). Measures of ODI were significantly greater on average across Per-Pro and Per-Per connections than for Con-Con ($p < 0.05$ | $p < 0.01$) and Con-Sat ($p < 0.001$ | $p < 0.001$) connections. The g-ratio (a composite measure of myelin and axonal volume fractions) was found to be significantly lower in Con-Con and Con-Sat connections compared to Per-Per connections ($p < 0.05$ | $p < 0.05$).

Grey matter microstructural covariance

The population covariance of nodal tissue property measurements was calculated for measures of MT, R1, R2*, MD and cortical thickness, and compared across edge classes (Fig. 4.4e). Structural covariance was typically in the range of 0.3-0.5 for the qMRI measures and 0.05-0.1 for cortical thickness. No significant effects were observed across the classes for the MT or R1 covariance measures. R2* covariance was greater for Con-Sat as compared to Per-Per connections ($p < 0.05$). The Per-Per edge class showed reduced MD covariance as compared to Con-Con ($p < 0.05$) and Per-Pro ($p < 0.01$) connections. Structural covariance of the cortical thickness measures found Con-Sat connections to have significantly lower structural covariance than Per-Pro ($p < 0.01$) and Per-Per ($p < 0.01$) connections. Marginally lower structural covariance was observed for the Con-Con connections as compared to the Per-Pro ($p = 0.12$) and Per-Per ($p = 0.08$) connections though these tests did not reach the threshold for significance.

Evidence from the replication dataset

Differences in microstructural measures across edge classes were additionally assessed in the second HCP dataset for network cost measures, FA, MD, RD, AD, ICVF, ODI and T1w/T2w ratio (Supplementary Fig. 4.4). Highly consistent effects were observed across all measures except for RD which showed no significant differences across edge classes. For the T1w/T2w ratio, an additional measure indicative of myelin content, Con-Con connections had higher values than Per-Pro ($p < 0.05$) and Per-Per ($p < 0.01$) connections. Con-Sat connection measures

for T1w/T2w were greater than Per-Pro ($p < 0.05$) and Per-Per connections ($p < 0.001$). T1w/T2w values in Per-Pro connections were also greater than those observed in Per-Per connections ($p < 0.05$). These results for T1w/T2w are highly consistent with the myelin sensitive measures (MT & R1) of the main CoLaus dataset.

4.4 Discussion

In the present work, we investigate hierarchically modular architectures in human structural brain networks and examine how microstructural tissue properties vary depending upon regional network communication roles. Hierarchically modular organization was estimated by applying a recently developed community detection algorithm (OSLOM; Lancichinetti et al., 2011) innately capable of estimating module evidence, overlapping communities and hierarchical structure. Cortical regions (nodes) and their connections (edges) were classified based on their intrinsic and extrinsic modular connections into either connector hub, satellite node, provincial hub or peripheral node classes (Bertolero et al., 2015; Guimerà and Nunes Amaral, 2005). Microstructural network properties were then assessed across interconnecting edge classes. Each step of the analysis was replicated in a second independent dataset in order to test for reproducibility and consistency.

The main findings of the work can be summarized as follows. Based on their interconnectivity profiles, cortical nodes subdivided into 12 modules which further grouped into 4 and then 2 larger modules at progressively higher levels of network hierarchy. The use of an information-based measure found the modular architecture of the replication dataset to be highly similar to that observed in the main dataset, both in terms of module-by-module and full modular organization comparisons. Depending upon the characteristic topological role that a pathway plays in the network, distinct microstructural fingerprints exist. Our findings suggest that the most integrative pathways of the brain exhibit higher wiring costs, elevated levels of myelination and increased white matter organization.

Hierarchical modularity in structural brain networks

Clear evidence for hierarchically modular architectures were observed in these data and the organization was highly consistent within a second independent dataset suggesting that these patterns of structural modularity are a replicable and robust phenomenon. This statement is further supported by the qualitative similarity between the observed modular

organization and previously well described brain structures and functional systems (Betzel et al., 2013; Chen et al., 2012; Meunier et al., 2009; Power et al., 2011). At the lowest observed hierarchical level, structural modules formed spatially contiguous communities in alignment with well-described brain systems specialized for different domains of behavior and cognition. For example, the bilateral ventral visual stream modules comprising areas of occipital and inferior temporal cortices form the structural architecture for visual object recognition processing (DiCarlo et al., 2012; Logothetis and Sheinberg, 1996). At the second hierarchical level the 12 sub-modules combine to form 4 larger modules which broadly divide the cortex into bilateral anterior and posterior modules which can also be combined into two hemispheric modules at the third and highest hierarchical level.

Another striking feature of the hierarchical network architecture was the high degree of symmetry for the anterior-posterior organization of modules in the left and right hemispheres. Each module was either bilaterally symmetric (as in the orbitofrontal module) or had an equivalent module represented on the contralateral hemisphere. The division of the adult cortex into spatially contiguous modules aligned along a posterior-to-anterior gradient is also consistent with well described neurodevelopmental findings of segmented rostro-caudal patterns of gene expression gradients (Redies and Puelles, 2001). Indeed, an investigation into how genes influence cortical surface area expansion in humans revealed a hierarchically modular organization, predominantly bilaterally symmetric across hemispheres (Chen et al., 2012). This modular organization, derived from genetically encoded surface expansion measures (Chen et al., 2012), has a striking resemblance to the hierarchically modular structural connectivity architecture presented here. For example, both parcellations - whether genetic or connectivity based – define 12 modules at the lowest level and contain orbitofrontal, medial-cingulate, prefrontal, posterior parietal and occipital modules. Further evidence for a high degree of heritability in white matter structures (Chiang et al., 2011) suggests that genetic factors might form a principle driving force for the development of modularity in structural brain networks. Despite the high degree of symmetry between hemispheres, we observed subtle differences in several modules spanning the lateral sulcus. These differences may be related to the highly asymmetric nature of left lateralized language pathways in the human brain (Catani et al., 2007) leading to greater interconnectivity between left hemispheric temporo-parieto-frontal cortices.

It is interesting to consider why the human brain might have evolved hierarchically modular connectivity architectures and invested so heavily in the anatomical structures facilitating inter-modular communication. Biological systems have been suggested to gain great evolutionary advantage by developing modular organization (Kirschner and Gerhart, 1998), promoting adaptations and flexibility in the face of a changing environment (Kashtan et al., 2007; Kashtan and Alon, 2005). When faced with an unpredictable environment, the swapping or rearrangement of maladaptive modules is less costly than adapting the system as a whole (see Sporns and Betzel, 2015). Furthermore, it has been shown that modular organization may infer evident cognitive advantages by preventing the loss of old skills upon learning new ones (Ellefsen et al., 2015) and promoting the persistence of functional specialization (Gallos et al., 2012). Hierarchical modularity in particular has been proposed as an important component for enabling dynamic regime criticality and consequently the facilitation of complex behaviors (Moretti and Muñoz, 2013; Rubinov et al., 2011). Perhaps an even stronger argument for the evolution of modular brain networks comes from a strong selection pressure to reduce wiring costs in a system with limited spatial and energetic resources (Bullmore and Sporns, 2012; Clune et al., 2013). Computational studies have shown that selective pressures to minimize wiring cost result in the evolution of modular networks that are capable of quickly adapting to new environments (Clune et al., 2013; Kashtan and Alon, 2005). Modular architectures help to reduce wiring costs if the modules remain compact, and we observe compact and spatially contiguous modules across both our main and replication datasets, at each hierarchical level.

Modular node class organization

One of the advantages of a modular network analysis is that it allows for a more precise definition of a node's topological role in the network. For example, instead of simply dividing nodes based on their degree, we classified nodes in terms of their specific role towards intra- and inter-modular communication. Connector hub nodes, forming the most highly integrative hubs in the network, are widely distributed across the modules, though predominantly found in posterior parietal, posterior cingulate, superior frontal, precuneus and anterior medial cortices. The spatial distribution of connector hubs is in good agreement with alternative network hub definitions (Bertolero et al., 2015; Buckner et al., 2009; Nicolini et al., 2017; van den Heuvel and Sporns, 2013, 2011). Though at least 1 connector hub was observed across 10

of the 12 modules, a particularly high concentration was noted for the bilateral medial modules (4 and 7). These medial structures have been shown to act as connector hub nodes in functional connectivity networks and have a high probability of activation across multiple cognitive tasks (Bertolero et al., 2015), suggesting a particularly prominent role in functional integration and contextualization. Regions which participate in multiple cognitive tasks and integrate across different modules might be expected to exhibit increased glucose utilization due to the high levels of functional activity (Bertolero et al., 2015). A qualitative comparison of the connector hub node positions to regional aerobic glycolysis levels in the human brain reveals that connector hub structures are also some of the most metabolically active (Vaishnavi et al., 2010).

We found 13 nodes with evidence for multiple community assignments (2 each) with 12 of these classified as satellite nodes and one as a connector hub, underlining the bridging communication role of these structures and the importance of considering network communities as overlapping covers rather than fully segregated partitions. Most approaches to community detection (e.g. modularity maximization or independent component analysis) generally ensure that each node is assigned to a single module but do not provide measures of confidence to the assignments nor do they allow for multiple assignments in the case of overlapping communities (for a review see Sporns and Betzel, 2015). Some evidence exists for the presence of overlapping nodes in otherwise segregated modules (Lee et al., 2012) and the approach used within this study provides a new perspective by inherently testing for the significance of node assignments across multiple putative communities.

Microstructural fingerprints of modular communication

Different aspects of microstructural organization across the modular edge classes were investigated by combining diffusion (DTI & NODDI), relaxometry (R1, R2* & T1w/T2w), magnetization transfer (MT), g-ratio and grey matter structural covariance measurements. Our findings are in support of earlier work suggesting that integrative structures and connections represent a high-cost feature of brain organization with enhanced microstructural tissue properties (Bertolero et al., 2015; Collin et al., 2017, 2014; Crossley et al., 2014; Mancini et al., 2017; Scholtens et al., 2014; van den Heuvel et al., 2013).

The most integrative connector hub connections (and to a lesser extent the connector-satellite node connections) were found to typically span longer distances and to have greater wiring costs than more peripheral connections. These classes of connections also possessed enhanced microstructural organization as reflected by their high values for FA, AD and ICVF and conversely for their low values in RD and ODI measurements. These results are consistent with preliminary findings in the anatomical rich club connections (Collin et al., 2014) which were also reproduced in our data with a high degree of regularity (Supplementary Fig. 4.6). Together these results suggest a set of highly organized integrative pathways with low fiber dispersion and highly efficient axonal packing. Furthermore, the connector-connector and connector-satellite connections had elevated levels for MT, R1 and T1w/T2w ratio measures indicative of greater myelin concentrations in these pathways.

Whether the increased levels of myelin in integrative pathways are due to increased axonal densities or more myelin per axon can be probed by an assessment of g-ratio measurements which provide an indirect estimate of the average myelin investment per axon (Campbell et al., 2017). We found lower g-ratio values in connector-connector and connector-satellite connections as compared to the most peripheral connections, indicative of thicker myelin sheaths in integrative pathways for a given axonal diameter. Increased myelin investment might provide information processing benefits to the network by reducing conduction delay along the extended axonal trajectories (Rushton, 1951) and enhancing network synchrony (Fields et al., 2015).

Microstructural covariance measures explore patterns of synchronized tissue change across cortical structures. Absolute levels of cortical covariance were consistently larger for the qMRI versus cortical thickness measures. We observed only a few relatively weak effects across edge classes for R2* and MD with no effects observed for the most myelin sensitive MT and R1 measures. This might be indicative of microstructural organization in the cortex (particularly myelination) being principally dependent upon features non-specific to modular communication roles. For example, it has been suggested that cortical development proceeds from sensory to motor to association cortex (Greenfield, 1991; Yakovlev and Lecours, 1967) and changes to intracortical myelin densities are known to continue well into the 5th decade of life (Grydeland et al., 2013). Using structural covariance, as measured by cortical thickness, we observed significantly higher synchronized tissue changes between the peripheral as

compared to integrative classes. The mechanisms driving structural covariance measures have been hypothesized to include genetic factors and synchronous neuronal activation between structures (Alexander-Bloch et al., 2013). Low levels of structural covariance in the most integrative pathways therefore supports the hypothesis that connector hub and satellite nodes participate in multiple functional communities, forming a distributed system spread across the brain's functional and genetic modules (Chen et al., 2013, 2012; Power et al., 2011).

Closing remarks

To summarize, our results suggest a hierarchically modular organization in human brain anatomical networks with particular enhancement and enriched microstructure across integrative connections. Despite being a high-cost feature of the network, the observed additional investment in network wiring and microstructural organization of the most integrative brain pathways may provide additional benefits to the system beyond the selection pressure to reduce costs (Bullmore and Sporns, 2012). A small number of highly integrative and microstructurally enriched connector hub regions could provide reduced communication delays (van den Heuvel et al., 2012) and improved robustness to randomized lesions (Paul et al., 2006). Indeed, evidence is beginning to emerge that a wide array of neuropsychiatric diseases specifically target network hub regions (Crossley et al., 2014; Fornito et al., 2015; van den Heuvel et al., 2013). We hypothesize that the hierarchical architecture and increased investment in inter-modular connections as presented in this study could provide an additional robustness and capacity for compensation to brain injury and disease.

Our findings support previous data on the structure-function relationships in brain hub regions (Bertolero et al., 2015; Collin et al., 2014; Harriger et al., 2012; Scholtens et al., 2014) and concepts of modular organization and specialization in human brain networks (Park and Friston, 2013; Sporns, 2013; Sporns and Betzel, 2015). Future work may lead to a greater understanding of how connectivity architectures and white matter microstructure relate to disease processes, normal aging and cognition (Fornito et al., 2015; Petersen and Sporns, 2015; Zuo et al., 2016).

5. General Discussion

Detailed discussions of the results presented in this thesis have been provided in the relevant project chapters. Here we aim to briefly summarize the main findings, to put them in context with the wider neuroscientific literature, to consider some of the limitations with the work, and to outline future directions for the field.

5.1 Main findings

Evolution of white matter tract microstructure across the lifespan

In this first study we investigated nonlinear aging effects across 20 major white matter tracts in a large imaging cohort (n=801, 7-84 years). We report robust nonlinear aging effects across tracts for the multiple qMRI measures of MT, R1, R2*, g-ratio, FA, MD, ICVF and ODI. Tract microstructure measurements typically peaked between the mid-twenties and mid-fifties with g-ratio measures peaking earliest and ODI measures peaking latest. Substantial spatial heterogeneity was observed in the maturational timings of tracts. Associations with gender, hemisphere, and their interactions with age were generally weak and inconsistent. A quantitative correlation analysis provides novel evidence in support of the well-established last-in-first-out retrogenesis hypothesis of aging, suggesting that the delayed myelination of a tract is predictive of greater accelerating decline in old age and total myelin modulation over the lifespan. This study represents one of the largest lifespan white matter investigations to date, combining more qMRI measures than in previous reports (Kochunov et al., 2012; Lebel et al., 2012; Yeatman et al., 2014), and providing the most comprehensive assessment of aging effects for the novel g-ratio qMRI measure (Berman et al., 2017; Cercignani et al., 2016).

Lifespan brain tissue changes reveal a modular architecture of human white matter

Multiple tissue microstructure measurements were sampled along the connecting edges of an anatomical brain network and their aging trends used as features in a data-driven clustering analysis. White matter pathways were grouped into clusters with coherent tissue aging trajectories, revealing a set of five 'lifespan modules' which broadly divided the white matter along functional-anatomical lines; we report distinct fronto-striatal, callosal, fronto-parieto-occipital, prefronto-temporal and limbic modules. Edges within a module have more consistent microstructural aging trends with each other than with edges in other modules. R1

was found to have strong and moderate partial correlations with MT and R2* respectively, highlighting that this measure, although principally driven by myelination, also has a non-trivial dependence on local iron content. Weak partial correlations between the MT, R2*, MD or ICVF lifespan measures suggest that these qMRI measurements are sensitive to different microstructural tissue properties and can be used in combination to assess the multiple biological processes that drive white matter tissue property changes across the lifespan.

Hierarchical modularity and microstructural enrichment of the brain's integrative architectures

Structural connections of the brain were estimated using advanced diffusion tractography procedures and used to construct a 'connectomic' description of the human anatomical brain network. Once described in this form tools from the field of graph theory were applied to estimate the organization of the network into modules and each cortical region's role in network communication. The use of a novel modularity detection algorithm suggested a division of human cortex into 12 modules which combined to form two higher hierarchical levels. Modular definitions were generally very similar between hemispheres and an information-based measure showed a high level of consistency between these modular definitions and those observed in a large replication dataset. The modular structure was used to define different modular classes, governed by the extent to which a region possesses a high degree of inter- or intra-modular connectivity. Measures of microstructure were found to be significantly different depending on the role of a connection in the network, with greater wiring costs and enhanced microstructural organization for the most integrative connections of the brain.

5.2 Lifespan investigations of the white matter

The first two projects of this thesis focus on patterns of microstructural change in the white matter over a large portion of the human lifespan. We report robust non-linear lifespan trends in good agreement with previous neurodevelopmental (Dean et al., 2014; Deoni et al., 2012; Yeatman et al., 2012a), aging (Bender and Raz, 2015; Bennett et al., 2010; Cox et al., 2016), and lifespan (Callaghan et al., 2014; Lebel et al., 2012; Yeatman et al., 2014) investigations. The extent of microstructural change over the lifespan varies between tracts with the corticospinal tract and corpus callosum segments typically being more stable than the association pathways of the brain. This is in good agreement with previous work suggesting

that the pathways supporting sensorimotor functions and interhemispheric communication develop earliest and remain relatively stable with age (Bartzokis et al., 2012; Kinney et al., 1988; Yakovlev and Lecours, 1967; Yeatman et al., 2014). Indeed, we found strong correlational relationships between the age of maturation in a tract and the relative amount of lifespan tissue change for the most myelin specific measures of MT, R1, R2* and the g-ratio. These findings provide novel quantitative evidence for the last-in-first-out retrogenesis hypothesis of aging (Raz, 2000; Reisberg et al., 2002) and contribute to previous reports of greater age-related tissue change in the latest myelinating pathways of the brain (Brickman et al., 2012; Davis et al., 2009; Gao et al., 2011; Stricker et al., 2009; Yeatman et al., 2014).

Of the previous investigations into retrogenesis hypotheses of the brain most provide only qualitative evidence in its support. One recent study by Yeatman et al. (2014) went further by formulating quantitative definitions for the retrogenesis hypotheses. Their results conflict with our own findings as they found no evidence for the last-in-first-out hypothesis when using R1 as a biomarker for myelin. One possible reason for the contrasting findings comes from the different ways in which we have tried to formulate and quantitatively test this hypothesis. Whilst we formulated a model which correlated maturational timings with the rate of quadratic (accelerating) microstructure change either side of the peak, Yeatman et al. (2014) used a piecewise linear model to test the relationship between peak age and the duration of maturational stability (plateau) around that peak. Our combined findings suggest that the late myelination of a region is predictive of increased levels of myelin reorganization over the lifespan but not the duration of a stable plateau at its peak (Yeatman et al., 2014).

Why might extended periods of tract development be associated with greater vulnerability in old age? One possible explanation is that functional neuroanatomy plays a role in organizing tissue change along a hierarchical sequence of development (Greenfield, 1991). Connections involved in more basic interhemispheric, motor or visual functions would reach maturity earlier than those involved in higher-order executive, social and emotional processing. Indeed, work in the macaque has shown protracted development and synaptic refinement in executive relative to sensory regions (Elston et al., 2009). Developmental studies in humans also provide evidence of earlier maturation in sensory-motor regions relative to higher-order association cortex (Krongold et al., 2015; Sotiras et al., 2017). Additionally, many of the cortical regions that develop latest are also the most evolutionarily novel (Hill et al., 2010), and

increased evolutionary novelty has recently been associated with greater age-related tissue change (Sotiras et al., 2017). Thus, a plausible link begins to emerge between evolutionary novelty, ontogenetic timings, and age-related vulnerability in the human brain.

The processes governing lifespan tissue changes are multiple and complex, being controlled via a combination of intrinsic genetic programs and extrinsic environmental influences. Evidence suggests that within mammalian white matter, levels of myelination (Emery, 2010; Gibson et al., 2014) and axonal caliber (Fancy et al., 2011) vary in response to electrical activity leading to ongoing experience dependent plasticity. Furthermore, appropriate levels of myelination are likely controlled by multiple intracellular signaling pathways that promote and/or inhibit myelination processes (Fancy et al., 2011). Recent evidence by Cantuti-Castelvetri et al. (2018) now suggests that progressive myelin loss in later life may be caused by defective cholesterol clearance mechanisms that lead to an imbalance between re-myelination and de-myelination processes in the brain. Within the human cortex, regional variations in maturational patterns have been shown to relate to shared genetic influences that may localize along functional lines (Chen et al., 2013) and extend to a regulation of tissue dynamics across the lifespan (Fjell et al., 2015). White matter microstructure is also heavily determined by genetics (Chiang et al., 2009; Pfefferbaum et al., 2001), particularly during adolescence and in subjects with an above average intelligence quotient (IQ) (Chiang et al., 2011). These findings highlight the multiple factors contributing to healthy white matter development and maintenance over the lifespan.

By applying a combination of multiple qMRI measurements in a large lifespan cohort we show that these measures have unique sensitivities to some of the concurrent tissue processes in action over the human lifespan. The combination of these measures in a data-driven clustering analysis revealed a set of five 'lifespan modules' that segregated the white matter along functional-anatomical lines. Previous work using a similar approach in the grey matter has found that cortical thickness developmental trajectories distinguished sensorimotor regions from association regions of the brain (Krongold et al., 2015). Further work has begun to link functional and developmental modules to disease vulnerability within human grey matter (Alexander-Bloch et al., 2014; Douaud et al., 2014; Seeley et al., 2009). Whether equivalent relationships to disease states exist in white matter developmental subsystems remains a question for future investigations.

5.3 Tissue microstructure of the human connectome

The human ‘connectome’ has become a buzz word in recent years with results from large multi-center studies, such as the \$40m NIH funded Human Connectome Project (<http://www.humanconnectome.org>), leading to novel descriptions of brain organization (Glasser et al., 2016) and brain-behavior-demographic relationships (S. M. Smith et al., 2015). Most connectomic investigations have focused on either functional connectivity (Bertolero et al., 2015; Crossley et al., 2013; Picchioni et al., 2013; Sun et al., 2017) or topological aspects of structural brain networks (Betzel et al., 2013; Hagmann et al., 2008; Korgaonkar et al., 2014; van den Heuvel et al., 2012; van den Heuvel and Sporns, 2011). More recently a growing appreciation for the role of tissue microstructure in network descriptions of the brain has begun to emerge (Collin et al., 2014; Daducci et al., 2015; Fields et al., 2015; Mancini et al., 2017; Scholtens et al., 2014; van den Heuvel et al., 2015).

Two previous studies investigated tissue microstructure properties in structural human brain networks using similar approaches to the one presented here in chapter 4. In the first study, Collin et al. (2014) combined T1w, DTI and MT image with several aspects of structural and functional connectivity to examine their organization in relation to the brain’s rich club architectures. The authors reported that rich club regions and rich club connections exhibited high levels of wiring volume, high levels of white matter organization, high levels of metabolic energy usage, and long maturational trajectories. These results are in good agreement with our findings from a secondary analysis comparing tissue microstructure properties in rich club connections, where we observed increased wiring costs and microstructural organization in rich club connections. The second study by Mancini et al. (2017) weighted their structural connectivity matrices by the g-ratio and reported that rich club connections presented higher myelination than peripheral connections. Taken together, these findings extend the notion that rich club organization represents a high-cost feature of brain architecture (van den Heuvel et al., 2012).

In the present work we were specifically interested in determining how white matter microstructure was organized across the brain’s modular connectivity architectures (Sporns and Betzel, 2015). Our modular definitions presented a high degree of similarity between the principle and replication datasets, suggesting that our patterns of structural modularity were

a replicable and robust phenomenon. Such statements are also supported by the high degree of similarity between the observed modular organization and previously well described brain modules and functional systems (Betzel et al., 2013; Chen et al., 2012; Meunier et al., 2009; Power et al., 2011).

One advantage of the modular network analysis approach is that it allows for a more precise definition of a node's topological role in the network. For example, instead of simply dividing nodes based on their degree, we classified nodes in terms of their specific role towards intra- and inter-modular communication (Bertolero et al., 2015; Guimerà and Nunes Amaral, 2005). Connector hub nodes, forming the most highly integrative hubs in the network, were widely distributed across the modules, though predominantly found in posterior parietal, posterior cingulate, superior frontal, precuneus and anterior medial cortices. The spatial distribution of connector hubs is in good agreement with alternative network hub definitions (Bertolero et al., 2015; Buckner et al., 2009; Nicolini et al., 2017; van den Heuvel and Sporns, 2013, 2011). These connector hub nodes are known to sit between distinct functional subsystems and become highly active in tasks requiring multiple cognitive functions (Bertolero et al., 2015), exemplifying their integrative capacity in the brain. We found that the connections serving these integrative brain hubs had elevated wiring costs, enriched microstructural organization and increased myelination. Our results are in good agreement with previous studies that have shown increased neuronal complexity in cortical hub regions (Scholtens et al., 2014) and enriched microstructure of the brains integrative pathways (Collin et al., 2014; Mancini et al., 2017). The large sample size and multiple qMRI measurements used in our study provide robust information about the microstructural differences between modular connection classes. Despite being a high-cost feature of the network, additional investment in the brain's most integrative pathways may be offset by the additional benefits they confer to the system beyond the selection pressure to reduce costs (Bullmore and Sporns, 2012).

5.4 Methodological considerations

Sample selection

The subjects recruited for these studies were in good health and were screened for any known brain diseases. We further conducted extensive quality control procedures whereby

the data for each subject was assessed for movement artifacts, preprocessing errors and overt pathology. Despite our best efforts to construct a large neuroimaging sample representative of the healthy population, we cannot rule out certain types of sample bias. For example, cross-sectional studies of age-related trajectories may imperfectly represent patterns of within-individual changes over time (Lindenberger et al., 2011). Furthermore, it is impossible to guarantee that the subjects recruited in old-age are fully representative of those obtained at younger ages. Nevertheless, the fully longitudinal study designs that would be required to account for these biases remain rare as the time course required to fully track the age ranges investigated here would become extremely prohibitive. This has led to the few longitudinal studies in the literature adopting semi-longitudinal studies whereby subjects are followed over short time periods but with a sample spanning a wide age range (Barrick et al., 2010; Bender and Raz, 2015; de Groot et al., 2016; Lebel and Beaulieu, 2011; Sexton et al., 2014; Teipel et al., 2010). Such challenges have led most lifespan studies to adopt cross-sectional designs like ours (Callaghan et al., 2014; Cox et al., 2016; Hasan et al., 2010; Kochunov et al., 2012; Lebel et al., 2012; Li et al., 2014; Westlye et al., 2010b; Yeatman et al., 2014). Thus, although our cross-sectional data provide well-powered insights into microstructural organization over the lifespan, the examination of intra-individual changes over the lifespan must await further data.

Diffusion imaging and tractography

A potential concern for tractography based microstructure assessments comes in the form of partial volume effects (Vos et al., 2011). Partial volume effects of white matter samples with grey matter and CSF can lead to biased estimates of a measure. We accounted for this in our first study by applying an automated fiber tract quantification algorithm that weights the sampled microstructure information of a tract's core more highly than samples from more peripheral streamlines (Yeatman et al., 2012b). In the final two studies that utilized microstructure weighted connectivity matrices, we applied advanced tractography preprocessing procedures that have been developed to account for certain known biases. Tractography was performed using a multi-shell, multi-tissue constrained spherical deconvolution algorithm that reduces the effect of grey matter and CSF partial volume biases while tracking through the white matter (Jeurissen et al., 2014). Furthermore, we employed an anatomically constrained tractography (ACT) framework which ensures that all streamlines

are connected to anatomically plausible cortical and subcortical structures and that they terminate at the grey matter interface (Smith et al., 2012). Finally, for each subject the full tractograms of 20m streamlines were filtered using the SIFT and SIFT2 algorithms to remove streamlines that were not supported by the raw data, improving reproducibility and biological accuracy in the estimated connectivity matrices (R. E. Smith et al., 2015a, 2015b; Smith et al., 2013; Yeh et al., 2016). These methodological choices greatly reduce the chance of streamlines being sampled outside of the white matter and consequent biases due to partial volume effects.

In addition to reducing partial volume effects our methods aim to make tractography derived connectivity estimates more reproducible and biologically accurate (R. E. Smith et al., 2015a). The development of HARDI tractography techniques has enabled previously unobserved connectivity patterns to be studied for the first time in humans (Thiebaut de Schotten et al., 2011; Wedeen et al., 2012). However, by estimating a fuller range or crossing fiber architectures in the brain this development has led to concerns about the occurrence of many false-positives in HARDI tractography datasets (Maier-Hein et al., 2017; Zalesky et al., 2016). These concerns are an ongoing topic of investigation and no current method exists to fully eliminate them. Despite these challenges we adopted a number of methodological choices that can reduce the risk of large biases due to false-positive connections: while tracking we ensured that all streamlines connected plausible brain structures (Smith et al., 2012) and we filtered out the most spurious streamlines (R. E. Smith et al., 2015a, 2015b; Smith et al., 2013); for the connectome matrices we used a consistency based threshold approach to only include edges that were found in at least 60% of the subjects (de Reus and van den Heuvel, 2013), and weighted connectivity matrices were used when relevant as false-positives in binarized connectivity matrices have been shown to have a severe impact on measures of network clustering (Zalesky et al., 2016). Future efforts using global tractography (Christiaens et al., 2015; Mangin et al., 2013) and additional tissue microstructure information (Daducci et al., 2016, 2015) may help to overcome the challenges of accurately representing brain connections using diffusion tractography (Maier-Hein et al., 2017).

5.5 Future perspectives

In this work we combine multimodal imaging measures to provide novel insights into the organization of human white matter. Our lifespan studies are conducted on a cross-sectional sample, the limitations of which are detailed above. Future longitudinal studies conducted over wide age ranges and in many subjects could allow for more complex models that characterize intra-individual trajectories of white matter tissue change over the lifespan. By extending multimodal microstructure assessments to patient populations their white matter measures could be compared directly to the quantitative curves in this work that represent normative trends. Indeed, we hypothesize that disruptions to a specific subset of the mechanisms coordinating a white matter lifespan module may underlie certain network dysfunction across a range of developmental and neurodegenerative disorders (Alexander-Bloch et al., 2014; Zhang et al., 2013). Such questions demand future investigations linking genetic and environmental influences to maintenance and degradation processes in human white matter.

Though there has been a recent impetus to conduct connectomic investigations across the lifespan (Melie-Garcia et al., 2017; Zuo et al., 2016), studies typically ignore important microstructural information (Betz et al., 2014; Fields et al., 2015; Zhao et al., 2015). Future work would benefit from a) establishing the stability of structural modularity with age, and b) assessing differences in aging trends based on a connection's role in network communication and integration. Evidence is beginning to emerge that a wide array of neuropsychiatric diseases specifically target network hub regions (Crossley et al., 2014; Fornito et al., 2015; van den Heuvel et al., 2013). Future work could assess whether microstructure abnormalities in the brain's most integrative pathways is associated with greater disease severity in patient populations.

Taken together, the findings presented in this work provide secure foundations for future investigations exploring white matter organization, healthy aging and cognition. Combining diffusion tractography with measures of brain tissue microstructure provides an important step towards inferring the biological mechanisms that link the white matter to cognition.

References

- Abe, O., Aoki, S., Hayashi, N., Yamada, H., Kunimatsu, A., Mori, H., Yoshikawa, T., Okubo, T., Ohtomo, K., 2002. Normal aging in the central nervous system: Quantitative MR diffusion-tensor analysis. *Neurobiol. Aging* 23, 433–441.
- Aboitiz, F., Scheibel, A.B., Fisher, R.S., Zaidel, E., 1992. Fiber composition of the human corpus callosum. *Brain Res.* 598, 143–153.
- Achard, S., Bullmore, E., 2007. Efficiency and cost of economical brain functional networks. *PLoS Comput. Biol.* 3, 0174–0183.
- Alexander-Bloch, A., Giedd, J.N., Bullmore, E., 2013. Imaging structural co-variance between human brain regions. *Nat. Rev. Neurosci.* 14, 322–336.
- Alexander-Bloch, A.F., Reiss, P.T., Rapoport, J., McAdams, H., Giedd, J.N., Bullmore, E.T., Gogtay, N., 2014. Abnormal Cortical Growth in Schizophrenia Targets Normative Modules of Synchronized Development. *Biol. Psychiatry* 76, 438–446.
- Alexander, D.C., Hubbard, P.L., Hall, M.G., Moore, E. a, Ptito, M., Parker, G.J.M., Dyrby, T.B., 2010. Orientationally invariant indices of axon diameter and density from diffusion MRI. *Neuroimage* 52, 1374–89.
- Alstott, J., Panzarasa, P., Rubinov, M., Bullmore, E.T., Vértes, P.E., 2014. A Unifying Framework for Measuring Weighted Rich Clubs. *Sci. Rep.* 4, 7258.
- Ameis, S.H., Catani, M., 2015. Altered white matter connectivity as a neural substrate for social impairment in Autism Spectrum Disorder. *Cortex* 62, 158–181.
- Anderson, V.C., Obayashi, J.T., Kaye, J.A., Quinn, J.F., Berryhill, P., Riccelli, L.P., Peterson, D., Rooney, W.D., 2014. Longitudinal relaxographic imaging of white matter hyperintensities in the elderly. *Fluids Barriers CNS* 11, 24.
- Andersson, J.L.R., Sotiropoulos, S.N., 2016. An integrated approach to correction for off-resonance effects and subject movement in diffusion MR imaging. *Neuroimage* 125, 1063–1078.
- Ashburner, J., 2009. Computational anatomy with the SPM software. *Magn. Reson. Imaging.*
- Ashburner, J., Hutton, C., Frackowiak, R., Johnsrude, I., Price, C., Friston, K., 1998. Identifying global anatomical differences: deformation-based morphometry. *Hum. Brain Mapp.* 6, 348–57.
- Assaf, Y., Basser, P.J., 2005. Composite hindered and restricted model of diffusion (CHARMED) MR imaging of the human brain. *Neuroimage* 27, 48–58.
- Barnea-Goraly, N., Menon, V., Eckert, M., Tamm, L., Bammer, R., Karchemskiy, A., Dant, C.C., Reiss, A.L., 2005. White Matter Development During Childhood and Adolescence: A Cross-sectional Diffusion Tensor Imaging Study. *Cereb. Cortex* 15, 1848–1854.
- Barres, B.A., Raff, M.C., 1993. Proliferation of oligodendrocyte precursor cells depends on electrical activity in axons. *Nature* 361, 258–60.
- Barrick, T.R., Charlton, R.A., Clark, C.A., Markus, H.S., 2010. White matter structural decline in normal ageing: A prospective longitudinal study using tract-based spatial statistics. *Neuroimage* 51, 565–577.
- Bartzokis, G., Beckson, M., Lu, P.H., Nuechterlein, K.H., Edwards, N., Mintz, J., 2001. Age-related changes in frontal and temporal lobe volumes in men: a magnetic resonance imaging study. *Arch Gen Psychiatry* 58, 461–465.
- Bartzokis, G., Lu, P.H., Heydari, P., Couvrette, A., Lee, G.J., Kalashyan, G., Freeman, F., Grinstead, J.W., Villablanca, P., Finn, J.P., Mintz, J., Alger, J.R., Altshuler, L.L., 2012. Multimodal magnetic resonance imaging assessment of white matter aging trajectories over the lifespan of healthy individuals. *Biol. Psychiatry* 72, 1026–1034.
- Basser, P., Mattiello, J., LeBihan, D., 1994. Estimation of the Effective Self-Diffusion Tensor from the NMR Spin Echo. *J. Magn. Reson.*
- Basser, P.J., Mattiello, J., LeBihan, D., 1994. MR diffusion tensor spectroscopy and imaging. *Biophys. J.* 66, 259–267.

- Bassett, D.S., Bullmore, E., Verchinski, B.A., Mattay, V.S., Weinberger, D.R., Meyer-Lindenberg, A., 2008. Hierarchical Organization of Human Cortical Networks in Health and Schizophrenia. *J. Neurosci.* 28, 9239–9248.
- Bassett, D.S., Greenfield, D.L., Meyer-Lindenberg, A., Weinberger, D.R., Moore, S.W., Bullmore, E.T., 2010. Efficient physical embedding of topologically complex information processing networks in brains and computer circuits. *PLoS Comput. Biol.* 6.
- Beaulieu, C., 2002. The basis of anisotropic water diffusion in the nervous system - a technical review. *NMR Biomed.* 15, 435–55.
- Behrens, T.E.J., Johansen-Berg, H., Woolrich, M.W., Smith, S.M., Wheeler-Kingshott, C. a M., Boulby, P. a, Barker, G.J., Sillery, E.L., Sheehan, K., Ciccarelli, O., Thompson, a J., Brady, J.M., Matthews, P.M., 2003. Non-invasive mapping of connections between human thalamus and cortex using diffusion imaging. *Nat. Neurosci.* 6, 750–7.
- Bells, S., Lefebvre, J., Prescott, S.A., Dockstader, C., Bouffet, E., Skocic, J., Laughlin, S., Mabbott, D.J., 2017. Changes in White Matter Microstructure Impact Cognition by Disrupting the Ability of Neural Assemblies to Synchronize. *J. Neurosci.* 37, 8227–8238.
- Bender, A.R., Raz, N., 2015. Normal-appearing cerebral white matter in healthy adults: mean change over 2 years and individual differences in change. *Neurobiol. Aging* 36, 1834–1848.
- Benes, F.M., Turtle, M., Khan, Y., Farol, P., 1994. Myelination of a key relay zone in the hippocampal formation occurs in the human brain during childhood, adolescence, and adulthood. *Arch. Gen. Psychiatry* 51, 477–84.
- Bennett, I.J., Madden, D.J., Vaidya, C.J., Howard, D. V., Howard, J.H., 2010. Age-related differences in multiple measures of white matter integrity: A diffusion tensor imaging study of healthy aging. *Hum. Brain Mapp.* 31, NA-NA.
- Bentivoglio, M., Mazzarello, P., 2009. Chapter 12 The anatomical foundations of clinical neurology, in: *Handbook of Clinical Neurology*. pp. 149–168.
- Berman, S., West, K.L., Does, M.D., Yeatman, J.D., Mezer, A.A., 2017. Evaluating g-ratio weighted changes in the corpus callosum as a function of age and sex. *Neuroimage*.
- Bernstein, J., 1868. Ueber den zeitlichen Verlauf der negativen Schwankung des Nervenstroms. *Pflugers Arch* 1, 173–207.
- Bertolero, M.A., Yeo, B.T.T., D’Esposito, M., 2015. The modular and integrative functional architecture of the human brain. *Proc. Natl. Acad. Sci. U. S. A.* 112, E6798-807.
- Betz, R. f., Griffa, A., Avena-Koenigsberger, A., Goñi, J., Thiran, J.-P., Hagmann, P., Sporns, O., 2013. Multi-scale community organization of the human structural connectome and its relationship with resting-state functional connectivity. *Netw. Sci.* 1, 353–373.
- Betz, R.F., Bassett, D.S., 2016. Multi-scale brain networks. *Neuroimage* 7, 446–451.
- Betz, R.F., Byrge, L., He, Y., Goñi, J., Zuo, X.N., Sporns, O., 2014. Changes in structural and functional connectivity among resting-state networks across the human lifespan. *Neuroimage* 102, 345–357.
- Billiet, T., Vandenbulcke, M., M??dler, B., Peeters, R., Dhollander, T., Zhang, H., Deprez, S., Van den Bergh, B.R.H., Sunaert, S., Emsell, L., 2015. Age-related microstructural differences quantified using myelin water imaging and advanced diffusion MRI. *Neurobiol. Aging* 36, 2107–2121.
- Blondel, V.D., Guillaume, J.-L., Lambiotte, R., Lefebvre, E., 2008. Fast unfolding of communities in large networks. *J. Stat. Mech. Theory Exp.* 2008, P10008.
- Bois-Reymond, E.H.D., 1848. Untersuchungen über thierische elektricität. G. Reimer.
- Brickman, A.M., Meier, I.B., Korgaonkar, M.S., Provenzano, F.A., Grieve, S.M., Siedlecki, K.L., Wasserman, B.T., Williams, L.M., Zimmerman, M.E., 2012. Testing the white matter retrogenesis hypothesis of cognitive aging. *Neurobiol. Aging* 33, 1699–1715.
- Broca, P., 1861. Nouvelle observation d’aphémie produite par une lesion de la partie postérieure des deuxième et troisième circonvolutions frontales. *Bull. Soc. Anat. Paris* 36, 398–407.

- Brodman, K., 1909. Vergleichende Localisationslehre der Grosshirnrinde in ihren Prinzipien dargestellt auf Grund des Zellenbaues. Barth, Leipzig.
- Buckner, R.L., Sepulcre, J., Talukdar, T., Krienen, F.M., Liu, H., Hedden, T., Andrews-Hanna, J.R., Sperling, R.A., Johnson, K.A., 2009. Cortical hubs revealed by intrinsic functional connectivity: mapping, assessment of stability, and relation to Alzheimer's disease. *J Neurosci* 29, 1860–1873.
- Bullmore, E., Sporns, O., 2009. Complex brain networks: graph theoretical analysis of structural and functional systems. *Nat. Rev. Neurosci.* 10, 186–98.
- Bullmore, E., Sporns, O., 2012. The economy of brain network organization. *Nat. Rev. Neurosci.* 13, 336–349.
- Cajal, S.R. y, 1893. Manual de histología normal y técnica micrográfica. Libreria de Pascual Aguilar.
- Callaghan, M.F., Freund, P., Draganski, B., Anderson, E., Cappelletti, M., Chowdhury, R., Diedrichsen, J., FitzGerald, T.H.B., Smittenaar, P., Helms, G., Lutti, A., Weiskopf, N., 2014. Widespread age-related differences in the human brain microstructure revealed by quantitative magnetic resonance imaging. *Neurobiol. Aging* 35, 1862–1872.
- Caminiti, R., Ghaziri, H., Galuske, R., Hof, P.R., Innocenti, G.M., 2009. Evolution amplified processing with temporally dispersed slow neuronal connectivity in primates. *Proc. Natl. Acad. Sci. U. S. A.* 106, 19551–6.
- Campbell, A.W., 1905. Histological studies on the localisation of cerebral function. Cambridge : C.U.P.
- Campbell, J.S.W., Leppert, I.R., Narayanan, S., Duval, T., Cohen-Adad, J., Pike, G.B., Stikov, N., 2017. Promise and pitfalls of g-ratio estimation with MRI. *Neuroimage* 1–17.
- Campbell, J.S.W., Stikov, N., Lavallée, M., Stroh, T., Frey, S., Novek, J., Nuara, S., Ho, M., Bedell, B., Pike, G.B., 2012. Full brain g-ratio mapping with NODDI-based axon volume fraction, in: ISMRM SCIENTIFIC WORKSHOP 2013. p. 2012.
- Cantuti-Castelvetri, L., Fitzner, D., Bosch-Queralt, M., Weil, M.T., Su, M., Sen, P., Ruhwedel, T., Mitkovski, M., Trendelenburg, G., Lütjohann, D., Möbius, W., Simons, M., 2018. Defective cholesterol clearance limits remyelination in the aged central nervous system. *Science (80-.)*. 1–8.
- Catani, M., Allin, M.P.G., Husain, M., Pugliese, L., Mesulam, M.M., Murray, R.M., Jones, D.K., 2007. Symmetries in human brain language pathways correlate with verbal recall. *Proc. Natl. Acad. Sci. U. S. A.* 104, 17163–8.
- Catani, M., Dell'Acqua, F., Bizzi, A., Forkel, S.J., Williams, S.C., Simmons, A., Murphy, D.G., Thiebaut de Schotten, M., 2012. Beyond cortical localization in clinico-anatomical correlation. *Cortex* 48, 1262–1287.
- Catani, M., Howard, R.J., Pajevic, S., Jones, D.K., 2002. Virtual in vivo interactive dissection of white matter fasciculi in the human brain. *Neuroimage* 17, 77–94.
- Catani, M., Jones, D.K., ffytche, D.H., 2005. Perisylvian language networks of the human brain. *Ann. Neurol.* 57, 8–16.
- Catani, M., Thiebaut de Schotten, M., Slater, D., Dell'acqua, F., 2013. Connectomic approaches before the connectome. *Neuroimage* 80, 2–13.
- Cercignani, M., Giulietti, G., Dowell, N.G., Gabel, M., Broad, R., Leigh, P.N., Harrison, N.A., Bozzali, M., 2016. Characterizing axonal myelination within the healthy population: a tract-by-tract mapping of effects of age and gender on the fiber g-ratio. *Neurobiol. Aging* 49, 109–118.
- Chang, Y.S., Owen, J.P., Pojman, N.J., Thieu, T., Bukshpun, P., Wakahiro, M.L.J., Berman, J.I., Roberts, T.P.L., Nagarajan, S.S., Sherr, E.H., Mukherjee, P., 2015. White matter changes of neurite density and fiber orientation dispersion during human brain maturation. *PLoS One* 10, e0123656.
- Chen, C.-H., Fiecas, M., Gutiérrez, E.D., Panizzon, M.S., Eyler, L.T., Vuoksima, E., Thompson, W.K., Fennema-Notestine, C., Hagler, D.J., Jernigan, T.L., Neale, M.C., Franz, C.E., Lyons, M.J., Fischl, B., Tsuang, M.T., Dale, A.M., Kremen, W.S., 2013. Genetic topography of brain morphology. *Proc. Natl. Acad. Sci. U. S. A.* 110, 17089–17094.
- Chen, C.H., Gutierrez, E.D., Thompson, W., Panizzon, M.S., Jernigan, T.L., Eyler, L.T., Fennema-Notestine, C., Jak, A.J., Neale, M.C., Franz, C.E., Lyons, M.J., Grant, M.D., Fischl, B.R., Seidman, L.J., Tsuang, M.T., Kremen, W.S., Dale, A.M., 2012. Hierarchical genetic organization of human cortical surface area. *Science (80-.)*.

313, 2010–2012.

- Chen, Z.J., He, Y., Rosa-Neto, P., Germann, J., Evans, A.C., 2008. Revealing modular architecture of human brain structural networks by using cortical thickness from MRI. *Cereb. Cortex* 18, 2374–2381.
- Chiang, M.-C., Barysheva, M., Shattuck, D.W., Lee, A.D., Madsen, S.K., Avedissian, C., Klunder, A.D., Toga, A.W., McMahon, K.L., de Zubicaray, G.I., Wright, M.J., Srivastava, A., Balov, N., Thompson, P.M., 2009. Genetics of brain fiber architecture and intellectual performance. *J. Neurosci.* 29, 2212–24.
- Chiang, M.C., McMahon, K.L., de Zubicaray, G.I., Martin, N.G., Hickie, I., Toga, A.W., Wright, M.J., Thompson, P.M., 2011. Genetics of white matter development: A DTI study of 705 twins and their siblings aged 12 to 29. *Neuroimage* 54, 2308–2317.
- Chomiak, T., Hu, B., 2009. What Is the Optimal Value of the g-Ratio for Myelinated Fibers in the Rat CNS? A Theoretical Approach. *PLoS One* 4, e7754.
- Christiaens, D., Reisert, M., Dhollander, T., Sunaert, S., Suetens, P., Maes, F., 2015. Global tractography of multi-shell diffusion-weighted imaging data using a multi-tissue model. *Neuroimage* 123, 89–101.
- Clarke, E., O'Malley, C.D., 1996. *The human brain and spinal cord : a historical study illustrated by writings from antiquity to the twentieth century.* Norman Pub.
- Clune, J., Mouret, J.-B., Lipson, H., 2013. The evolutionary origins of modularity. *Proc. R. Soc. B Biol. Sci.* 280, 20122863–20122863.
- Colgan, N., Siow, B., O'Callaghan, J.M., Harrison, I.F., Wells, J.A., Holmes, H.E., Ismail, O., Richardson, S., Alexander, D.C., Collins, E.C., Fisher, E.M., Johnson, R., Schwarz, A.J., Ahmed, Z., O'Neill, M.J., Murray, T.K., Zhang, H., Lythgoe, M.F., 2016. Application of neurite orientation dispersion and density imaging (NODDI) to a tau pathology model of Alzheimer's disease. *Neuroimage* 125, 739–744.
- Colizza, V., Flammini, A., Serrano, M.A., Vespignani, A., 2006. Detecting rich-club ordering in complex networks. *Nature* 2, 110–115.
- Collin, G., Scholtens, L.H., Kahn, R.S., Hillegers, M.H.J., van den Heuvel, M.P., 2017. Affected Anatomical Rich Club and Structural-Functional Coupling in Young Offspring of Schizophrenia and Bipolar Disorder Patients. *Biol. Psychiatry.*
- Collin, G., Sporns, O., Mandl, R.C.W., Van Den Heuvel, M.P., 2014. Structural and functional aspects relating to cost and benefit of rich club organization in the human cerebral cortex. *Cereb. Cortex* 24, 2258–2267.
- Conturo, T.E., Lori, N.F., Cull, T.S., Akbudak, E., Snyder, A.Z., Shimony, J.S., McKinstry, R.C., Burton, H., Raichle, M.E., 1999. Tracking neuronal fiber pathways in the living human brain. *Proc. Natl. Acad. Sci. U. S. A.* 96, 10422–7.
- Cox, S.R., Ritchie, S.J., Tucker-Drob, E.M., Liewald, D.C., Hagenaars, S.P., Davies, G., Wardlaw, J.M., Gale, C.R., Bastin, M.E., Deary, I.J., 2016. Ageing and brain white matter structure in 3,513 UK Biobank participants. *Nat. Commun.* 7, 13629.
- Crossley, N.A., Mechelli, A., Scott, J., Carletti, F., Fox, P.T., McGuire, P., Bullmore, E.T., 2014. The hubs of the human connectome are generally implicated in the anatomy of brain disorders. *Brain* 137, 2382–2395.
- Crossley, N.A., Mechelli, A., Vertes, P.E., Winton-Brown, T.T., Patel, A.X., Ginestet, C.E., McGuire, P., Bullmore, E.T., 2013. Cognitive relevance of the community structure of the human brain functional coactivation network. *Proc. Natl. Acad. Sci.* 110, 11583–11588.
- Daducci, A., Canales-Rodriguez, E., Zhang, H., 2014. Accelerated Microstructure Imaging via Convex Optimization (AMICO) from diffusion MRI data. *Neuroimage* 41.
- Daducci, A., Dal Palú, A., Descoteaux, M., Thiran, J.-P., 2016. Microstructure Informed Tractography: Pitfalls and Open Challenges. *Front. Neurosci.* 10, 247.
- Daducci, A., Dal Palu, A., Lemkaddem, A., Thiran, J., 2015. COMMIT: Convex Optimization Modeling for Microstructure Informed Tractography. *IEEE Trans. Med. Imaging* 34, 246–57.
- Dale, A.M., Fischl, B., Sereno, M.I., 1999. Cortical surface-based analysis. I. Segmentation and surface reconstruction. *Neuroimage* 9, 179–94.

- Danon, L., Díaz-Guilera, A., Duch, J., Arenas, A., 2005. Comparing community structure identification. *J. Stat. Mech. Theory Exp.* 2005, P09008–P09008.
- Davis, S.W., Dennis, N. a, Buchler, N.G., White, L.E., Madden, D.J., Cabeza, R., 2009. Assessing the effects of age on long white matter tracts using diffusion tensor tractography. *Neuroimage* 46, 530–541.
- de Groot, M., Cremers, L.G.M., Ikram, M.A., Hofman, A., Krestin, G.P., van der Lugt, A., Niessen, W.J., Vernooij, M.W., 2016. White Matter Degeneration with Aging: Longitudinal Diffusion MR Imaging Analysis. *Radiology* 279, 532–541.
- Dean, D.C., O’Muircheartaigh, J., Dirks, H., Travers, B.G., Adluru, N., Alexander, A.L., Deoni, S.C.L., 2016. Mapping an index of the myelin g-ratio in infants using magnetic resonance imaging. *Neuroimage* 132, 225–237.
- Dean, D.C., O’Muircheartaigh, J., Dirks, H., Waskiewicz, N., Walker, L., Doernberg, E., Piryatinsky, I., Deoni, S.C.L., 2014. Characterizing longitudinal white matter development during early childhood. *Brain Struct. Funct.* 220, 1921–1933.
- de Reus, M.A., van den Heuvel, M.P., 2013. Estimating false positives and negatives in brain networks. *Neuroimage* 70, 402–409.
- Déjerine, J.J., Dejerine-Klumpke, A., 1895. *Anatomie des centres nerveux*, vol. 1. Rueff et Cie, Paris.
- Dekaban, A.S., Sadowsky, D., 1978. Changes in brain weights during the span of human life: Relation of brain weights to body heights and body weights. *Ann. Neurol.* 4, 345–356.
- Dell’acqua, F., Scifo, P., Rizzo, G., Catani, M., Simmons, A., Scotti, G., Fazio, F., 2010. A modified damped Richardson-Lucy algorithm to reduce isotropic background effects in spherical deconvolution. *Neuroimage* 49, 1446–1458.
- Deoni, S.C.L., Dean, D.C., O’Muircheartaigh, J., Dirks, H., Jerskey, B.A., 2012. Investigating white matter development in infancy and early childhood using myelin water fraction and relaxation time mapping. *Neuroimage* 63, 1038–1053.
- Descartes, R., 1662. *De homine*. apud Franciscum Moyardum & Petrum Leffen.
- Descoteaux, M., Angelino, E., Fitzgibbons, S., Deriche, R., 2007. Regularized, fast, and robust analytical Q-ball imaging. *Magn. Reson. Med.* 58, 497–510.
- Desikan, R.S., Ségonne, F., Fischl, B., Quinn, B.T., Dickerson, B.C., Blacker, D., Buckner, R.L., Dale, A.M., Maguire, R.P., Hyman, B.T., Albert, M.S., Killiany, R.J., 2006. An automated labeling system for subdividing the human cerebral cortex on MRI scans into gyral based regions of interest. *Neuroimage* 31, 968–980.
- DiCarlo, J.J., Zoccolan, D., Rust, N.C., 2012. How does the brain solve visual object recognition? *Neuron* 73, 415–34.
- Dobbing, J., Sands, J., 1973. Quantitative growth and development of human brain. *Arch. Dis. Child.* 48, 757–67.
- Douaud, G., Groves, A.R., Tamnes, C.K., Westlye, L.T., Duff, E.P., Engvig, A., Walhovd, K.B., James, A., Gass, A., Monsch, A.U., Matthews, P.M., Fjell, A.M., Smith, S.M., Johansen-Berg, H., 2014. A common brain network links development, aging, and vulnerability to disease. *Proc. Natl. Acad. Sci.* 111, 201410378.
- Douglas Fields, R., 2015. A new mechanism of nervous system plasticity: activity-dependent myelination. *Nat. Rev. Neurosci.* 16, 756–67.
- Draganski, B., Ashburner, J., Hutton, C., Kherif, F., Frackowiak, R.S.J., Helms, G., Weiskopf, N., 2011. Regional specificity of MRI contrast parameter changes in normal ageing revealed by voxel-based quantification (VBQ). *Neuroimage* 55, 1423–34.
- Du, F., Ongür, D., 2013. Probing myelin and axon abnormalities separately in psychiatric disorders using MRI techniques. *Front. Integr. Neurosci.* 7, 24.
- Ellefsen, K.O., Mouret, J.-B., Clune, J., 2015. Neural Modularity Helps Organisms Evolve to Learn New Skills without Forgetting Old Skills. *PLOS Comput. Biol.* 11, e1004128.
- Elston, G.N., Oga, T., Fujita, I., 2009. Spinogenesis and pruning scales across functional hierarchies. *J. Neurosci.* 29, 3271–5.
- Eluvathingal, T.J., Hasan, K.M., Kramer, L., Fletcher, J.M., Ewing-Cobbs, L., 2007. Quantitative diffusion tensor

- tractography of association and projection fibers in normally developing children and adolescents. *Cereb. Cortex* 17, 2760–8.
- Emery, B., 2010. Regulation of Oligodendrocyte Differentiation and Myelination. *Science* (80-.). 330, 779–782.
- Fancy, S.P.J., Chan, J.R., Baranzini, S.E., Franklin, R.J.M., Rowitch, D.H., 2011. Myelin Regeneration: A Recapitulation of Development? *Annu. Rev. Neurosci.* 34, 21–43.
- Fatouros, P.P., Marmarou, A., 1999. Use of magnetic resonance imaging for in vivo measurements of water content in human brain: method and normal values. *J. Neurosurg.* 90, 109–115.
- Feinberg, D.A., Moeller, S., Smith, S.M., Auerbach, E., Ramanna, S., Glasser, M.F., Miller, K.L., Ugurbil, K., Yacoub, E., 2010. Multiplexed Echo Planar Imaging for Sub-Second Whole Brain fMRI and Fast Diffusion Imaging. *PLoS One* 5, e15710.
- Felleman, D.J., Van Essen, D.C., 1991. Distributed hierarchical processing in the primate cerebral cortex. *Cereb. Cortex* 1, 1–47.
- Fields, R.D., 2008. White matter in learning, cognition and psychiatric disorders. *Trends Neurosci.* 31, 361–370.
- Fields, R.D., Woo, D.H., Basser, P.J., 2015. Glial regulation of the neuronal connectome through local and long-distant communication. *Neuron* 86, 374–386.
- Filley, C.M., Fields, R.D., 2016. White matter and cognition: making the connection. *J. Neurophysiol.* 116, 2093–2104.
- Firmann, M., Mayor, V., Vidal, P.M., Bochud, M., Pécoud, A., Hayoz, D., Paccaud, F., Preisig, M., Song, K.S., Yuan, X., Danoff, T.M., Stirnadel, H.A., Waterworth, D., Mooser, V., Waeber, G., Vollenweider, P., 2008. The CoLaus study: a population-based study to investigate the epidemiology and genetic determinants of cardiovascular risk factors and metabolic syndrome. *BMC Cardiovasc. Disord.* 8, 6.
- Fischl, B., Salat, D.H., Busa, E., Albert, M., Dieterich, M., Haselgrove, C., van der Kouwe, A., Killiany, R., Kennedy, D., Klaveness, S., Montillo, A., Makris, N., Rosen, B., Dale, A.M., 2002. Whole Brain Segmentation: Neurotechnique Automated Labeling of Neuroanatomical Structures in the Human Brain. *Neuron* 33, 341–355.
- Fischl, B., Salat, D.H., Van Der Kouwe, A.J.W., Makris, N., Ségonne, F., Quinn, B.T., Dale, A.M., 2004. Sequence-independent segmentation of magnetic resonance images. *Neuroimage* 23, 69–84.
- Fischl, B., Sereno, M.I., Dale, A.M., 1999a. Cortical Surface-Based Analysis: II: Inflation, Flattening, and a Surface-Based Coordinate System. *Neuroimage* 9, 195–207.
- Fischl, B., Sereno, M.I., Tootell, R.B.H., Dale, a M., 1999b. High-resolution inter-subject averaging and a surface-based coordinate system. *Hum. Brain Mapp.* 8, 272–284.
- Fjell, A.M., Grydeland, H., Krogsrud, S.K., Amlien, I., Rohani, D. a, Ferschmann, L., Storsve, A.B., Tamnes, C.K., Sala-Llonch, R., Due-Tønnessen, P., Bjørnerud, A., Sølvsnes, A.E., Håberg, A.K., Skranes, J., Bartsch, H., Chen, C.-H., Thompson, W.K., Panizzon, M.S., Kremen, W.S., Dale, A.M., Walhovd, K.B., 2015. Development and aging of cortical thickness correspond to genetic organization patterns. *Proc. Natl. Acad. Sci. U. S. A.* 112, 15462–15467.
- Fjell, A.M., Walhovd, K.B., Westlye, L.T., ??stby, Y., Tamnes, C.K., Jernigan, T.L., Gamst, A., Dale, A.M., 2010. When does brain aging accelerate? Dangers of quadratic fits in cross-sectional studies. *Neuroimage* 50, 1376–1383.
- Flechsig, P.E., 1896. *Gehirn und seele*. Verlag von Veit & Comp, Leipzig.
- Forkel, S.J., Thiebaut de Schotten, M., Dell’Acqua, F., Kalra, L., Murphy, D.G.M., Williams, S.C.R., Catani, M., 2014. Anatomical predictors of aphasia recovery: a tractography study of bilateral perisylvian language networks. *Brain* 137, 2027–39.
- Fornito, A., Zalesky, A., Breakspear, M., 2015. The connectomics of brain disorders. *Nat. Rev. Neurosci.* 16, 159–172.
- Fortunato, S., Barthélemy, M., 2007. Resolution limit in community detection. *Proc. Natl. Acad. Sci. U. S. A.* 104, 36–41.

- Friston, K., Holmes, A., 1995. Statistical parametric maps in functional imaging: a general linear approach. *Hum. Brain Mapp.* 2, 189–210.
- Fukunaga, M., Li, T.-Q., van Gelderen, P., de Zwart, J.A., Shmueli, K., Yao, B., Lee, J., Maric, D., Aronova, M.A., Zhang, G., Leapman, R.D., Schenck, J.F., Merkle, H., Duyn, J.H., 2010. Layer-specific variation of iron content in cerebral cortex as a source of MRI contrast. *Proc. Natl. Acad. Sci.* 107, 3834–3839.
- Gallos, L.K., Makse, H.A., Sigman, M., 2012. A small world of weak ties provides optimal global integration of self-similar modules in functional brain networks. *Proc. Natl. Acad. Sci. U. S. A.* 109, 2825–30.
- Galvani, L., 1791. *De viribus electricitatis in motu musculari: Commentarius.*
- Gao, J., Cheung, R.T.F., Lee, T.M.C., Chu, L.W., Chan, Y.S., Mak, H.K.F., Zhang, J.X., Qiu, D., Fung, G., Cheung, C., 2011. Possible retrogenesis observed with fiber tracking: An anteroposterior pattern of white matter disintegrity in normal aging and alzheimer's disease. *J. Alzheimer's Dis.* 26, 47–58.
- Gelman, N., Ewing, J.R., Gorell, J.M., Spickler, E.M., Solomon, E.G., 2001. Interregional variation of longitudinal relaxation rates in human brain at 3.0 T: relation to estimated iron and water contents. *Magn. Reson. Med.* 45, 71–9.
- Geschwind, N., 1965. Disconnexion syndromes in animals and man. I. *Brain* 88, 237–294.
- Gibson, E.M., Purger, D., Mount, C.W., Goldstein, A.K., Lin, G.L., Wood, L.S., Inema, I., Miller, S.E., Bieri, G., Zuchero, J.B., Barres, B.A., Woo, P.J., Vogel, H., Monje, M., 2014. Neuronal Activity Promotes Oligodendrogenesis and Adaptive Myelination in the Mammalian Brain. *Science (80-.)*. 344, 1252304–1252304.
- Glasser, M.F., Coalson, T.S., Robinson, E.C., Hacker, C.D., Harwell, J., Yacoub, E., Ugurbil, K., Andersson, J., Beckmann, C.F., Jenkinson, M., Smith, S.M., Van Essen, D.C., 2016. A multi-modal parcellation of human cerebral cortex. *Nature* 1–11.
- Glasser, M.F., Sotiropoulos, S.N., Wilson, J.A., Coalson, T.S., Fischl, B., Andersson, J.L., Xu, J., Jbabdi, S., Webster, M., Polimeni, J.R., Van Essen, D.C., Jenkinson, M., 2013. The minimal preprocessing pipelines for the Human Connectome Project. *Neuroimage* 80, 105–124.
- Glasser, M.F., Van Essen, D.C., 2011. Mapping human cortical areas in vivo based on myelin content as revealed by T1- and T2-weighted MRI. *J. Neurosci.* 31, 11597–616.
- Golgi, C., 1873. Sulla struttura della sostanza grigia del cervello. *Gazz. Med. Ital.* 33, 244–246.
- Good, B.H., de Montjoye, Y.-A., Clauset, A., 2010. Performance of modularity maximization in practical contexts. *Phys. Rev. E* 81, 46106.
- Good, C.D., Johnsrude, I.S., Ashburner, J., Henson, R.N., Friston, K.J., Frackowiak, R.S., 2001. A voxel-based morphometric study of ageing in 465 normal adult human brains. *Neuroimage* 14, 21–36.
- Gordon, E.M., Laumann, T.O., Adeyemo, B., Huckins, J.F., Kelley, W.M., Petersen, S.E., 2016. Generation and Evaluation of a Cortical Area Parcellation from Resting-State Correlations. *Cereb. Cortex* 26, 288–303.
- Graf von Keyserlingk, D., Schramm, U., 1984. Diameter of axons and thickness of myelin sheaths of the pyramidal tract fibres in the adult human medullary pyramid. *Anat. Anz.* 157, 97–111.
- Greenfield, P.M., 1991. Language, tools and brain: The ontogeny and phylogeny of hierarchically organized sequential behavior. *Behav. Brain Sci.* 14, 531–551.
- Gregory, S., 2010. Finding overlapping communities in networks by label propagation. *New J. Phys.* 12, 103018.
- Griswold, M.A., Jakob, P.M., Heidemann, R.M., Nittka, M., Jellus, V., Wang, J., Kiefer, B., Haase, A., 2002. Generalized autocalibrating partially parallel acquisitions (GRAPPA). *Magn. Reson. Med. Off. J. Soc. Magn. Reson. Med. / Soc. Magn. Reson. Med.* 47, 1202–1210.
- Grydeland, H., Walhovd, K.B., Tamnes, C.K., Westlye, L.T., Fjell, A.M., 2013. Intracortical myelin links with performance variability across the human lifespan: results from T1- and T2-weighted MRI myelin mapping and diffusion tensor imaging. *J. Neurosci.* 33, 18618–30.
- Guimerà, R., Nunes Amaral, L.A., 2005. Functional cartography of complex metabolic networks. *Nature* 433, 895–900.

- Gur, R.C., Turetsky, B.I., Matsui, M., Yan, M., Bilker, W., Hughett, P., Gur, R.E., 1999. Sex differences in brain gray and white matter in healthy young adults: correlations with cognitive performance. *J. Neurosci.* 19, 4065–72.
- Häggqvist, G., 1936. Analyse der Faserverteilung in einem Rückenmarkquerschnitt (Th 3). *Z Mikrosk Anat Forsch* 39, 1–34.
- Hagmann, P., Cammoun, L., Gigandet, X., Meuli, R., Honey, C.J., Wedeen, V.J., Sporns, O., 2008. Mapping the structural core of human cerebral cortex. *PLoS Biol.* 6, e159.
- Harriger, L., van den Heuvel, M.P., Sporns, O., 2012. Rich Club Organization of Macaque Cerebral Cortex and Its Role in Network Communication. *PLoS One* 7.
- Hasan, K.M., Kamali, A., Abid, H., Kramer, L.A., Fletcher, J.M., Ewing-Cobbs, L., 2010. Quantification of the spatiotemporal microstructural organization of the human brain association, projection and commissural pathways across the lifespan using diffusion tensor tractography. *Brain Struct. Funct.* 214, 361–373.
- He, Y., Chen, Z.J., Evans, A.C., 2007. Small-World Anatomical Networks in the Human Brain Revealed by Cortical Thickness from MRI. *Cereb. Cortex* 17, 2407–2419.
- Helms, G., Dathe, H., Dechent, P., 2008. Quantitative FLASH MRI at 3T using a rational approximation of the Ernst equation. *Magn. Reson. Med. Off. J. Soc. Magn. Reson. Med. / Soc. Magn. Reson. Med.* 59, 667–672.
- Helms, G., Draganski, B., Frackowiak, R., Ashburner, J., Weiskopf, N., 2009. Improved segmentation of deep brain grey matter structures using magnetization transfer (MT) parameter maps. *Neuroimage* 47, 194–198.
- Hill, J., Inder, T., Neil, J., Dierker, D., Harwell, J., Van Essen, D., 2010. Similar patterns of cortical expansion during human development and evolution. *Proc. Natl. Acad. Sci. U. S. A.* 107, 13135–40.
- Hubel, D.H., Wiesel, T.N., 1962. Receptive fields, binocular interaction and functional architecture in the cat's visual cortex. *J. Physiol.* 160, 106–154.2.
- Huttenlocher, P.R., 1979. Synaptic density in human frontal cortex - developmental changes and effects of aging. *Brain Res.* 163, 195–205.
- Huttenlocher, P.R., Dabholkar, A.S., 1997. Regional differences in synaptogenesis in human cerebral cortex. *J. Comp. Neurol.* 387, 167–78.
- Huttenlocher, P.R., de Courten, C., 1987. The development of synapses in striate cortex of man. *Hum. Neurobiol.* 6, 1–9.
- Hutton, C., Bork, A., Josephs, O., Deichmann, R., Ashburner, J., Turner, R., 2002. Image distortion correction in fMRI: A quantitative evaluation. *Neuroimage* 16, 217–40.
- Imperati, D., Colcombe, S., Kelly, C., Di Martino, A., Zhou, J., Castellanos, F.X., Milham, M.P., 2011. Differential development of human brain white matter tracts. *PLoS One* 6, e23437.
- Inder, T.E., Huppi, P.S., Warfield, S., Kikinis, R., Zientara, G.P., Barnes, P.D., Jolesz, F., Volpe, J.J., 1999. Periventricular white matter injury in the premature infant is followed by reduced cerebral cortical gray matter volume at term. *Ann. Neurol.* 46, 755–60.
- Ishibashi, T., Dakin, K.A., Stevens, B., Lee, P.R., Kozlov, S. V., Stewart, C.L., Fields, R.D., 2006. Astrocytes promote myelination in response to electrical impulses. *Neuron* 49, 823–832.
- Jenkinson, M., Bannister, P., Brady, M., Smith, S., 2002. Improved optimization for the robust and accurate linear registration and motion correction of brain images. *Neuroimage* 17, 825–41.
- Jenkinson, M., Beckmann, C.F., Behrens, T.E.J., Woolrich, M.W., Smith, S.M., 2012. FSL. *Neuroimage* 62, 782–790.
- Jeurissen, B., Leemans, A., Tournier, J.-D., Jones, D.K., Sijbers, J., 2012. Investigating the prevalence of complex fiber configurations in white matter tissue with diffusion magnetic resonance imaging. *Hum. Brain Mapp.* 0, 1–20.
- Jeurissen, B., Tournier, J.-D., Dhollander, T., Connelly, A., Sijbers, J., 2014. Multi-tissue constrained spherical deconvolution for improved analysis of multi-shell diffusion MRI data. *Neuroimage* 103, 411–26.
- Jones, D., Williams, S., 2002. Isotropic resolution diffusion tensor imaging with whole brain acquisition in a

- clinically acceptable time. *Hum. brain ...* 230, 216–230.
- Jones, D.K., 2008. Studying connections in the living human brain with diffusion MRI. *Cortex*. 44, 936–52.
- Jones, D.K., Catani, M., Pierpaoli, C., Reeves, S.J.C., Shergill, S.S., O’Sullivan, M., Golesworthy, P., McGuire, P., Horsfield, M. a, Simmons, A., Williams, S.C.R., Howard, R.J., 2006. Age effects on diffusion tensor magnetic resonance imaging tractography measures of frontal cortex connections in schizophrenia. *Hum. Brain Mapp.* 27, 230–8.
- Jones, D.K., Knösche, T.R., Turner, R., 2013. White matter integrity, fiber count, and other fallacies: the do’s and don’ts of diffusion MRI. *Neuroimage* 73, 239–54.
- Jones, D.K., Simmons, A., Williams, S.C., Horsfield, M.A., 1999. Non-invasive assessment of axonal fiber connectivity in the human brain via diffusion tensor MRI. *Magn. Reson. Med.* 42, 37–41.
- Kanaan, R.A., Shergill, S.S., Barker, G.J., Catani, M., Ng, V.W., Howard, R., McGuire, P.K., Jones, D.K., 2006. Tract-specific anisotropy measurements in diffusion tensor imaging. *Psychiatry Res. - Neuroimaging* 146, 73–82.
- Kashtan, N., Alon, U., 2005. Spontaneous evolution of modularity and network motifs. *Proc. Natl. Acad. Sci.* 102, 13773–13778.
- Kashtan, N., Noor, E., Alon, U., 2007. Varying environments can speed up evolution. *Proc. Natl. Acad. Sci. U. S. A.* 104, 13711–6.
- Kertesz, A., Black, S.E., Tokar, G., Benke, T., Carr, T., Nicholson, L., 1988. Periventricular and subcortical hyperintensities on magnetic resonance imaging. “Rims, caps, and unidentified bright objects”. *Arch. Neurol.* 45, 404–8.
- Kinney, H.C., Brody, B.A., Kloman, A.S., Gilles, F.H., 1988. Sequence of central nervous system myelination in human infancy. II. Patterns of myelination in autopsied infants. *J. Neuropathol. Exp. Neurol.* 47, 217–34.
- Kirschner, M., Gerhart, J., 1998. Evolvability. *Proc. Natl. Acad. Sci.* 95, 8420–8427.
- Koay, C.G., Chang, L.-C., Carew, J.D., Pierpaoli, C., Basser, P.J., 2006. A unifying theoretical and algorithmic framework for least squares methods of estimation in diffusion tensor imaging. *J. Magn. Reson.* 182, 115–25.
- Kochunov, P., Williamson, D.E., Lancaster, J., Fox, P., Cornell, J., Blangero, J., Glahn, D.C., 2012. Fractional anisotropy of water diffusion in cerebral white matter across the lifespan. *Neurobiol. Aging* 33, 9–20.
- Kodiweera, C., Alexander, A.L., Harezlak, J., McAllister, T.W., Wu, Y.-C., 2016. Age effects and sex differences in human brain white matter of young to middle-aged adults: A DTI, NODDI, and q-space study. *Neuroimage* 128, 180–192.
- Korgaonkar, M.S., Fornito, A., Williams, L.M., Grieve, S.M., 2014. Abnormal Structural Networks Characterize Major Depressive Disorder: A Connectome Analysis. *Biol. Psychiatry* 76, 567–574.
- Kraus, M.F., Susmaras, T., Caughlin, B.P., Walker, C.J., Sweeney, J. a, Little, D.M., 2007. White matter integrity and cognition in chronic traumatic brain injury: a diffusion tensor imaging study. *Brain* 130, 2508–19.
- Krongold, M., Cooper, C., Bray, S., 2015. Modular Development of Cortical Gray Matter Across Childhood and Adolescence. *Cereb. Cortex* bhv307-.
- Kucharczyk, W., Macdonald, P.M., Stanisz, G.J., Henkelman, R.M., 1994. Relaxivity and magnetization transfer of white matter lipids at MR imaging: importance of cerebroside and pH. *Radiology* 192, 521–529.
- Kunz, N., Zhang, H., Vasung, L., O’Brien, K.R., Assaf, Y., Lazeyras, F., Alexander, D.C., Hüppi, P.S., 2014. Assessing white matter microstructure of the newborn with multi-shell diffusion MRI and biophysical compartment models. *Neuroimage* 96, 288–99.
- LaMantia, A.S., Rakic, P., 1990. Axon overproduction and elimination in the corpus callosum of the developing rhesus monkey. *J. Neurosci.* 10, 2156–2175.
- LaMantia, A.S., Rakic, P., 1994. Axon overproduction and elimination in the anterior commissure of the developing rhesus monkey. *J. Comp. Neurol.* 340, 328–336.
- Lancichinetti, A., Fortunato, S., Kertész, J., 2009. Detecting the overlapping and hierarchical community structure in complex networks. *New J. Phys.* 11, 1–18.

- Lancichinetti, A., Radicchi, F., Ramasco, J.J., 2010. Statistical significance of communities in networks. *Phys. Rev. E* 81, 46110.
- Lancichinetti, A., Radicchi, F., Ramasco, J.J., Fortunato, S., 2011. Finding statistically significant communities in networks. *PLoS One* 6.
- Lebel, C., Beaulieu, C., 2011. Longitudinal Development of Human Brain Wiring Continues from Childhood into Adulthood. *J. Neurosci.* 31, 10937–10947.
- Lebel, C., Gee, M., Camicioli, R., Wieler, M., Martin, W., Beaulieu, C., 2012. Diffusion tensor imaging of white matter tract evolution over the lifespan. *Neuroimage* 60, 340–352.
- Lebel, C., Walker, L., Leemans, A., Phillips, L., Beaulieu, C., 2008. Microstructural maturation of the human brain from childhood to adulthood. *Neuroimage* 40, 1044–1055.
- Lee, M.H., Hacker, C.D., Snyder, A.Z., Corbetta, M., Zhang, D., Leuthardt, E.C., Shimony, J.S., 2012. Clustering of resting state networks. *PLoS One* 7, 1–12.
- Leemans, A., Jones, D.K., 2009. The B-matrix must be rotated when correcting for subject motion in DTI data. *Magn. Reson. Med.* 61, 1336–49.
- Li, W., Wu, B., Batrachenko, A., Bancroft-Wu, V., Morey, R.A., Shashi, V., Langkammer, C., De Bellis, M.D., Ropele, S., Song, A.W., Liu, C., 2014. Differential developmental trajectories of magnetic susceptibility in human brain gray and white matter over the lifespan. *Hum. Brain Mapp.* 35, 2698–2713.
- Liewald, D., Miller, R., Logothetis, N., Wagner, H.-J., Schüz, A., 2014. Distribution of axon diameters in cortical white matter: an electron-microscopic study on three human brains and a macaque. *Biol. Cybern.* 108, 541–57.
- Lin, W., Paczynski, R.P., Venkatesan, R., He, Y.Y., Powers, W.J., Hsu, C.Y., Haacke, E.M., 1997. Quantitative regional brain water measurement with magnetic resonance imaging in a focal ischemia model. *Magn. Reson. Med.* 38, 303–10.
- Lindenberger, U., von Oertzen, T., Ghisletta, P., Hertzog, C., 2011. Cross-sectional age variance extraction: What's change got to do with it? *Psychol. Aging* 26, 34–47.
- Logothetis, N.K., Sheinberg, D.L., 1996. Visual Object Recognition. *Annu. Rev. Neurosci.* 19, 577–621.
- Lohse, C., Bassett, D.S., Lim, K.O., Carlson, J.M., 2014. Resolving Anatomical and Functional Structure in Human Brain Organization: Identifying Mesoscale Organization in Weighted Network Representations. *PLoS Comput. Biol.* 10.
- Lorio, S., Lutti, a, Kherif, F., Ruef, a, Dukart, J., Chowdhury, R., Frackowiak, R.S., Ashburner, J., Helms, G., Weiskopf, N., Draganski, B., 2014. Disentangling in vivo the effects of iron content and atrophy on the ageing human brain. *Neuroimage* 103C, 280–289.
- Ludwig, E., Klingler, J., 1956. *Atlas Cerebri Humani*. Karger.
- Lutti, A., Dick, F., Sereno, M.I., Weiskopf, N., 2014. Using high-resolution quantitative mapping of R1 as an index of cortical myelination. *Neuroimage* 93, 176–188.
- Lutti, A., Hutton, C., Finsterbusch, J., Helms, G., Weiskopf, N., 2010. Optimization and validation of methods for mapping of the radiofrequency transmit field at 3T. *Magn. Reson. Med.* 64, 229–38.
- Lutti, A., Stadler, J., Josephs, O., Windischberger, C., Speck, O., Bernarding, J., Hutton, C., Weiskopf, N., 2012. Robust and fast whole brain mapping of the RF transmit field B1 at 7T. *PLoS One* 7, e32379.
- Madden, D.J., Bennett, I.J., Burzynska, A., Potter, G.G., Chen, N.-K., Song, A.W., 2012. Diffusion tensor imaging of cerebral white matter integrity in cognitive aging. *Biochim. Biophys. Acta* 1822, 386–400.
- Maier-Hein, K.H., Neher, P.F., Houde, J.-C., Côté, M.-A., Garyfallidis, E., Zhong, J., Chamberland, M., Yeh, F.-C., Lin, Y.-C., Ji, Q., Reddick, W.E., Glass, J.O., Chen, D.Q., Feng, Y., Gao, C., Wu, Y., Ma, J., Renjie, H., Li, Q., Westin, C.-F., Deslauriers-Gauthier, S., González, J.O.O., Paquette, M., St-Jean, S., Girard, G., Rheault, F., Sidhu, J., Tax, C.M.W., Guo, F., Mesri, H.Y., Dávid, S., Froeling, M., Heemskerk, A.M., Leemans, A., Boré, A., Pinsard, B., Bedetti, C., Desrosiers, M., Brambati, S., Doyon, J., Sarica, A., Vasta, R., Cerasa, A., Quattrone, A., Yeatman, J., Khan, A.R., Hodges, W., Alexander, S., Romascano, D., Barakovic, M., Auría, A., Esteban, O., Lemkaddem, A., Thiran, J.-P., Cetingul, H.E., Odry, B.L., Mailhe, B., Nadar, M.S., Pizzagalli, F., Prasad, G.,

- Villalon-Reina, J.E., Galvis, J., Thompson, P.M., Requejo, F.D.S., Laguna, P.L., Lacerda, L.M., Barrett, R., Dell'Acqua, F., Catani, M., Petit, L., Caruyer, E., Daducci, A., Dyrby, T.B., Holland-Letz, T., Hilgetag, C.C., Stieltjes, B., Descoteaux, M., 2017. The challenge of mapping the human connectome based on diffusion tractography. *Nat. Commun.* 8, 1349.
- Mancini, M., Giulietti, G., Dowell, N., Spanò, B., Harrison, N., Bozzali, M., Cercignani, M., 2017. Introducing axonal myelination in connectomics: A preliminary analysis of g-ratio distribution in healthy subjects. *Neuroimage* 1–9.
- Mangin, J.-F., Fillard, P., Cointepas, Y., Le Bihan, D., Frouin, V., Poupon, C., 2013. Toward global tractography. *Neuroimage* 80, 290–6.
- Marcus, D.S., Harwell, J., Olsen, T., Hodge, M., Glasser, M.F., Prior, F., Jenkinson, M., Laumann, T., Curtiss, S.W., Van Essen, D.C., 2011. Informatics and Data Mining Tools and Strategies for the Human Connectome Project. *Front. Neuroinform.* 5, 4.
- Matteucci, C., 1830. Sulla contrazione provata dagli animali all'aprirsi del circolo elettrico in che trovansi.
- Meilä, M., 2007. Comparing clusterings—an information based distance. *J. Multivar. Anal.* 98, 873–895.
- Melie-Garcia, L., Slater, D., Ruef, A., Sanabria-Diaz, G., Preisig, M., Kherif, F., Draganski, B., Lutti, A., 2017. Networks of myelin covariance. *Hum. Brain Mapp.*
- Mesulam, M.M., 1998. From sensation to cognition. *Brain* 121 (Pt 6), 1013–52.
- Meunier, D., Lambiotte, R., Fornito, A., Ersche, K.D., Bullmore, E.T., 2009. Hierarchical modularity in human brain functional networks. *Front. Hum. Neurosci.* 3, 1–12.
- Mezer, A., Yeatman, J.D., Stikov, N., Kay, K.N., Cho, N.-J., Dougherty, R.F., Perry, M.L., Parvizi, J., Hua, L.H., Butts-Pauly, K., Wandell, B.A., 2013. Quantifying the local tissue volume and composition in individual brains with magnetic resonance imaging. *Nat. Med.* 19, 1667–72.
- Milchenko, M., Marcus, D., 2013. Obscuring Surface Anatomy in Volumetric Imaging Data. *Neuroinformatics* 11, 65–75.
- Mishkin, M., 1966. Visual mechanisms beyond the striate cortex, in: Russel, R. (Ed.), *Frontiers in Physiological Psychology*. Academic Press, New York.
- Moeller, S., Yacoub, E., Olfman, C.A., Auerbach, E., Strupp, J., Harel, N., Uğurbil, K., 2010. Multiband multislice GE-EPI at 7 tesla, with 16-fold acceleration using partial parallel imaging with application to high spatial and temporal whole-brain fMRI. *Magn. Reson. Med.* 63, 1144–1153.
- Mohammadi, S., Carey, D., Dick, F., Diedrichsen, J., Sereno, M.I., Reiser, M., Callaghan, M.F., Weiskopf, N., 2015. Whole-Brain In-vivo Measurements of the Axonal G-Ratio in a Group of 37 Healthy Volunteers. *Front. Neurosci.* 9, 4413389–441.
- Morecraft, R.J., Ugolini, G., Lanciego, J.L., Wouterlood, F.G., Pandya, D.N., 2009. Classic and contemporary neural tract tracing techniques, in: Johansen-Berg, H., Behrens, T.E.J. (Eds.), *Diffusion MRI*. Elsevier, pp. 273–308.
- Moretti, P., Muñoz, M.A., 2013. Griffiths phases and the stretching of criticality in brain networks. *Nat. Commun.* 4.
- Mountcastle, V.B., Powell, T.P., 1959. Neural mechanisms subserving cutaneous sensibility, with special reference to the role of afferent inhibition in sensory perception and discrimination. *Bull. Johns Hopkins Hosp.* 105, 201–232.
- Neumann, H., Kotter, M.R., Franklin, R.J.M., 2009. Debris clearance by microglia: An essential link between degeneration and regeneration. *Brain* 132, 288–295.
- Newman, M.E.J., Girvan, M., 2004. Finding and evaluating community structure in networks. *Phys. Rev. E* 69, 26113.
- Nicolini, C., Bordier, C., Bifone, A., 2017. Community detection in weighted brain connectivity networks beyond the resolution limit. *Neuroimage* 146, 28–39.
- O'Muircheartaigh, J., Dean, D.C., Ginestet, C.E., Walker, L., Waskiewicz, N., Lehman, K., Dirks, H., Piryatinsky, I., Deoni, S.C.L., 2014. White matter development and early cognition in babies and toddlers. *Hum. Brain*

Mapp. 35, 4475–4487.

- Ota, M., Obata, T., Akine, Y., Ito, H., Ikehira, H., Asada, T., Suhara, T., 2006. Age-related degeneration of corpus callosum measured with diffusion tensor imaging. *Neuroimage* 31, 1445–1452.
- Pajevic, S., Basser, P.J., Fields, R.D., 2014. Role of myelin plasticity in oscillations and synchrony of neuronal activity. *Neuroscience* 276, 135–147.
- Pajevic, S., Pierpaoli, C., 2000. Color schemes to represent the orientation of anisotropic tissues from diffusion tensor data: application to white matter fiber tract mapping in the human brain. *Magn. Reson. Med.* 43, 921.
- Panagiotaki, E., Schneider, T., Siow, B., Hall, M.G., Lythgoe, M.F., Alexander, D.C., 2012. Compartment models of the diffusion MR signal in brain white matter: a taxonomy and comparison. *Neuroimage* 59, 2241–54.
- Park, H.J., Friston, K.J., 2013. Structural and functional brain networks: from connections to cognition. *Science* 342, 1238411.
- Patenaude, B., Smith, S.M., Kennedy, D.N., Jenkinson, M., 2011. A Bayesian model of shape and appearance for subcortical brain segmentation. *Neuroimage* 56, 907–922.
- Paul, G., Sreenivasan, S., Havlin, S., Eugene Stanley, H., 2006. Optimization of network robustness to random breakdowns. *Phys. A Stat. Mech. its Appl.* 370, 854–862.
- Perge, J.A., Koch, K., Miller, R., Sterling, P., Balasubramanian, V., 2009. How the Optic Nerve Allocates Space, Energy Capacity, and Information. *J. Neurosci.* 29, 7917–7928.
- Perge, J. a, Niven, J.E., Mugnaini, E., Balasubramanian, V., Sterling, P., 2012. Why do axons differ in caliber? *J. Neurosci.* 32, 626–38.
- Peters, A., 2002. The effects of normal aging on myelin and nerve fibers: A review. *J. Neurocytol.* 31, 581–593.
- Peters, A., 2009. The effects of normal aging on myelinated nerve fibers in monkey central nervous system. *Front. Neuroanat.* 3, 11.
- Peters, A., Sethares, C., 2003. Is there remyelination during aging of the primate central nervous system? *J. Comp. Neurol.* 460, 238–254.
- Peters, B.D., Ikuta, T., Derosse, P., John, M., Burdick, K.E., Gruner, P., Prendergast, D.M., Szeszko, P.R., Malhotra, A.K., 2014. Age-related differences in white matter tract microstructure are associated with cognitive performance from childhood to adulthood. *Biol. Psychiatry* 75, 248–256.
- Petersen, S.E., Sporns, O., 2015. Brain Networks and Cognitive Architectures. *Neuron* 88, 207–219.
- Pfefferbaum, A., Lim, K.O., Zipursky, R.B., Mathalon, D.H., Rosenbloom, M.J., Lane, B., Ha, C.N., Sullivan, E. V., 1992. Brain Gray and White Matter Volume Loss Accelerates with Aging in Chronic Alcoholics: A Quantitative MRI Study. *Alcohol. Clin. Exp. Res.* 16, 1078–1089.
- Pfefferbaum, A., Sullivan, E. V, Carmelli, D., 2001. Genetic regulation of regional microstructure of the corpus callosum in late life. *Neuroreport* 12, 1677–81.
- Pfefferbaum, A., Sullivan, E. V, Hedehus, M., Lim, K.O., Adalsteinsson, E., Moseley, M., 2000. Age-related decline in brain white matter anisotropy measured with spatially corrected echo-planar diffusion tensor imaging. *Magn. Reson. Med.* 44, 259–68.
- Picchioni, D., Duyn, J.H., Horovitz, S.G., 2013. Sleep and the functional connectome. *Neuroimage* 80, 387–96.
- Piccolomini, A., 1586. *Anatomicae Praelectiones, explicantes mirificam corporis humani fabricam.* Bonfadini.
- Pierpaoli, C., Basser, P.J., 1996. Toward a quantitative assessment of diffusion anisotropy. *Magn. Reson. Med.* 36, 893–906.
- Power, J.D., Cohen, A.L., Nelson, S.M., Wig, G.S., Barnes, K.A., Church, J.A., Vogel, A.C., Laumann, T.O., Miezin, F.M., Schlaggar, B.L., Petersen, S.E., 2011. Functional Network Organization of the Human Brain. *Neuron* 72, 665–678.
- Preibisch, C., Deichmann, R., 2009. Influence of RF spoiling on the stability and accuracy of T1 mapping based on spoiled FLASH with varying flip angles. *Magn. Reson. Med.* 61, 125–135.

- Preisig, M., Waeber, G., Vollenweider, P., Bovet, P., Rothen, S., Vandeleur, C., Guex, P., Middleton, L., Waterworth, D., Mooser, V., Tozzi, F., Muglia, P., 2009. The PsyCoLaus study: methodology and characteristics of the sample of a population-based survey on psychiatric disorders and their association with genetic and cardiovascular risk factors. *BMC Psychiatry* 9, 9.
- Raffelt, D., Tournier, J.-D., Rose, S., Ridgway, G.R., Henderson, R., Crozier, S., Salvado, O., Connelly, A., 2012. Apparent Fibre Density: a novel measure for the analysis of diffusion-weighted magnetic resonance images. *Neuroimage* 59, 3976–94.
- Raz, N., 2000. Aging of the brain and its impact on cognitive performance: integration of structural and functional findings BT - Handbook of Aging and Cognition, in: *The Handbook of Aging and Cognition*. Lawrence Erlbaum Associates, pp. 1–90.
- Redies, C., Puelles, L., 2001. Modularity in vertebrate brain development and evolution. *BioEssays* 23, 1100–1111.
- Reisberg, B., Franssen, E.H., Souren, L.E.M., Auer, S.R., Akram, I., Kenowsky, S., 2002. Evidence and mechanisms of retrogenesis in Alzheimer's and other dementias: management and treatment import. *Am. J. Alzheimers. Dis. Other Demen.* 17, 202–212.
- Rilling, J.K., 2014. Comparative primate neuroimaging: Insights into human brain evolution. *Trends Cogn. Sci.* 18, 46–55.
- Rilling, J.K., Glasser, M.F., Preuss, T.M., Ma, X., Zhao, T., Hu, X., Behrens, T.E.J., 2008. The evolution of the arcuate fasciculus revealed with comparative DTI. *Nat. Neurosci.* 11, 426–428.
- Rosvall, M., Bergstrom, C.T., 2008. Maps of random walks on complex networks reveal community structure. *Proc. Natl. Acad. Sci. U. S. A.* 105, 1118–23.
- Rubinov, M., Sporns, O., 2010. Complex network measures of brain connectivity: uses and interpretations. *Neuroimage* 52, 1059–69.
- Rubinov, M., Sporns, O., 2011. Weight-conserving characterization of complex functional brain networks. *Neuroimage* 56, 2068–2079.
- Rubinov, M., Sporns, O., Thivierge, J.-P., Breakspear, M., 2011. Neurobiologically Realistic Determinants of Self-Organized Criticality in Networks of Spiking Neurons. *PLoS Comput. Biol.* 7, e1002038.
- Rushton, W.A.H., 1951. A theory of the effects of fibre size in medullated nerve. *J. Physiol.* 115, 101–122.
- Saito, N., Sakai, O., Ozonoff, A., Jara, H., 2009. Relaxo-volumetric multispectral quantitative magnetic resonance imaging of the brain over the human lifespan: global and regional aging patterns. *Magn. Reson. Imaging* 27, 895–906.
- Sandell, J.H., Peters, A., 2002. Effects of age on the glial cells in the rhesus monkey optic nerve. *J. Comp. Neurol.* 445, 13–28.
- Sandell, J.H., Peters, a, 2001. Effects of age on nerve fibers in the rhesus monkey optic nerve. *J. Comp. Neurol.* 429, 541–553.
- Schmithorst, V.J., Wilke, M., Dardzinski, B.J., Holland, S.K., 2002. Correlation of White Matter Diffusivity and Anisotropy with Age during Childhood and Adolescence: A Cross-sectional Diffusion-Tensor MR Imaging Study. *Radiology* 222, 212–218.
- Schoenemann, P.T., Sheehan, M.J., Glotzer, L.D., 2005. Prefrontal white matter volume is disproportionately larger in humans than in other primates. *Nat. Neurosci.* 8, 242–52.
- Scholtens, L.H., Schmidt, R., de Reus, M.A., van den Heuvel, M.P., 2014. Linking macroscale graph analytical organization to microscale neuroarchitectonics in the macaque connectome. *J. Neurosci.* 34, 12192–205.
- Ségonne, F., Dale, A.M., Busa, E., Glessner, M., Salat, D., Hahn, H.K., Fischl, B., 2004. A hybrid approach to the skull stripping problem in MRI. *Neuroimage* 22, 1060–1075.
- Setsompop, K., Gagoski, B. a, Polimeni, J.R., Witzel, T., Wedeen, V.J., Wald, L.L., 2012. Blipped-controlled aliasing in parallel imaging for simultaneous multislice echo planar imaging with reduced g-factor penalty. *Magn. Reson. Med.* 67, 1210–24.

- Setsompop, K., Kimmlingen, R., Eberlein, E., Witzel, T., Cohen-Adad, J., McNab, J. a, Keil, B., Tisdall, M.D., Hoecht, P., Dietz, P., Cauley, S.F., Tountcheva, V., Matschl, V., Lenz, V.H., Heberlein, K., Potthast, a, Thein, H., Van Horn, J., Toga, a, Schmitt, F., Lehne, D., Rosen, B.R., Wedeen, V., Wald, L.L., 2013. Pushing the limits of in vivo diffusion MRI for the Human Connectome Project. *Neuroimage* 80, 220–33.
- Sexton, C.E., Walhovd, K., Storsve, A.B., Tamnes, C.K., Westlye, L.T., Johansen-Berg, H., Fjell, A.M., 2014. Accelerated Changes in White Matter Microstructure During Ageing: A Longitudinal Diffusion Tensor Imaging Study. *J. Neurosci.* 34, 15425–15436.
- Shafee, R., Buckner, R.L., Fischl, B., 2015. Gray matter myelination of 1555 human brains using partial volume corrected MRI images. *Neuroimage* 105, 473–485.
- Silver, J., Miller, J.H., 2004. Regeneration beyond the glial scar. *Nat. Rev. Neurosci.* 5, 146–156.
- Smith, R.E., Tournier, J.-D., Calamante, F., Connelly, A., 2012. Anatomically-constrained tractography: improved diffusion MRI streamlines tractography through effective use of anatomical information. *Neuroimage* 62, 1924–38.
- Smith, R.E., Tournier, J.-D., Calamante, F., Connelly, A., 2013. SIFT: Spherical-deconvolution informed filtering of tractograms. *Neuroimage* 67, 298–312.
- Smith, R.E., Tournier, J.-D., Calamante, F., Connelly, A., 2015a. The effects of SIFT on the reproducibility and biological accuracy of the structural connectome. *Neuroimage* 104, 253–65.
- Smith, R.E., Tournier, J.-D., Calamante, F., Connelly, A., 2015b. SIFT2: Enabling dense quantitative assessment of brain white matter connectivity using streamlines tractography. *Neuroimage*.
- Smith, S.M., 2002. Fast robust automated brain extraction. *Hum. Brain Mapp.* 17, 143–155.
- Smith, S.M., Nichols, T.E., Vidaurre, D., Winkler, A.M., J Behrens, T.E., Glasser, M.F., Ugurbil, K., Barch, D.M., Van Essen, D.C., Miller, K.L., 2015. A positive-negative mode of population covariation links brain connectivity, demographics and behavior. *Nat. Neurosci.* 18, 1–7.
- Sotiras, A., Toledo, J.B., Gur, R.E., Gur, R.C., Satterthwaite, T.D., Davatzikos, C., 2017. Patterns of coordinated cortical remodeling during adolescence and their associations with functional specialization and evolutionary expansion. *Proc. Natl. Acad. Sci.* 114, 3527–3532.
- Sotiropoulos, S.N., Jbabdi, S., Xu, J., Andersson, J.L., Moeller, S., Auerbach, E.J., Glasser, M.F., Hernandez, M., Sapiro, G., Jenkinson, M., Feinberg, D. a, Yacoub, E., Lenglet, C., Van Essen, D.C., Ugurbil, K., Behrens, T.E.J., 2013a. Advances in diffusion MRI acquisition and processing in the Human Connectome Project. *Neuroimage* 80, 125–43.
- Sotiropoulos, S.N., Moeller, S., Jbabdi, S., Xu, J., Andersson, J.L., Auerbach, E.J., Yacoub, E., Feinberg, D., Setsompop, K., Wald, L.L., Behrens, T.E.J., Ugurbil, K., Lenglet, C., 2013b. Effects of image reconstruction on fiber orientation mapping from multichannel diffusion MRI: reducing the noise floor using SENSE. *Magn. Reson. Med.* 70, 1682–9.
- Sowell ER, Peterson BS, Thompson PM, Welcome SE, Henkenius AL, Toga AW, 2003. Mapping cortical change across the human life span. *Nat. Neurosci.* 6, 309–315.
- Sporns, O., 2013. Network attributes for segregation and integration in the human brain. *Curr. Opin. Neurobiol.* 23, 162–171.
- Sporns, O., Betzel, R.F., 2015. Modular Brain Networks. *Annu. Rev. Psychol.* 67, annurev-psych-122414-033634.
- Sporns, O., Tononi, G., Kötter, R., 2005. The Human Connectome: A Structural Description of the Human Brain. *PLoS Comput. Biol.* 1, e42.
- Stanisz, G.J., Kecojevic, A., Bronskill, M.J., Henkelman, R.M., 1999. Characterizing white matter with magnetization transfer and T(2). *Magn. Reson. Med.* 42, 1128–36.
- Steno, N., 1669. Discours de Monsieur Steno, sur l’anatomie du cerveau à Messieurs de l’Assemblée, qui se fait chez Monsieur Theuenot. chez Robert de Ninuille.
- Stikov, N., Campbell, J.S.W., Stroh, T., Lavelée, M., Frey, S., Novek, J., Nuara, S., Ho, M.-K., Bedell, B.J., Dougherty, R.F., Leppert, I.R., Boudreau, M., Narayanan, S., Duval, T., Cohen-Adad, J., Picard, P., Gasecka, A., Côté, D., Bruce Pike, G., 2015. In vivo histology of the myelin g-ratio with magnetic resonance imaging. *Neuroimage*

118, doi: 10.1016/j.neuroimage.2015.05.023.

- Storsve, A.B., Fjell, A.M., Tamnes, C.K., Westlye, L.T., Overbye, K., Aasland, H.W., Walhovd, K.B., 2014. Differential longitudinal changes in cortical thickness, surface area and volume across the adult life span: regions of accelerating and decelerating change. *J. Neurosci.* 34, 8488–98.
- Stricker, N.H., Schweinsburg, B.C., Delano-Wood, L., Wierenga, C.E., Bangen, K.J., Haaland, K.Y., Frank, L.R., Salmon, D.P., Bondi, M.W., 2009. Decreased white matter integrity in late-myelinating fiber pathways in Alzheimer's disease supports retrogenesis. *Neuroimage* 45, 10–16.
- Stüber, C., Morawski, M., Schäfer, A., Labadie, C., Wähnert, M., Leuze, C., Streicher, M., Barapatre, N., Reimann, K., Geyer, S., Spemann, D., Turner, R., 2014. Myelin and iron concentration in the human brain: A quantitative study of MRI contrast. *Neuroimage* 93, 95–106.
- Sun, Y., Dai, Z., Li, J., Collinson, S.L., Sim, K., 2017. Modular-level alterations of structure-function coupling in schizophrenia connectome. *Hum. Brain Mapp.* 38, 2008–2025.
- Tamnes, C.K., Østby, Y., Fjell, A.M., Westlye, L.T., Due-Tønnessen, P., Walhovd, K.B., 2010. Brain Maturation in Adolescence and Young Adulthood: Regional Age-Related Changes in Cortical Thickness and White Matter Volume and Microstructure. *Cereb. Cortex* 20, 534–548.
- Tardif, C.L., Gauthier, C.J., Steele, C.J., Bazin, P.L., Schäfer, A., Schaefer, A., Turner, R., Villringer, A., 2016. Advanced MRI techniques to improve our understanding of experience-induced neuroplasticity. *Neuroimage* 131, 55–72.
- Teipel, S.J., Meindl, T., Wagner, M., Stieltjes, B., Reuter, S., Hauenstein, K.-H., Filippi, M., Ernemann, U., Reiser, M.F., Hampel, H., 2010. Longitudinal Changes in Fiber Tract Integrity in Healthy Aging and Mild Cognitive Impairment: A DTI Follow-Up Study. *J. Alzheimer's Dis.* 22, 507–522.
- Thiebaut de Schotten, M., Dell'Acqua, F., Forkel, S.J., Simmons, A., Vergani, F., Murphy, D.G.M., Catani, M., 2011. A lateralized brain network for visuospatial attention. *Nat. Neurosci.* 14, 1245–6.
- Thomsen, C., Henriksen, O., Ring, P., 1987. In vivo measurement of water self diffusion in the human brain by magnetic resonance imaging. *Acta Radiol* 28, 353–361.
- Tigges, J., Gordon, T.P., McClure, H.M., Hall, E.C., Peters, A., 1988. Survival rate and life span of rhesus monkeys at the Yerkes regional primate research center. *Am. J. Primatol.* 15, 263–273.
- Tofts, P., 2004. *Quantitative MRI of the Brain: Measuring Changes Caused by Disease*. Wiley.
- Tournier, J.-D., 2010. The Biophysics of Crossing Fibers, in: Jones, D.K. (Ed.), *Diffusion MRI: Theory, Methods, and Applications*. Oxford, pp. 465–481.
- Tournier, J.-D., Calamante, F., Connelly, A., 2007. Robust determination of the fibre orientation distribution in diffusion MRI: non-negativity constrained super-resolved spherical deconvolution. *Neuroimage* 35, 1459–72.
- Tournier, J.-D., Calamante, F., Connelly, A., 2010. Improved probabilistic streamlines tractography by 2nd order integration over fibre orientation distributions, in: *Proceedings of the International Society for Magnetic Resonance in Medicine*. p. 1670.
- Tournier, J.-D., Calamante, F., Connelly, A., 2012. MRtrix: Diffusion tractography in crossing fiber regions. *Int. J. Imaging Syst. Technol.* 22, 53–66.
- Tournier, J.-D., Calamante, F., Gadian, D.G., Connelly, A., 2004. Direct estimation of the fiber orientation density function from diffusion-weighted MRI data using spherical deconvolution. *Neuroimage* 23, 1176–85.
- Towson, E.K., Vertes, P.E., Ahnert, S.E., Schafer, W.R., Bullmore, E.T., 2013. The Rich Club of the *C. elegans* Neuronal Connectome. *J. Neurosci.* 33, 6380–6387.
- Traag, V.A., Krings, G., Van Dooren, P., 2013. Significant Scales in Community Structure. *Sci. Rep.* 3, 2930.
- Vaishnavi, S.N., Vlassenko, A.G., Rundle, M.M., Snyder, A.Z., Mintun, M.A., Raichle, M.E., 2010. Regional aerobic glycolysis in the human brain. *Proc. Natl. Acad. Sci.* 107, 17757–17762.
- van den Heuvel, M.P., Kahn, R.S., Goni, J., Sporns, O., 2012. High-cost, high-capacity backbone for global brain communication. *Proc. Natl. Acad. Sci.* 109, 11372–11377.

- van den Heuvel, M.P., Scholtens, L.H., Feldman Barrett, L., Hilgetag, C.C., de Reus, M.A., 2015. Bridging Cytoarchitectonics and Connectomics in Human Cerebral Cortex. *J. Neurosci.* 35, 13943–13948.
- van den Heuvel, M.P., Sporns, O., 2011. Rich-Club Organization of the Human Connectome. *J. Neurosci.* 31, 15775–15786.
- van den Heuvel, M.P., Sporns, O., 2013. Network hubs in the human brain. *Trends Cogn. Sci.* 17, 683–696.
- van den Heuvel, M.P., Sporns, O., Collin, G., Scheewe, T., Mandl, R.C.W., Cahn, W., Goñi, J., Hulshoff Pol, H.E., Kahn, R.S., 2013. Abnormal Rich Club Organization and Functional Brain Dynamics in Schizophrenia. *JAMA Psychiatry* 70, 783.
- van den Heuvel, M.P., Yeo, B.T.T., 2017. A Spotlight on Bridging Microscale and Macroscale Human Brain Architecture. *Neuron* 93, 1248–1251.
- van Leeuwenhoek, A., 1719. *Epistola XXXII. Epistolae Physiologicae Super Compluribus Naturae Arcanis.*
- Vesalius, A., 1543. *De Humani Corporis Fabrica.* Johann Oporinus, Basel.
- von Bechterew, W., 1900. *Les voies de conduction du cerveau et de la moelle.* Storck and Doin.
- Vos, S.B., Jones, D.K., Viergever, M. a, Leemans, A., 2011. Partial volume effect as a hidden covariate in DTI analyses. *Neuroimage* 55, 1566–76.
- Voyvodic, J.T., 1989. Target size regulates calibre and myelination of sympathetic axons. *Nature* 342, 430–3.
- Walhovd, K.B., Fjell, A.M., Giedd, J., Dale, A.M., Brown, T.T., 2016. Through Thick and Thin: a Need to Reconcile Contradictory Results on Trajectories in Human Cortical Development. *Cereb. Cortex* 1989, bhv301.
- Walhovd, K.B., Johansen-Berg, H., Káradóttir, R.T., 2014. Unraveling the secrets of white matter – Bridging the gap between cellular, animal and human imaging studies. *Neuroscience* 276, 2–13.
- Walhovd, K.B., Westlye, L.T., Amlien, I., Espeseth, T., Reinvang, I., Raz, N., Agartz, I., Salat, D.H., Greve, D.N., Fischl, B., Dale, A.M., Fjell, A.M., 2011. Consistent neuroanatomical age-related volume differences across multiple samples. *Neurobiol. Aging* 32, 916–932.
- Wandell, B.A., Yeatman, J.D., 2013. Biological development of reading circuits. *Curr. Opin. Neurobiol.* 23, 261–268.
- Waxman, S.G., 1975. Integrative properties and design principles of axons. *Int. Rev. Neurobiol.* 18, 1–40.
- Wedeen, V.J., Hagmann, P., Tseng, W.-Y.I., Reese, T.G., Weisskoff, R.M., 2005. Mapping complex tissue architecture with diffusion spectrum magnetic resonance imaging. *Magn. Reson. Med.* 54, 1377–86.
- Wedeen, V.J., Rosene, D.L., Wang, R., Dai, G., Mortazavi, F., Hagmann, P., Kaas, J.H., Tseng, W.-Y.I., 2012. The geometric structure of the brain fiber pathways. *Science* 335, 1628–34.
- Weiskopf, N., Callaghan, M.F., Josephs, O., Lutti, A., Mohammadi, S., 2014. Estimating the apparent transverse relaxation time ($R2^*$) from images with different contrasts (ESTATICS) reduces motion artifacts. *Front. Neurosci.* 8, 278.
- Weiskopf, N., Suckling, J., Williams, G., Correia, M.M., Inkster, B., Tait, R., Ooi, C., Bullmore, E.T., Lutti, A., Correia M., M.M., Inkster, B., Tait, R., Ooi, C., Bullmore T., E.T., Lutti, A., 2013a. Quantitative multi-parameter mapping of $R1$, PD^* , MT , and $R2^*$ at 3T: a multi-center validation. *Front. Neurosci.* 7, 95.
- Weiskopf, N., Suckling, J., Williams, G., Correia M., M.M., Inkster, B., Tait, R., Ooi, C., Bullmore T., E.T., Lutti, A., 2013b. Quantitative multi-parameter mapping of $R1$, PD^* , MT , and $R2^*$ at 3T: A multi-center validation. *Front. Neurosci.* 7, 95.
- Wesbey, G.E., Moseley, M.E., Ehman, R.L., 1984. Translational molecular self-diffusion in magnetic resonance imaging: II. Measurement of the self-diffusion coefficient. *Invest. Radiol.* 19, 491–498.
- Westlye, L.T., Walhovd, K.B., Dale, A.M., Bjørnerud, A., Due-Tønnessen, P., Engvig, A., Grydeland, H., Tamnes, C.K., Østby, Y., Fjell, A.M., 2010a. Differentiating maturational and aging-related changes of the cerebral cortex by use of thickness and signal intensity. *Neuroimage* 52, 172–185.
- Westlye, L.T., Walhovd, K.B., Dale, A.M., Bjørnerud, A., Due-Tønnessen, P., Engvig, A., Grydeland, H., Tamnes, C.K., Østby, Y., Fjell, A.M., 2010b. Life-Span Changes of the Human Brain White Matter: Diffusion Tensor

- Imaging (DTI) and Volumetry. *Cereb. Cortex* 20, 2055–2068.
- White, J.G., Southgate, E., Thomson, J.N., Brenner, S., 1986. The structure of the nervous system of the nematode *Caenorhabditis elegans*. *Philos. Trans. R. Soc. Lond. B. Biol. Sci.* 314, 1–340.
- Xia, M., Wang, J., He, Y., 2013. BrainNet Viewer: A Network Visualization Tool for Human Brain Connectomics. *PLoS One* 8.
- Yakovlev, P.I., Lecours, A.-R., 1967. The myelogenetic cycles of regional maturation of the brain., in: *Regional Development of Brain in Early Life*. pp. 3–70.
- Yeatman, J.D., Dougherty, R.F., Ben-Shachar, M., Wandell, B.A., 2012a. Development of white matter and reading skills. *Proc. Natl. Acad. Sci. U. S. A.* 109, E3045-53.
- Yeatman, J.D., Dougherty, R.F., Myall, N.J., Wandell, B.A., Feldman, H.M., 2012b. Tract Profiles of White Matter Properties: Automating Fiber-Tract Quantification. *PLoS One* 7.
- Yeatman, J.D., Wandell, B.A., Mezer, A.A., 2014. Lifespan maturation and degeneration of human brain white matter. *Nat. Commun.* 5, 4932.
- Yeh, C.H., Smith, R.E., Liang, X., Calamante, F., Connelly, A., 2016. Correction for diffusion MRI fibre tracking biases: The consequences for structural connectomic metrics. *Neuroimage* 142, 150–162.
- Yeo, B.T.T., Krienen, F.M., Sepulcre, J., Sabuncu, M.R., Lashkari, D., Hollinshead, M., Roffman, J.L., Smoller, J.W., Zolke, L., Polimeni, J.R., Fischl, B., Liu, H., Buckner, R.L., 2011. The organization of the human cerebral cortex estimated by intrinsic functional connectivity. *J. Neurophysiol.* 106, 1125–1165.
- Zalesky, A., Fornito, A., Cocchi, L., Gollo, L.L., van den Heuvel, M.P., Breakspear, M., 2016. Connectome sensitivity or specificity: which is more important? *Neuroimage* 142, 407–420.
- Zhang, H., Schneider, T., Wheeler-Kingshott, C. a, Alexander, D.C., 2012. NODDI: practical in vivo neurite orientation dispersion and density imaging of the human brain. *Neuroimage* 61, 1000–16.
- Zhang, Y., Brady, M., Smith, S., 2001. Segmentation of brain MR images through a hidden Markov random field model and the expectation-maximization algorithm. *IEEE Trans. Med. Imaging* 20, 45–57.
- Zhao, T., Cao, M., Niu, H., Zuo, X.N., Evans, A., He, Y., Dong, Q., Shu, N., 2015. Age-related changes in the topological organization of the white matter structural connectome across the human lifespan. *Hum. Brain Mapp.* 36, 3777–3792.
- Zuo, X.-N., He, Y., Betzel, R.F., Colcombe, S., Sporns, O., Milham, M.P., 2016. Human Connectomics across the Life Span. *Trends Cogn. Sci.* xx, 1–14.

Supplementary materials

Supplementary methods

3. Lifespan brain tissue changes reveal a modular architecture of human white matter

Model 1 was a linear model described by the equation:

$$Y = \beta_1 \times Age + \beta_2$$

where Y is the vector of microstructure measurements across subjects and each β_i is a weight estimated using linear least squares (LLS) regression.

Model 2 was a second order polynomial described by the equation:

$$Y = \beta_1 \times Age^2 + \beta_2 \times Age + \beta_3$$

The β_i weights were estimated using linear least squares (LLS) regression.

Model 3 was a Poisson curve which can model asymmetric growth and decline. The model has previously been used to fit diffusivity aging trajectories (Lebel et al., 2012; Yeatman et al., 2014) and is described by the equation:

$$Y = \beta_1 \times Age \times e^{-\beta_2 \times Age} + \beta_3$$

where the β_i parameters were estimated using nonlinear optimization to fit the model (Levenberg–Marquardt algorithm implemented in the MATLAB Optimization Toolbox).

Model 4 was a smoothing-spline model implemented in Matlab. The smoothing spline, s , minimizes:

$$\sum_i (y_i - s(Age_i))^2 + (1-p) \int \left(\frac{d^2 s}{dAge^2} \right)^2 dAge$$

where the smoothing parameter p controls the trade-off between fidelity (closeness of $s(Age_i)$ to y_i) and smoothness (the size of the average second derivative $\left| \frac{d^2 s}{dAge^2} \right|$). With no smoothing ($p = 1$), $s(Age_i)$ follows a cubic spline interpolant, whereas infinite smoothing

($p = 0$) results in the least-square straight line fit. The nonparametric smoothing spline model can assume any shape and thus imposes very few assumptions about the form of the lifespan trajectories as well as being more robust when modeling a reduced age range across the lifespan (Fjell et al., 2010). The smoothing spline parameter, p , was optimized for each microstructure measure by performing repeated 5-Fold cross-validation on 20 values of p logarithmically spaced between 10^{-7} and 10^{-1} . The value which minimized cross-validated error across the network was used to fit the aging trajectories of the respective microstructure measure.

The three parameters used to summarize key lifespan features (peak age, Age_{Peak} ; peak value, Y_{Peak} ; and lifespan change, ΔY) are defined as follows:

$$Age_{Peak} = Age\left(\frac{dY}{dAge} = 0\right)$$

$$Y_{Peak} = Y(Age_{Peak})$$

$$\Delta Y = \int_{Age_{10}}^{Age_{Peak}} \frac{dY}{dAge} dAge - \int_{Age_{Peak}}^{Age_{75}} \frac{dY}{dAge} dAge$$

$$\Delta Y = 2Y(Age_{Peak}) - Y(Age_{10}) - Y(Age_{75})$$

In the case of the smoothing spline model there may be cases in which multiple local minima/maxima and/or extended plateaus of development occur due to the increased model flexibility. As such we defined Age_{Peak} for measures best fit by the smoothing spline model as follows:

$$Age_{Peak} = \arg \min \left[Age \left(\frac{dY}{dAge} < 0.05 * \sigma_{\frac{dY}{dAge}} \right) \right]$$

where $\sigma_{\frac{dY}{dAge}}$ is the standard deviation of the tissue measure derivative with respect to age.

This definition provides highly consistent MT and R1 lifespan parameter estimates when compared to a second order polynomial model for peak age ($R^2=0.999$), peak value ($R^2=1.00$), and lifespan change ($R^2=0.997$).

4. Hierarchical modularity and microstructural enrichment of the brain's integrative architectures

Topological measure definitions

All topological graph measures were calculated with the BCT Matlab package (brain-connectivity-toolbox.net; Rubinov and Sporns, 2010). In the following definitions N is the set of all nodes in the network and n is the total number of nodes. (i, j) represents an edge linking nodes i and j ($i, j \in N$). a_{ij} is the connection status between the i th and j th nodes; $a_{ij} = 1$ if the (i, j) edge is present and $a_{ij} = 0$ otherwise. The (i, j) edge is associated with a connection weight w_{ij} .

Degree and strength

Degree of node i ,

$$k_i = \sum_{j \in N} a_{ij}$$

The weighted degree (strength) of node i ,

$$k_i^W = \sum_{j \in N} w_{ij}$$

Shortest path length

Shortest path length (distance) between nodes i and j ,

$$d_{ij} = \sum_{a_{uv} \in g_{i \leftrightarrow j}} a_{uv}$$

Where $g_{i \leftrightarrow j}$ is the shortest geodesic path connecting nodes i and j .

Global efficiency

Global efficiency of the network,

$$E = \frac{1}{n} \sum_{i \in N} E_i = \frac{1}{n} \sum_{i \in N} \frac{\sum_{j \in N, j \neq i} d_{ij}^{-1}}{n-1}$$

where E_i is the efficiency of node i .

Clustering coefficient

Clustering coefficient of the network,

$$C = \frac{1}{n} \sum_{i \in N} C_i = \frac{1}{n} \sum_{i \in N} \frac{\sum_{j, h \in N} a_{ij} a_{ih} a_{jh}}{k_i(k_i - 1)}$$

where C_i is the clustering coefficient of the i th node.

Within-module degree z-score

Given the partition of the network into a set of modules, M , the within-module degree z-score of node i is,

$$Z_i = \frac{k_i(m_i) - \bar{k}(m_i)}{\sigma^{k(m_i)}}$$

where m_i is the module containing node i , $k_i(m_i)$ is the within-module degree of node i (the number of connecting edges between node i and all other nodes in module m_i), $\bar{k}(m_i)$ and $\sigma^{k(m_i)}$ are respectively the mean and standard deviation of the within-module m_i degree distribution.

Participation coefficient

The weighted participation coefficient of node i ,

$$P_i^W = 1 - \sum_{m \in M} \left(\frac{k_i^W(m)}{k_i^W} \right)^2$$

where M is the set of modules and $k_i^W(m)$ is the weighted number of connections (connection strength) from the i th node to other nodes within the module.

Rich club assessment

Anatomical rich club organization was investigated following previously described methods (Alstott et al., 2014; Collin et al., 2014; van den Heuvel and Sporns, 2011). Binarized connectivity matrices were used to calculate the degree of each node by summing across columns. At each level of degree, k , the rich club coefficient, ϕ , was calculated by selecting the subgraph of nodes with degree $>k$ and summing the number of connections, E , within the

subgraph. At each k level the rich club coefficient was compared to an equivalent k level distribution obtained from a set of null model random graphs. Null model graphs were obtained by randomly rewiring each connection (5 times on average) while preserving the original degree sequence (Rubinov and Sporns, 2011). The normalized topological rich club coefficient, ϕ_{norm} , was then computed as (Alstott et al., 2014):

$$\phi_{norm}(k) = \frac{\phi(k)}{\phi_{rand}(k)} = \frac{E(k)}{E_{rand}(k)}$$

where ϕ_{rand} is the random graph rich club coefficient and E_{rand} the number of connections present in the random network's subgraph with richness level $>k$. This simplified definition of the normalized topological rich club coefficient arises from selection of an appropriate null model that preserves the original degree distributions (Alstott et al., 2014).

For each subject, ϕ_{norm} was estimated across 1000 random graphs and averaged to provide a mean estimate for the normalized rich club coefficient for richness levels $k>6$ to $k>152$. Rich club organization is said to be present within a graph when $\phi_{norm} > 1$ is observed over a range of k (Colizza et al., 2006). To test for the significance of topological rich club organization over the group of subjects, a 1-sample t -test was performed at each level of k to test whether $\phi_{norm} > 1$ and $p<0.05$ (Bonferroni corrected) was taken as supportive evidence for statistical significance.

Once the presence of a topological rich club had been established, nodes were ordered by the highest rich club level they participated in. Two rich club levels were defined following previous methods (Harriger et al., 2012): level 1 at $k>104$ and level 2 at $k>90$. These two levels both fall within the high rich club regime where the most heavily connected regions of level 1 also form a subset of the level 2 nodes.

Rich club edge classes and microstructure

Network edges were assigned into one of three edge classes based on their connectivity to rich club and non-rich club nodes (Supplementary Figure 4a; van den Heuvel et al., 2012): i) rich club connections were defined as linking rich club nodes; ii) feeder connections linking rich club and non-rich club nodes; and iii) local connections linking non-rich club nodes. Average microstructure measurements across the three rich club edge classes were compared

following the same procedure described for the modular edge classes (see the *Quantification of white matter tissue properties* and *Structural properties across modular node classes and connections* methods sections).

Supplementary results

4. Hierarchical modularity and microstructural enrichment of the brain's integrative architectures

Rich club organization

Topological rich club organization was found to be present, as indicated by an above chance level of interconnectivity between high degree nodes, confirming a number of previous reports (Supplementary Figure 4b; Collin et al., 2014; van den Heuvel et al., 2012; van den Heuvel and Sporns, 2011). The normalized rich club coefficient, ϕ_{norm} , was significantly greater than 1 over a wide range of k values ($p < 0.05$, Bonferroni corrected). The brain's anatomical rich club at level 1 ($k > 104$) comprises a set of highly interconnected hub regions spread across precuneus, superior frontal, middle frontal, pars opercularis, inferior parietal, posterior cingulate and insular cortices (Supplementary Figure 4c). A list of all Level 1 rich club nodes is provided in Supplementary Table 1. The connections linking rich club nodes - the rich club edges - form a bihemispheric core network (Supplementary Figure 4d) which are linked to more peripheral parts of the network by feeder (Supplementary Figure 4e) and local (Supplementary Figure 4e) connections.

Microstructural organization of the topological rich club

Wiring cost economy: streamline density and length

On average there was an increased number of streamlines in rich club connections versus feeder connections ($p < 0.05$). Rich club connections were longer than feeder ($p < 0.05$) and local ($p < 0.001$) connections. Feeder connections were also found to be longer than local connections ($p < 0.001$). Rich club connections were significantly more costly to the network architecture than feeder ($p < 0.01$) and local ($p < 0.01$) connections. These results are in agreement with previous assessments of rich club network costs (Collin et al., 2014; van den Heuvel et al., 2012).

Myelination and iron content: MT, R1 & R2*

Rich club connections had significantly higher values for MT and R1 (indicative of myelin content) on average than local connections ($p < 0.05$ | $p < 0.05$). Feeder connections also had significantly higher MT and R1 than local connections ($p < 0.001$ | $p < 0.001$). No effect was found for differences in R2* between rich club edge classes.

Diffusion tensor imaging (DTI)

Local connections were found to have lower FA than rich club ($p < 0.01$) and feeder ($p < 0.001$) connections. Average MD across local edges was significantly lower than across feeder connections ($p < 0.05$). RD showed the opposite effect to FA with higher average values for RD in local connections as compared to rich club ($p < 0.001$) and feeder ($p < 0.001$) connections. Marginally higher values for AD were found for rich club connections as compared to feeder and local connections but these did not pass the significance threshold ($p = 0.056$ | $p = 0.057$).

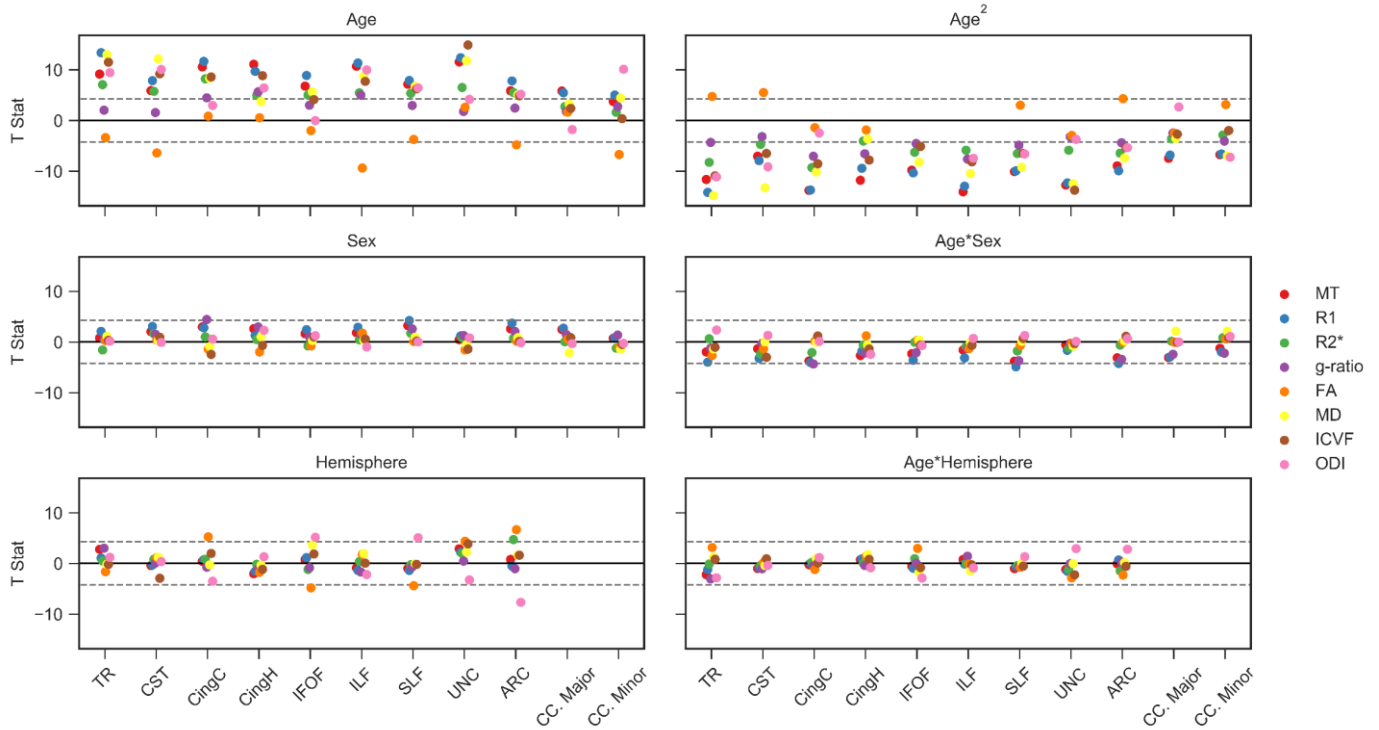
NODDI and q-ratio imaging

The average ICVF across local edges was found to be significantly lower than that observed across rich club ($p < 0.001$) and local ($p < 0.001$) connections. In contrast, the average value for ODI across local edges was greater than that observed in rich club ($p < 0.01$) and feeder ($p < 0.001$) connections. No effect was observed for differences in average g-ratio values across the rich club edge classes which contrasts with a recent report of g-ratio differences along rich club edges (Mancini et al., 2017).

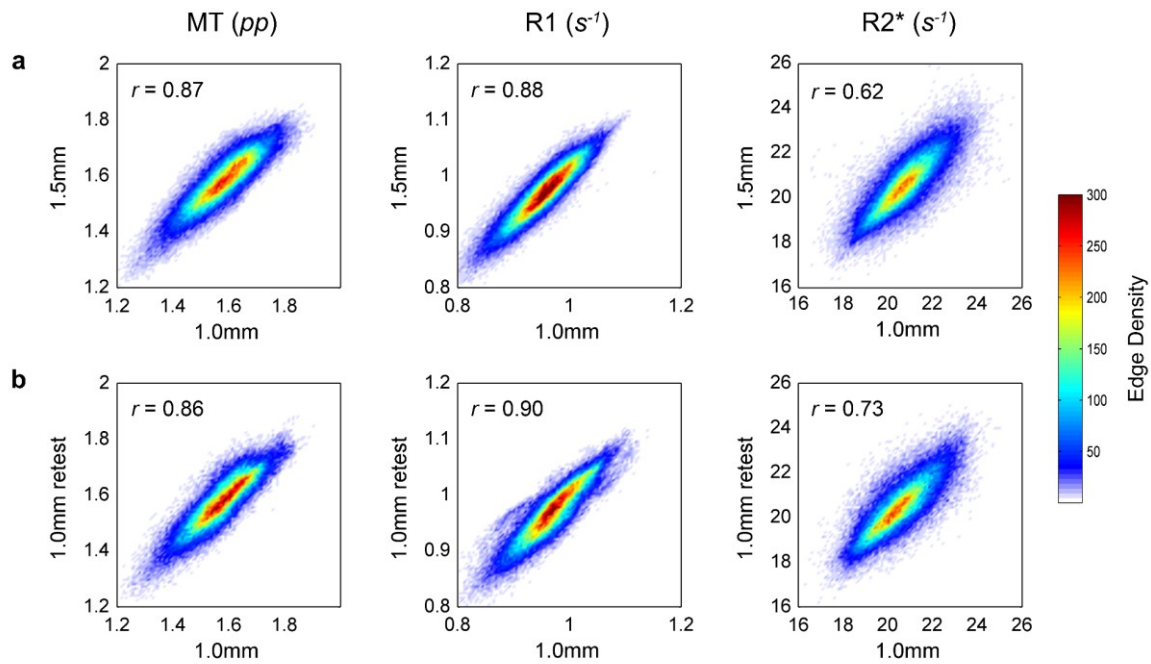
Grey matter microstructural covariance

No effects were found between edge classes for the nodal microstructure covariance measures of MT, R1 or MD. R2* covariance was significantly higher on average in rich club connections than in feeder ($p < 0.05$) and local ($p < 0.01$) connections. Feeder connections had higher R2* covariance than local connections ($p < 0.05$). Structural covariance as measured by cortical thickness was higher on average across local rather than feeder connections ($p < 0.001$).

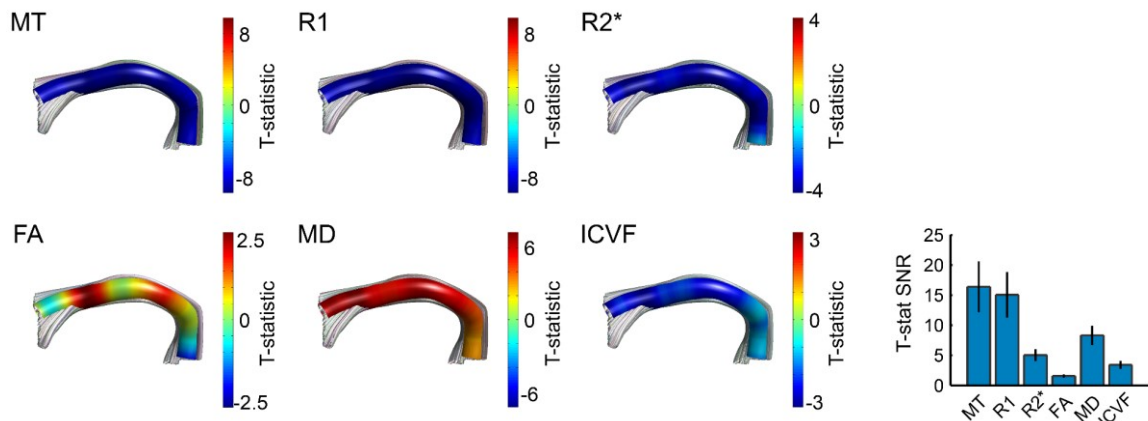
Supplementary figures



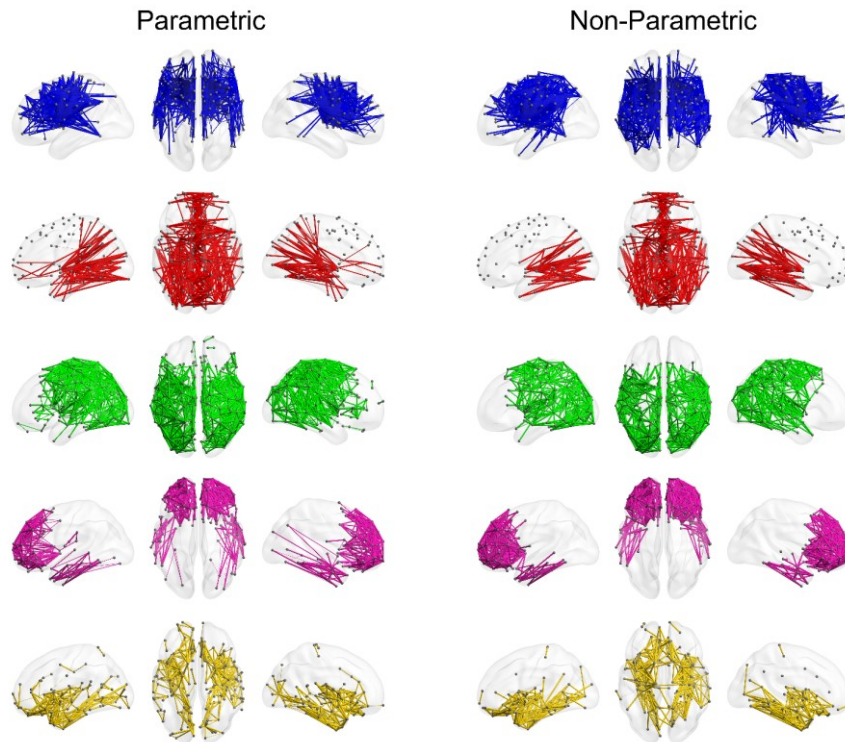
Supplementary Figure 2.1. Tissue measurement associations with age, sex and hemisphere in all subjects imaged at the higher resolution ($n = 718$). GLMs were used to estimate T-statistics for MT, R1, R2*, g-ratio, FA, MD, ICVF and ODI with age, sex, hemisphere and their interactions with age. Associations were highly consistent to models results when including the additional low-resolution subjects (see Fig. 7). Male and left hemisphere coded as 0. The valance of the g-ratio and MD associations have been reflected for visualization purposes across each of the panels. Horizontal dashed grey lines display the FEW-corrected significance level at $p \leq 0.001$.



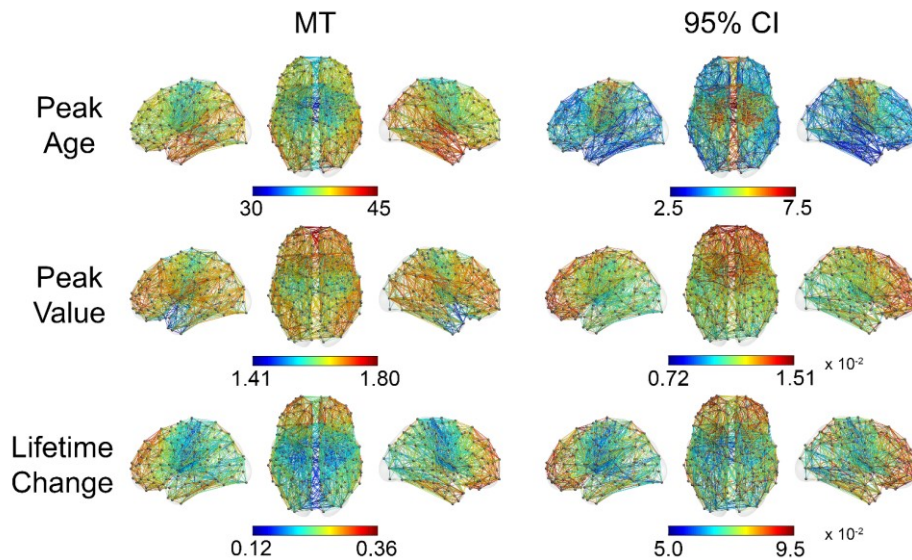
Supplementary Figure 3.1. MT, R1 and R2* microstructure measurements are reliable across 1 mm³ and 1.5 mm³ protocols. MT, R1 and R2* values sampled across 3,015 network edges for 38 individuals evaluate (a) measurement reliability across 1 mm³ and 1.5 mm³ image resolutions, and (b) test-retest reproducibility of the 1 mm³ datasets. Edge microstructure measures are consistent for both imaging resolutions with a comparable consistency to test-retest measurements made at 1 mm³.



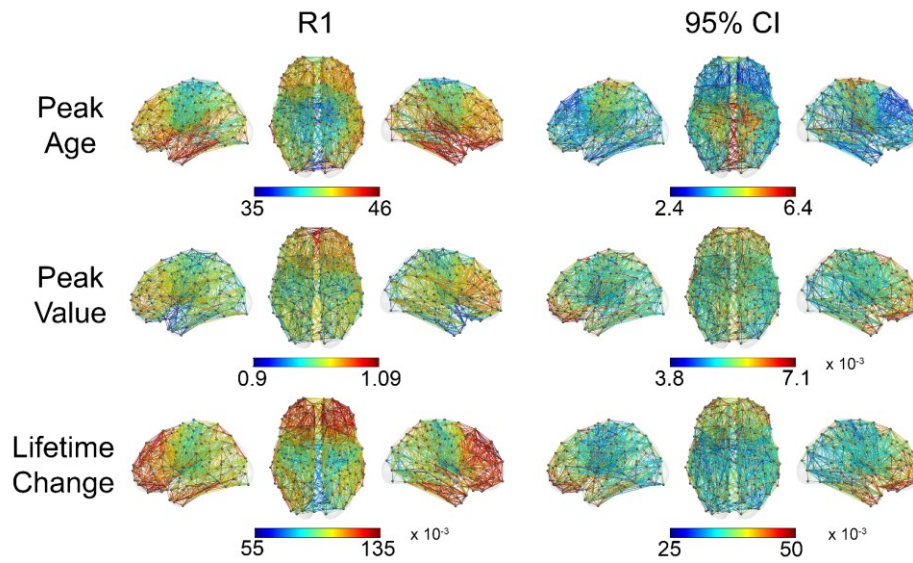
Supplementary Figure 3.2. Aging rates are consistent along a fascicle for MT, R1, R2*, MD and ICVF but not for FA. The linear effects of age were tested along 12 major white matter pathways (left/right thalamic radiation, left/right cingulum, left/right inferior longitudinal fasciculus, left/right superior longitudinal fasciculus, left/right uncinate and left/right arcuate) for all subjects over 45 yrs of age. The t-statistic is plotted for each MRI measure along the left arcuate fasciculus as a representative example. Strong and consistent aging effects are observed along the length of the arcuate for all measures except FA. This is reflected in the bar plot of the mean t-stat of a fascicle divided the t-stat standard deviation along its length – the t-stat SNR. Error bars represent the standard error of this measure across the 12 fascicles.



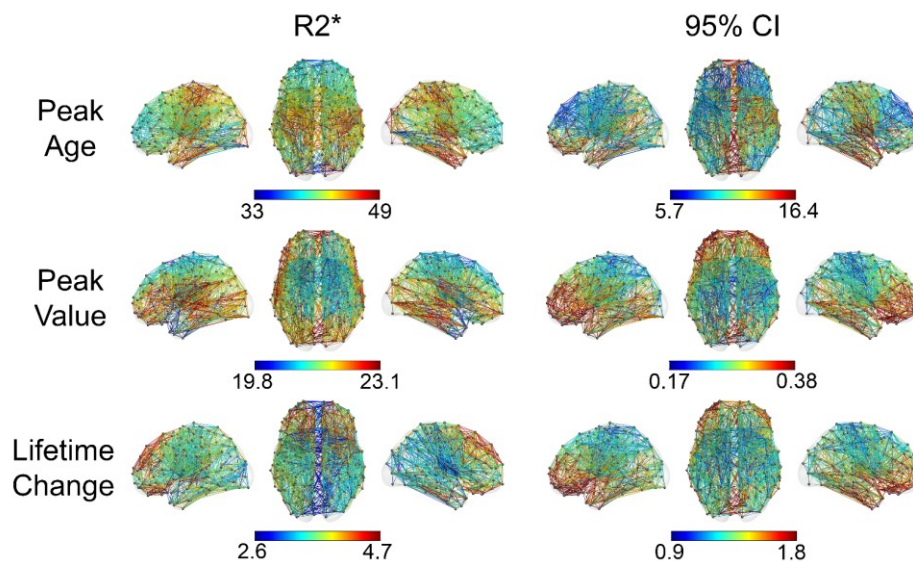
Supplementary Figure 3.3. Consistent clustering results using parametric and non-parametric models. Linear mixed effects (LME) clustering was performed to assess the consistency of results when using a non-parametric description of lifespan trajectories. Highly consistent clustering results emerge as compared to the parametric approach employed in this study. Summarizing lifespan trajectories as 15 lifespan measures (3 lifespan parameters x 5 MRI biomarkers) thus captures the key white matter aging features while also improving interpretability.



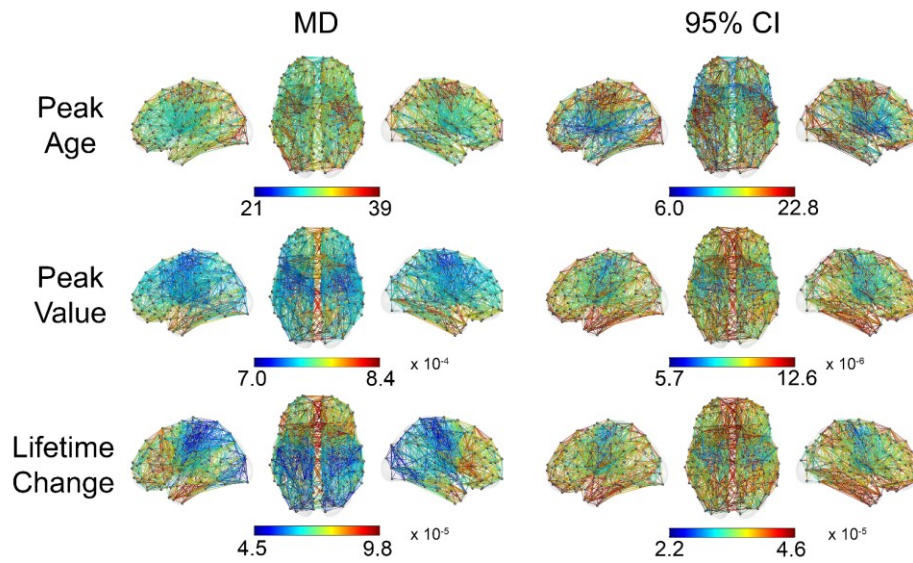
Supplementary Figure 3.4.1. MT lifespan measures and confidence intervals (CIs). Lifespan measures for the age of peak maturity (Peak Age), the tissue value at peak maturity (Peak Value) and the cumulative tissue change from age 10 to age 75 (Lifetime Change) are shown for each of the 3015 network edges connecting 349 cortical and sub-cortical nodes. 95% CIs were estimated from model bootstrapping. Peak Age values are in years; Peak Value and Lifetime Change measures are expressed in percentage points.



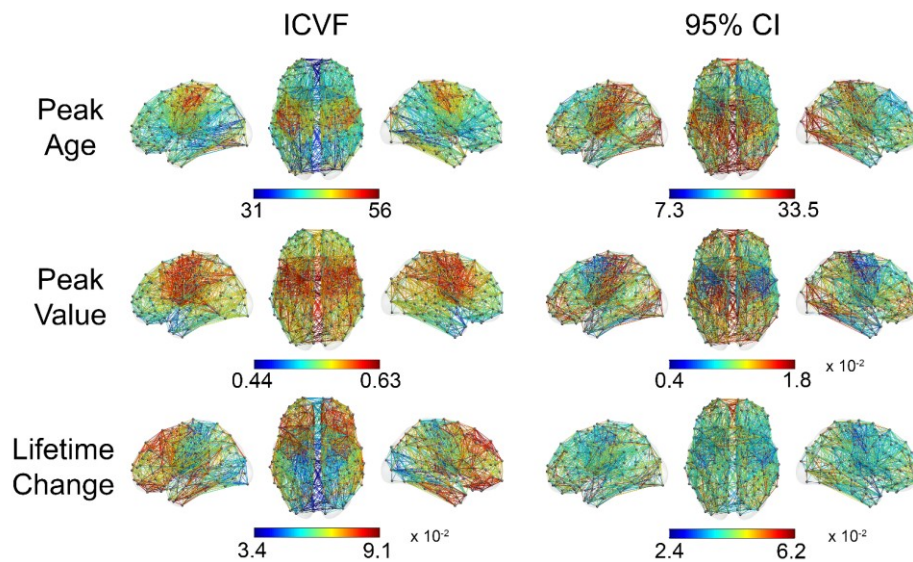
Supplementary Figure 3.4.2. R1 lifespan measures and confidence intervals (CIs). Lifespan measures for the age of peak maturity (Peak Age), the tissue value at peak maturity (Peak Value) and the cumulative tissue change from age 10 to age 75 (Lifetime Change) are shown for each of the 3015 network edges connecting 349 cortical and sub-cortical nodes. 95% CIs were estimated from model bootstrapping. Peak Age values are in years; Peak Value and Lifetime Change measures are expressed in units of s^{-1} .



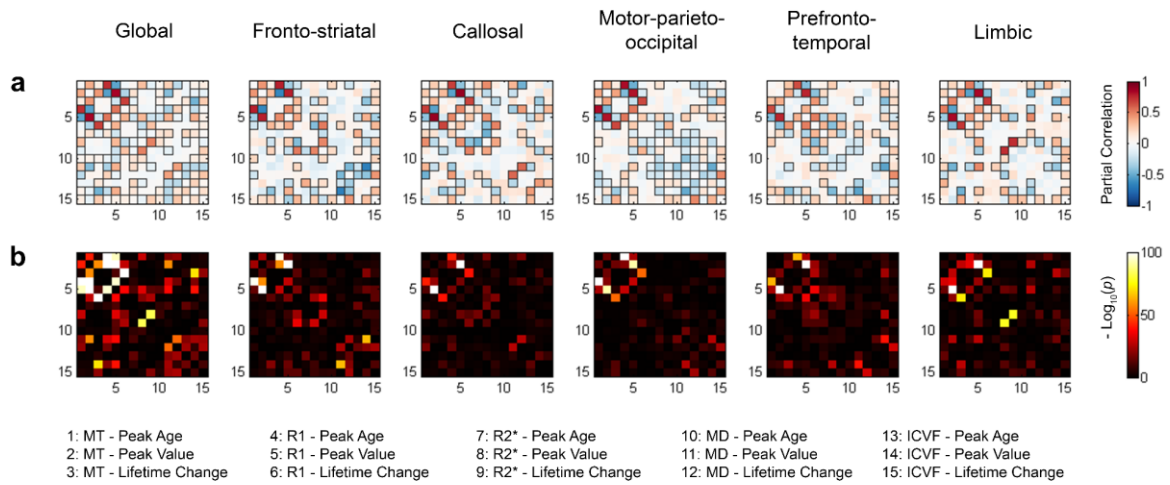
Supplementary Figure 3.4.3. R2* lifespan measures and confidence intervals (CIs). Lifespan measures for the age of peak maturity (Peak Age), the tissue value at peak maturity (Peak Value) and the cumulative tissue change from age 10 to age 75 (Lifetime Change) are shown for each of the 3015 network edges connecting 349 cortical and sub-cortical nodes. 95% CIs were estimated from model bootstrapping. Peak Age values are in years; Peak Value and Lifetime Change measures are expressed in units of s^{-1} .



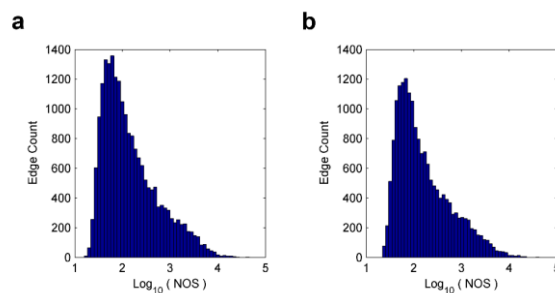
Supplementary Figure 3.4.4. MD lifespan measures and confidence intervals (CIs). Lifespan measures for the age of peak maturity (Peak Age), the tissue value at peak maturity (Peak Value) and the cumulative tissue change from age 10 to age 75 (Lifetime Change) are shown for each of the 3015 network edges connecting 349 cortical and sub-cortical nodes. 95% CIs were estimated from model bootstrapping. Peak Age values are in years; Peak Value and Lifetime Change measures are expressed in units of mm^2s^{-1} .



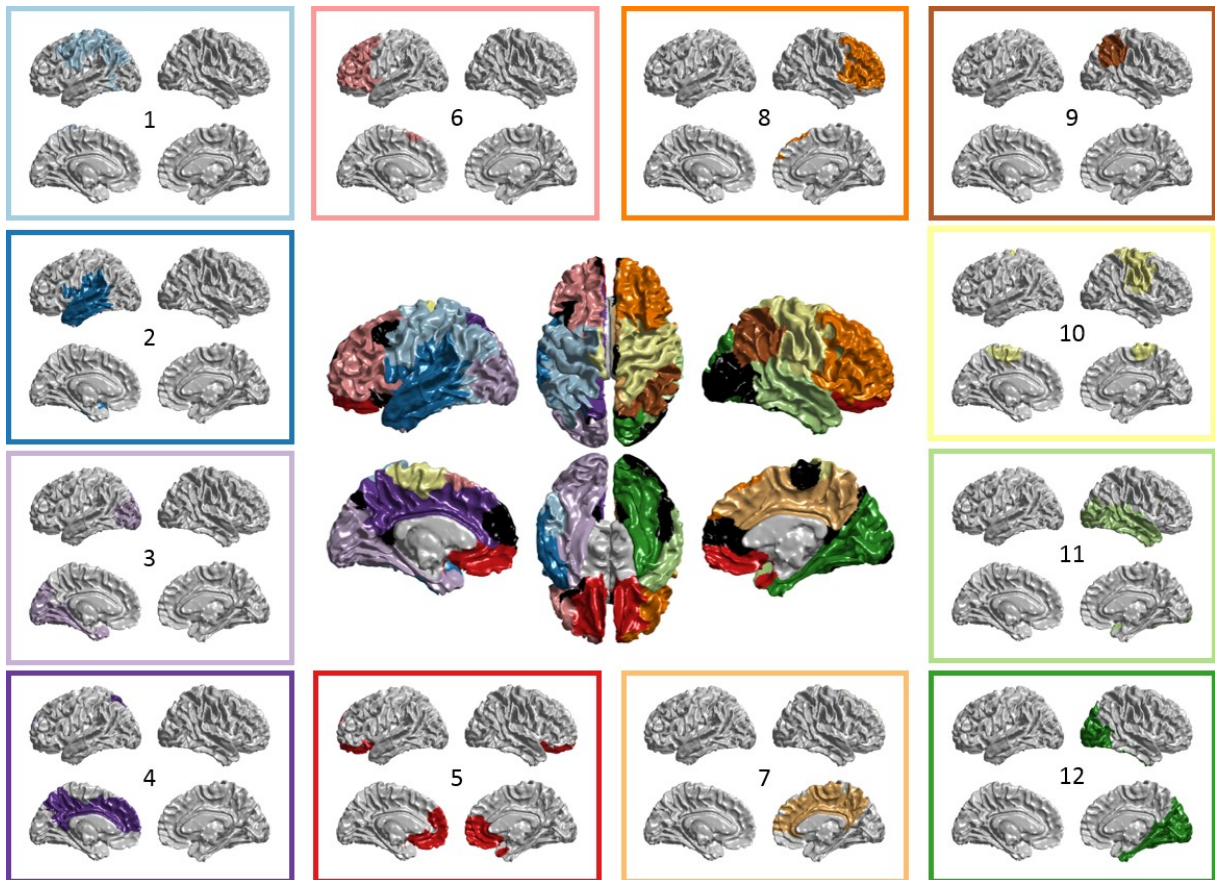
Supplementary Figure 3.4.5. ICVF lifespan measures and confidence intervals (CIs). Lifespan measures for the age of peak maturity (Peak Age), the tissue value at peak maturity (Peak Value) and the cumulative tissue change from age 10 to age 75 (Lifetime Change) are shown for each of the 3015 network edges connecting 349 cortical and sub-cortical nodes. 95% CIs were estimated from model bootstrapping. Peak Age values are in years; Peak Value and Lifetime Change measures are expressed in fractional units.



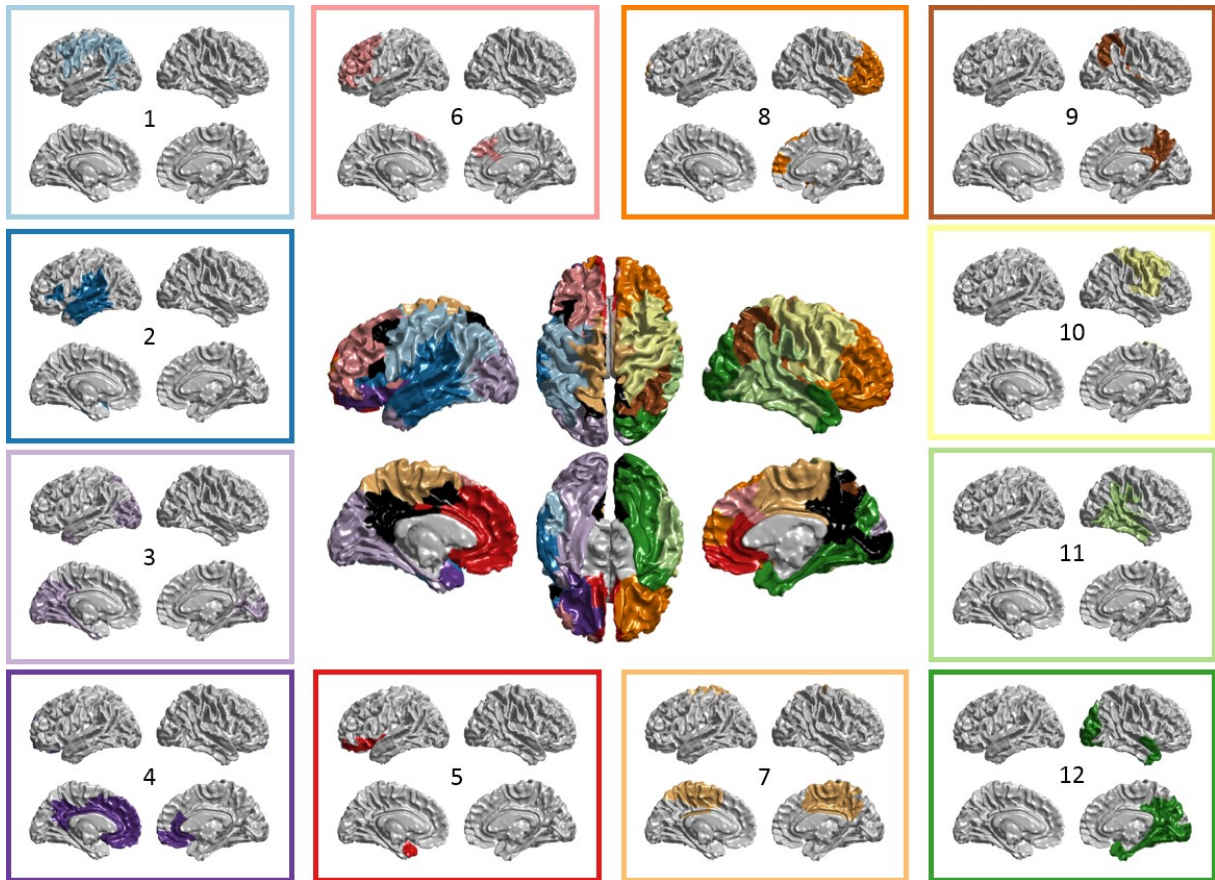
Supplementary Figure 3.5. Partial correlations of lifespan measures. (a) Partial correlations of all pair-wise relationships between lifespan measures across the entire white matter (global) and for each lifespan module. Significant correlations ($p < 0.05$, Bonferroni corrected) are highlighted using an outlined box. Each lifespan module exhibits a unique maturational fingerprint of tissue microstructure interactions (b) Associated p-values for each partial correlation. The order of matrix elements is outlined below.



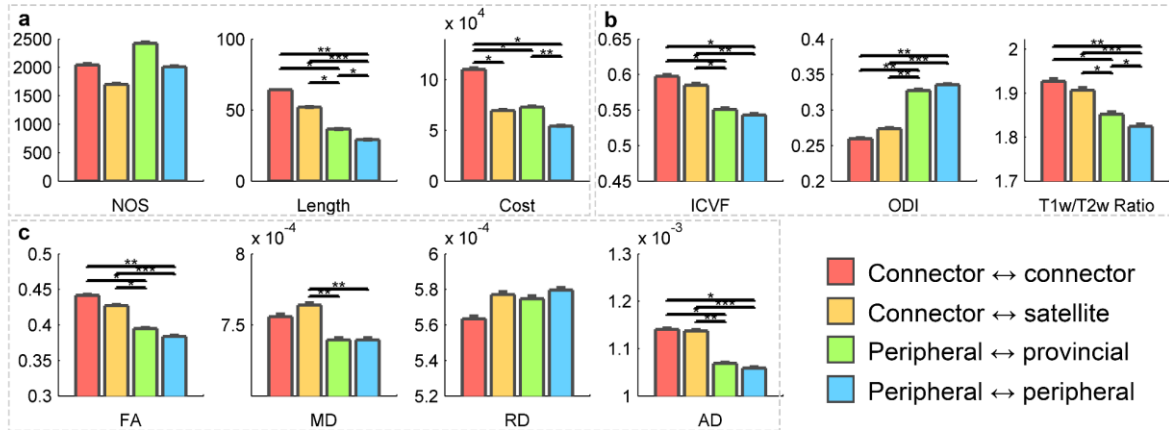
Supplementary Figure 4.1. Edge weight histograms (number of streamlines, NOS) for a) the principal CoLau dataset and b) the replication HCP dataset.



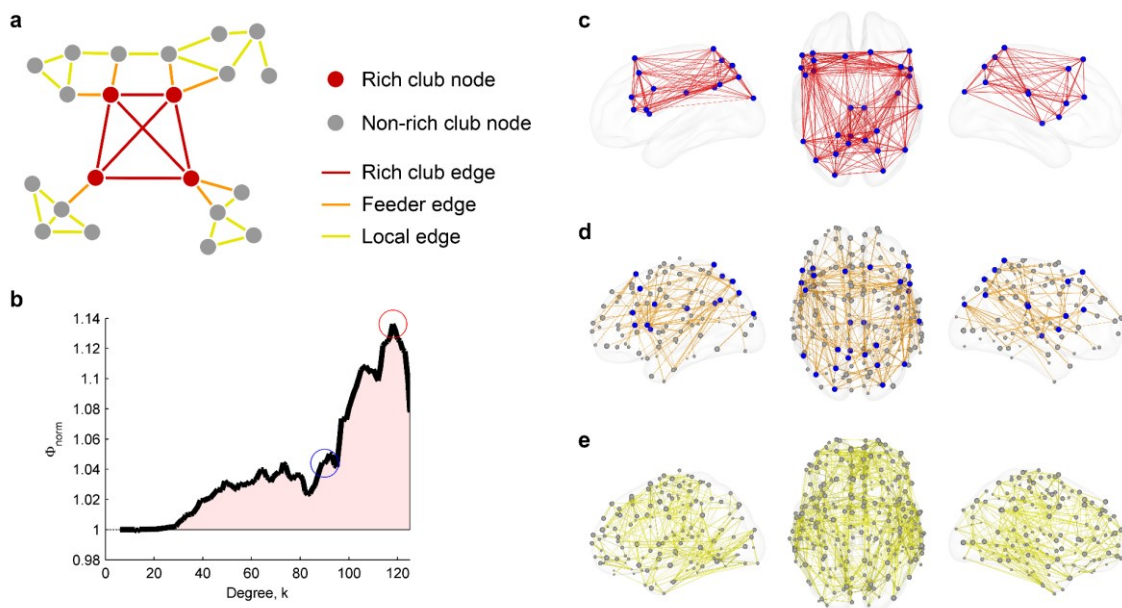
Supplementary Figure 4.2. Modular organization for the CoLauS dataset at level 1. Nodes are projected onto the cortical surface and colored according to their module assignment. Notice the high degree of hemispheric symmetry across the majority of modules.



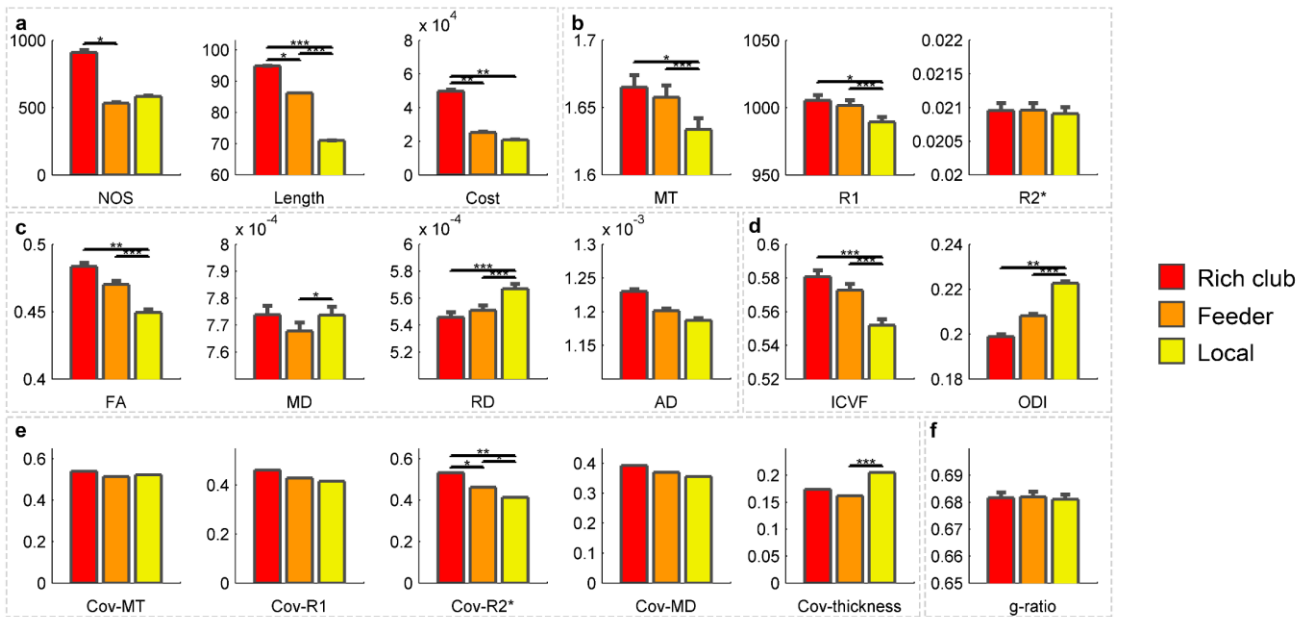
Supplementary Figure 4.3. Modular organization for the CoLauS dataset at level 1. Nodes are projected onto the cortical surface and colored according to their module assignment. Notice the high degree of hemispheric symmetry across the majority of modules.



Supplementary Figure 4.4. Structural characteristics of modular edge class connections in the HCP replication dataset. Edge class types ordered from most- to least-integrative are connector-connector (red), connector-satellite (orange), peripheral-provincial (green) and peripheral-peripheral (blue) connections. Bar graphs show the mean microstructural tissue property values across the edge classes for multiple structural measurements. Data on edge class values are provided for: a) the number of streamlines (NOS) and length of edges for the 4 edge classes; d) NODDI measures of ICVF and ODI, and the T1w/T2w ratio measurement; c) DTI measures of FA, MD, RD and AD. The general trends are extremely similar to the main CoLauS dataset, showing increased microstructural organization and investment in the brain's most integrative connections. Error bars express the standard deviation of a measurement over the group of subjects. Significance assessed using permutation testing (10,000 permutations): * $P < 0.05$, ** $P < 0.01$, *** $P < 0.001$.



Supplementary Figure 4.5. Rich club organization of structural brain networks. a) A toy network detailing how a graph can be classified into rich club (red) and non-rich club (grey) nodes, and rich club (red), feeder (orange) and local (yellow) edges. b) Normalized rich club curve (black) taken as the ratio between the average richness at each degree level, k , over the group of subjects and a randomized rich club curve in representative control networks (1000 randomized networks per subject, controlling for degree sequence). Blue and red circles highlight the lowest and highest rich club levels investigated in this work. Rich club organization is presented on glass brains, detailing the spatial organization of rich club nodes (blue), non-rich club nodes (grey), and c) rich club edges (red), d) feeder edges (orange) and e) local (yellow) edges.



Supplementary Figure 4.6. Structural characteristics of rich club connections in the principal CoLauS dataset. Edge class types represent rich club (red), feeder (orange) and local (yellow) edges. Bar graphs show the mean microstructural tissue property values across the edge classes for multiple structural measurements. Data on edge class values are provided for: a) the number of streamlines (NOS) and length of edges for the 4 edge classes; b) quantitative measures of MT, R1 and R2*; c) DTI measures of FA, MD, RD and AD; d) NODDI measures of ICVF and ODI; e) structural covariance of MT, R1m R2*, MD and cortical thickness; and f) the *g*-ratio tissue measurements. The general trends show increased microstructural organization and investment in the brain's rich club connections. Error bars express the standard deviation of a measurement over the group of subjects. Significance assessed using permutation testing (10,000 permutations): * $P < 0.05$, ** $P < 0.01$, *** $P < 0.001$.

Supplementary tables

	CingC	CingH	IFOF	ILF	SLF	UNC	ARC	TR	CST	CC. Major	CC. Minor	Mean ± Std
FA												
Maturation	0.71	0.72	0.11	0.09	-3.17	1.41	-2.99	-1.05	-3.23	1.02	-11.49	-1.62 ±3.71
Senescence	-2.36	-4.45	-3.67	-6.45	-0.31	-2.95	0.40	4.64	0.55	-2.42	0.00	-1.55 ±3.01
ICVF												
Maturation	6.06	8.78	2.23	5.15	3.69	10.04	3.22	6.10	5.09	2.98	0.21	4.87 ±2.85
Senescence	-2.87	-3.40	-4.65	-4.56	-2.60	-4.36	-2.69	-2.47	-0.35	-3.61	-5.58	-3.38 ±1.42
g-ratio												
Maturation	-0.19	-0.97	-0.34	-0.45	-0.04	-0.48	-0.10	-0.13	-0.01	-0.11	-0.45	-0.30 ±0.28
Senescence	2.76	2.14	1.54	2.26	2.21	1.61	2.07	2.18	1.53	2.40	2.36	2.10 ±0.39
MD												
Maturation	-3.24	-2.60	-1.27	-3.56	-2.49	-4.51	-1.12	-3.54	-2.75	-1.92	-2.45	-2.68 ±1.01
Senescence	3.49	0.54	5.72	4.35	4.13	3.22	4.07	3.17	2.11	0.88	5.68	3.40 ±1.69
MT												
Maturation	3.10	7.24	2.51	4.27	1.19	7.21	1.29	3.28	1.73	2.04	1.45	3.21 ±2.20
Senescence	-8.53	-7.75	-7.89	-9.22	-7.47	-8.06	-7.32	-7.37	-4.50	-8.18	-10.06	-7.85 ±1.39
ODI												
Maturation	6.03	8.67	6.50	11.12	6.35	9.94	4.41	7.64	13.95	-1.25	21.59	8.63 ±5.81
Senescence	-0.33	5.13	-0.92	-0.39	-3.17	-1.68	-2.50	-11.33	-3.63	7.47	-0.09	-1.04 ±4.82
R1												
Maturation	3.53	6.54	3.32	4.05	1.71	6.54	1.89	4.74	2.88	1.80	2.30	3.57 ±1.76
Senescence	-5.70	-4.41	-5.20	-5.79	-5.18	-5.00	-4.87	-5.02	-2.95	-6.54	-5.94	-5.15 ±0.94
R2*												
Maturation	7.17	12.18	6.84	6.74	4.34	10.41	4.34	8.92	7.20	3.75	3.69	6.87 ±2.79
Senescence	-5.77	-1.89	-5.19	-4.14	-5.38	-3.49	-4.60	-6.45	-1.64	-5.41	-5.63	-4.51 ±1.58

Supplementary Table 2.1. Percentage measurement change during maturation and senescence. Maturation defined as percentage change from age 15 to peak; senescence defined as percentage change from peak to age 75. CingC: cingulum-cingulate; CingH: cingulum-hippocampus; IFOF: inferior fronto-occipital fasciculus; ILF: inferior longitudinal fasciculus; SLF: superior longitudinal fasciculus; UNC: uncinate fasciculus; ARC: arcuate fasciculus; TR: thalamic radiations; CST: corticospinal tract; CC. Major: corpus callosum forceps-major; CC. Minor: corpus callosum forceps-minor.

	Age	Age ²	Sex	Hemisphere	Resolution	Age*Sex	Age*Hemisphere	Age*Resolution	R ²
MT									
TR	1.418 [<0.001]	-1.720 [<0.001]	-0.003 [0.963]	0.183 [0.005]	0.065 [0.249]	-0.104 [0.150]	-0.146 [0.085]	0.069 [0.213]	0.276
CST	0.922 [<0.001]	-1.081 [<0.001]	0.065 [0.372]	-0.009 [0.905]	0.287 [<0.001]	-0.021 [0.790]	-0.103 [0.176]	-0.120 [0.049]	0.123
CingC	1.512 [<0.001]	-1.888 [<0.001]	0.142 [0.028]	0.048 [0.456]	-0.082 [0.561]	-0.223 [0.002]	-0.035 [0.609]	0.015 [0.785]	0.310
CingH	1.959 [<0.001]	-2.040 [<0.001]	0.125 [0.117]	-0.163 [0.072]	-0.035 [0.598]	-0.154 [0.083]	0.032 [0.701]	0.036 [0.579]	0.161
FOF	1.278 [<0.001]	-1.675 [<0.001]	0.093 [0.249]	0.059 [0.222]	-0.044 [0.527]	-0.167 [0.056]	-0.076 [0.370]	0.044 [0.514]	0.299
ILF	1.656 [<0.001]	-2.059 [<0.001]	0.093 [0.160]	-0.058 [0.564]	-0.050 [0.376]	-0.085 [0.243]	0.032 [0.643]	0.039 [0.482]	0.285
SIF	0.905 [<0.001]	-1.326 [<0.001]	0.188 [0.004]	-0.063 [0.338]	0.050 [0.374]	-0.247 [<0.001]	-0.084 [0.223]	-0.062 [0.256]	0.285
UNC	2.005 [<0.001]	-2.152 [<0.001]	-0.011 [0.889]	0.257 [0.002]	-0.023 [0.734]	-0.006 [0.945]	-0.100 [0.214]	-0.071 [0.271]	0.197
ARC	0.904 [<0.001]	-1.297 [<0.001]	0.157 [0.019]	0.073 [0.273]	0.002 [0.978]	-0.211 [0.004]	-0.020 [0.776]	-0.007 [0.905]	0.261
CC_Major	1.225 [<0.001]	-1.568 [<0.001]	0.195 [0.050]	-0.057 [0.402]	-0.157 [0.068]	-0.284 [0.010]		0.051 [0.545]	0.256
CC_Minor	0.801 [<0.001]	-1.324 [<0.001]	0.024 [0.787]	-0.068 [0.360]	0.020 [0.791]	-0.087 [0.364]		0.108 [0.142]	0.359
R1									
TR	2.063 [<0.001]	-2.116 [<0.001]	0.100 [0.140]	0.072 [0.288]	-0.210 [<0.001]	-0.269 [<0.001]	-0.087 [0.218]	0.019 [0.732]	0.238
CST	1.260 [<0.001]	-1.245 [<0.001]	0.168 [0.023]	-0.059 [0.889]	-0.042 [0.626]	-0.208 [0.010]	-0.081 [0.257]	-0.044 [0.479]	0.097
CingC	1.742 [<0.001]	-1.963 [<0.001]	0.151 [0.024]	0.064 [0.330]	-0.291 [<0.001]	-0.274 [<0.001]	-0.010 [0.891]	0.057 [0.308]	0.270
CingH	1.707 [<0.001]	-1.628 [<0.001]	0.024 [0.762]	-0.088 [0.212]	-0.045 [0.645]	-0.086 [0.325]	0.050 [0.546]	0.021 [0.745]	0.175
FOF	1.657 [<0.001]	-1.810 [<0.001]	0.189 [0.025]	0.136 [0.107]	-0.223 [0.002]	-0.316 [<0.001]	-0.112 [0.201]	-0.023 [0.745]	0.235
ILF	1.796 [<0.001]	-1.970 [<0.001]	0.195 [0.005]	-0.086 [0.159]	-0.233 [<0.001]	-0.229 [0.003]	-0.018 [0.800]	0.026 [0.644]	0.230
SIF	1.195 [<0.001]	-1.381 [<0.001]	0.276 [<0.001]	-0.068 [0.190]	-0.166 [0.005]	-0.359 [<0.001]	-0.063 [0.375]	0.010 [0.858]	0.229
UNC	2.018 [<0.001]	-1.970 [<0.001]	0.078 [0.312]	0.158 [0.101]	-0.070 [0.611]	-0.119 [0.157]	-0.142 [0.076]	-0.087 [0.178]	0.202
ARC	1.199 [<0.001]	-1.459 [<0.001]	0.257 [<0.001]	-0.027 [0.608]	-0.156 [0.009]	-0.324 [<0.001]	0.039 [0.588]	0.012 [0.837]	0.191
CC_Major	1.116 [<0.001]	-1.404 [<0.001]	0.222 [0.030]	-0.027 [0.608]	-0.271 [0.002]	-0.280 [0.014]		0.077 [0.371]	0.210
CC_Minor	1.133 [<0.001]	-1.432 [<0.001]	0.041 [0.675]	-0.051 [0.603]	-0.251 [0.003]	-0.184 [0.083]		0.058 [0.474]	0.216

R2*	Age		Age ²		Sex		Hemisphere		Resolution		Age*Sex		Age*Hemisphere		Age*Resolution		R ²
	β	p	β	p	β	p	β	p	β	p	β	p	β	p	β	p	
TR	1.376	<0.001	-1.489	<0.001	-0.051	(0.487)	0.027	(0.710)	-0.025	(0.698)	-0.029	(0.718)	0.000	(0.996)	0.088	(0.153)	0.098
CST	1.048	<0.001	-0.867	<0.001	0.098	(0.200)	0.066	(0.386)	0.041	(0.533)	-0.171	(0.089)	-0.029	(0.713)	0.005	(0.937)	0.044
CingC	1.441	<0.001	-1.552	<0.001	0.072	(0.323)	0.066	(0.360)	0.017	(0.805)	-0.175	(0.027)	0.016	(0.837)	0.130	(0.033)	0.126
CingH	1.001	<0.001	-0.850	<0.001	-0.037	(0.662)	-0.020	(0.811)	0.225	(0.001)	0.029	(0.753)	0.012	(0.893)	0.240	<0.001	0.083
IFOF	1.160	<0.001	-1.313	<0.001	-0.086	(0.352)	-0.063	(0.497)	0.071	(0.371)	-0.001	(0.990)	0.046	(0.637)	0.025	(0.744)	0.080
ILF	1.162	<0.001	-1.199	<0.001	0.019	(0.799)	0.026	(0.724)	0.205	(0.002)	-0.076	(0.362)	0.005	(0.954)	0.195	(0.002)	0.068
SILF	0.876	<0.001	-1.011	<0.001	0.154	(0.040)	0.003	(0.971)	0.018	(0.775)	-0.170	(0.038)	-0.057	(0.467)	-0.008	(0.902)	0.070
UNC	1.252	<0.001	-1.128	<0.001	0.074	(0.377)	0.173	(0.038)	0.038	(0.598)	-0.108	(0.240)	-0.101	(0.246)	0.021	(0.767)	0.056
ARC	0.950	<0.001	-1.057	<0.001	0.075	(0.299)	0.377	<0.001	0.009	(0.881)	-0.070	(0.373)	-0.111	(0.142)	0.001	(0.986)	0.133
CC_Major	0.780	<0.001	-0.972	<0.001	0.007	(0.953)			0.102	(0.296)	0.017	(0.890)			0.073	(0.440)	0.052
CC_Minor	0.573	(0.005)	-0.811	<0.001	-0.071	(0.506)			0.097	(0.287)	0.027	(0.815)			0.123	(0.166)	0.068
g-ratio																	
TR	-0.190	(0.174)	0.505	<0.001	0.062	(0.387)	-0.175	(0.015)	-0.474	<0.001	0.004	(0.963)	0.186	(0.013)	-0.453	<0.001	0.146
CST	-0.068	(0.643)	0.314	(0.027)	-0.018	(0.812)	-0.019	(0.789)	0.156	(0.016)	-0.068	(0.412)	0.091	(0.248)	-0.195	(0.002)	0.066
CingC	-0.397	(0.004)	0.735	<0.001	-0.185	(0.009)	0.051	(0.472)	0.468	<0.001	0.205	(0.008)	0.036	(0.624)	-0.332	<0.001	0.178
CingH	-0.643	<0.001	0.769	<0.001	-0.142	(0.081)	0.060	(0.661)	0.615	<0.001	0.095	(0.293)	0.055	(0.515)	-0.426	<0.001	0.127
IFOF	-0.589	<0.001	0.770	<0.001	-0.083	(0.357)	0.017	(0.828)	0.680	<0.001	0.196	(0.044)	0.048	(0.607)	-0.571	<0.001	0.132
ILF	-0.522	<0.001	0.852	<0.001	-0.045	(0.536)	0.098	(0.276)	0.534	<0.001	0.033	(0.680)	-0.082	(0.282)	-0.377	<0.001	0.134
SILF	-0.220	(0.116)	0.503	<0.001	-0.089	(0.219)	0.042	(0.538)	0.160	(0.010)	0.192	(0.015)	0.064	(0.394)	-0.108	(0.073)	0.143
UNC	-0.386	(0.011)	0.602	<0.001	-0.062	(0.449)	-0.023	(0.723)	0.577	<0.001	-0.020	(0.820)	-0.005	(0.953)	-0.405	<0.001	0.090
ARC	-0.235	(0.097)	0.522	<0.001	-0.071	(0.332)	0.068	(0.349)	0.239	<0.001	0.190	(0.016)	-0.008	(0.919)	-0.175	(0.004)	0.128
CC_Major	-0.320	(0.133)	0.490	(0.019)	-0.161	(0.142)			0.306	(0.001)	0.297	(0.014)			-0.160	(0.083)	0.096
CC_Minor	-0.489	(0.013)	0.760	<0.001	-0.039	(0.704)			0.406	<0.001	0.153	(0.173)			-0.394	<0.001	0.128

Supplementary Table 2. Regression models of age, sex, hemisphere and resolution on tract-averaged white matter R2* and g-ratio. Associations significant at p<0.001 (uncorrected) highlighted in bold. Male, high resolution and left hemisphere coded as 0. Cing: cingulate cortex; CST: corpus callosum forceps-major; ILF: inferior longitudinal fasciculus; IFOF: inferior occipital fasciculus; ILF: inferior longitudinal fasciculus; UNC: uncinata fasciculus; TR: transverse occipital fasciculus; CC_Major: corpus callosum forceps-major; CC_Minor: corpus callosum forceps-minor.

	Age		Age ²		Sex		Hemisphere		Resolution		Age*Sex		Age*Hemisphere		Age*Resolution		R ²
FA																	
TR	-0.647	<0.0001	0.811	<0.0001	-0.048	(0.512)	-0.121	(0.098)	-0.094	(0.138)	-0.169	(0.086)	0.256	<0.0001	0.109	(0.076)	0.099
CST	-0.988	<0.0001	0.792	<0.0001	-0.058	(0.444)	0.100	(0.179)	-0.319	<0.0001	-0.032	(0.697)	0.010	(0.896)	0.211	<0.0001	0.073
CingC	0.242	(0.086)	-0.321	(0.018)	-0.148	(0.042)	0.450	<0.0001	0.082	(0.183)	0.042	(0.594)	-0.127	(0.093)	0.019	(0.749)	0.140
CingH	0.076	(0.655)	-0.299	(0.067)	-0.187	(0.029)	-0.170	(0.046)	0.212	(0.003)	0.107	(0.260)	0.141	(0.113)	0.122	(0.079)	0.038
IFOB	0.192	(0.259)	-0.290	(0.071)	-0.089	(0.341)	-0.448	<0.0001	0.078	(0.385)	0.049	(0.631)	0.259	(0.008)	-0.070	(0.369)	0.049
ILF	-0.426	<0.0001			0.071	(0.318)	0.137	(0.053)	0.382	<0.0001	-0.056	(0.468)	-0.004	(0.957)	0.316	<0.0001	0.178
SLF	-0.414	(0.002)	0.296	(0.024)	0.024	(0.731)	-0.342	<0.0001	0.246	<0.0001	-0.073	(0.341)	-0.065	(0.378)	0.140	(0.017)	0.188
UNC	0.520	<0.0001	-0.554	<0.0001	-0.132	(0.105)	0.410	<0.0001	0.218	(0.002)	-0.045	(0.614)	-0.277	(0.001)	0.078	(0.256)	0.102
ARC	-0.569	<0.0001	0.462	<0.0001	-0.004	(0.953)	0.524	<0.0001	0.332	<0.0001	0.016	(0.841)	-0.188	(0.012)	0.263	<0.0001	0.157
CC_Major	0.334	(0.128)	-0.547	(0.011)	-0.017	(0.883)			0.215	(0.032)	0.068	(0.585)			0.212	(0.026)	0.036
CC_Minor	-1.107	<0.0001	0.464	(0.004)	-0.091	(0.291)			0.127	(0.086)	0.050	(0.596)			0.089	(0.218)	0.387
MD																	
TR	-1.902	<0.0001	2.040	<0.0001	-0.135	(0.048)	-0.009	(0.998)	0.614	<0.0001	0.157	(0.036)	-0.067	(0.350)	0.445	<0.0001	0.224
CST	-1.740	<0.0001	1.794	<0.0001	-0.090	(0.204)	-0.102	(0.071)	0.718	<0.0001	0.070	(0.366)	0.050	(0.500)	0.527	<0.0001	0.183
CingC	-1.415	<0.0001	1.595	<0.0001	0.013	(0.858)	0.009	(0.997)	0.428	<0.0001	0.058	(0.454)	-0.063	(0.399)	0.284	<0.0001	0.158
CingH	-0.760	<0.0001	0.729	<0.0001	-0.044	(0.599)	0.012	(0.887)	0.436	<0.0001	0.025	(0.791)	-0.139	(0.112)	0.242	<0.0001	0.067
IFOB	-0.937	<0.0001	1.295	<0.0001	-0.001	(0.994)	-0.305	<0.0001	0.396	<0.0001	-0.063	(0.482)	0.137	(0.111)	0.338	<0.0001	0.269
ILF	-1.502	<0.0001	1.687	<0.0001	-0.062	(0.392)	-0.153	(0.032)	0.334	<0.0001	0.051	(0.516)	0.119	(0.113)	0.238	<0.0001	0.166
SLF	-1.143	<0.0001	1.435	<0.0001	-0.152	(0.033)	0.003	(0.963)	0.186	(0.003)	0.071	(0.359)	-0.006	(0.938)	0.158	(0.008)	0.162
UNC	-1.870	<0.0001	1.914	<0.0001	0.053	(0.491)	-0.210	(0.007)	0.424	<0.0001	0.076	(0.368)	0.026	(0.749)	0.364	<0.0001	0.188
ARC	-0.925	<0.0001	1.208	<0.0001	-0.147	(0.040)	-0.129	(0.068)	0.173	(0.005)	0.063	(0.419)	-0.009	(0.903)	0.145	(0.015)	0.157
CC_Major	-0.828	<0.0001	0.868	<0.0001	0.204	(0.073)			0.389	<0.0001	-0.220	(0.079)			0.299	(0.002)	0.030
CC_Minor	-0.983	<0.0001	1.412	<0.0001	0.076	(0.423)			0.407	<0.0001	-0.155	(0.134)			0.297	<0.0001	0.254

	Age		Age ²		Sex		Hemisphere		Resolution		Age*Sex		Age*Hemisphere		Age*Resolution		R ²
ODI																	
TR	1.460	<0.001	-1.576	<0.001	0.134	(0.055)	0.072	(0.299)	0.604	<0.001	0.043	(0.576)	-0.183	(0.012)	-0.462	<0.001	0.190
CST	1.475	<0.001	-1.276	<0.001	0.086	(0.239)	0.035	(0.624)	0.687	<0.001	0.001	(0.993)	-0.041	(0.588)	-0.459	<0.001	0.126
CingC	0.518	<0.001	-0.419	(0.003)	0.125	(0.095)	-0.305	<0.001	0.390	<0.001	-0.069	(0.401)	0.124	(0.115)	-0.236	<0.001	0.078
CingH	0.484	(0.003)	-0.229	(0.151)	0.144	(0.084)	0.101	(0.224)	0.621	<0.001	-0.153	(0.099)	-0.065	(0.455)	-0.397	<0.001	0.087
IFOF	-0.026	(0.626)			0.097	(0.292)	0.478	<0.001	0.170	(0.115)	-0.049	(0.620)	-0.252	(0.009)	-0.080	(0.275)	0.087
ILF	1.248	<0.001	-0.908	<0.001	0.029	(0.681)	-0.117	(0.098)	0.783	<0.001	-0.044	(0.576)	-0.064	(0.390)	-0.545	<0.001	0.174
SLF	0.857	<0.001	-0.833	<0.001	0.028	(0.674)	0.390	<0.001	0.390	<0.001	0.071	(0.326)	0.084	(0.228)	-0.243	<0.001	0.266
UNC	0.598	<0.001	-0.522	<0.001	0.044	(0.590)	-0.240	(0.003)	0.729	<0.001	0.028	(0.750)	0.214	(0.012)	-0.500	<0.001	0.102
ARC	0.754	<0.001	-0.724	<0.001	0.065	(0.354)	-0.568	<0.001	0.407	<0.001	-0.023	(0.762)	0.206	(0.005)	-0.360	<0.001	0.197
CC. Major	-0.322	(0.143)	0.536	(0.013)	0.036	(0.751)			0.235	(0.022)	-0.070	(0.576)			-0.212	(0.027)	0.035
CC. Minor	1.743	<0.001	-1.222	<0.001	0.022	(0.815)			0.583	<0.001	0.054	(0.590)			-0.385	<0.001	0.293
KVF																	
TR	1.458	<0.001	-1.336	<0.001	0.071	(0.319)	0.006	(0.931)	0.852	<0.001	-0.114	(0.142)	0.029	(0.696)	-0.607	<0.001	0.156
CST	1.230	<0.001	-0.932	<0.001	0.058	(0.422)	-0.135	(0.660)	0.788	<0.001	-0.171	(0.029)	0.032	(0.668)	-0.529	<0.001	0.147
CingC	1.339	<0.001	-1.264	<0.001	-0.056	(0.437)	0.137	(0.857)	0.722	<0.001	-0.012	(0.875)	-0.016	(0.836)	-0.511	<0.001	0.133
CingH	1.240	<0.001	-1.101	<0.001	-0.025	(0.749)	-0.048	(0.539)	0.895	<0.001	-0.091	(0.298)	0.035	(0.670)	-0.603	<0.001	0.179
IFOF	0.652	<0.001	-0.779	<0.001	0.014	(0.869)	0.101	(0.246)	0.829	<0.001	0.016	(0.868)	-0.026	(0.773)	-0.686	<0.001	0.186
ILF	1.222	<0.001	-1.229	<0.001	0.040	(0.581)	0.009	(0.901)	0.737	<0.001	-0.055	(0.488)	-0.024	(0.750)	-0.501	<0.001	0.143
SLF	1.200	<0.001	-1.171	<0.001	0.117	(0.119)	-0.019	(0.801)	0.485	<0.001	-0.050	(0.538)	-0.038	(0.628)	-0.363	<0.001	0.071
UNC	1.831	<0.001	-1.666	<0.001	-0.113	(0.141)	0.252	(0.001)	0.938	<0.001	0.002	(0.985)	-0.155	(0.053)	-0.745	<0.001	0.202
ARC	0.993	<0.001	-1.003	<0.001	0.089	(0.235)	0.121	(0.004)	0.532	<0.001	0.005	(0.955)	-0.048	(0.535)	-0.370	<0.001	0.079
CC. Major	0.684	(0.002)	-0.769	<0.001	0.010	(0.976)			0.280	(0.043)	0.078	(0.531)			-0.087	(0.363)	0.032
CC. Minor	0.349	(0.067)	-0.598	(0.001)	0.021	(0.832)			0.623	<0.001	0.017	(0.874)			-0.429	<0.001	0.190

Associations significant at $p < 0.001$ (uncorrected) highlighted in bold. Male, high resolution and left hemisphere coded as 0. Cing: cingulate cortex; IFOF: inferior fronto-occipital fasciculus; ILF: inferior longitudinal fasciculus; SLF: superior longitudinal fasciculus; UNC: uncinata fasciculus; CC: corpus callosum; C.Major: corpus callosum forceps-major; C.Minor: corpus callosum forceps-minor.

Metric	Model	p-value versus opposing model			
		Linear	Poly2	Poisson	LOWESS
MT	Linear				
	Poly2	<0.001		<0.001	
	Poisson	<0.001			
	LOWESS	<0.001		<0.001	
R1	Linear			<0.001	
	Poly2	<0.001		<0.001	<0.05
	Poisson				
	LOWESS	<0.001		<0.001	
R2s	Linear				
	Poly2	<0.001			
	Poisson	<0.001	<0.001		<0.05
	LOWESS	<0.001			
MD	Linear				
	Poly2	<0.001			
	Poisson	<0.001	<0.05		
	LOWESS	<0.001	<0.001	<0.05	
ICVF	Linear				
	Poly2	<0.001			
	Poisson	<0.001	<0.001		
	LOWESS	<0.001	<0.001	<0.001	

Supplementary Table 3.1. Aging model selection for each MR biomarker using repeated 5-fold cross-validation. Four aging models were tested using repeated 5-fold cross-validation. These models were: a linear model (linear), a second order polynomial (Poly2), a Poisson curve (Poisson), and a smoothing spline (LOWESS). Cross-validated errors across all white matter edges and iterations were compared for each MRI biomarker using a Wilcoxon rank sum test. The table lists all significant results ($p < 0.05$, Bonferroni corrected) and optimal models are highlighted in green. If two models performed comparably the simplest model was selected (e.g. for MT Poly2 was selected).

aparc name	HCP-MMP1	N-times connector
lh-caudalmiddlefrontal	L_8Av	2
lh-parsopercularis	L_44	2
	L_6r	2
lh-posteriorcingulate	L_RSC	3
lh-precentral	L_43	2
	L_6r	2
lh-precuneus	L_POS2	2
lh-superiorfrontal	L_24dv	2
	L_8BL	2
	L_SFL	2
lh-superiorparietal	L_7AL	2
rh-caudalmiddlefrontal	R_8Av	2
rh-insula	R_PoI1	3
rh-middletemporal	R_TE1p	2
rh-parsopercularis	R_6r	3
rh-posteriorcingulate	R_RSC	2
rh-precentral	R_FOP1	2
	R_PEF	2
rh-precuneus	R_7Am	2
rh-rostralmiddlefrontal	R_9a	2
rh-superiorfrontal	R_8BM	2
	R_SFL	3
rh-superiorparietal	R_7AL	3
	R_V3A	2
rh-supramarginal	R_PF	3

Supplementary Table 4.1. Connector hub nodes. Connector hub regions listed along with their aparc and HCP-MMP1 atlas names. N-times connector reports the number of times the region was determined to be a connector hub across the three hierarchical levels. Only connector hub nodes which were selected at 2 or more hierarchical levels are reported here. aparc refers to the Desikan-Killiany freesurfer atlas (Desikan et al., 2006); HCP-MMP1 refers to the regional definitions from a recent multi-modal parcellation of human cerebral cortex (Glasser et al., 2016).

aparc name	HCP-MMP1	Degree
lh-caudalmiddlefrontal	L_8Av-ii	134
lh-inferiorparietal	L_PGs	115
lh-inferiorparietal	L_PFm	107
lh-parsopercularis	L_44	127
lh-parsopercularis	L_6r-i	118
lh-parsopercularis	L_FOP4	111
lh-posteriorcingulate	L_RSC	144
lh-precentral	L_6r-ii	107
lh-precuneus	L_7Am	112
lh-precuneus	L_7m	108
lh-rostralmiddlefrontal	L_IFSp	113
lh-superiorfrontal	L_8BL	124
lh-superiorparietal	L_MIP	136
lh-superiorparietal	L_7AL	125
lh-superiorparietal	L_V3A	107
rh-caudalmiddlefrontal	R_8Av	143
rh-inferiorparietal	R_PGs	131
rh-insula	R_Po1-i	113
rh-parsopercularis	R_6r	152
rh-posteriorcingulate	R_RSC	142
rh-precentral	R_FOP1	115
rh-precuneus	R_7Am	139
rh-rostralmiddlefrontal	R_IFSp	114
rh-superiorfrontal	R_SFL	131
rh-superiorparietal	R_7AL	141
rh-superiorparietal	R_MIP	120
rh-supramarginal	R_PF	132

Supplementary Table 4.2. Rich club nodes. Rich club regions listed along with their aparc and HCP-MMP1 atlas names and degree level. aparc refers to the Desikan-Killiany freesurfer atlas (Desikan et al., 2006); HCP-MMP1 refers to the regional definitions from a recent multi-modal parcellation of human cerebral cortex (Glasser et al., 2016).